Application of experimental and analytical approaches in characterizing coronary stents

VORGELEGT VON
M.E. Muhammad Saqib

Dissertation
Zur Erlangung des akademischen Grades Doktoringenieur
(Dr. -Ing)

Lehrstuhl für Materialwissenschaft und Nanotechnik
Institut für Werkstoffwissenschaft
Fakultät Maschinenwesen
Technische Universität Dresden

June 21, 2023

Eingereicht am 12.04.2022

1. Gutachter: Prof. Dr. Gianaurelio Cuniberti (TU Dresden)
2. Gutachter: Prof. Dr. Markus Kästner (TU Dresden)
3. Gutachter: Dr. Nadia Licciardello (University of Catania)

Verteidigt am 11.07.2022

Declaration of Authorship

I, Muhammad SAQIB, declare that this thesis titled, "Application of experimental and analytical approaches in characterizing coronary stents" and the work presented in it are my own. I confirm that:

- This work was done wholly or mainly while in candidature for a research degree at this University.
- Where I have consulted the published work of others, this is always clearly attributed.
- Where I have quoted from the work of others, the source is always given. With the exception of such quotations, this thesis is entirely my own work.
- I have acknowledged all main sources of help.
- Where the thesis is based on work done by myself jointly with others, I have made clear exactly what was done by others and what I have contributed myself.

Signed: _____

Date: _____

"Verily, along with every hardship is relief."

Al Qura'n, (30:94)

TECHNISCHE UNIVERSITÄT DRESDEN

Abstract

Fakultät Maschinenwesen
Lehrstuhl für Materialwissenschaft und Nanotechnik

Doktoringenieur (Dr. -Ing)

Application of experimental and analytical approaches in characterizing coronary stents

by Muhammad SAQIB

Coronary artery disease (CAD) affects every fifth person in the world. The gold-standard treatment for CAD is stent implantation, however, the existing therapy is not sufficient due to many reasons. For instance, in-stent restenosis, biocompatibility, controlled degradation rate, protein adsorption, and adequate endothelialization are still the main concerns. In the last two decades, the field of stent technology has been grown rapidly and many new stent types and in vitro testing methods for stent characterization have been developed to minimize the aforementioned issues. In this vicinity, there are still many unaddressed issues: i) the quantitative analysis of corrosion is conducted with simpler samples made of stent material instead of stents, in most cases due to the absence of a mathematical model to calculate the entire stent surface area (ESSA); ii) in vitro stent testing in environments that are very far from actual physiological environments; iii) Evaluation of the influence of in-vitro test conditions on coated metallic stents; iv) absence of flow-induced shear stress (FISS) corrosion model, to mention a few. This thesis presents the novel ESSA model, the fluid dynamic experimental setup with the integration of various sensors and pH control, the influence of in vitro degradation behavior of the titanium oxynitride (TiO_xN_y) coated stainless steel stents and anodized AZ31 samples, and the FISS corrosion model. The results show some important contributions in this field, however, there is still a huge potential for the development of promising stent characterization solutions.

Kurzfassung

Die koronare Herzkrankheit (KHK) betrifft jeden fünften Menschen auf der Welt. Der Goldstandard bei der Behandlung von KHK ist die Stent-Implantation, doch die bestehende Therapie ist aus vielen Gründen nicht ausreichend. So sind beispielsweise die Restenose im Stent, die Biokompatibilität, die kontrollierte Abbaugeschwindigkeit, die Proteinadsorption und die angemessene Endothelialisierung nach wie vor die Hauptprobleme. In den letzten zwei Jahrzehnten hat sich die Stenttechnologie rasant weiterentwickelt, und es wurden viele neue Stenttypen und In-vitro-Testmethoden zur Stentcharakterisierung entwickelt, um die oben genannten Probleme zu minimieren. In dieser Umgebung gibt es noch viele ungelöste Probleme: i) die quantitative Analyse der Korrosion wird mit einfacheren Proben aus Stentmaterial anstelle von Stents durchgeführt, in den meisten Fällen aufgrund des Fehlens eines mathematischen Modells zur Berechnung der gesamten Stentoberfläche (ESSA); ii) In-vitro-Stent-Tests in Umgebungen, die sehr weit von der tatsächlichen physiologischen Umgebung entfernt sind; iii) Bewertung des Einflusses von In-vitro-Testbedingungen auf beschichtete metallische Stents; iv) Fehlen eines FISS-Korrosionsmodells (flow-induced shear stress), um nur einige zu nennen. In dieser Arbeit werden das neuartige ESSA-Modell, der strömungsdynamische Versuchsaufbau mit der Integration verschiedener Sensoren und pH-Kontrolle, der Einfluss des In-vitro-Degradationsverhaltens der mit Titanoxynitrid (TiO_xN_y) beschichteten Edelstahlstents und anodisierten AZ31-Proben sowie das FISS-Korrosionsmodell vorgestellt. Die Ergebnisse zeigen einige wichtige Beiträge in diesem Bereich, jedoch gibt es noch ein großes Potenzial für die Entwicklung von vielversprechenden Lösungen zur Charakterisierung von Stents.

Acknowledgements

I would like to express my gratitude to my supervisors Prof. Dr. Gianaurelio Cuniberti (TU Dresden), Dr. Natalia Beshchasna (Fraunhofer IKTS) and Dr. Jörg Opitz (Fraunhofer IKTS). They gave me chance to work on a very interesting research topic in a collaborative research environment. This thesis was not possible without their constant support and encouragement. Truly, I do not have the actual words to thank them for their supervision.

I am equally thankful to Prof. Markus Kästner (TU Dresden) for the co-supervision of this dissertation in the modeling part and for being a second reviewer of this work. I could materialize scientifically this part of my research due to many fruitful discussions with him.

I also thank Dr. Nadia Licciardello (University of Catania) for being a third reviewer of this dissertation. I also appreciate her professional feedback in the annual thesis assessment committe (TAC) meetings.

I would especially thank Dr. Malgorzata Kopycinska-Müller for her critical feedback in the presentation of scientific results.

I also thank Dr.-Ing. Lotta Römhildt for their supervision in the early phase of my PhD.

I am grateful to Prof. Anton Ficai for the ICPMS measurements and equally thankful to Dr. Ricardo Bernhardt for the micro-CT measurements.

I am indebted to Hans Matthes, Au Yeung Kwan Ho, Selim Trinervedi, Conner Philips, Martin Küttner, Dr. Benjamin Kruppke and Muaz Draz Salama for their direct or indirect help in my work.

I also appreciate the support from the secretaries Sylvi Katzarrow (TU Dresden), Grit Kost (TU Dresden), and Sylvana Dietz (Fraunhofer IKTS) for all the day-to-day official matters.

I also acknowledge the financial supports that lead me to complete my doctoral studies. The joint PhD scholarship (4 years) from Higher education commission (HEC) Pakistan and the DAAD Germany, the wrapping up Grant from the graduate academy TU Dresden, the bridging grant from the Friends of TU Dresden, and the KMM-VIN Fellowship for my research stay to University of Modena and Reggio Emilia (UNIMORE), Italy.

In last, I warmly thank my family, especially my father (Eijaz Hussain[late]), my mother (Farzana Eijaz), my wife (Tooba Saqib), and my uncle (Abdul Rasheed) whose sacrifice, continuous support and motivation made me today eligible to be a Doctor of Engineering.

Contents

List of Figures

List of Tables

List of Abbreviations

AFM	**A**tomic **F**orce **M**icroscopy
C	**C**arbon
Ca	**Ca**lcium
CA	**C**ontact **A**ngle
CR	**C**orrosion **R**ate
EC	**E**lectro **C**hemical
EDX	**E**nergy **D**ispersive **X**-Ray Analysis
FTIR	**F**ourier **T**ransform **I**nfra **R**ed spectroscopy
H	**H**ydrogen
Mg	**M**agnesium
ML	**M**ass **L**oss
MLR	**M**ass **L**oss **R**ate
N	**N**itrogen
O	**O**xygen
P	**P**hosphorus
RHE	**R**eversible **H**ydrogen **E**lectrode
S	**S**ulphur
SCE	**S**aturated **C**alomel **E**lectrode
SEM	**S**canning **E**lectron **M**icroscopy
TEM	**T**ransmission **E**lectron **M**icroscopy

Dedicated to my parents…

1 Introduction

1.1 Coronary Artery Disease and Stenting

The biggest threat to human life in the 21^{st} century before the corona pandemic was coronary artery disease (CAD) or ischemic heart disease (IHD). In Europe, every fifth person is a victim of this life-threatening disease [1]. According to the study from the European Heart Network, CAD is the major cause of death in Europe. 20% of women and 19% of men die due to this disease annually [1]. The early diagnosis and treatment might help in saving a life.

CAD slowly progresses in the artery in the form of plaque which builds up over years as fatty depositions on the artery wall which restricts the normal blood flow. In order to ensure normal blood flow, stents are used as a common treatment procedure among coronary artery disease patients, their main role being to maintain the normal flow through the blood vessels.

Figure 1.1(a) shows the affected artery having plaque, restricted blood flow and blocked cross-sectional area [2]. Among all the treatment procedures, stent deployment (Figure 1.1(b)) [3] is the common treatment procedure because of the following reasons: a) It is less invasive; b) Less expensive; c) Shorter hospital stay.

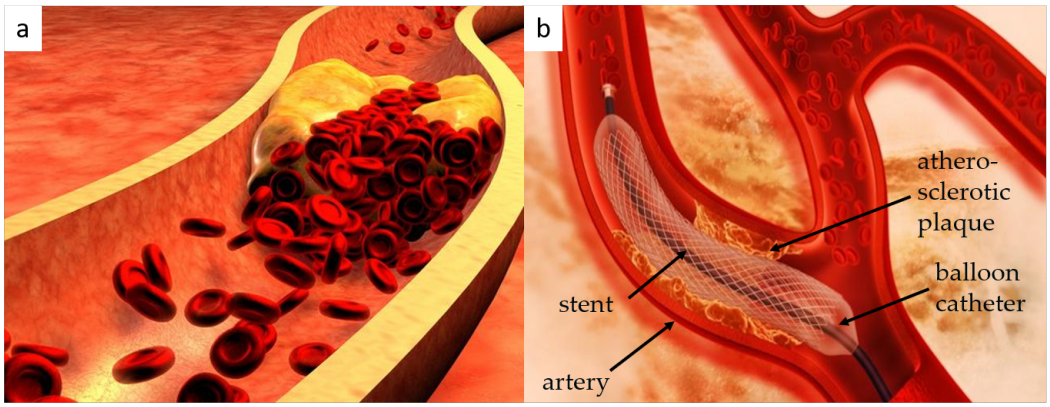

FIGURE 1.1: Coronary artery and its treatment. (a) Human vessel with atherosclerotic plaque [2], (b) Stent implantation [3].

Stent is a synthetic tubular structure intended for permanent implant in native or graft vasculature. Since the beginning of stent development in 1986, starting with bare metal stents (BMS), these devices have been continuously improved by applying new materials; developing stent coatings based on inorganic and organic materials including drugs, nanoparticles, or biological components like genes and cells as well as improving stent designs using different fabrication technologies. Drug eluting stents (DES) were also developed to overcome the main shortcomings of the bare-metal stents or coated stents. To obtain the desired characteristics; different kinds of testing (mechanical, physical, chemical, electrochemical), surface modification, characterization, and modeling techniques have been used by

researchers. In this vicinity, there are still plenty of questions that are still unanswered and a lot of things to be discovered for the more efficient technology and its application e.g.:

- Degradation of stents under physiological pH (controlling of constant pH throughout the experiment) along with monitoring of different parameters in the fluid dynamic environment.
- Corrosion and mass loss measurements on stents rather than on simpler samples.
- Effect of shear stress on the degradation of stents.

1.2 Scope of the thesis

In this research, the degradation studies of biostable and bioabsorbable stents are focused. The degradation behavior of TiO_XN_Y coated stainless steel stents, and AZ31 (Mg-alloy) samples were studied. Resoloy (Mg-alloy) stents were also used for the development of the entire stent surface model.

TiO_XN_Y coatings aim to improve the biocompatibility and long-term functionality of stents by using a surface modification of stents. In these stents, the special characteristic of TiO_XN_Y coating is that we can manipulate its surface properties by changing the ratio of O_2/N_2. Different TiO_XN_Y coated stainless steel stents were obtained using different O_2/N_2 ratio in the plasma of magnetron. These coated stents are biostable and thus degradation is undesired.

On the other hand, Mg alloys are bioabsorbable and fast degradable, thus, degradation is desired. AZ31 has the potential to be used as a biodegradable stent material due to its low mass density and good mechanical characteristics, but its higher degradation rate makes it difficult. Therefore, surface modification of AZ31 was conducted using an electrochemical anodized layer, and with a polymer coating. The degradation studies of these functionalized AZ31 surfaces were then conducted and compared.

Different stent types have different in vitro testing requirements based on the material properties. For example, pH is an important parameter to be controlled in the Mg (and its alloys) degradation, but for the stents made of stainless steel, the pH is not so relevant. Therefore, In this work, the methods have been developed to address the degradation studies of all kinds of stents. The main objectives addressing different scientific tasks in the present thesis are the following.

1.3 Main objectives

Figure 1.2 shows the main objectives addressing different scientific tasks of this research work. Following are the details of these objectives.

- Development of surface area model for stents.
  - To evaluate the degradation of any implant material, corrosion, and mass loss tests are conducted. In the case of stents, so far, corrosion experiments are conducted for qualitative analysis.
  - For quantitative analysis, simpler geometrical samples are used instead of stents. The reason is the exposed surface area is needed to calculate the corrosion rates.

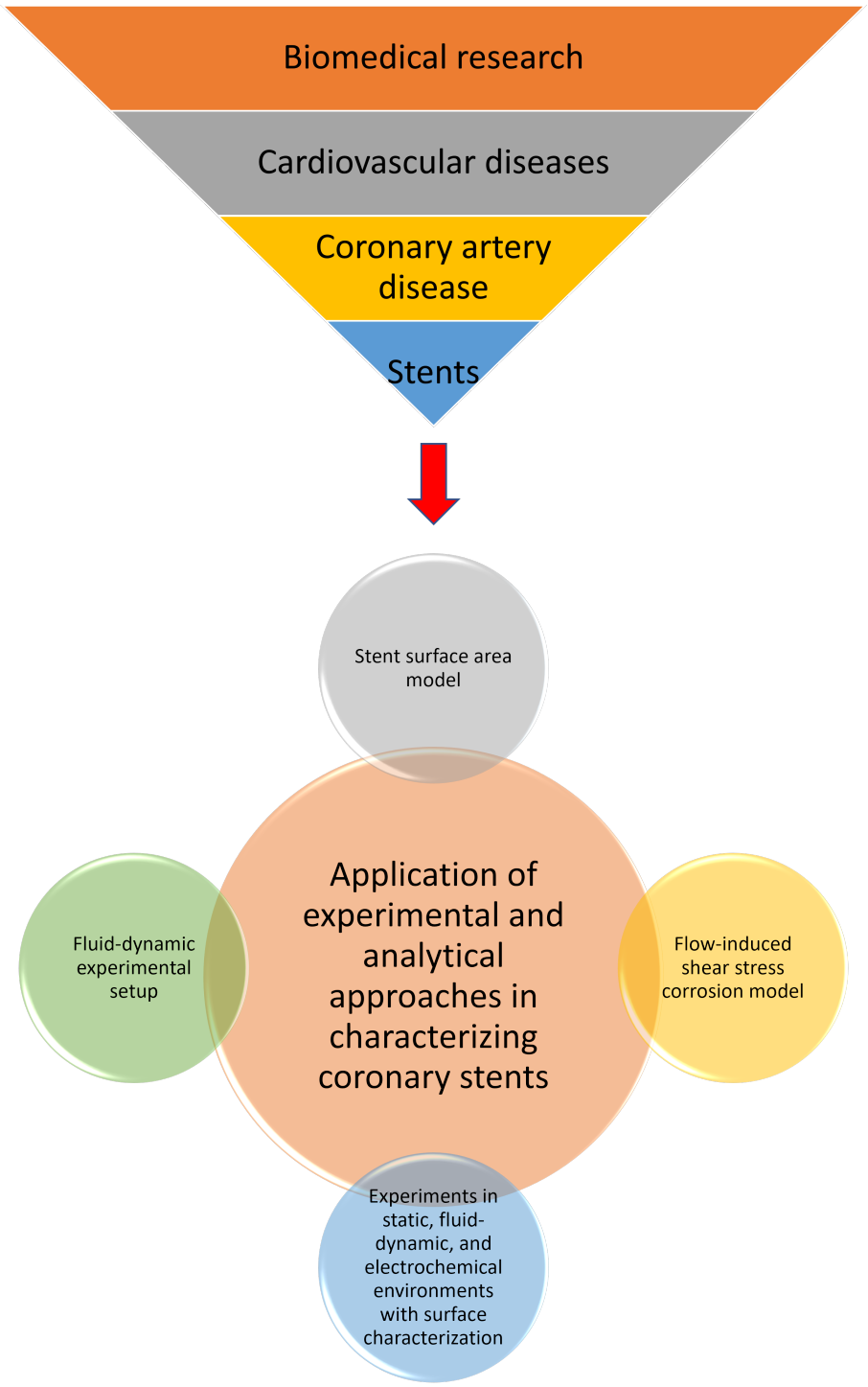

FIGURE 1.2: Scope and objectives of the thesis.

– Stents have complex geometry and there is an unavailability of methods to calculate the entire stent surface area. The entire stent surface area model has been developed.

- Development and validation of fluid-dynamic experimental setup.
  - pH plays an important role in material degradation. In the human body, the pH remains constant 7.35-7.45 by the action of physiological buffers.
  - To replicate the similar degradation rate as inside the human body, the advanced fluid-dynamic system with the monitoring and control of temperature, pressure, flow velocity, and pH is developed.
- Experiments in static, fluid-dynamic, and electrochemical environments with surface characterization.
  - The biostability of different TiO_XN_Y coatings on the stainless steel stents and the biodegradation of anodized AZ31 samples were also studied.
  - To evaluate the coating durability deposition-free degradation is needed, the optimized experimental conditions for the coated stents are also achieved.
- Development of analytical model expressing the effect of flow-induced shear stress on corrosion.
  - Stents have effective life ranging from a few months to many years. Therefore, accelerated *in vitro* testings are needed to predict the effective life in a shorter period.
  - There are many studies available taking temperature as an accelerating degradation parameter. But, in the case of Mg alloys, a small change in temperature does not have a strong influence on the degradation rate.
  - There is no predictive model exists, which can predict the degradation rate of implant materials or stents based on the change in shear stress or flow velocity.
  - Inside the human coronary artery, the shear stress ranges (10-70 dyn/cm^2), and, in the case of blockage, the arteries have to experience more than 70 dyn/cm^2. Experiments in the static, and fluid-dynamic environment were conducted and the effect of shear stress on corrosion is realized.

The present thesis comprises ten chapters including this introduction as the first Chapter 1. Chapter 2 discusses the necessary fundamentals briefly. Materials and methods including the characterization techniques used, experimental methods, and sample preparation, are discussed in Chapter 3. Chapter 4 describes the development of the entire stent surface area model with the validation by micro CT. Chapter 5 introduces the newly developed fluid dynamic experimental setup with the integration of various sensors. To get the deposition free degradation of TiO_xN_y coated stents, optimized experimental conditions are needed, which is explained in Chapter 6. Whereas, Chapter 7 discusses the in vitro biostability of TiO_xN_y coated stents in different kinds of degradation tests. Chapter 8 explains the biodegradation of AZ31 (Mg-alloy) in a fluid dynamic environment. Chapter 9 describes the effect of flow-induced shear stress on the AZ31 (Mg-alloy) surface with the help of the model. In last, Chapter 10 summarizes all of the results and provides the future possible tasks.

2 Fundamentals

Stent implantation is a multidisciplinary field that requires knowledge of anatomy, physiology, and biomechanics of coronary arteries, the internal physiological environment of the human body, bio instrumentation, materials science, and chemistry for the successful design of the stent. To provide a basic understanding of the topic and related issues Section 2.1 gives an overview of coronary arteries. Section 2.2 describes the coronary stent and its types. In last, Section 2.4 addresses the biostability and degradation of stents.

2.1 Anatomy, Physiology and Biomechanics of Coronary Arteries (normal and diseased vessels)

The heart is a great pump that is responsible to provide oxygen and nutrients through continuous blood circulation to the whole body. Because of the continuous activity of the heart throughout life, it also needs oxygen and nutrients via blood like all other organs. For this purpose, the heart has its circulation system called coronary circulation. This non-continuous and cyclic circulation attains a peak when the heart muscle is relaxed and nearly ceasing while it is contracting [4].

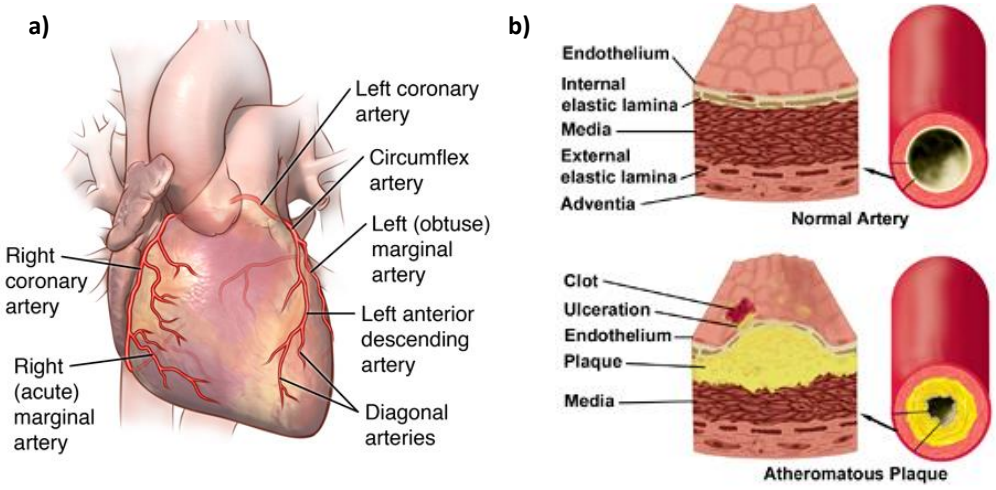

FIGURE 2.1: a) Coronary arteries of the heart [5], b) Layers of coronary arteries [6].

Coronary arteries are the branches of the ascending aorta that supply blood to the heart through coronary circulation (Figure 2.1a). These arteries originate from the aorta in to right and left coronary arteries (RCA and LCA). The left coronary artery supplies (LCA) blood to the left side of the heart, the left atrium and ventricle, and the interventricular septum. Whereas, the right coronary artery (RCA) supplies blood to the right atrium, portions of both ventricles, and the heart conduction system. Figure 2.1b shows the layers of healthy and diseased artery.

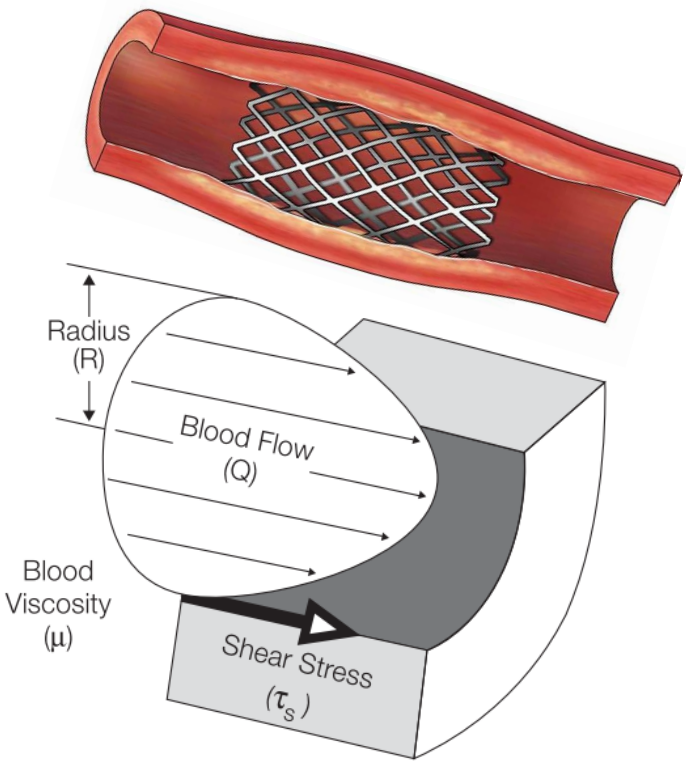

FIGURE 2.2: Implanted stent in an artery (Adapted from [7, 8])

.

Coronary arteries show both active and passive mechanical behavior. The active mechanical contribution is due to the contraction of smooth muscle cells (SMCs), which can function to act as control points for blood distribution, maintain vascular tone, and resistance. Whereas, passive mechanical behavior is mainly governed by the extrafibrillar matrix (e.g., proteoglycans and water), collagen, and elastic fibers. In atherosclerosis, significant changes are caused in the mechanical properties of the arteries [9, 10].

When the stent is implanted inside the coronary artery (Figure 2.2), it is exposed to different physiological stresses and its material should be strong enough to provide continuous mechanical support to the artery throughout its effective lifetime.

The blocked artery does not influence the chemical parameters (eg. visocity, ph, and temperature) but it influences the blood pressure and shear stress to that blocked part. This causes extra pressure on the artery and heart. Therefore, stents are implanted to normalize the restricted blood flow and to save heart failure. When designing stents, the material is selected ensuring that it should fully degrade within few months in the case of the temporary stent, but, in the case of a permanent stent, it should bear these stresses throughout its life ensuring the desired mechanical support to the affected artery without losing its mechanical integrity. Table 2.1 shows the physical parameters and their standard values inside the vascular environment.

TABLE 2.1: Arterial parameters.

S. No.	Physiological parameter	Normal arteries
1	Temperature	35.8 – 37.2 °C
2	Pressure	120/80 mmHg
3	Flow rate	5 l/min
4	Flow velocity	0.03 – 40 cm/s
5	Shear stress	1 – 7 Pa
6	Viscosity	3– 4 mPas
7	pH	7.35 – 7.45
8	Gases	O_2, CO_2

2.2 Coronary stents, types and properties

A stent is a tubular structure to provide a continuous mechanical support to the affected artery throhout its effective life.

Stenting of arteries is the most common treatment procedure for coronary artery disease [11]. Undeniably, stenting is a very fast-growing field since its beginning [12, 13]. Due to the rapid advancements in stent technology, different kinds of stents are being implanted for the treatment of blocked arteries. For instance, bare-metal stents, drug-eluting stents, bioresorbable stents, coated stents, dual therapy stents, bioengineered stents [14].

Stenting of arteries helps re-opening the narrowed or partially blocked vessels and restoring the normal blood flow. The essential properties of stents presented in [15]: (1) ability to be crimped on the balloon catheter; (2) good expandability ratio; (3) sufficient radial hoop strength and negligible recoil; (4) sufficient flexibility; (5) adequate radiopacity/magnetic resonance imaging (MRI) compatibility; (6) high thromboresistivity; (7) absence of restenosis after implantation; (8) non-toxicity and (9) drug delivery capacity.

Stenting of arteries became a common treatment procedure for CAD in 1980s. The first generation of stents comprises bare-metal stents (BMS) manufactured usually from stainless steel (316L), cobalt-chromium (Co–Cr), and platinum-iridium (Pt–Ir) alloys, tantalum (Ta), or nitinol (Ni-Ti). Despite the many advantages over CABG, these stents have shown numerous problems leading to tissue hyperplasia, in-stent restenosis, and the necessity to explant them or to keep them as a foreign body during the whole life.

These considerations led this field to the development of coated stents, DES, and biodegradable stents (BDS) [16]. Yoon et al. [17] have shown the potential of coated stents, DES [18, 19] and BDS for future applications in the treatment of ischemic stroke, describing the commonly used stents and defining the development trends in their fabrication technologies.

The rapid development of DES made it possible to expand the stent application also by patients with complicated diseases [20]. In general, DES demonstrates good efficacy with a low rate of treatment failure. However in-stent restenosis, late thrombosis, local chronic inflammation, and re-occlusion rates still belonging to results of stent implantations [21]. This stresses the necessary further development of stent technology and in-depth analysis of their long-term stability and failure mechanisms.

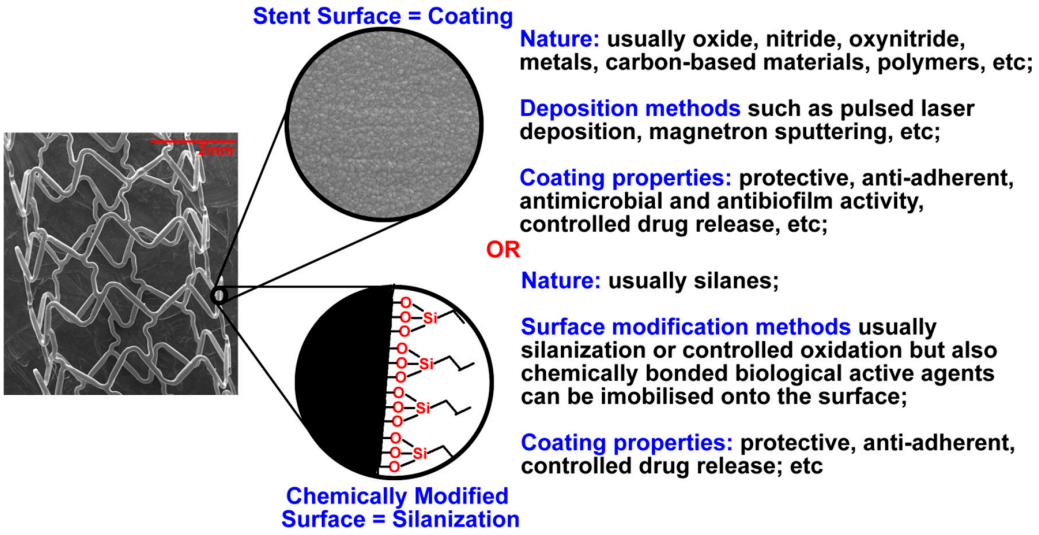

FIGURE 2.3: Stents surface modification techniques [24].

Additionally, the restenosis rate in high-risk patients (e.g. having small vessels, diabetes, and long diffusion diseased arteries) remains on higher values ((30-60) % in BMS and (6-18) % in DES) [20]. The aforementioned facts demonstrate the challenge of stent technology and encourage to look for new more safe solutions for all patient categories.

2.2.1 Bare Metal Stents (BMS)

BMSs are the first generation of stents, fabricated usually from stainless steel (316L), cobalt-chromium (Co–Cr) and platinum-iridium (Pt–Ir) alloys, tantalum (Ta), or nitinol (Ni-Ti).

From the first stent used in medical practice by Jacques Puel and Ulrich Sigwart [22] and the first FDA approved BMS by Cesare Gianturco and Gary S. Roubin [23], there is a wide variety of stents available in the market including biodegradable stents, drug-eluting stents, and coated stents.

The main issues associated with this generation are tissue hyperplasia, in-stent restenosis, and the necessity to explant them or to keep them as a foreign body during the whole life.

2.2.2 Coated Stents

Figure 2.3 shows several classes of materials that have been tested as potential coatings for stent manufacturing [24]. The surface modification of stents can be done by using the deposition of metals, oxides and nitrides of metals, and polymers by magnetron sputtering, pulsed laser deposition, matrix assisted pulsed laser evaporation etc. Surface modification can be also achieved by chemically by molecular layer deposition. For instance, silanization technology utilizing commercially available silanes (ethyltrietoxysilane, octyltriethoxysilane, vinyltrimethoxysilane, n-octadecyltriethoxysilane, phenyltriethoxysilane, (3-aminopropyl)triethoxysilane, (3-mercaptopropyl)triethoxysilane, etc.) rich on diverse functional groups used to achieve the desired stent properties [24].

Coatings can also be used to modulate the delivery rate of the biologically active agents loaded into/onto them [25, 26]. For instance, the patent US9101689B2 [27] demonstrates a stent with created reservoir regions containing an active ingredient to release the active ingredients at different rates.

The development of the coated stents aimed to improve the properties of BMS providing better biocompatibility, non-toxicity, suitable surface roughness, and surface free energy, regulated adsorption of biological molecules and cells, and stable corrosion rate [17], desirable biodegradable properties and serving as platforms for drug delivery. Various materials have been evaluated as stent coatings [17, 28]. For the enhancement of stent biocompatibility, coating materials with better biocompatibility comparing to stent material have been used. For instance, inorganic coating like titanium nitride, titanium oxide, or titanium oxynitride has been applied for stainless steel stents.

Coating types and materials

Stent coatings can be broadly classified into biocompatible coatings and drug-delivery coatings. Based on the coating materials, it can be classified as organic coatings, bio-based coatings and in-organic coatings.

- **Organic coatings** - Organic coatings act as the corrosion barrier between the underlying metal and the corrosive environment. They maintain the durability of implant structures and provide resistance to corrosive environments e.g. human blood. In particular, their efficiency depends on the mechanical properties of the coating system, pretreatment of the metal surface, adhesion of the coating to the underlying base material, and use of substrate corrosion inhibitors as additives [29].

- **Bio-based coatings** - These coatings are based on biological materials. Primarily, these are endothelial cells placed on the stent surface before its implantation. Their main function is to control proliferation, differentiation, release growth, and inhibition of thrombosis and neointimal hyperplasia. So far, all the attempts that have been made are unsuccessful to seed endothelial cells on medical grafts [24].

- **In-organic coatings** - These coatings contain inorganic materials capable of improving the properties of the implant surface. Titanium oxide and oxynitride stent coatings are of great interest nowadays due to their excellent biocompatibility. Inorganic materials used for manufacturing stent coatings are oxides, nitrides, silicide and carbide, noble metals, hydroxyapatite-based materials, diamond, and diamond-like carbon [24].

  - Titanium oxynitride (TiO_XN_Y): Titanium oxide (TiO_2)and titanium oxynitride(TiO_XN_Y) coatings are the most promising coatings for cardiovascular stent applications among all inorganic coatings. Their physical, chemical, and biological properties highly depend on the deposition technique, N/O concentration [30], and dopants incorporated into the coating [31]. For example, the implantation of phosphorus into titanium oxide film improves the thromboresistivity of stents [31].

    Titanium-oxynitride (TiO_XN_Y) coatings deposited on L316 stainless steel by reactive magnetron sputtering showed high biocompatibility. These coatings possessed a negatively charged surface and negative zeta

potential, prevents in vitro adhesion of salts on the surface, and alters the surface wettability [32].

The surface properties of these coatings can be influenced by the oxygen to nitrogen feeding ratio. Desired surface performance can be achieved by varying and controlling the oxygen to nitrogen ratio. Subsequently, coatings with unique structures and properties can be manufactured, making it possible to modify the stent surface concerning the patient's needs (personalized stents) [24].

Nitric oxide (NO) is considered one of the most important molecules in biological systems. Whereas, TiO_2 is widely used in different biomedical applications due to its high biocompatibility. Therefore, the titanium oxynitride films combine the benefits of two components: titanium oxide and nitric oxide (NO) in its atomic form.

In TiO_xN_y films, presented in [33], (NO) is located at intergranular positions in the form of an NO two-dimensional layer located at the TiO_2 grains boundary. This encouraging result suggests that TiO_xN_y films can serve as the nitrogen oxides depot if they are used as stent coatings. Based on these facts, the expected mechanism of interaction of the TiO_xN_y coating with a biological system may be the following:

1. Titanium and its oxides increase the corrosion resistance of implants
2. These films reduce the risk of inflammation.
3. Titanium oxide film reduces platelet aggregation and fibrinogen coagulation.
4. Nitric oxide (NO) released from the coating promotes endothelialization, activating the growth of endothelial cells [24].

$\mathbf{TiO_XN_Y}$ stents

The concept of BioActive Stent (BAS) was firstly developed by Hexacath (Paris, France). That demonstrates no drug, - no polymer is related to nitrogen-doped titanium oxide (TiO_xN_y) coatings. This concept was generalized in the study [34], presenting the results of a comparative trial of BAS to the paclitaxel-eluting stent (PES) in 425 patients with acute myocardial infarction. Subsequently, Stainless steel bio-active stent Titan2 (Hexacath, Paris, France) coated by plasma-enhanced vapor deposition of titanium in a mixed nitrogen-oxygen atmosphere has proven to be effective to inhibit platelet aggregation, minimize fibrin deposition, reduce inflammation and promote healing. Recently, a new generation of titanium oxynitride coated stents TiNOX and TITAX-AMI have been proven to be safe and successful in reducing in-stent restenosis (ISR) in recent clinical trials [35, 36, 37, 38] and are available at the market. The clinical outcomes of these stents were comparable to those of DES (TAXUS-Liberte Stent).

Tantalum doped Titanium oxide films formed by the plasma immersion ion implantation and deposition (PIIID) technique possess significantly better hemocompatibility comparing to undopped coatings [39]. The TiO_xN_y coatings fabricated by the application of microwave-assisted process show a higher photocatalytic activity of nitrogen-containing films providing better suitability for medical applications [40, 24].

We [30] presented surface properties of TiO_xN_y coated (at different O_2/N_2 feeding ratio, namely 1/2, 1/5 and 1/10) stainless steel stents and flat experimental models. The study investigated the influence of the O_2/N_2 ratio on the adhesion

between TiO_xN_y layer and the substrate, surface morphology, ability to adsorb proteins, and salts crystallization from simulated body fluid. TiO_xN_y (O_2/N_2 = 1/5) coatings showed the lowest protein adsorption and minimal deposition of salts from the simulated body fluids. The surfaces with higher nitrogen content are smoother, have a lower grain size and lower roughness comparing to the surfaces with low nitrogen concentration. The variation of the O_2/N_2 ratio influences the morphology of the surface. For instance, the increase of nitrogen content in the coating leads to a significant decrease in albumin adsorption. The presented coatings showed promising properties, but they have shown an insufficient adhesion to the substrate (stainless steel).

In general, TiO_xN_y coated stents is a promising research area based on the properties they have shown. These stents could be a good solution for the for the problems exists with BMS. However, applying a uniform and stable coating providing high physicochemical and adhesive properties after opening the stent is a big challenge.

2.2.3 Bioresorbable Stents

Bioresorbable or Biodegradable stents are manufactured from a material that may dissolve or absorbed in the body. The concept of bioresorbable stents is considered ground-breaking (stents of third-generation) according to Erne et al [41]. Despite these stents are new, although they captured the attention and interest of scientists around the world as witnessed by the already published reviews focusing on both clinical and material aspects [18, 42, 43, 44, 45, 46]. In past years, different works on bioresorbable stent materials are published and two types of materials have been reported: metals (Fe, Mg, Zn, and their alloys) and polymers (mainly PLLA). So far, Mg-alloys and several polymers such as poly-L-lactic acid, poly-L-glycolic acid, polyorthoester, polycaprolactone, fibrin, hyaluronic acid, etc. already showed encouraging properties as biodegradable materials [15, 47, 42].

Mani et al. 2007 [15] presented the characteristics of different materials (used for stent fabrication) surface and their influence on restenosis. Various coating materials (inorganic materials, polymers, endothelial cells, and porous materials) are used to improve the performance of biodegradable stents. The coatings were first used to increase the biocompatibility and durability of the stents. Later, they became the platforms for drug delivery to inhibit intimal hyperplasia or to targeted delivery of the specific biological active agents.

Metallic Bioresorbable Stents

Low mechanical characteristics and higher strut thickness of polymer-based stents lead to the development of metallic stents made from resorbable metals. The Iron (Fe) [15, 48] and magnesium (Mg) including alloys [49, 48] were first used for the fabrication of degradable stents. They captured the attention of scientists around the world, as, in particular, magnesium (Mg) and iron (Fe) have better mechanical characteristics than polymers and appropriate biocompatibility [50, 51]. Recently, many research groups are examining zinc (Zn) as a bioresorbable metal for stents.

The problems related to the application of bioresorbable metals for the fabrication of stents are discussed in various reviews [15, 42, 52].

Mg-based bioresorbable stents: Magnesium is a naturally occurring biomaterial in the body, with proven biocompatibility. That means that the body can remove

magnesium degradation products easily. Furthermore, blood examination of patients following the use of magnesium implants within the body revealed that resorption caused little change to the composition, with no disorder to the organs e.g. liver or kidneys. World Health Organization (WHO) recommends that adults need between 280 and 300 mg of magnesium per day for effective heart, muscle, nerve, bone, and kidney function [53].

Magnesium alloys are now considered as an improved alternative to polymer materials. They demonstrate a good tensile strength in comparison to polymers that is more suited for use in load-bearing mechanical medical devices. To improve the mechanical properties and corrosion resistance of Mg most commonly used alloying elements are aluminum (Al), calcium (Ca), zinc (Zn), zirconium (Zr), strontium (Sr), and rare earth elements (REEs) such as yttrium (Y), gadolinium (Gd), lanthanum (La), and dysprosium (Dy) [54].

Despite the aforementioned facts, magnesium alloys have a too high rate of degradation (60 to 90 days from implantation, which is not suitable for vascular stenting applications) and the evolved hydrogen gas leads to important systemic toxicity [55]. To overcome these issues several studies have been conducted with different approaches to Mg and its alloys. For instance, corrosion properties of a matrix composed of Mg and ZnO powder by spark plasma sintering technics were investigated by Cao et al. 2017 [56]. The obtained results indicate that Mg-10 wt% ZnO composite exhibits a lower corrosion rate compared to pure Mg and is promising as a temporary implant.

In a review by Gladius Lewis [57], the methods to reduce the biocorrosion rate of Mg and Mg-based alloys are focused. Moreover, they proposed a way of decreasing the in vivo resorption time i.e. improving the clinical efficacy of Mg-based grafts.

Salinization is used as an alternative way to reduce the resorbability of magnesium in many studies. Patil et al. 2017 [58] demonstrated the ability of alkylsilane self-assembled multilayer coatings to reduce the rate of Mg corrosion. The results show their good cytocompatibility and great potential of these coatings on developing resorbable Mg devices, including stents.

Biotronik AG developed various mg-based stents e.g. AMS-1 (Abrobable magnesium stent -1), AMS-2, and AMS-3.

- The AMS-1 BDS (AMS-1, Biotronik AG, Bülach, Switzerland) is composed of 93% of Mg and 7% rare earth metals [59]. It is the balloon-expandable Mg-based stent that has a strength-to-weight ratio compared with that of stainless steel - L316 and strong aluminum alloys. The pre-clinical assessment of AMS-1 shows the rapid endothelialization and too high degradation rate (about 60 days) into inorganic salt [24].

- The AMS-2 stent uses a different magnesium alloy, resulting in the stent having a higher collapse pressure and also a slower degradation time [24].

- The AMS-3 stent (DREAMS - Drug-Eluting AMS) is a modification of the AMS-2 stent. It is designed to reduce neointimal hyperplasia by incorporating a bioresorbable coating based on PLLA for the controlled release of an antiproliferative drug and reduces the rate of body-stent degradation at the initial stage [24]. The first-in-man BIOSOLVE-I trial assessed the safety and performance of AMS-3 in 46 patients with 47 lesions at five European centers [59].

Recently Mg alloys captured the attention of scientists to use ut in stent technology. Magnesium Elektron, and Biotronik, jointly developed a cardiovascular

TABLE 2.2: Useful studies on Mg-alloy stents.

Mg- alloy	Key features	Ref.
Mg–Zn (up to 3% Zn)	Increasing in adsorption for the surface of the Mg–Zn alloy with the increase of Zn concentration (up to 3%).	[60]
Mg–Y (1% Y) Mg–Nd (1% Nd)	The adsorption of peptides is slightly weakened compared to that on the clean Mg (0001) surfaces.	
Mg (3.5 or 6.5wt%)-Li (0.5, 2 or 4wt%)-Zn	Good mechanical properties, degradation behavior, cytocompatibility, and hemocompatibility. Enhanced mechanical properties – yield strength, ultimate strength, and elongation (twice as compared to pure Zn) and corrosion resistance without losing the viability of the Human Umbilical Vein Endothelial Cells and (HUVECS) and Human Aorta Vascular Smooth Muscle Cells (VSMCS).	[61]
Mg-Al alloy AZ61	Highly susceptible to stress corrosion cracking (SCC) as compared to Zn which is highly ductile with limited susceptibility to SCC.	[62]
MgZnYNd (coated with arginine (Arg)-based poly (ester urea urethane) (Arg-PEUU))	Super corrosion retardation, high hemocompatibility, high cytocompatibility. High hemocompatibility High cytocompatibility	[63]
Mg stent (coated with phytic acid (PA)); heparin loaded PA and bivalirudin loaded PA	Effective control of corrosion rate. Provides a biofunctional effect. Shows good hemocompatibility Inhibits platelets adhesion Promote endothelial cells growth Superior stents comparing with the bare magnesium stents Super-hydrophilic surface (the contact angle is very close to 0°) Hydrogen evolution versus immersion time exhibits a slightly linear release between 5 and 10days as compared to uncoated samples where an exponential hydrogen release was noticed within this interval.	[64]

stent Magmaris® that resorbs over time using SynergMag® 410, a magnesium alloy system as a key structural backbone of the scaffold. The Magmaris® magnesium stent was launched in 2016 by Biotronik, and it is now the world's first clinically proven magnesium-based resorbable scaffold to obtain a CE mark [53].

Several patients have been treated successfully with Magmaris® in Germany, Belgium, Denmark, the Netherlands, Switzerland, Spain, Brazil, New Zealand, and Singapore, and Australasia since its launch. Recently a patient who had 90 percent of his heart vessels blocked, causing ongoing angina and chest pain was treated with Magmaris® stent successfully [53]. Table 2.2 summarises some useful studies in Mg-alloy stents.

Fe-based bioresorbable stents: In the recent past, plenty of works on Fe application for bioresorbable stent were done in recent years [65, 66]. Because Fe i) has superior radial strength [15], ii) has satisfactory mechanical characteristics [15], iii) is nontoxic, and iv) Fe ions may inhibit neointimal hyperplasia [50]. Despite these properties, the main problem is related to the slow kinetics of Fe degradation [65, 66]. Based on this shortcoming, instead of using pure Fe, new alloys (i.e. Fe32Mn) were developed and tested for stent development [67].

The corrosion rate of this alloy is slightly lower than that of pure Fe and it exhibits an antiferromagnetic character having the mechanical characteristics corresponding to the requirements for biodegradable implants. This alloy was fabricated by the magnetron sputtering technique in combination with UV-lithography demonstrating the new way for the development of biodegradable FeMn-based alloys for the fabrication of stents [67].

Pure Fe is the major component in degradable Fe stents. Mueller et al. 2006 [65] presented the in vivo analysis of the iron-based stents. The results showed that the

TABLE 2.3: Useful studies on Zn-alloy stents.

Zn- alloy	Key Features	Ref.
pure Zn	Stents maintained mechanical integrity while no severe inflammation, platelet aggregation, thrombosis formation, or intimal hyperplasia were observed in abdominal aorta of rabbits. Good mechanical integrity for 6 months. After 12 months of implantation, the degraded volume of the stents was 41.75 ± 29.72%.	[77]
Zinc wires coated with PLLA/MPS	Corrodes at half the rate of uncoated Zn. Reduction of the biocompatibility and increasing cell toxicity and neointimal hyperplasia takes place.	[75]
Zn-1%Mg and Zn-1% Mg-0.5%Ca	These zinc alloys can be considered as good candidates for biodegradable implants.	[78]
Zn-Li alloy	Increase of ultimate tensile strength from <120 MPa (pure Zn) to >560 MPa. In vitro corrosion was evaluated by immersion tests in simulated body fluid and reveal higher resistance to corrosion compared to pure Zn. Samples containing 4% Li have shown the best results	[74]
Zn-3Cu-xFe (x=0, 0.5 and 1 wt.%) alloys	The mechanical characteristics and in vitro behavior of Zn-3Cu-xFe alloys are more suitable than that of Zn-3Cu alloys as candidates for biodegradable materials.	[79]
Zn–Al alloys (containing up to 5.5 wt. % Al)	Important mechanical characteristics: Yield strength 190–240 MPa; ultimate tensile strength 220–300 MPa, elongation 15–30%, elastic ranges 0.19–0.27%. Intergranular corrosion of Zn–Al alloys and cracking related to corrosion are observed. Absences of necrosis traces, though chronic and acute inflammatory indications were present	[72]

corrosion product reduces the cross-section of the lumen and alters the integrity of the arterial wall suggesting Fe is an unsuitable material for stent application [65].

Zn-based bioresorbable stents: zinc-based class of materials demonstrates the potential for an absorbable stent with the optimal performance in terms of mechanical and biodegradation characteristics required for the stent. Zinc promotes healthy vessels and it combines the best behaviors of both current bioabsorbable stent materials: iron and magnesium. Therefore, zinc is proposed as an exciting new biomaterial for use in bioabsorbable cardiac stents [24].

The study presented by Bowen et al. [68], is the first introduction of zinc (Zn) and its alloys, which harmlessly degrade with an appropriate rate for stent applications of ~0.02 mm/year [68, 52]. The obtained results showed Zn achieves high biocompatibility, ideal degradation rate, and has appropriated mechanical characteristics required for the bioresorbable stent. In general, Zn and its alloys may avoid many problems associated with Mg and Fe. Pure Mg has a corrosion rate 10 times greater than Zn, while the corrosion of iron leads to non-resorbable Fe oxides.

Until now, little information about Zn corrosion, toxicity, and biocompatibility as a model stent material is available [52]. However, Zn-based materials, including Zn-Mg, Zn-Ca, Zn-Sr, Zn-Al-Cu alloys, and pure Zn with appropriate mechanical characteristics (e.g. ultimate tensile strength UTS (20 ÷ 440)MPa and elongation to failure (10 - 65)% for stent application can be produced by conventional methods [52, 69].

The development of new Zn-based stent materials is only at the beginning and many scientific groups are involved in the work on Zn-based materials [68, 70, 71, 72, 73, 74, 75, 76, 77]. Table 2.3 summarises some useful studies in Zn-alloy stents.

Polymeric Bioresorbable Stents

Biodegradable polymeric materials are widely used in different medical applications. Shukla et al. 2016 [80] presented biodegradable polymers and polymeric nanostructures and discussed their future perspectives.

Poly L-lactic acid (PLLA) is the commonly used biodegradable polymer in manufacturing biodegradable stents (BDS). It has high biocompatibility [81] and it is metabolized via the Krebs cycle over approximately 12 to 18 months into carbon dioxide and water. Therefore, there are no toxic products of degradation, and no side effects are expected.

Igaki-Tamai et al. 2000 [82] were the first to report the development of a PLLA-based biodegradable coronary stent. It was also the first fully degradable stent (Kyoto Medical Planning, Kyoto, Japan).

Abbott (Chicago, IL, USA) developed another PLLA stent (the ABSORB Bioresorbable Vascular Scaffold [BVS]) which elutes everolimus. The stune demonstrates good mechanical support for 3 months, but then its strength diminishes rapidly.

BDS (Bioabsorbable Therapeutics, Menlo Park, California) shows antiproliferative and anti-inflammatory properties due to the presence of poly-anhydride ester together with salicylic acid, and sirolimus [47]. Some other PLLA-based BDS which are under investigation is Elixir (Sunnyvale, CA, USA), ARTDIVA from Arterial Remodeling Technologies (Noisy le Roi, France), Tissue Gen (Dallas, Texas) [47, 80].

Other commonly used biodegradable polymeric materials are polyhydroxy carboxylic acids, poly(3 − hydroxybutyrate), and poly(ε − caprolactone). Biomimetic polymers including Phosphoryl choline (PC), poly (vinylidene fluoride) − hexafluoropropylene (PVDF − HFP) are used for DES of the second- or third-generation [83]. Moreover, polymers such as polylactides and poly(lactide − co − glycolide) (PLGA) studied intensively to improve their characteristics and biocompatibility. Despite positive aspects, some biodegrading polymers may generate harmful fragments [84]. These problems have been discussed extensively in several reviews such as [85, 86].

Comparison of metallic bioresorbable stents and polymeric bioresorbable stents

Despite challenges faced in-stent materials selection, it seems that metals have an edge over polymers due to the following reasons:

- Polymers exhibit lower Young's modulus (0.2÷7.0 GPa) value as compared to metals having a better Young's modulus value (54÷200 GPa). Therefore, metallic stents are considered to be better than polymeric grafts in terms of mechanical performance [52] with other comparable characteristics.
- Polymers were compared with Fe- and Mg-based metallic grafts in review [52] and presented that:
  - Polymers exhibit radial force similar to those of stainless steel [87] and cobalt-chromium stents [88].
  - Polymers have the characteristics required for the successful deliverability of scaffold [15].
  - Polymers show the required degradation rate [59].
- Low ultimate tensile strength of polymers requires greater struts thickness than those of metal causing the inability to expand completely with balloon dilatation.
- Similar restenosis rates in polymer stents to that of bare metal stents gives BMS the advantage.

- Ho et al. 2016 [43] presented the evolution of coronary artery stents from bare-metal stents through drug-eluting stents to bioresorbable stents. Their manuscript highlights that:
  - Bare-metal stents are suitable for cardiovascular application but their properties highly depend on the structure platform, size, length, and strut thickness.
  - Stents with thinner struts and covered by bioresorbable polymers can represent the reduced restenosis rate.
  - At first, the reduction of the restenosis rate was achieved by using thinner struts with new metal compounds, then, improvements were achieved also by using drug-eluting stents and polymer-coated stents [89, 90, 91, 43].
- Magnesium (Mg) and iron (Fe) have been defined as an alternative to biodegradable polymers in stents fabrication.

Based on the literature review presented, we can conclude that the problems of biocompatibility of polymers are insufficiently understood. Therefore, plenty of future works are still needed for the development of biomaterials designed for the coating of stents.

2.2.4 Drug Eluting Stent (DES)

Drug-eluting stents are stents with drug-eluting functions, being realized by means of an anti-inflammatory/antithrombotic drug-containing polymer coating or direct immobilization of drugs on the stent surface. Since the first approved DES, CYPHER^{TM} in 2003, different stents have been developed to ensure quick endothelialization, low proliferation of Smooth Muscle Cells (SCMs) and to avoid late in-stent restenosis. Although, the first generation of DES loaded with sirolimus and paclitaxel have shown reduced in-stent restenosis rates, these stents are still associated with a risk of late stent thrombosis due to the hypersensitivity [92]. Biodegradable polymer coating is designed in order to avoid inflammation and delayed vascular healing as compared to the use of durable polymers.

In the second generation, the development of zotarolimus- and everolimus-eluting stents have further reduced that risk exhibiting lower hypersensitivity, high flexibility, acceptable recoil and better compliance [92].

The third generation of DES belongs to the bioresorbable drug-eluting vascular scaffolds (BVS), which disappear or degrade completely after a certain time in the vessel [93, 94, 95, 96, 97]. Just as metal DES, BVS have the advantage of no long-term limitations of permanent vessel caging and possible malapposition (incomplete stent apposition), significantly reducing risks of late restenosis, neoatherosclerosis, thrombosis, and local inflammation [98, 99, 100, 101, 102, 103, 104]. The whole polymer stent may be used as drug reservoir [85] and exhibits difficulties with implantation in accurate position within vessels [85, 105]. The resorbable metal stent (Biotronik, Berlin, Germany), which is composed of magnesium and some other rare metals, is the first bioresorbable metal stent implanted in humans. The device showed high mechanical strength and properties similar to other metal stents. The stent resorption is completed within four months without causing any significant inflammatory response [100, 104, 106, 107, 108, 109]. A PowerStent® Absorb prototype (blended ACP with high molecular weight PLLA to address two major challenges in BDES development: inferior radial strength and

biocompatibility) was manufactured and tested in vivo in the coronary artery of a porcine model, which reduced stenosis, recoiling and inflammation [110].

Furthermore, stents can be improved by using DNA, siRNA, and miRNA [111, 112, 113, 114, 115, 116, 117, 118, 119, 120] as well as nanoparticles [93, 121, 122] instead of drugs. For example, Zhao et al. 2018 [93] developed a novel coating method using sirolimus-loaded PDLLA (Poly DL Lactide) nanoparticles applied on a 3D-printed PLLA biodegradable stent with the result of a better inhibition effect on smooth muscle cell proliferation than on endothelial cell proliferation.

Currently, there is a tendency to fabricate polymer-free drug-coated stents (PF-DES). Examples for this are the stainless steel sirolimus-containing stent VESTAsyn (MIV Therapeutics, Atlanta, GA, USA), the stainless steel BioFreedom stent (Biosensors) coated with Biolimus A9, and the polymer-free cobalt chromium Amazonia Pax stent (Minvasys, Genevilliers, France) with paclitaxel [43].

In general, commonly used DES can be divided into (a) polymer-coated; (b) polymer-free; (c) gene-eluting [111, 112, 113, 114, 115, 116, 117, 118, 119]; (d) nanoparticle-eluting; and (e) bioresorbable.

Surface modification of DES: Optimal drug-release kinetics is the most important part after DES implantation. Burst drug release (elution of 90% of the drug amount within 2 days) in various PF-DES failed to achieve the desirable inhibition of neointima proliferation [123, 124, 125]. To overcome this barrier different physical and chemical methods have been used for the surface modification of stents to achieve sustained drug release kinetics (elution of 60-70% of the drug amount within the first week and the remaining drug within 4-6 weeks) to attain the optimal efficacy profile of DES platforms [25, 126, 123]. The coating techniques used for the surface modification of stents include Direct coating, Crystalline coating, Nanoporous or microporous surface coating, Inorganic porous coating, Reservoir-based coating, Nanoparticle coating on the stent, and the Coating of self-assembled monolayers on stent surfaces. The direct coating is the technique to coat the drug on the surface of the stent is by immersing the stent into a drug solution followed by evaporation [127]. In Crystalline coating, direct crystallization of the drug from a solvent on the surface of the stent leads to a partially crystalline drug-coated stent or an amorphous drug-coated stent [128]. The nanoporous or microporous surface coating uses a sandblasting technique and mechanical modification [129]. The inorganic porous coating includes the coating of micro or nanoporous biocompatible thin inorganic material on stents by an anodization technique [130]. The reservoir-based coating uses macropores (grooves, channels, or holes) created by mechanical treatment on stents which acts as reservoir-based systems for drugs [131]. Nanoparticle coating on stent is a recent approach used for NPDES by coating nanoparticulate-based chemotherapeutics onto stent platforms [132, 133]. Silica-based magnetic nanoparticles and carbon nanotubes are used as nanoparticulate systems [134]. Coating of self-assembled monolayers on stent surfaces applied by a two-step deposition method: (a) immersion into the solution and (b) dip evaporation [135]. The most frequently used method is surface modification through the creation of micropores by sandblasting or mechanical modification. The first microporous surface PF-DES platform used in clinical studies was the Yukon DES stent [124].

Drug delivery mechanisms: The controlled drug delivery mechanisms [136, 137, 138, 139, 140, 141, 142] can be classified as either physical or chemical mechanisms,

but also more complex situations exist, which combine both. The physical mechanisms include diffusion of drug molecules through a polymer layer, dissolution or degradation of polymer matrix controlling the drug release rate, osmotic pressure for drug release, and use of ion exchange for ionized drugs. Whereas, the chemical mechanisms are based on the breaking of covalent bonds that connect drug molecules to a delivery vehicle, such as polymer chains, by either chemical or enzymatic degradation. Physical mechanisms have an advantage over chemical mechanisms to control the drug release kinetics by the drug delivery system itself and also there is no need for the drug molecules to be chemically modified like in chemical mechanisms. These are the reasons that physical mechanisms are preferred over chemical mechanisms.

Following are the commonly present drug delivery mechanisms.

- Diffusion [143, 144].
- Dissolution or degradation [145, 146, 147, 148, 132].
- Ion exchange [149].
- Osmosis [136].
- Prodrug [136].

Drugs used in DES: Many drugs have been used till now in the drug-eluting stents. Among all, the limus family is especially evaluated. The purpose of these drugs is to inhibit inflammation and neointimal formation after stent implantation [150]. The drugs used in DES's are immunosuppressive, anti-inflammatory, anti-thrombogenic, or antiproliferative drugs.

2.3 Magnetron sputtering and Plasma electrloytic oxidation (PEO) process

2.3.1 Magnetron sputtering

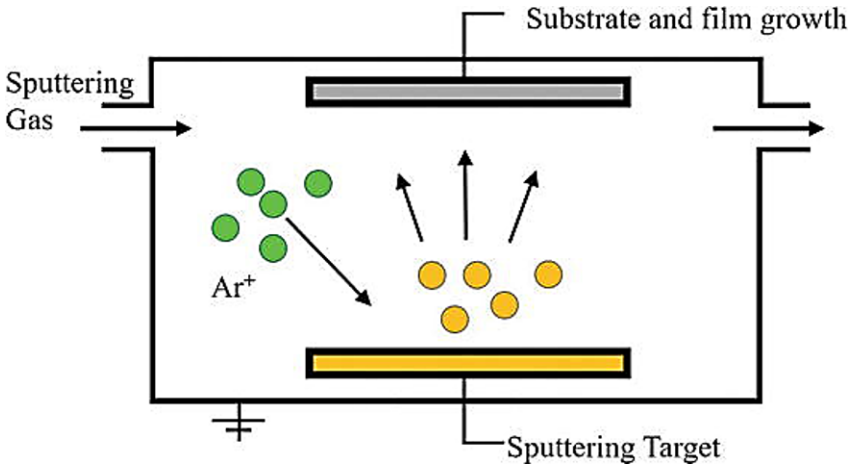

FIGURE 2.4: Schematic diagram of magnetron sputtering [151].

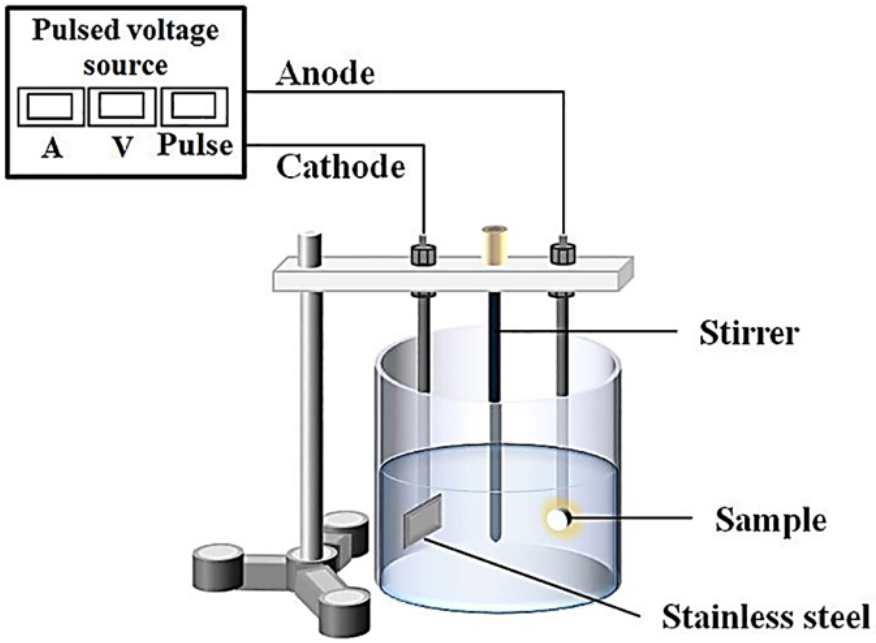

FIGURE 2.5: Schematic of PEO setup [154].

Magnetron sputtering is a well-established high-rate vacuum coating technology and is used for depositing metals, alloys, and compounds onto a wide range of materials [152].

It is a deposition technology in which a gaseous plasma is generated and confined to the target. The target is a space containing the material to be deposited. The liberated atoms from the high-energy ions within the plasma travel through the vacuum environment and deposit onto a substrate to form a thin film [153].

Figure 2.4 represents the schematic diagram of magnetron sputtering.

2.3.2 Plasma electrloytic oxidation process

Plasma electrolytic oxidation (PEO) is a technology used for producing oxide-ceramic coatings on metals. It is also termed micro-arc oxidation (MAO) or anodic spark deposition (ASD) or plasma chemical oxidation (PCO). It is an innovative method that has been used in the production of oxides of light metals such as aluminum, titanium, magnesium, zirconium, etc [154, 155].

Commonly used salts for PEO of magnesium, titanium and their alloys in the alkaline media are silicates, phosphates, aluminates, fluorides, borates, and stannates [155].

In this process, the composition of the oxide can be altered significantly by incorporating elements provided by the electrolyte [155].

The PEO process is characterized by discharges (develop in a strong electric field) in a system that consists of the substrate, the oxide layer, a gas envelope, and the electrolyte. A plasma state establishes in this system due to the electric breakdown that converts the substrate material to a compound consisting of the substrate material itself (including alloying elements) and oxygen in addition to the electrolyte components [155].

The standard PEO process schematic diagram is presented in Figure 2.5.

2.4 Biostability and degradation of stents

Biostability means the relative stability of biomaterials in the physiological environment as a function of time. Whereas degradation is the deterioration of the material as a function of time. In the case of stents, biostability and degradation behavior both are of equal importance. The stent should not provide infection and degrades at the expected rate.

Stents, like all implant materials, are exposed to numerous external mechanical and environmental factors during their effective life. Those factors include temperature, chemical attack, mechanical vibration, applied mechanical loads, etc. Under the influence of these degradation factors, stent materials get degraded i.e. they lose their ability to perform the desired task [156].

In metals, material loss occurs either by dissolution or by the formation of a non-metallic scale or film. Ceramics are relatively resistant to degradation, but ceramics also get deteriorated at extreme temperatures. Polymers may dissolve or distort in presence of a liquid solvent or even when exposed to electromagnetic radiation [156]. Stents are manufactured either by metals or by polymers.

2.4.1 Degradation properties

Degradation due to chemical or electro-chemical factors is termed as corrosion, whereas, the formation of nonmetallic scales in metals is termed as oxidation.

The degradation can be desired and undesired. For example, in the case of bare-metal stents, long-term biostability is needed and thus the degradation is undesired. On the other hand, in the case of a bioresorbable stent, full degradation in the desired time-frame (6 months) is expected and thus the degradation is desired.

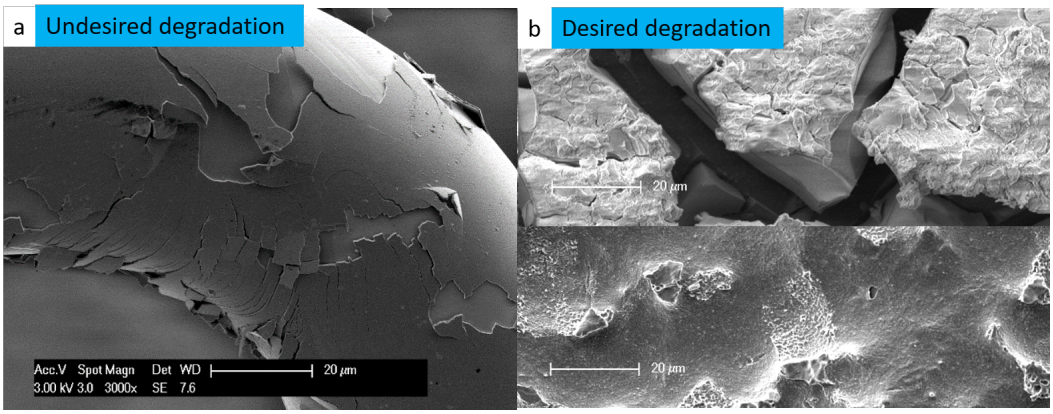

FIGURE 2.6: Degradation types: a) BMS with TiON-coating (delamination of the stent coating due to bad adhesion), b) Mg-alloy (AZ31) vs. t = 14 d, V = 20 cm/s, t= 37 °C, HBSS: with (above) and without (below) degradation products

Undesired degradation: In undesired degradation, the implant material is needed to continue to support without losing its potential features e.g. delamination of coating (Figure 2.6a)

Desired degradation: In the desired degradation, the implant material is needed to degrade completely after a specified time e.g. Mg-alloy degradation (Figure 2.6b)

TABLE 2.4: Corrosion types.

Type of Corrosion	Reported in
Uniform corrosion	[158, 159]
Localized corrosion	[158, 159]
Flow-induced corrosion	[160, 161]
Erosion corrosion	[162]
Galvanic corrosion	[163, 164]
Pitting corrosion	[165, 166]
Stress corrosion	[167, 168]
Atmospheric corrosion	[169, 170]
Hydrogen cracking	[171, 172]
Intergranular corrosion	[173, 174]

For an ideal bioabsorbable implant, the degradation products should be non-toxic and the degradation behavior should be predictable and controllable.

Corrosion: Corrosion is defined as 'an irreversible interfacial reaction of a material (metal, ceramic, and polymer) with its environment which results in the consumption of the material or dissolution into the material of a component of the environment' (IUPAC, 2012). Table 2.4 is showing different types of corrosion and the studies where they reported. The graphical representation of different corrosion types can be seen in Figure 2.7.

Corrosion rate: It is the speed at which any given metal deteriorates in a specific environment. The rate, or speed, is dependent upon environmental conditions as well as the type and condition of the metal. [Further details are written in Section 4.1 such as how to calculate the rate of corrosion]

Factors affecting corrosion rate

Stent upon implantation has two different kinds of interaction. The stent-blood and stent-tissue interfaces are particularly important for the optimization of any cardiovascular stent. The inner stent surface interacts with flowing blood while the outer surface contacts with a vessel tissue. Stent materials should be biocompatible and stable and must prevent the adhesion of minerals, proteins, and multi-layered cells [reference article]. Numerous factors affect the degradation of and corrosion of the stent inside the artery. Following are the important ones.

1. Flow rate

   It is the amount of flowing liquid per unit of time. It is measured in L/m or ml/s. The flow rate of blood in a normal human being ranges from 5-6 L/min or 5000-6000ml/min. However, in in vitro fluid dynamic experiments, the flow rate keeps in the range of 50-1000 ml/min. These flow rates are enough to generate similar flow velocities and shear stress as in the physiological vessel.

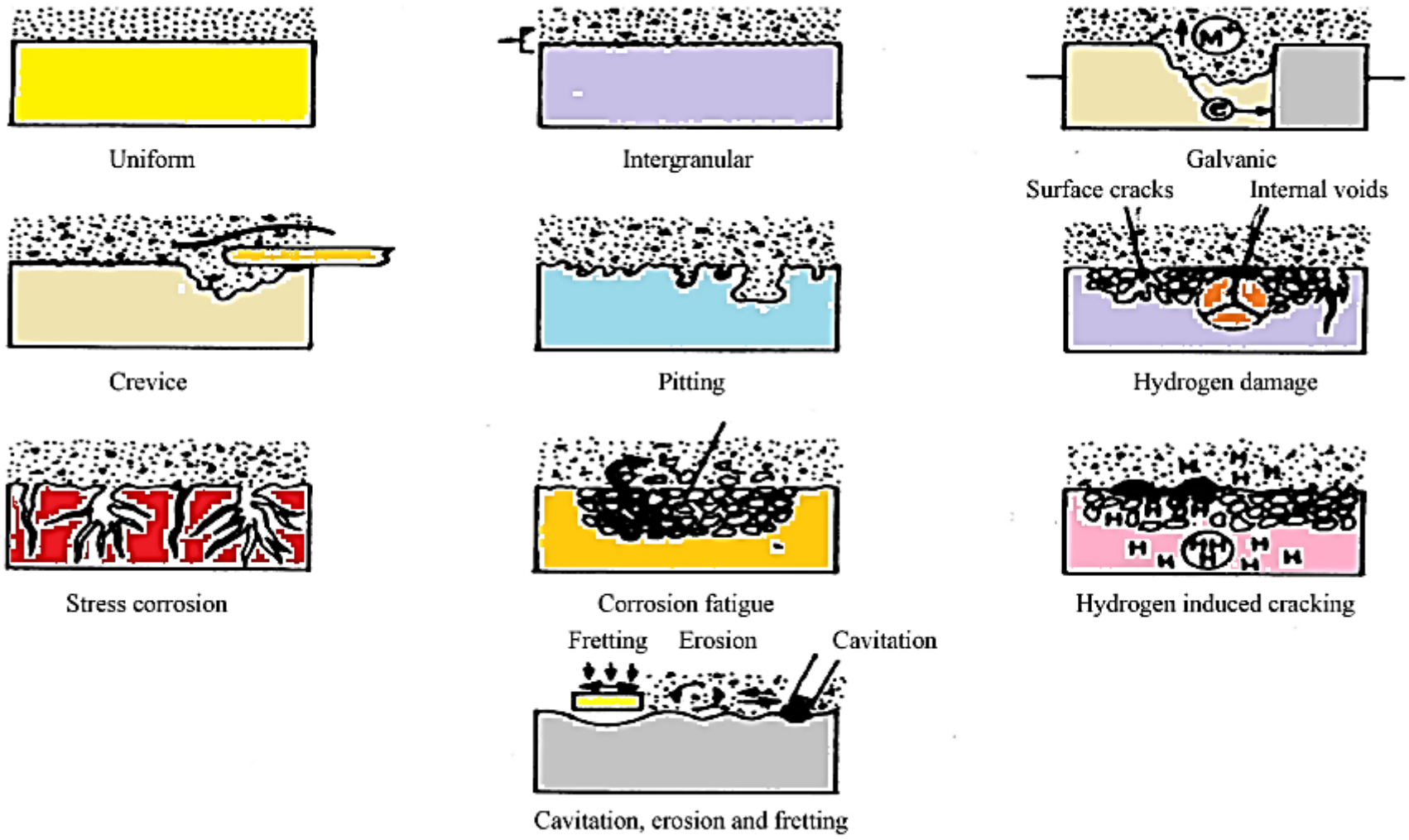

FIGURE 2.7: Corrosion types summary [157].

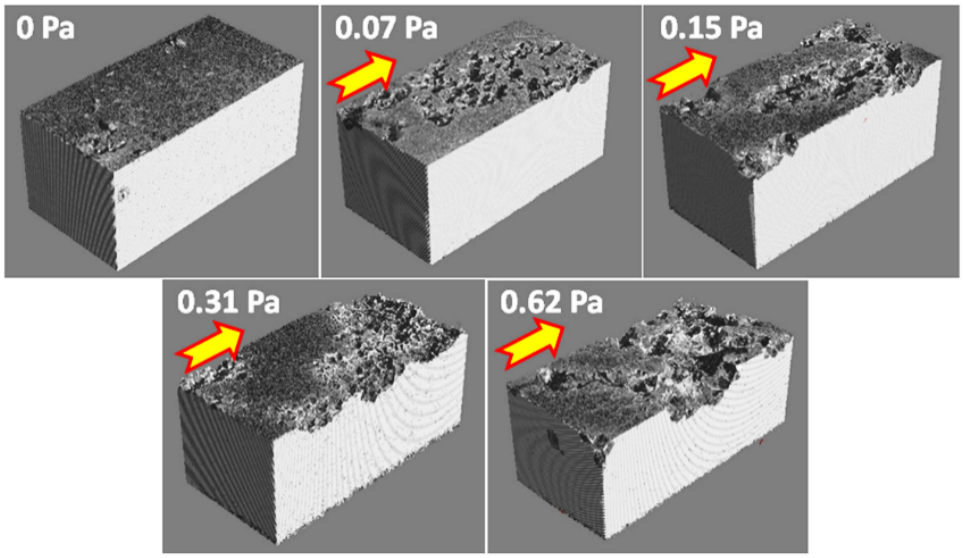

FIGURE 2.8: X-ray micro-CT 3-D renderings of full view samples under the FISS values of 0, 0.07, 0.15, 0.31 and 0.62 Pa. The arrows indicate the flow direction of corrosion medium [177].

2. Flow velocity

   It is the velocity of fluids at a certain time and position [175]. It is also called macroscopic velocity. It is usually expressed in cm/s or mm/s. The flow velocities of blood inside human vessels ranges from 0.03 – 40 cm/s [176]. The increase in the flow velocity increases the shear stress to the stent.

3. Shear stress

   Shear stress is the stress on the surface of the material that arises from the force vector parallel to the cross-section of the material. Unlike the normal stress which arises from the force vector perpendicular to the surface of the material. It tends to accelerate the overall corrosion rate (including localized, uniform, pitting, and erosion corrosions) due to the increase of mass transfer and mechanical force [178]. Additionally, also increases the thickness of the uniform corrosion layer. Wang et al. 2014 [177] reported a significant increase in mass or volume loss with the increasing shear stress (Figure 2.8).

   The magnitude of flow-induced shear stress on the vessel walls can be calculated in vasculature situations by Poiseuille's law [178]. In the case of the stent and tube samples, the wall shear stress estimated by Poiseuille's law represents the shear stress on the sample. Since the stent has complex geometry and each wire has four surfaces. Therefore, the highest shear stress on the stent occurs on the surface of struts facing the flow direction simulated using a three-dimensional (3-D) computational fluid dynamics (CFD) model. This highest shear stress value is more than twice the wall shear stress value [178].

   Levesque et al. 2008 [179] investigated the effect of shear stress on Mg alloy AM60B-F in modified Hank´s solution. The specimens were submitted to a laminar flow and shear stresses of 0.88, 4.4, and 8.8 Pa. The choice of these stresses was based on previous studies [180, 181]. The presented results showed the mass loss in the samples increase by increasing shear stress

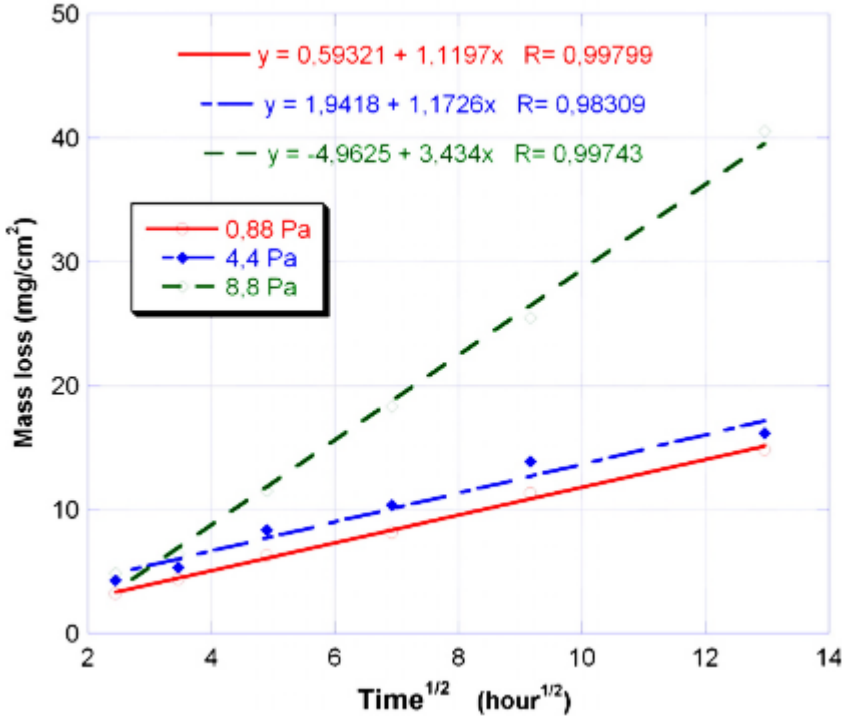

FIGURE 2.9: Mean Mg loss plotted for three different dynamic testing conditions [179]

(Figure 2.9). The ratio 1:10 was chosen between the minimal and maximal values following biomechanical engineering considerations: in stenosed arteries (as those requiring to be stented), shear stress is higher than in healthy arteries [179]. It was found that low shear stress protects the surface from localized corrosion. However, high shear stress values induce, in addition to high uniform corrosion, some localized corrosion [179].

4. Viscosity

   It is the internal resistance of the liquid against its flow. It is usually expressed in centipoise (cP). The human blood has a viscosity of 3-4 cP. Whereas, the viscosity of simulated body fluids used for degradation testings is approximately 1.00 ± 0.05 cP [182]. The increase in the viscosity corresponds to the increase in the shear stress and ultimately it increases the degradation rate. Gordon et al [183] reported that an increase in blood viscosity is associated with the increase in blood pressure of the population by 10 mmHg. This correlation is stronger for diastolic than systolic blood pressure.

5. pH

   pH is the measure of the negative logarithm of Hydrogen ion concentration in an aqueous solution. In humans, it is maintained within the physiological range (7.35-7.45) with the action of different buffers and reactions inside the body. In the Mg degradation, the pH of the fluid around the Mg surface increases due to the formation of H_2 and OH^- in a reaction with the medium. At local pH levels over 11, the degradation process can be slow down due to the formation of the magnesium hydroxide film on the Mg surface which

creates a barrier with the corrosion solution [178]. Furthermore, the hydroxyapatite as a passivation layer can be adsorbed on the surface under a high pH microenvironment [178]. Therefore, to mimic *in vivo* environment, degradation solution must be monitored and replaced with fresh medium consistently to ensure normal pH levels. In the dynamic fluid environment, test pH shows better stability at around basic physiological value, due to rapid ion diffusion. Based on these facts, the results from the fluid-dynamic tests may be closer to that in vascular environments as compared to static immersion tests [178].

6. Temperature

   The effect of temperature in the human physiological range 35.8– 37.2°C is reported as less important for magnesium corrosion, it may influence the adsorption of proteins and thus the response of the biological environment [184, 178]. Although there was a considerable effect on mass loss in Mg alloy reported (Li et al 2017) at 25°C and 50°C as compared to the physiological temperature. Slight temperature variation is not significant but an increase in temperature by 10 cannot be avoided. This means that temperature can be used for accelerated degradation modeling in Mg/Mg alloys. In the case of 316L and TiO_xN_y coated SS surface the effect of temperature on degradation is less important. 316L and TiO_xN_y are stable at the physiological temperature range.

7. Hydrogen evolution

   H_2 evolution measurement is only related to the implants based on Mg and its alloys. This is an approach to find the instantaneous mass loss (ML) of Mg and its alloys samples without taking them out from corrosion medium. Unlike ML experiments, H_2^{evo} is not influenced by the formation of corrosion products. The main advantage in H_2^{evo} test is the possibility of measurements at multiple time points which allows the analysis of the changes in corrosion rate occurring over the time in the experiment [185]. This can be easily implemented in static immersion tests. However, in fluid dynamic tests it is not applied yet due to the complicated behavior of released hydrogen molecules.

   The setup is quite similar as used in traditional mass loss measurements via immersion test. In the hydrogen evolution test the sample is immersed in the corrosive fluid and the evolved H_2 gas that is produced with the following reaction (1) is collected in the medium directly above the sample. One atom of Mg generates one hydrogen gas molecule [27]. Thus, the evolution of 1mol of hydrogen gas (22.4L) directly corresponds to the dissolution of 1mol of Mg (24.31g).

$$Mg + 2H_2 = Mg^{2+} + 2(OH)^{-1} + H_2 \tag{1}$$

   This demonstrate that in the H_2 evolution, the volume of H_2 gas is equivalent to the mass loss of the Mg [185]. In reality, most of the literature concerning hydrogen evolution has not reported the theoretical 1:1 ratio of hydrogen evolved to actual mass loss [185, 178]. This belongs to the inadequacies of the hydrogen collection method, given that (i) inefficient hydrogen collection in cases where experiment design is not ideal, (ii) variation in the solubility of hydrogen in water relative to sea level and temperature [178, 187], and (iii)

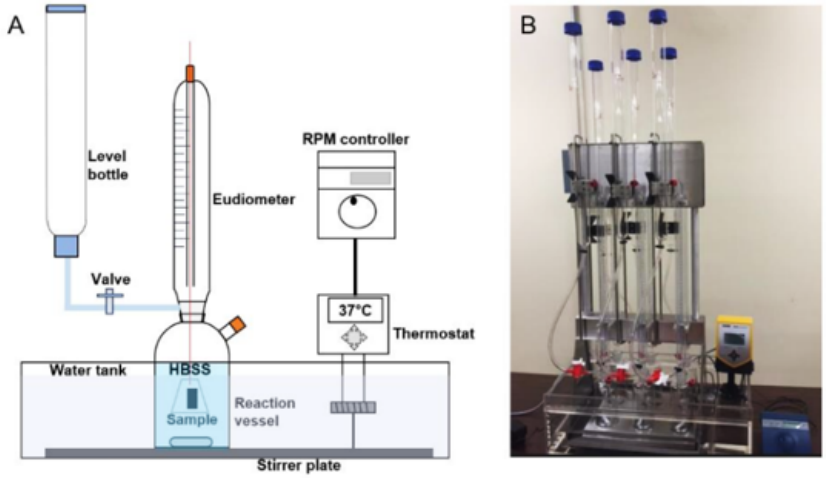

FIGURE 2.10: Eudiometer system. (A) Schematic design of one eudiometer; (B) image of eudiometer system [186].

TABLE 2.5: Effect of ions in the degradation of Mg alloys.

Presence of ions in solution	**Effect**	**Ref.**
Cl^- and OH^-	Ca^{2+} is not present in corrosion product.	[189, 178]
Cl^- and HPO_4^{2-}	Formation of magnesium phosphate corrosion product layer.	[189, 178]
HPO_4^{2-} and Ca^{2+}	Octacalcium phosphate and hydroxyapatite are deposited on the surface of the Mg alloy.	[189, 178]
HCO_3^-	Degradation rate accelerates in presence of bicarbonate and increases with the increase in its concentration.	[189, 178]
HCO_3^- with HPO_4^{2-} and Ca^{2+}	Degradation rate decreases due to the formation of insoluble hydroxyapatite.	[189, 178]

rare pre-saturation of the corrosion medium with hydrogen [178, 188]. In a recent study by Liu et al. 2018 [186], Eudiometer (Figure 2.10) is used for the hydrogen evolution measurement. They reported that eudiometer can provide better real-time measurement of corrosion rates using hydrogen volume evolution. Eudiometer allows the access of measurement without touching the samples, which is not possible by mass loss and volume loss.

8. Ions

   The role of ions is very crucial in the degradation behavior of materials. For instance Table 2.5 shows the effect of different ions on the degradation of Mg alloys. Different simulated body fluids are being used to degrade biomaterials and each gives a different degradation and corrosion response. The selection of body fluids in a particular experiment highly depends on the desired outcome. For instance, HBSS without Ca^{2+} and Mg^{2+} ions are used instead of normal HBSS to avoid the Ca and Mg phosphates on the surface of biomaterials.

TABLE 2.6: Available in vitro recommendations observing the V/A ratio to apply [191].

	DIN EN ISO 10993-12 (2007) Biological evaluation of medical devices – Part 12: Sample preparation and reference materials
Volume/area (ml/cm^2) ±10%	0.17-0.8 (depending on the shape)
Volume/mass (ml/g) ±10%	5-10 (depending on the shape)
	ASTM G31-72 (2004) Standard Practice for Laboratory Immersion Corrosion Testing of Metals
Volume/area (ml/cm^2)	20-40

9. Volume/Area ratio

   This is the volume of fluid per unit exposed surface area of the sample. It is usually expressed in ml/cm^2. It is an important factor that is often neglected. A less V/A may lead to incorrect corrosion or mass loss rate. Table 2.6 is showing the recommendations from ISO and ASTM standards regarding V/A for degradation tests.

10. Pressure

    It is the force per unit area and is usually measured in N/m^2 or Pa. In the physiological environment, it is measured as mmHg and the normal pressure of flowing blood through the artery is 120/80 mmHg. There are both kinds of pumps used in in-vitro testing like peristaltic (continuous flow) and pulsatile (pulsed flow) pumps to replication the blood pulses.

    It is known that the pulsatile effect on shear stress can be neglected in small diameter vessels (such as human coronary arteries) [190]. Therefore, peristaltic pumps can also be used in fluid-dynamic experiments without compromising on degradation behavior in the case of stents.

2.4.2 In vitro testing

In vitro comes from the Latin term meaning "within the glass". The term refers to studies of biological properties that are done in a test tube (i.e. in a glass vessel or outside living environment) rather than in a human or animal. *In vitro* studies are opposite to *in vivo* ("in life") studies that are supposed to be done inside an organism [194].

In general, *in vitro* tests are simple, cheap, and faster as compared to *in vivo* tests. In *in vitro* tests, one can isolate specific cells, bacteria, and viruses and study them outside the biological environment. Since the physiological environment inside humans are much more complex than we produce *in vitro* tests. Therefore, sometimes results produced by *in vitro* studies do not translate well to "real life" [195, 194].

Sometimes, experiments are conducted in an *ex vivo* environment. *Ex vivo* comes from the Latin term meaning "out of the living" which takes place outside an organism. This belongs to the conducted investigations in or on tissue from an

TABLE 2.7: Comparison of fluid-dynamic setups around the world.

S. No.	In vitro setup	Salient features	Limitations	Tested samples	Ref.
1	Dynamic test bench (Julie Levesque et al. 2007) Figure 2.11	PMMA test channel with predetermined shear stress. Photography of samples is possible during test. A compliance chamber was used to break the flow pattern from the hose. Laminar flow to the samples site. A valve is added in the reservoir with a pump to regulate different flow velocities, resulting in different values of Reynolds number and shear stress.	Test channel is for specific shape and sized samples.	Plates of AM60B of 5 mm thickness were obtained by melting AM60B ingots.	[179]
2	In Vitro stent test setup (Qiyi Luo et al. 2014) Figure 2.12	It is mainly comprised of a mock artery loop and a plasma pump. A pressure monitor was also used to monitor and set up specified pressures. The plasma pump provided the systolic/diastolic pressures and frequencies similar to the human circulatory system, where the systolic and diastolic pressures of the pump were set to 920 mmHg and 840 mmHg respectively.	The circulation medium was replaced once every two weeks in order to maintain a pH value range of 7.4 ± 0.2. The proposed setup is dedicated for stent testing.	PLLA stents made by using ultrafast laser cutting machine.	[192]
3	Stent testing with bioreactor (Youngmi Koo et al. 2017) Figure 2.14	In this setup, the bioreactor (CartiGen C9, Instron, Norwood, MA) consisted of: (i) a load cell combined reactor; (ii) a pump with a multi-channel flow system; (iii) a reservoir; and (iv) a controller was used as a test setup. the samples can be subjected to simultaneous dynamic compressive loading and interstitial flow with no risk of crevice corrosion. Tests were performed in a humidified incubator at 37°C in 5% CO2 with 250ml SBF in the bioreactor reservoir at flow rate of 1.5 mL/min (1.6 mm/s).	The proposed setup is dedicated for the cylindrical shape samples i.e. pins. Stents can not be tested.	5.0 mm-long Mg-based pins with 1.7mm diameter including pure Mg and Mg-Zn-Mn pins (as-cast and extruded).	[21]
4	Microfluidic system (Lumei Liu et al. 2017) Figure 2.13	This microfluidic system has two main parts, a pump system, and a microfluidic chip. The shear stress range for this system is 4 ∼37.1 dyn/cm^2 for the standard 0.4 μ-slide flow chamber. The microfluidic chip was fabricated following the protocol of the soft-lithography negative photoresist process for SU-8 2100 (Microchem Corp., USA) [36]	The proposed setup is dedicated for the cuboid shape samples. Stents can not be tested. No pH controlling.	Cuboids of Magnesium-based alloys WE43, AZ31, ZWEK-L and ZWEK-C and stainless steel 316L SS was used with dimension 5mm x 2 mm x3 mm .	[61]
5	Porcine arteriovenous shunt model (Fumiyuki Otsuka et al. 2015) Figure 2.15	This is an ex-vivo arteriovenous shunt model. It was developed to study the extent of platelet adherence, thrombus formation, and acute inflammation in Xience-EES. The main purpose was to examine inherent platelet mediated thrombus formation induced by contemporary DES of differential design. The target blood activated clotting times between 150s and 190s were achieved with intravenous heparin (100 IU/kg) dosing without antiplatelet agents.	The proposed setup is dedicated for stent testing. No pH controlling.	Following four different contemporary DESs with biodegradable coatings were used. 1. BioMatrix Flex biolimus-eluting stent (BES) (Biosensors, Newport Beach, California), (n = 6). 2. Nobori-BES (Terumo, Tokyo, Japan), (n = 6). 3. Synergy-EES (Boston Scientific, Natick, Massachusetts), (n = 6). 4. Orsiro sirolimus-eluting stent (SES) (Biotronik AG, Bülach, Switzerland), (n = 6).	[193]

organism in an external environment with minimal alteration of natural conditions [195, 194].

In vitro dynamic loading setups are widely used to degrade implant materials providing the dynamic flow of simulated body fluids. These tests aim to predict the degradation behavior of implant material inside the human body. The following are different *in vitro* setups being used to degrade different implant materials and conditions.

Table 2.7 shows some important *invitro* setups reported around the world for the degradation tests of implpant materials. All the presented setups are compared according to their salient features, limitations, and tested samples.

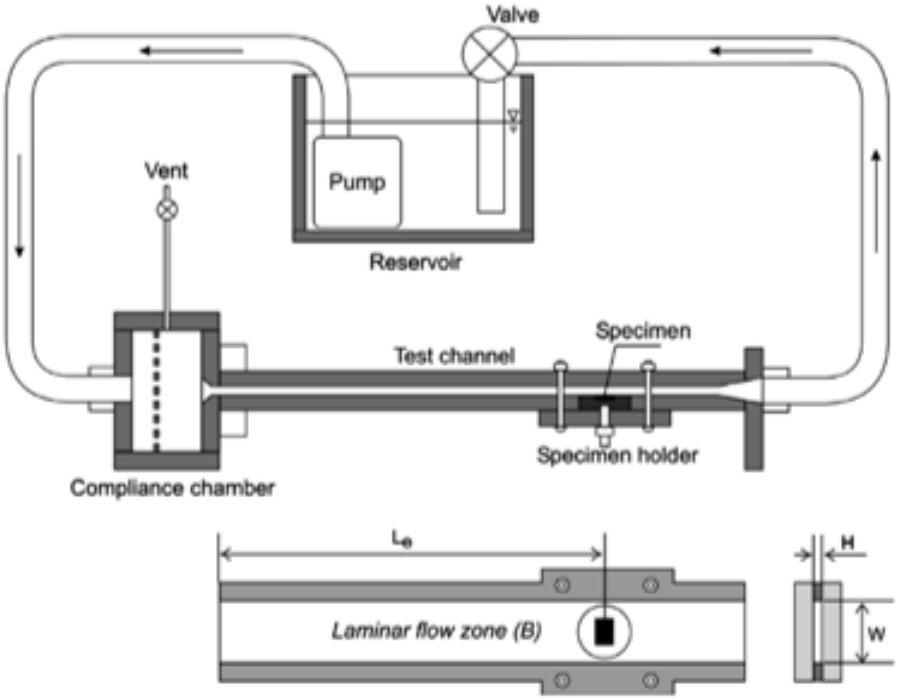

FIGURE 2.11: Dynamic test bench by Julie Levesque et al. 2007 [179].

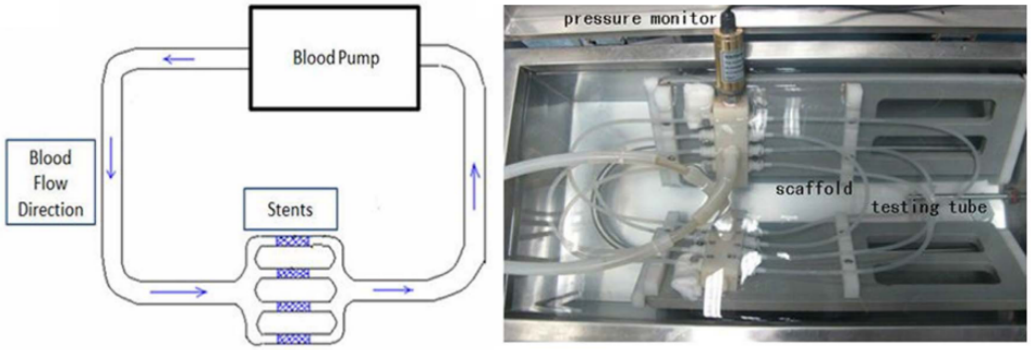

FIGURE 2.12: *In vitro* test setup by Qiyi Luo et al. 2014 [192].

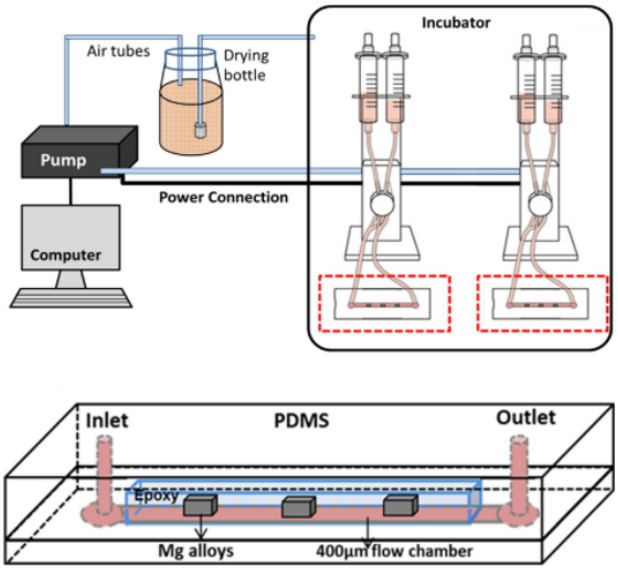

FIGURE 2.13: Microfluidic system design by Lumei Liu et al. 2017. (a) A schematic setup of the microfluidic system (b) A diagram of the plate flow chamber with reusable epoxy-embedded alloys [61].

- Dynamic test bench, Levesque 2007
  This test bench was developed to approximately replicate the physiological conditions encountered in coronary arteries. The main components of this setup are a test channel, compliance chamber, pump, pseudo-physiological solution.

  The test channel is made of polymethyl-methacrylate (PMMA) which allows the possibility to observe the samples and to take the photographs during tests. It is placed in a closed-loop system in which a special saline solution is flowing. This test channel was used to apply predetermined shear stress on the sample surface. To ensure the uniform shear stress the width of the channel was set to 40 mm and its height was 5 mm. the channel (in front of the sample) is long enough to develop laminar flow (230 mm) at the location of the sample. This test channel allows tests with a Reynolds number as high as 500, which is high enough to simulate physiological conditions.

  A compliance chamber was used to break the flow pattern from the hose. The solution flows in this chamber through a perforated plate. A small vent was used on the top of this chamber to evacuate the trapped.

  The pump used in this setup is a centrifugal submersible pump. All contacted parts of the pump with the solution are made of or coated with polymers which allow working in a saline environment. A valve is added in the reservoir with a pump to regulate different flow velocities, resulting in different values of Reynolds number and shear stress.

  The pseudo-physiological solution used was modified Hanks' solution (H1387, Sigma–Aldrich, Canada). Since the chloride ion has a significant effect on the corrosion of magnesium alloys, the solution was diluted to reproduce physiological Cl- concentration. Carbonate ions were also adjusted by adding sodium bicarbonate (NaHCO3). During preliminary tests, a rapid

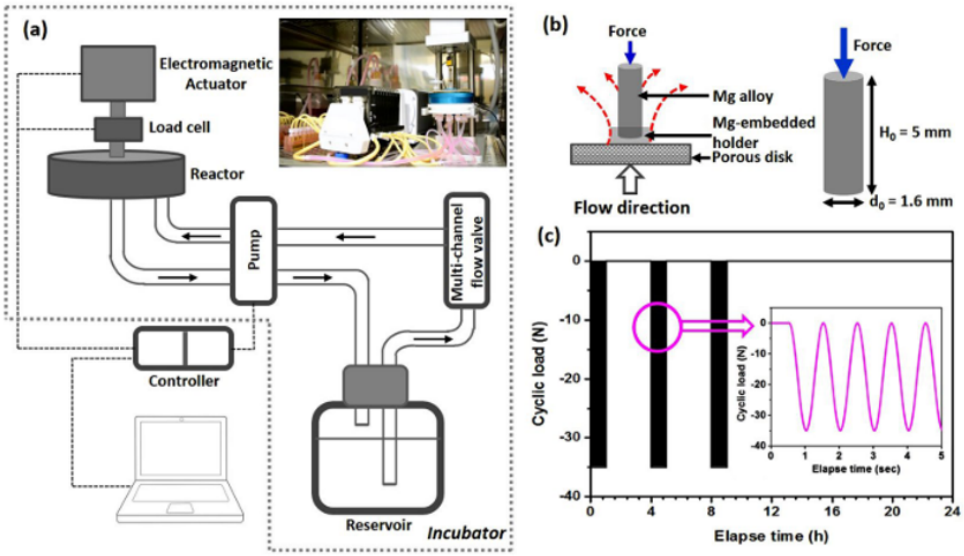

FIGURE 2.14: Microfluidic system design by Youngmi Koo et al. 2017. (a) A schematic setup of the microfluidic system (b) A diagram of the plate flow chamber with reusable epoxy-embedded alloys [21].

rise in the pH of the solution was noted during tests. To solve the problem of the rapid rise of pH initially, HEPES buffer was added to the solution.

- In Vitro stent test setup, Luo Q 2014
  This is a custom-made system for the simulation of an in-vivo environment. It is mainly comprised of a mock artery loop and a plasma pump. The plasma pump provided the systolic/diastolic pressures and frequencies similar to the human circulatory system, where the systolic and diastolic pressures of the pump were set to 920 mmHg and 840 mmHg respectively. A pressure monitor was also used to monitor and set up specified pressures. Phosphate buffer solution (PBS) was used as a circulation fluid at a frequency of 70 times per minute to simulate the in vivo circulation medium.

- Microfluidic system, Lumei Liu 2017
  This microfluidic system has two main parts, a pump system, and a microfluidic chip. In this setup, a pump system (ibidi®, München, Germany) for the simulation of blood flow microenvironment. The shear stress range for this system is $4 \sim 37.1$ dyn/cm^2 for the standard 0.4 μ-slide flow chamber (50 x 5 x 0.4 mm3 ibidi®, München, Germany). To simulate blood vessels a microfluidic chip was designed in which Mg alloys were implanted. The microfluidic chip was fabricated following the protocol of the soft-lithography negative photoresist process for SU-8 2100 (Microchem Corp., USA) [196].

- Stent testing with bioreactor, Youngmi Koo 2017
  In this setup, the bioreactor (CartiGen C9, Instron, Norwood, MA) consisted of: (i) a load cell combined reactor; (ii) a pump with a multi-channel flow system; (iii) a reservoir; and (iv) a controller was used as a test setup. Mg pins were partially mounted in epoxy resin and placed on porous disks (316LSS, 100-micron grade, 12.7 mm OD, 1.7 mm thick). In this configuration, the

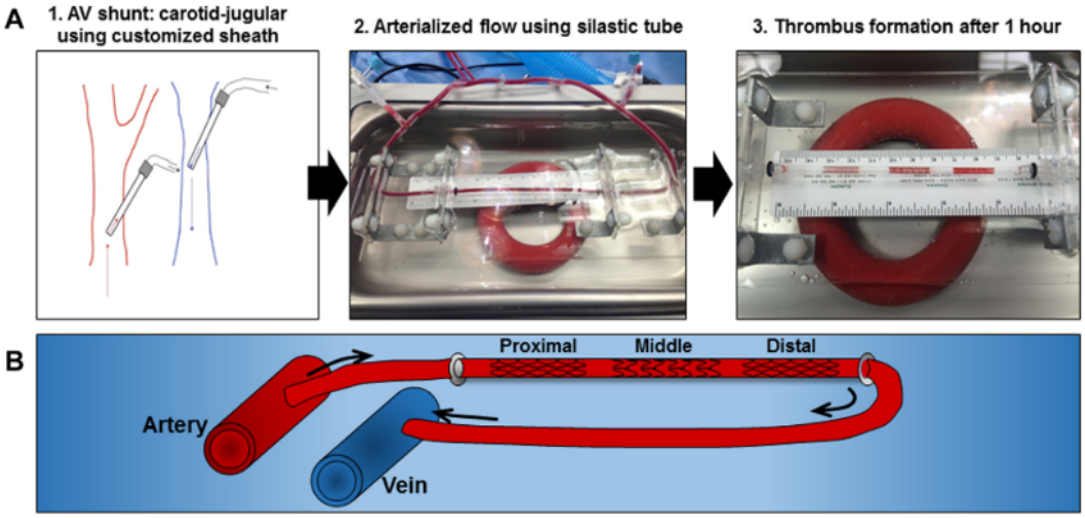

FIGURE 2.15: Porcine arteriovenous shunt model by Fumiyuki Otsuka et al. 2015. (A) A porcine ex vivo carotid to jugular arteriovenous (AV) shunt model involving a test circuit of 3 in-line stents within a silastic tube was used to test thrombogenicity with 1 h of circulating blood. (B) Schematic illustration of the acute shunt model [193].

samples were subjected to simultaneous dynamic compressive loading and interstitial flow (Fig. 1b) with no risk of crevice corrosion. Dulbecco's modified Eagle's medium (DMEM) with 10% fetal bovine serum (FBS) and 1% penicillin-streptomycin (P/S) was used as a simulated body fluid (SBF). Tests were performed in a humidified incubator at 37°C in 5% CO2 with 250ml SBF in the bioreactor reservoir at flow rate of 1.5 mL/min (1.6 mm/s).

- Porcine arteriovenous shunt model, Fumiyouki 2015
  This is an ex vivo arteriovenous shunt model. It was developed to study the extent of platelet adherence, thrombus formation, and acute inflammation in Xience-EES (n = 24) compared with the following 4 contemporary DES with biodegradable coatings.

  1. BioMatrix Flex biolimus-eluting stent (BES) (Biosensors, Newport Beach, California), (n = 6)
  2. Nobori-BES (Terumo, Tokyo, Japan), (n = 6)
  3. Synergy-EES (Boston Scientific, Natick, Massachusetts), (n = 6)
  4. Orsiro sirolimus-eluting stent (SES) (Biotronik AG, Bülach, Switzerland), (n = 6)

  Each shunt model had 3 stents and each animal had 2 shunt experiments. In each shunt, 2 Xience-EES deployed separated by biodegradable polymer DES or vice versa. Therefore, a total of 48 stents were deployed in 16 shunts from 9 swine for the assessment of acute thrombogenicity. All DES were deployed at nominal pressure in Sylgard (Dow Corning, Midland, Michigan) mock vascular phantoms (Ref8) (inner diameter: 2.70 mm x 11 cm length) fabricated using 316L stainless steel tubing and commercial elastomer kit (Sylgard-184, Dow Corning).

The amount of platelet aggregation to struts was studied after exposure to circulating blood for 1h through an established arteriovenous carotid to jugular shunt. This research was specifically designed to examine inherent platelet mediated thrombus formation induced by contemporary DES of differential design. Therefore, the target blood activated clotting times between 150s and 190s were achieved with intravenous heparin (100 IU/kg) dosing without antiplatelet agents.

The temperature of stented tubing was maintained in a 37°C water bath and flow rates were also monitored continuously. After each run, stents were gravity perfused with Ringer'slactate with 10% neutral buffered solution. Stents are bisected and one half was immunostained and examined by confocal microscopy, whereas the other one-half was examined under scanning electron microscopy (SEM).

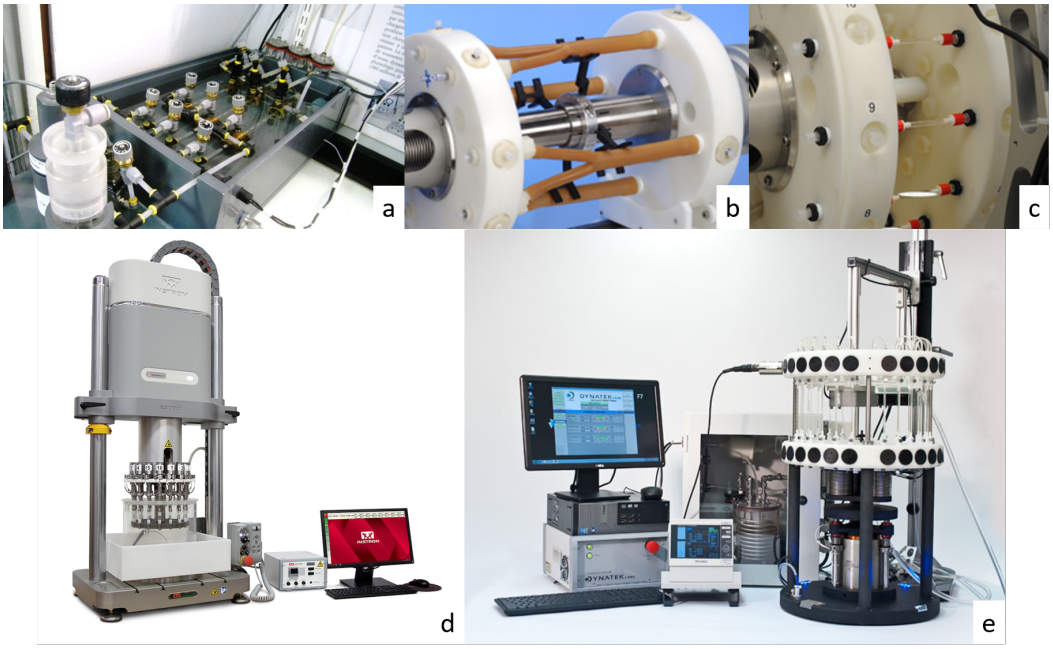

FIGURE 2.16: *In vitro* stent testers: a) Stent fatigue tester, Protomed Labs [197], b) BOSE 9100 series pulsatile radial fatigue tester [198], c) Pulsatile durability testing of vascular stents [198] , d) ElectroPuls® 16-Station testing system, Instron [199], e) UST stent tester, Dynatek Labs [200].

All of the aforementioned degradation test setups are different from each other with the possibility to degrade samples in different shapes and under different conditions. To better evaluate the degradation properties of stents, or biomaterials used for stents there is a need for a standardized way of testing. Therefore, a standard degradation testing setup is needed which can degrade all material types used for stents.

However, there are several standard commercial stent testers Figure 2.16 for in vitro mechanical fatigue testing to determine pulsatile radial fatigue, pulsatile durability, circumferential tensile strength longitudinal tensile strength, kink radius, dynamic compliance, crush resistance, local compression, migration resistance, pull test for modular components, radial force, strength of stent to graft

are available from manufacturers like medical device testing services (MDT) [198], Dynatek Labs [200], Protomed Labs [197], Instron [199], TA Instruments [201] to name a few. However, in vitro testing in the environment close to the in vivo conditions or to the human physiological environment is still an open and challenging task.

3 Materials and Methods

This Chapter discusses the standardized form of experimental setups, characterization techniques, samples and other materials and methdos. All of the specific details are provided in respective chapters. Section 3.1 introduces the degradation experiments in the static immersion, fluidic-dynamic, and electrochemical corrosion environment and their experimental setups. Section 3.2 describes the characterization techniques used for the experiments. Section 3.3 presents the samples used for the research. To replicate the fluidic properties of blood, different simulated body fluids were used which is addressed in Section 3.4. Section 3.5 provides the short introduction of the LabVIEW platform where the virtual instrument of the fluid dynamic setup has been built.

3.1 Experimental setups

There are three different kinds of experiments for the evaluation of degradation or corrosion in the simulated blood conditions. These methods differ from each other by the presence of fluid flow and electric potential.

3.1.1 Static immersion test

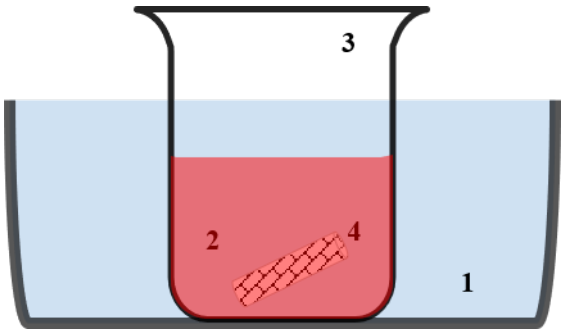

FIGURE 3.1: Schematical representation of the immersion test: 1) Circulating water bath; 2) Hank's Balanced Salt Solution (HBSS); 3) Glass container; 4) Stent.

It is the simplest test in which the sample is immersed in a simulated body fluid or corrosive medium in static conditions and the mass loss is measured as a function of time Figure 3.1 . In this method, no effect of fluid flow or fluid velocity is present. This method is used to study the degradation without any influence of flow velocity and shear stress.

The standards for the volume of the fluid in the static immersion testing are described in Table 2.6. After the specified fluidic exposure, the fluid and material samples are characterized and analyzed.

The degradation studies in static immersion tests are supported by the application of various characterization techniques like SEM-EDX, Fourier-transform infrared spectroscopy (FTIR), contact angle, transmission electron microscopy (TEM), atomic force microscopy (AFM), Laser profilometry to name a few for analyzing the degradation induced changes in sample volume and on its surface before and after the degradation test.

3.1.2 Fluid- dynamic test

In this method, the samples are exposed to fluid-dynamic loading (Figure 3.2). The main purpose of this method to study the effect of flow velocity and shear stress on the sample surface. This method is used in parallel to the static immersion test.

The standard for fluid volume per sample is the same as the static immersion test. Similarly, all the characterization techniques used in static immersion tests are used in the fluid dynamic test.

Various existing fluid dynamic testing setups have been introduced in Section 2.4.2. All presented systems are different from each other having a similar feature of exposing the sample to the fluid flow. These systems are custom designed based on the research needs. They have a flow rate of few $\mu l/min$ to few l/min.

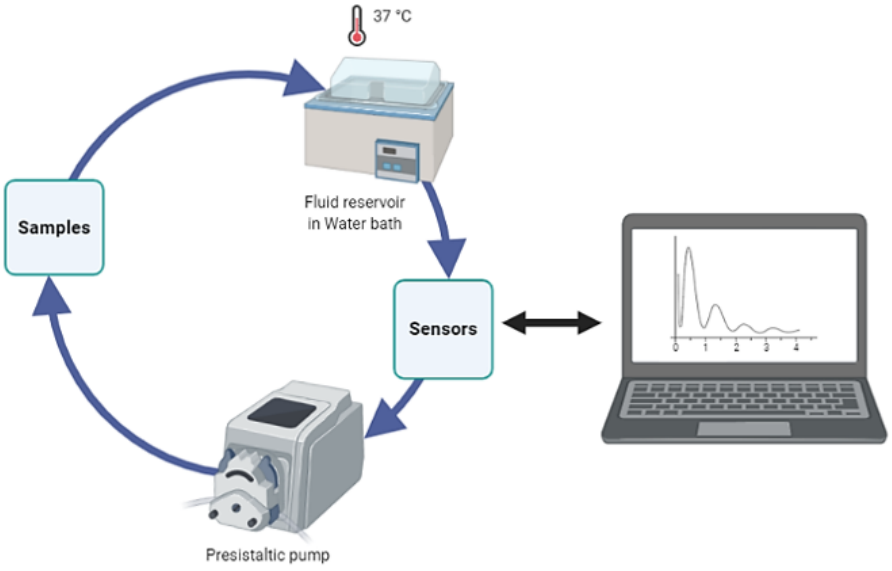

FIGURE 3.2: Illustration of fluid dynamic testing. This illustration is created with BioRender.com

3.1.3 Electrochemical Corrosion test

In this method, an electrical biasing voltage is applied and the corresponding current is measured. The test setup contains three electrodes including the reference electrode, the working electrode, and the counter electrode. The device used for this experiment is called the potentiostat whereas the combination of the three electrodes is called the corrosion cell.

The electrochemical cell used for the corrosion tests of TiO_xN_y coated stainless steel stents (Figure 3.3) comprises three electrodes. Stents were used as the working electrode (WE), saturated calomel electrode (Hg_2Cl_2 (SCE)) was used as a reference

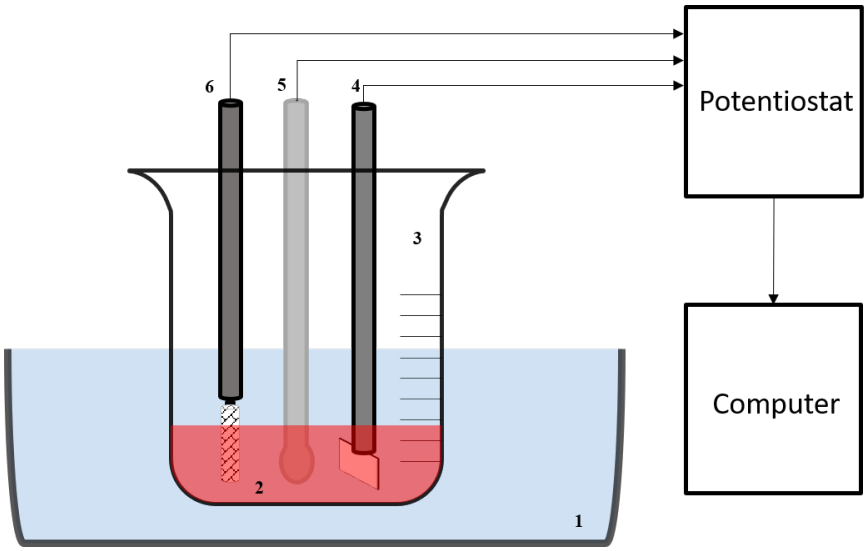

FIGURE 3.3: Schematical representation of the electrochemical setup:1) Circulating water bath; 2) Hank's Balanced Salt Solution(HBSS); 3) Glass beaker; 4) Working electrode – TiO_xN_y stent; 5) Reference electrode – Saturated Calomel Electrode (SCE); 6) Counter electrode – Platinum sheet (20mm x 20mm).

electrode (RE) and a platinum sheet (20mm x 20mm) was used as a counter electrode (CE). The electrochemical cell was coupled to IviumStat.h (Ivium Technologies Eindhoven, The Netherlands) and the data recording was performed by IviumSoft (Ivium Technologies, Eindhoven, The Netherlands). To regulate the temperature, circulating a laboratory water bath (TX150, Grant Instruments, UK) was used. To better estimate the surface area exposed to the fluid, only 10mm of each sample was immersed in the fluid.

3.2 Characterization of physical and chemical properties

3.2.1 SEM

Scanning Electron Microscopy (SEM) is a powerful technique in Material Analysis producing high magnification greyscale images of samples by scanning their surface with a finely focused electron beam. This electron bombardment causes the emission of secondary electrons, backscattering of high energy primary electrons, and the creation of element-specific X-rays [202]. In particular, X-rays are a "fingerprint" of each element used to identify the type of elements that exist in a sample [203]. Following are the commonly used detectors in Electron Microscopy.

- SE detectors only collect low energy secondary electrons originate from the top nanometers of the sample. It provides excellent surface topography images with very reasonable resolution.
- Backscatter detector only collects primary electrons. It is used for layer determination, as each layer contains a different element.
- Inlens- or Through Lens Detector is not recommended for surface topography but it does achieve the highest magnitudes possible [202].

- EDX detector collects X-rays and is used for elemental detection, mapping, and quantification.

Environmental scanning electron microscope Philips XL30 ESEM FEG was used for all the SEM images presented in this work. The accelerating voltage was set to 3.0kV with spot size 3 for SEM.

3.2.2 EDX

Energy-dispersive X-ray spectroscopy (EDS, EDX, EDXS, or XEDS) is an analytical technique used for the elemental analysis or chemical characterization of a sample. It is also called energy dispersive X-ray analysis (EDXA) or energy dispersive X-ray microanalysis (EDXMA) [204].

It can be used in a combination with Scanning Electron Microscopy (SEM), Transmission Electron Microscopy (TEM), and Scanning Transmission Electron Microscopy (STEM) [202].

EDX coupled with SEM provides elemental analysis on areas as low as nanometers in scale. In EDX, X-rays are produced with the impact of an electron beam on the sample [202]. They serve as a "fingerprint" of each element and can be used to identify the type of elements that exist in a sample [203]. The measured intensities produce quantitative information on the element composition and distribution. The depth from where the X-rays originate depends on the sample material and the used primary electron beam energy. Typically, it is in the range of 10 to 20 keV [202].

Samples for SEM and/or EDX need to be high vacuum compatible. However, for moisturous or non-conductive samples Environmental SEM (ESEM) can be used with chamber pressures up to 1 mbar [202].

The accelerating Voltage was set to 10.0kV with spot size 5 for EDX.

3.2.3 Micro-CT

Characterization of 3-dimensional (3D) structure and morphology of tissues with high-resolution imaging is becoming increasingly important in biomedical research [205]. Micro-CT also called microtomography or micro-computed tomography is a 3D imaging technique that uses X-rays to see inside an object, slice by slice [206].

It is similar to hospital CT or "CAT" scan imaging but on a small scale (as large as 200 millimeters in diameter) with greatly increased resolution (with pixel sizes as small as 100 nanometers) [206].

Micro-CT scanners capture a series of 2D planar X-ray images and reconstruct the data into 2D cross-sectional slices which can further be processed into 3D models and even printed as 3D physical objects for analysis. With the power of 3D micro-CT systems, you can see inside the object and reveal its internal features, whereas, With 2D X-ray systems you can only see through an object. It is a non-destructive technique that provides volumetric information about the microstructure [206].

Recently, new contrast agents made micro CT scanning of soft tissue, an emerging area particularly in cardiovascular and pulmonary research [205]. With the help of micro-CT, internal structure, geometry, and composition are accessible without staining, slicing, cutting, or cross-sectioning [207].

In the presented work, micro CT is used for the surface area calculations of Mg-alloy stent. All micro-CT measurements were conducted on pre-clinical micro-CT scanner SCANCO Medical viva CT 75 (Figure 3.4). The max. X-ray energy used was 70 keV at 114 μA. The voxel resolution was 20 μm using 2000 scan positions and

FIGURE 3.4: SCANCO Medical viva CT 75 micro CT scanner

exposure time per position of 350 ms. The volume and surface quantification was done with the Scanco evaluation software. Figure X is showing the reconstructed images of Mg alloy stent after micro CT.

3.2.4 ICPMS

The Inductively Coupled Plasma Mass Spectrometry (ICP-MS) analysis is a technique that uses a high-frequency inductively coupled plasma as ionization source and a Mass Spectrometer as mass/charge filter device [208]. It is a method to determine low-concentrations (range: ppb = parts per billion = μg/l) and ultra-low-concentrations of elements (range: ptt = parts per trillion = ng/l) [209]. Therefore, it is ideal for the elemental analysis of sample solutions where the lowest detection limits are demanded.

In this work, it is used for the detection of elemental release in TiO_XN_Y stent corrosion tests.

3.3 Samples

The samples used for this study include the stainless steel 316L planar and stent samples, TiO_XN_Y coated stainless steel planar and stent samples, and Mg alloy samples including the AZ31 (rod , semi rod and planar samples) and resoloy stents.

TABLE 3.1: TiO_XN_Y samples.

Batch No.	O_2/N_2	Sample type	Experiment(s)
Batch-I	1/2, 1/5, 1/10	Planar (10mm diameter, 2mm thickness), Stents	Fluid-dynamic
Batch-II	6/10, 13/10, 27/10	Stents	Static immersion, Fluid-dynamic, Electrochemcial
Batch-III	1/1, 2/1, 2/3	Stents	Fluid-dynamic

TABLE 3.2: Mg-alloy samples.

Mg Alloy	Geometry	Sample type	Experiment
AZ31	11mm x 11m x 1 mm	Square samples	Fluid-dynamic
AZ31	Length = 10mm; radius = 3mm	Semi rod samples	Static immersion, Fluid-dynamic
Resoloy	Complex	Stents	Analytical modeling

3.3.1 TiO_XN_Y samples

Standard flat samples of 10mm diameter and 2mm height made of 316L stainless steel and medical-grade stents made of the same material were provided by Balton Sp. z o.o. , Warsaw, Poland. TiO_XN_Y films on these samples were deposited by Tomsk Polytechnic University, Tomsk, Russian Federation. The UVN-200MI vacuum pulsed magnetron sputtering system (VIP Technologies LTD, Russia) was used for the deposition of TiO_XN_Y thin films. Coating thickness was in the range of 150 - 170 nm. Table 3.1 shows the TiO_XN_Y samples used in the presented research fabricated in three different batches. Details of TiO_XN_Y film depositions are described in [30].

3.3.2 Mg alloy samples

Table 3.2 shows the Mg-alloy samples used in this study. AZ31 (Al=3%, Zn=1%, Mg=balance) is a Mg alloy used for biodegradable implants. Extruded AZ31 rods of 3mm diameter and 980mm length were obtained by Goodfellow, UK. The rods were cut by a metallic cutter into 10mm long pieces and scratched onto sandpaper of grit size 400 to transform into semi rod samples. Table 3.3 shows the AZ31 anodized samples prepared by Dr. Kerstin Kremmer at Fraunhofer IKTS. The oxide layer of $\sim$ 550nm was obtained via plasma electrolytic process using different anodizing periods. To further stabilize the degradation of AZ31 polymer coating with different drying protocols was also realized. Resoloy stents were provided by MeKo Laser Material Processing GmbH, Sarstedt, Germany for development of analytical model of entire stent surface area.

Cleaning of AZ31 samples

The samples were cleaned in chromic acid before the experiment to remove the dust residues. After every exposure to fluid AZ31 samples were first cleaned in chromic acid solution for 5 minutes, then cleaned in ultra pure water in ultra sonic bath. Before mass measurements samples were dried by using nitrogen flush.

TABLE 3.3: AZ31 samples.

AZ31 samples	Treatment protocol
Reference sample	Untreated AZ31
Sample A	Electrochemically treated AZ31, 6g/L NaOH + 6.3g/L Na_2SiO_3, with anodising time 1000s
Sample B	Electrochemically treated AZ31, 6g/L NaOH + 6.3g/L Na_2SiO_3, with anodising time 500s
Sample C	Electrochemically treated AZ31, 6g/L NaOH + 6.3g/L Na_2SiO_3, with anodising time 500s, Ubias = 200V,
Sample D	Electrochemically treated AZ31, 6g/L NaOH + 6.3g/L Na_2SiO_3, with anodising time 500s, Ubias = 200V, 3% resomer (polymer), dried @ 35°C 72h, 80°C 2h
Sample E	Electrochemically treated AZ31, 6g/L NaOH + 6.3g/L Na_2SiO_3, with anodising time 500s, Ubias = 200V, 3% resomer (polymer), dried @ 35°C 72h

3.4 Fluids

To simulate the ionic concentrations in the blood, simulated body fluid (SBF) and Hanks balanced salt solution (HBSS) without Ca^{++} and Mg^{++} ions are used. The details of salts and their concentrations are given in Appendix A.

3.5 LabVIEW

LabVIEW (National Instruments) is a widely used system-design platform. LabVIEW programs are called virtual instruments (VIs) that use graphical programming. Each VI has two windows: 1) Front panel; and 2) Block diagram. In this research, LabVIEW is used to develop the VI of the fluid-dynamic experimental setup (Chapter 5).

By using LabVIEW a program was written to monitor the sensor values for fluid-dynamic experimental setup. All the sensors were integerated to the Arduino platform. A separate program for Arduino was written to convert all the sensor signals into the meaningful values, while those values were send to LabVIEW via USB interface to show the sensors output on the front panel.

4 Development and validation of stent surface area model

This chapter presents the analytical model to determine the surface area of stents that is needed for quantified degradation tests. Section 4.1 introduces the whole topic followed by Section 4.2 which explains the stent outer surface area and the available methods for its calculation. In Section 4.3, the analytical method of entire stent surface area calculation is explained. An algorithm to use this model is presented in the Section 4.4 for corrosion rate calculation. Validation protocol is presented in Section 4.5. Results of the ESSA of resoloy stents and the validation is given in Section 4.6. In last, the concluding remarks are presented in Section 4.7.

4.1 Background

In vitro corrosion tests include static immersion tests, fluid-dynamic tests, and electrochemical tests. For the quantitative analysis of corrosion, the surface area exposed to the corrosive medium has to be defined [210, 211].

For instance, the mass loss rate (ML) and the corrosion rate (CR) in static immersion and fluid dynamic tests are calculated by Equation (2) and (3) [211]. For the calculation of corrosion rates using electrochemical tests, Equation (4) [210] is used.

$$ML = \frac{m_f - m_i}{A} \tag{2}$$

Where ML is the mass loss in mg/cm^2, m_i is the initial mass in mg, m_f is the final mass in mg, and A is the exposed surface area in cm^2.

$$CR = \frac{W \times 8.76 \times 10^4}{At\rho} \tag{3}$$

Where CR is the corrosion rate in mm/yr, W is the mass loss in g, A is the original surface area exposed to the corrosive media (simulated body fluids) in cm^2, t is the exposure time in hr, and ρ is the standard density in g/cm^3.

$$CR = K_1 \frac{i_{corr}}{\rho} EW \tag{4}$$

Where CR is the corrosion rate in mm/yr, K_1 is the constant and its value is 3.27×10^{-3} $mm.g/\mu A.cm.yr$, i_{corr} is the corrosion current density in $\mu A/cm^2$(it is the amount of current flow per unit exposed surface area of the sample), EW is the equivalent weight in g/eq, and ρ is the standard density in g/cm^3.

In both the aforementioned equations, the exposed surface area is essential for the calculation of the corrosion rate. This is simple in the case of regular-shaped geometrical samples—e.g., rounded and square samples, wire, or hollow tubes.

Stents have a very complex geometry, which makes it difficult to calculate the exposed surface area. Therefore, in the case of stents, quantitative corrosion tests cannot be performed due to the lack of methods for the calculation of the surface area. For this reason, simpler geometrically shaped samples are used as a reference to predict the corrosion behavior of stents inside the in vivo environment [97, 212, 213].

In the last two decades, plenty of studies have been conducted on stent mechanical testing, fatigue analysis, etc. [214, 215]. However, in the case of corrosion testing with stents, only a limited number of studies have been conducted. For instance, there are studies focused on the corrosion behavior of stents [216, 217, 218] which do not use quantitative analysis or use only the outer or upper stent surface [216]. The aforementioned work, by Hertel et al. 2016 [217], includes only a small part of the outer side of the stent struts on various regions exposed to the corrosive medium and conducted electrochemical corrosion tests on bare-metal stents. The study does not consider the influence of geometry on the corrosion behavior of stents. The variability of coating thickness on different surfaces of a coated metallic stent may also affect the results. Furthermore, this technique is also not applicable to other kinds of degradation tests and corrosion tests—for example, immersion and fluid dynamic tests.

Several techniques have been developed to investigate the stent outer surface area (SOSA) or metallic surface area (MSA) of the stent [219, 220]. The SOSA or MSA is the ratio of the outer stent surface which is in contact with the vessel. It includes only the outer side of the strut and does not represent the entire stent surface area.

Although micro-CT is a well-established non-destructive method, it can be cost and time intensive and is therefore not a standard procedure for stent surface quantification within a common laboratory. As a consequence, a new characterization method is needed for stent surface quantification.

Subsequently, to enable the corrosion experiments directly with stents instead of using only a small part to better replicate the degradation behavior inside the artery, this study aimed to develop a non-destructive method for the entire stent surface area calculation with the help of the mathematical model.

4.2 Stent Outer Surface Area (SOSA)

As mentioned above, this surface area only covers the outer surface of the stent. It can also be expressed as the metallic surface area (MSA) of the stent or the metal to artery ratio (MAR). SOSA is a ratio between the stent outer surface and the covered vessel inner surface area (Equation (5)). In the ISO standard 25539-2 [221], the SOSA has been defined as the contact area between the stent and the vessel. The SOSA is inversely proportional to the stent-free surface area (SFSA), which is a percentage of the surface area of the cylinder formed by the implant frame which is not covered by implant material [221]. In practical applications, SOSA or MSA are preferred by manufacturers to the SFSA.

$$SOSA = \frac{A_{stent}}{A_{vessel}} 100(\%) \tag{5}$$

where A_{stent}: outer surface of the stent; A_{vessel}: surface of the covered vessel. Karoly et al. [219] and Kovacs et al. [220] developed and presented the following three methods for the calculation of the SOSA.

4.2.1 Calculation Method

Karoly et al. [219] developed this method using various stent values, such as stent diameter, length, and strut thickness. The ratio of the mass of the hollow tube (same material properties and wall thickness to those of the stent) to the mass of the stent is considered a metallic surface area. Equation (6) shows the mass of the ideal tube which has a 100% MSA value given as:

$$m_{tube} = d\pi l s \rho \tag{6}$$

where m_{tube}: mass of the tube; d: stent outer diameter; l: stent length; s: tube's wall thickness (strut thickness of the stent); ρ: density of the stent. The metallic surface area can be calculated using Equation (5) with the ratio of the stent mass (m_{stent}) and the calculated mass of the ideal tube:

$$SOSA = \frac{m_{stent}}{m_{tube}} \tag{7}$$

4.2.2 Manual Method

This method is based on manual stereomicroscopy. The stents were rotated by increments of 15° from the starting 0° position to 360°, and high-resolution digital images were taken of each segment of the stents' mantle with a Olympus SZX16 stereomicroscope (Olympus Corporation, Shinjuku, Tokyo, Japan) fitted to a precision rotary unit. The pictures were then joined and examined with JMicroVision image analysis software.

4.2.3 Automatic Method

In this method, the stents were pulled up to a shaft connected to a motor. The stents were rotated during the scanning process to produce one whole picture of the stent pattern. In the scanning platform, the rotational speeds and direction can be changed.

4.3 Entire Stent Surface Area (ESSA)

The $ESSA$ covers all surfaces of the stent and is the sum of all of the surface areas. In particular, the entire or total stent surface area is the sum of the surface area of all four sides (Figure 4.1) of all crowns of the stent (Equation (8)). For simplicity, we use ESSA as A and SOSA as Aout. Consider stent as a hollow cylinder, where r_1 is the radius of that cylinder from the outer surface, whereas r_2 is the radius from the inner surface (Figure 4.2). The inner and outer surface areas (S_1 and S_2) of this hollow cylinder can be expressed as Equations (9) and (10).

$$A = A_1 + A_2 + A_3 + A_4 \tag{8}$$

$$S_1 = 2\pi r_1 l \tag{9}$$

$$S_2 = 2\pi r_2 l \tag{10}$$

Since S_1 and S_2 are the surface areas of the cylinder, to get the surface area of the stent we have to multiply it with the $SOSA$. The surface areas of all sides will be:

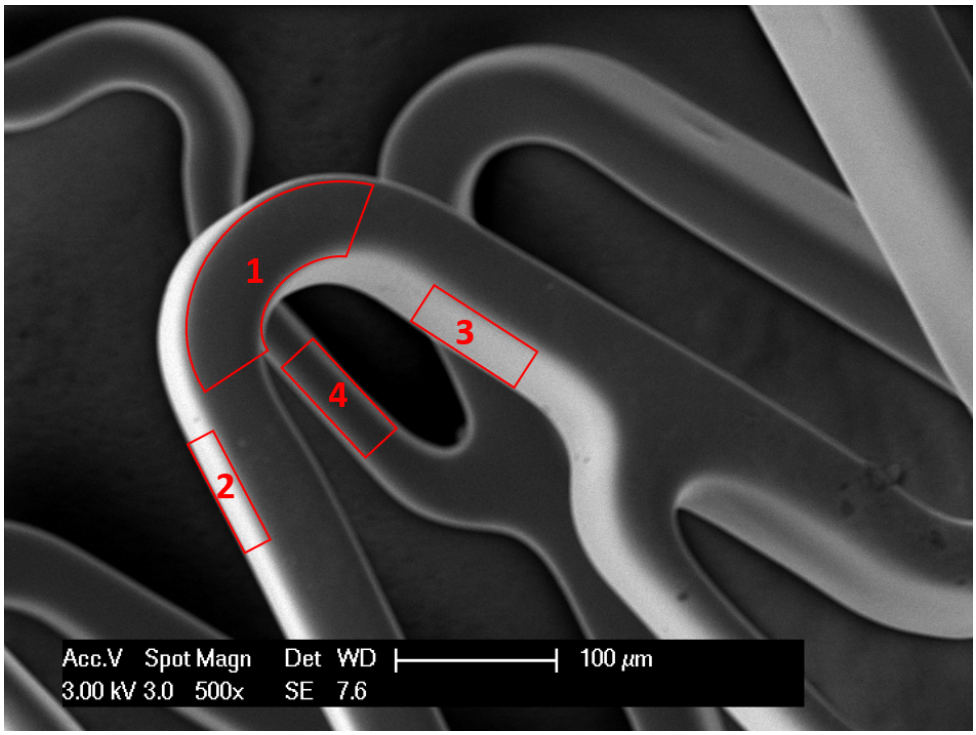

FIGURE 4.1: Scanning electron microscopy (SEM) image of a stent showing 4 surfaces of stent wire: upper or outer surface (1), bottom or inner surface (4), right and left surfaces (2,3).

$$A_1 = S_1 A_{out} \tag{11}$$

$$A_2 = S_2 A_{out} \tag{12}$$

$$A_3 = cS_1 A_{out} = cA_1 \tag{13}$$

$$A_4 = cS_2 A_{out} = cA_2 \tag{14}$$

where c is the ratio between the strut thickness (s) and the average width of the outer surface of the stent wire (w).

$$c = \frac{s}{w} \tag{15}$$

Substituting the values of A_1, A_2, A_3, and A_4 from Equations (11), (12), (13), and (14) in Equation (8), we get:

$$A = S_1 A_{out} + S_2 A_{out} + cS_1 A_{out} + cS_2 A_{out} \tag{16}$$

$$A = A_{out}.(1 + c).(S_1 + S_2) \tag{17}$$

$$A = 2\pi l.A_{out}.(1 + c).(S_1 + S_2) \tag{18}$$

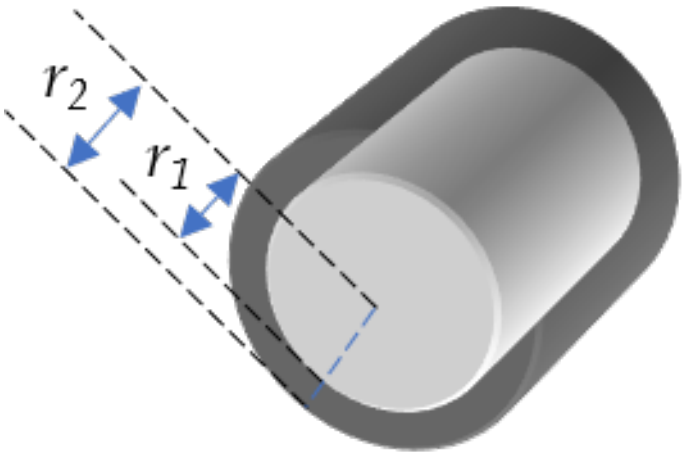

FIGURE 4.2: Hollow cylinder with inner radius r_1 and outer radius r_2.

This is the standard equation to calculate the stent total surface area. Variation in widths in the stent outer surface area may increase the error. The less the variation in widths of outer surface, the more accurate the calculation of the surface area will be.

4.3.1 Value of c

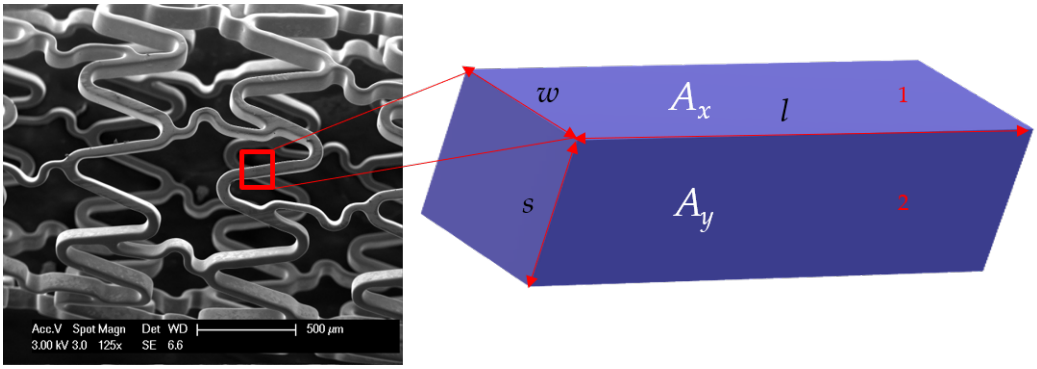

FIGURE 4.3: Cross sectional part of stent wire with length l, width of outer surface w, and strut thickness s. The three sides of this rectangular block are s, l, and w. A_x is the area of surface 1 with sides w and l. A_y is the area of surface 2 with sides s and l.

Let A_x and A_y be the areas of surfaces 1 and 2, respectively (Figure 4.3). Then,

$$A_x = l.w \tag{19}$$

$$A_y = l.s \tag{20}$$

Rearranging Equation (19):

$$l = \frac{A_x}{w} \tag{21}$$

Put the value of l from Equation (21) in Equation (20):

$$A_y = \frac{A_x}{w}.\, s \tag{22}$$

$$\frac{A_y}{A_x} = \frac{s}{w} = c \tag{23}$$

or:

$$A_y = c.A_x \tag{24}$$

where:

$$c = \frac{s}{w} \tag{15}$$

4.3.2 Value of w

The width of all different sides of the outer surfaces of stents was measured at 200 spots and then all lengths were averaged according to the weighted percentage of the particular part, as shown in Equation (25).

$$w = \frac{\Sigma_{i=1}^{n} a_i w_i}{\Sigma_{i=1}^{n} w_i} \tag{25}$$

where w_i is the individual width and ai is the weight of that width. n is the number of measurements taken.

4.4 Algorithm of the New Model for Corrosion Rate Calculation

Figure 4.4 presents the schematic flow diagram showing all the steps to calculate the ESSA or A and its application for the corrosion rate calculations in different experiments. After the calculation of A, the corrosion rates of stents can be calculated using Equation (3) for the static immersion test and fluid-dynamic test. Whereas, Equation (4) can be used for the calculation of the electrochemical corrosion rate. The whole length of the stent is not used in electrochemical corrosion tests. Therefore, AEC should be used instead of A (Equation (26)).

$$A_{EC} = \frac{l_{EC}}{l}.\, A \tag{26}$$

where A_{EC} is the stent surface area used in the electrochemical corrosion test, l is the total stent length, l_{EC} is the length of the stent used in the electrochemical corrosion test, and A is the $ESSA$.

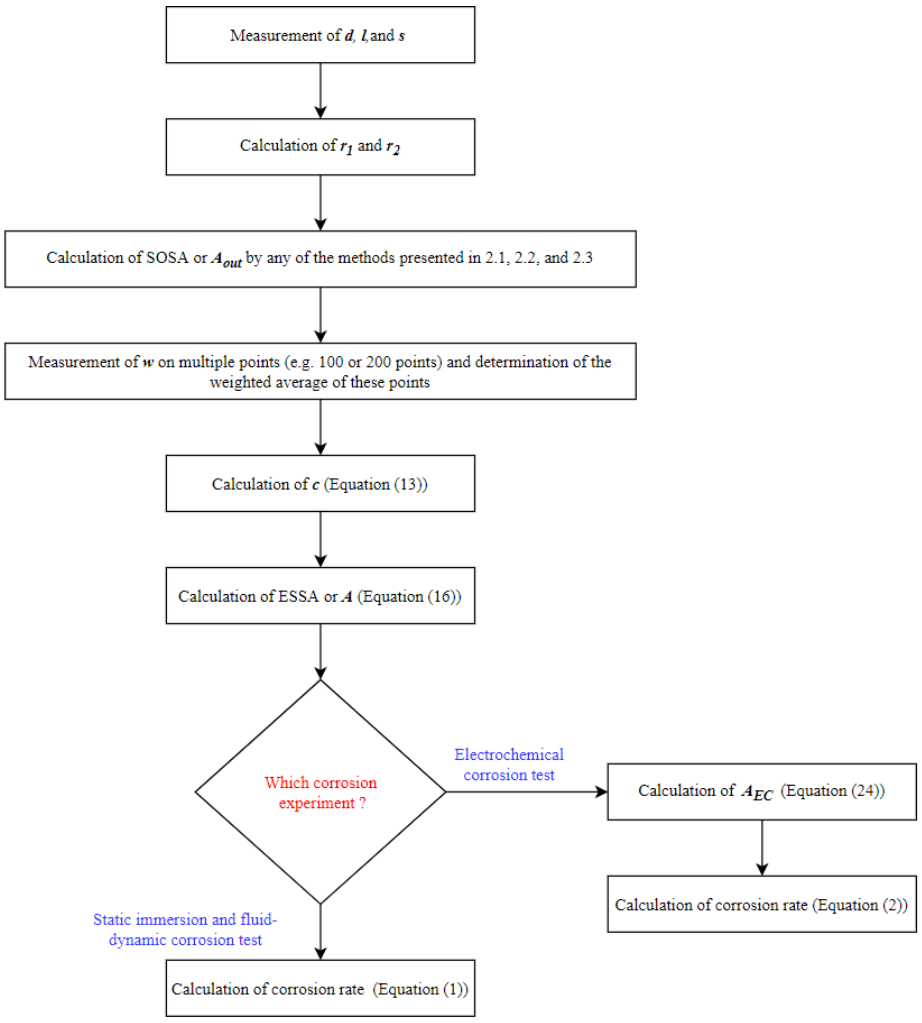

FIGURE 4.4: Schematic diagram of the algorithm to apply the surface area model for corrosion rate calculation.

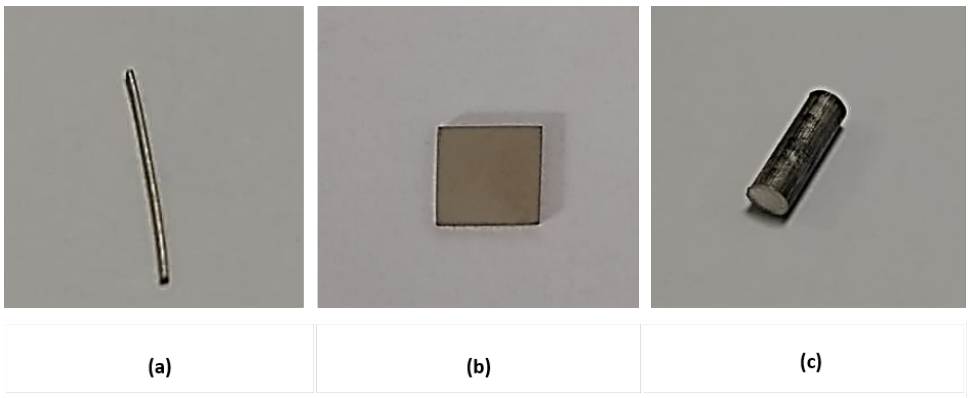

FIGURE 4.5: Samples with simpler geometry: (a) Mg alloy wire, (b) stainless steel, and (c) Mg alloy AZ31.

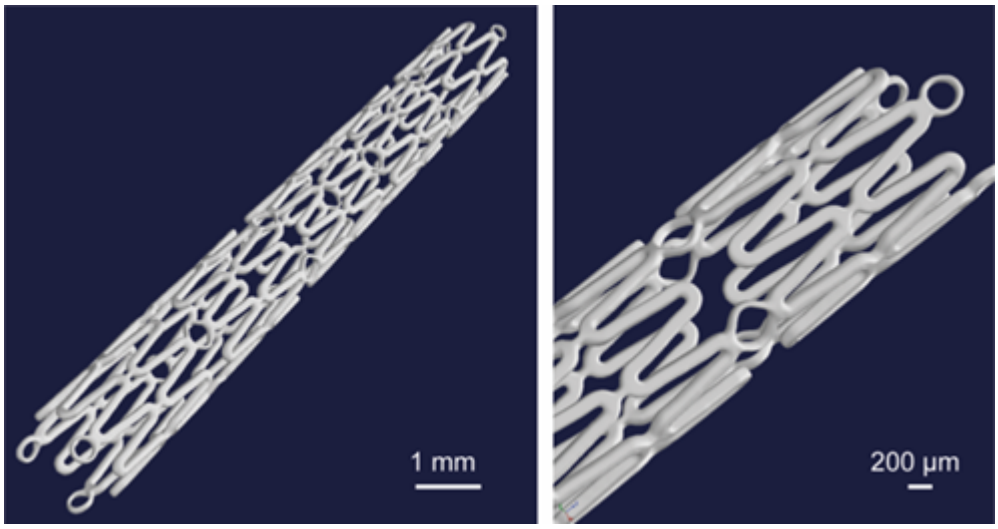

FIGURE 4.6: 3D representation of the whole stent volume from the micro-CT investigation.

4.5 Validation of the ESSA Model

The obtained results were validated by the following protocol.

1. Surface area calculation of the simpler samples by micro-CT.
   (a) Samples with a different geometry and material were selected (Figure 4.5).
   (b) Micro-CT needs a reference volume for the surface area calculation of samples. Two different methods were used for the volume calculation of samples.
   (c) Micro-CT measurement of samples was conducted.
   (d) Reference volume by mass was used for the surface area calculation of samples.
2. Surface area calculation of stents by micro-CT.
   (a) Volume determination of stents by mass.
   (b) Micro-CT measurement of Mg alloy stent samples was conducted.
   (c) Surface area calculation using the reference volume by mass.
   (d) Comparison of the results by model and micro-CT.

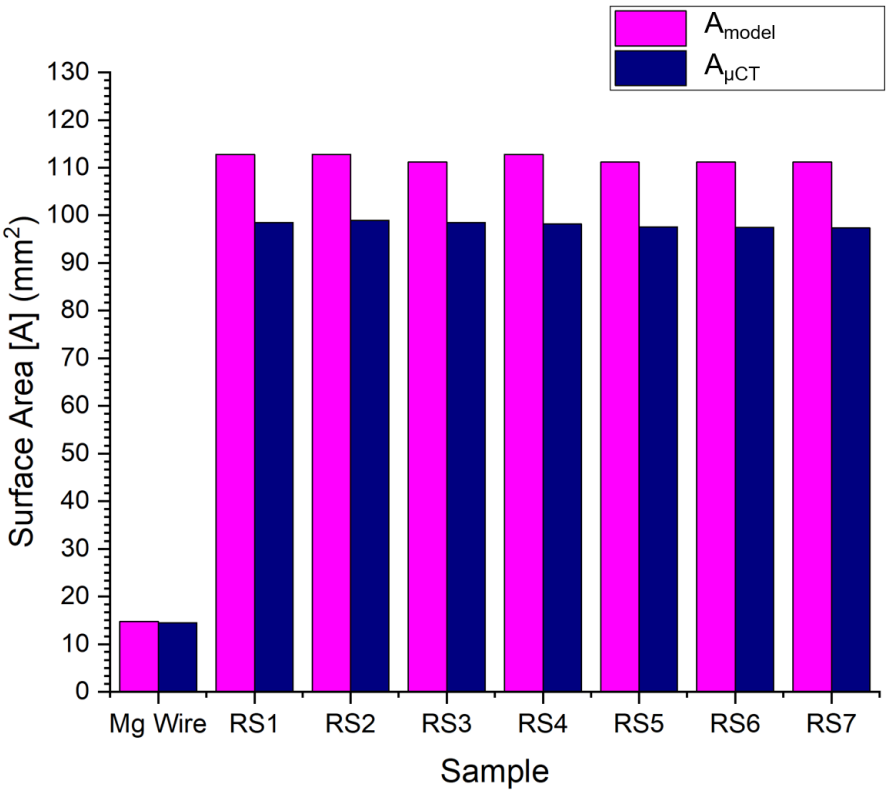

FIGURE 4.7: Results of the entire stent surface area, calculated by the developed model and micro-CT.

TABLE 4.1: Surface area calculation using the developed model.

S.No.	Sample	Average Width of Upper Surface	Surface Co-Efficient	Stent Outer Surface Area (SOSA)	Entire Stent Surface Area (ESSA)
		w (mm)	c	A_{out} (%)	A (mm^2)
1	RS-I	0.121	1.03	33.62	112.77
2	RS-II	0.121	1.03	33.62	112.77
3	RS-III	0.121	1.03	33.14	111.18
4	RS-IV	0.121	1.03	33.62	112.77
5	RS-V	0.121	1.03	33.14	111.18
6	RS-VI	0.121	1.03	33.14	111.18
7	RS-VII	0.121	1.03	33.14	111.18

TABLE 4.2: Validation of the calculated surface area with micro-CT measurement.

S.No.	Sample	Volume		ESSA		Difference
		Calculated	Micro-CT	Calculated	Micro-CT	-
		V_{Model} (mm^3)	$V_{\mu CT}$ (mm^3)	A_{Model} (mm^2)	$A_{\mu CT}$ (mm^2)	%
1	Mg alloy wire	1.59	1.59	14.77	14.45	2.17
2	RS-I	3.7	3.67	112.77	98.49	12.66
3	RS-II	3.7	3.66	112.77	98.95	12.26
4	RS-III	3.65	3.63	111.18	98.49	11.42
5	RS-IV	3.7	3.7	112.77	98.2	12.92
6	RS-V	3.65	3.65	111.18	97.53	12.28
7	RS-VI	3.65	3.63	111.18	97.41	12.39
8	RS-VII	3.65	3.63	111.18	97.34	12.45

4.6 ESSA of resoloy stents

The structure of the used resoloy (RS) (Mg alloy) stents can be seen in the 3D reconstructed images (Figure 4.6). The symbol RS is used for simplicity instead of the full name of the used resoloy stents for the presentation of the results. The outer radius (r_1) and inner radius (r_2) were measured at 1 mm and 0.875 mm, respectively. The strut thickness of all the samples was 125 μm. Table 4.1 shows the Stent outer surface area and the Entire stent surface area calculations based on the derived equation. The average width of the upper surface was 0.121 mm. The obtained s and w gave the value of c as 1.03. The maximum calculated $SOSA$ and $ESSA$ were 33.62% and 112.77 mm^2, respectively (RS-I, RS-II, and RS-IV).

Table 4.2 shows the comparison of the ESSA calculated from the derived equation and the micro-CT. The maximum difference between the calculated value and the micro-CT value is 12.92% (RS-IV). The maximum difference in the calculated reference volume for micro-CT and the nearest volume value used as the threshold was 0.04 mm3 in the case of RS-II.

The volume obtained by the density formula was highly dependent upon the mass of the stent. All seven samples have two mass values, therefore we obtained two values for the reference volumes for all the samples so far.

However, the micro-CT measurements directly depend on the geometry but are

not influenced by mass. Therefore, we obtained variable values of micro-CT calculated surface areas for all samples.

Figure 4.7 shows the surface areas calculated by equation and micro-CT measurement. The bar chart shows the consistent results of the samples.

4.7 Conclusions

Stenting is a fast-growing research field due to its being less invasive, its live-saving capabilities, and it being less risky than coronary artery bypass grafting (CABG). Despite huge advancements, still significant restenosis rates and undesirable clinical outcomes make this field still very open for advancements. One important step towards the further development of this technology is to use stents for all experiments rather than using simpler samples of the stent material. Therefore, we have introduced a novel mathematical model for the calculation of the entire stent surface area. The model was used for the calculation of the surface area of Mg alloy stents, and the results have been validated with micro-CT measurements. The difference in the results from the model and micro-CT can be minimized using the manual and automatic stent scanning methods for the calculation of the stent outer surface area and avoiding beam-hardening effects for micro-CT—for example, using synchrotron sources for micro-computed tomography (SR micro-CT).

5 Development of Fluid-dynamic setup

This Chapter is dedicated to introduce the newly developed fluid dynamic setup with the intergration of various sensors. The motivation for this development is described in Section 5.1. Section 5.2 highlights the used sensors. The hardware of the fluid dynamic system is explained in Section 5.3, whereas Section 5.4 is dedicated to the descriptiopn of the software of this system. Section 5.5 addresses the general working conditions of the experimental setup. In last, Section 5.6 concludes the whole chapter. The protocol to use the fluid dynamic setup is given in Appendix B.

5.1 Motivation

According to the FDA, "Medical implants are devices or tissues that are placed inside or on the surface of the body". The biomaterials used in implants expose to the different kinds of stresses in the aggressive physiological environment. For example, The implants like stents upon implantation, interact not only with tissues, they are exposed to the flowing blood and have to bear all the stresses caused by the flow.

When a stent is implanted into the artery the upper side is exposed to the tissue whereas the inner sides interact with the bloodstream i.e characterized by temperature, pressure, flow rate, flow velocity, shear stress, viscosity, pH, gases.

Before clinical studies, every new implant has to pass the preclinical studies stage containing in vitro and in vivo studies.

To minimize the animal sacrifice in the development of the safe implant device based on the 3Rs strategy for animal trials (Replacement, Reduction, and Refinement), in vitro tests possess an important role in medical device testing.

To perform in vitro tests close to in vivo environment we developed the fluid dynamic setup capable to mimic some physiological parameters with the monitoring of temperature, pressure, flow rate, flow velocity, and pH with controlling as shown in the schematic diagram (Figure 5.1).

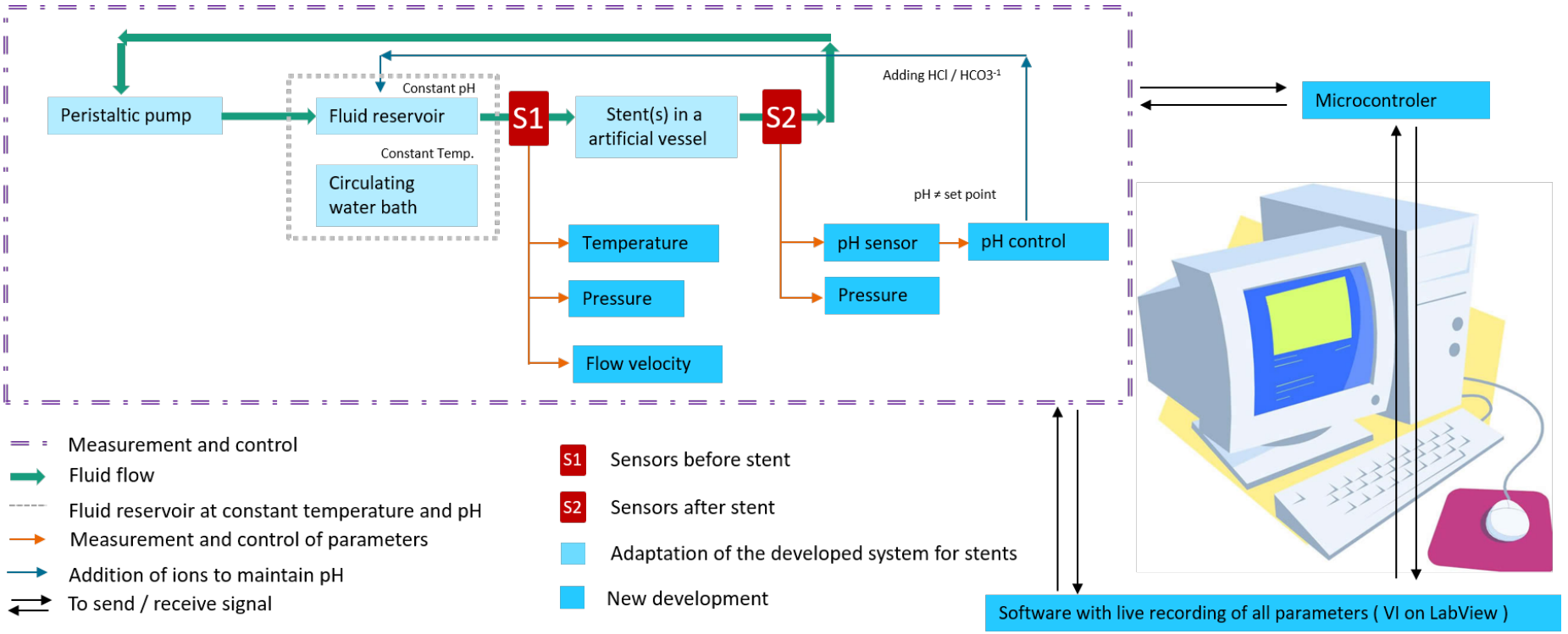

FIGURE 5.1: Schemcatic diagram of fluid dyanmic setup.

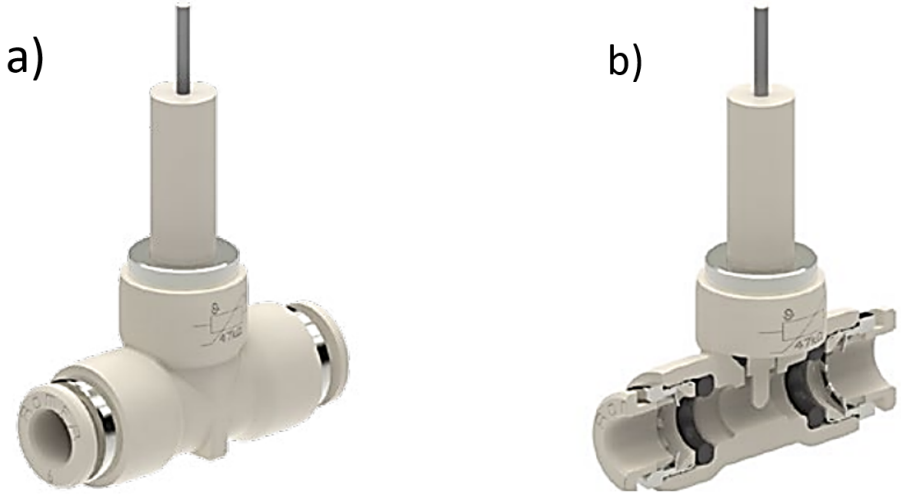

FIGURE 5.2: Inline temperature sensor. a) full view, b) cross-sectional view (Copied from manufacturer product catalog).

5.2 Sensors

Table 5.1 shows the specifications of different sensors used in the fluid dynamic setup.

5.2.1 Temperature sensor

Figure 5.2 shows the Inline temperature sensor which is purchased from AVS Römer for measuring the temperature of simulating body fluids during degradation experiments. The key features of this sensor are its fast response time and minimal dead space.

5.2.2 Pressure sensor

Figure 5.3 shows the Inline pressure sensor which is purchased from AVS Römer for measuring the temperature of simulating body fluids during degradation experiments. The key features of this sensor are its temperature-compensated elevation electronics and minimal dead space.

5.2.3 pH sensor

Figure 5.4 shows the pH sensor with controlling unit purchased from Saint clair systems, USA. This pH sensor is placed in the special housing (Figure 5.1) manufactured by the company to allow the inline monitoring of pH at high flow rates without any risk of damage to the sensor.

5.2.4 Flow sensor

A traditional flow sensor is used for the fluid dynamic setup (Figure 5.5).it can measure the flow rates in the range of 0.5 l/min to 5 l/min.

TABLE 5.1: Sensors and their specifications.

Sensor	Parameters	Specification
Temperature	Ambient temperature	0 °C to +60 °C
	Medium temperature	0 °C to +130 °C
	Medium viscosity	up to approx. 35 cP
	Tubing connection	6mm (external diameter) - non elastic tubing
Pressure	Ambient temperature	0 °C to +60 °C
	Fluid temperature	0 °C to +140 °C
	Fluid viscosity	up to approx. 35 cP
	Tubing connection	6mm (external diameter) - non elastic tubing
pH	pH range	0-14
	Operating temperature	$\leq$ 80°C
	Fluid temperature	$\leq$ 120°C
	Fluid pressure	$\leq$ 2.0MPa
	Tubing connection	8-10 mm (inner diameter) - elastic tubing
Flow	Flow rate range	0.3 - 6 l/min
	Operating temperature	$\leq$ 80°C
	Fluid temperature	$\leq$ 120°C
	Fluid pressure	$\leq$ 2.0MPa
	Tubing connection	6mm (external diameter) - elastic tubing

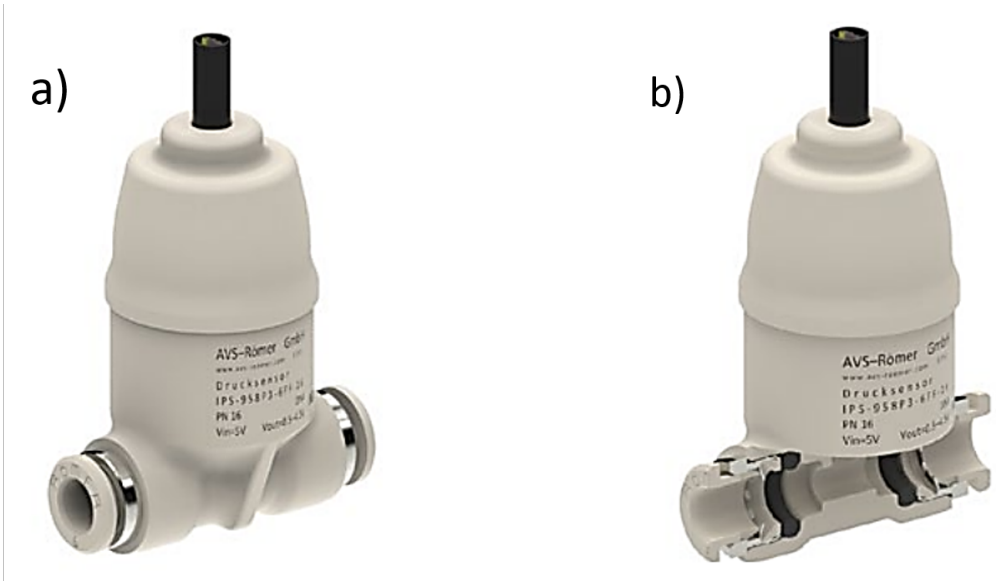

FIGURE 5.3: Inline pressure sensor. a) full view, b) cross-sectional view (Copied from manufacturer product catalog).

FIGURE 5.4: Inline pH sensor.

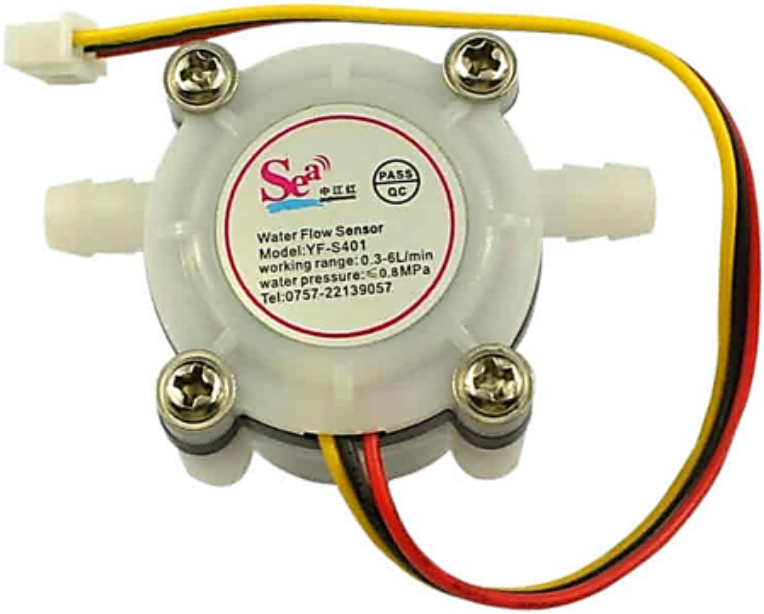

FIGURE 5.5: Flow sensor used in the fluid dynamic setup (Copied from manufacturer product catalog).

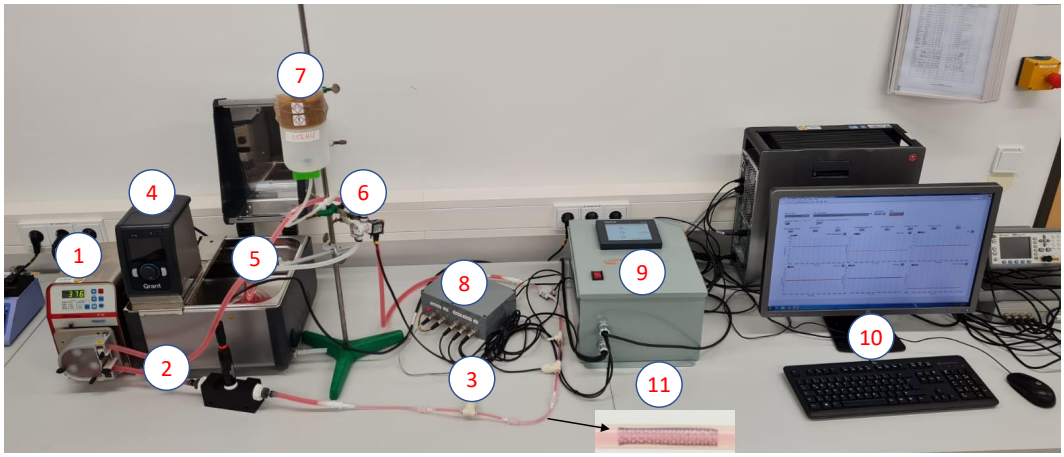

FIGURE 5.6: Schemcatic diagram of fluid dyanmic setup.

5.3 Fluid dynamic experimental setup

Figure 5.6 shows the fluid dynamic experimental test setup to provide the physiological environment with monitoring of various parameters and controlling pH. The experimental setup includes: 1) a presitaltic pump (to simulate the pumping action of the heart); 2) puriflex tubes (as an artificial blood vessel); 3) sensors (for pressure, temperature, flow velocity, pH); 4) circulating water bath (to maintain a constant temperature); 5) fluid reservoir; 6) solenoid valve; 7) dilute acid container; 8) microcontroller unit box; 9) pH controlling unit; 10) computer system (LabVIEW program or VI to control and monitor the parameters and display the results); and 11) stent implanted in artificial vessel.

5.4 Software

The VI was built on a LabVIEW platform. The user interface or front panel (Figure 5.7) of a LabVIEW based Virtual instrument is divided into three sub-interfaces.

1. User-controlled interface (blue outline)
2. Digital display interface (orange outline)
3. Graphical display interface (green outline)

1. **User-controlled interface**
   This interface is dedicated to the features that can be controlled by the user. Figure 5.8 shows the tabs for this interface. The details of all the individual features are given below.

   - *Date & Time*
     This is to show the current date and time.
   - *Stop*
     This button is to stop the experiment at any time.
   - *File saving path*
     This option is to type the address of the destination folder with the filename to record all the parameters.

- *Insert the cross-sectional area in cm ∧ 2*
  This option is to insert the cross-sectional area of the region where samples are placed. This value should be accurately inserted for the present conditions. Wring entry will affect the result of other values e.g. Flow velocity.
- *Separator Switch*
  This is to change the decimal separator between "." and "," as per user need.
- *Serial port*
  This option is to select the right communication port where the main controller box is connected to the PC.

2. **Digital display interface**
   This user interface is dedicated to the digital displays of instantaneous values of flow velocity, total fluid, ml/s, fluid temperature, flow rate, pressure, and pH. Figure 5.9 shows the tabs for this interface. The definitions of all the individual features are as follows.

   - *Flow velocity (cm/s)*
     This display shows the instantaneous fluid flow velocity in cm/s
   - *Total Fluid*
     This display shows the total fluid flow from the starting point of an experiment to the observation point.
   - *ml/s*
     This display shows the instantaneous flow rate in ml/s. It measures the milliliters of flowing fluid every second.
   - *Fluid temperature*
     This display shows the instantaneous inline temperature of the flowing fluid.
   - *Flow rate (l/min)*
     This shows the instantaneous flow rate of the flowing fluid on L/min.
   - *Pressure 1 (kPa)*
     This shows the pressure exerted by the flowing fluid to the samples in KPa.
   - *Pressure 2 (kPa)*
     This shows the pressure of the simulated blood plasma after passing through the samples.
   - *pH*
     This shows the instantaneous inline pH of the simulated blood plasma.

3. **Graphical display interface**
   This user interface is dedicated to the graphical displays of real-time monitoring of flow velocity, pressure, temperature, flow rate, and pH. Figure 5.10 shows one of the graphs from this interface.

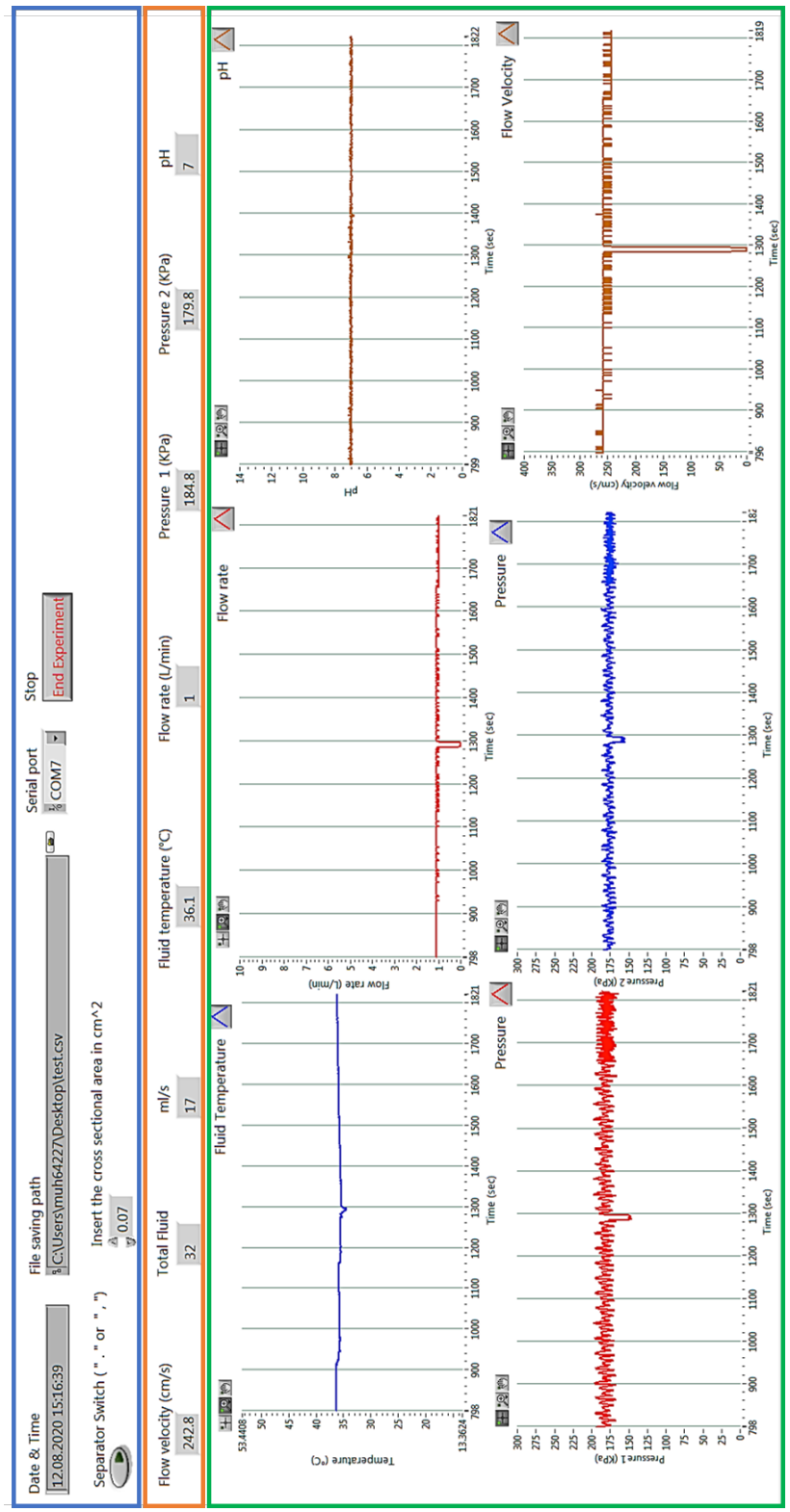

FIGURE 5.7: Front panel of Virtual Instrument.

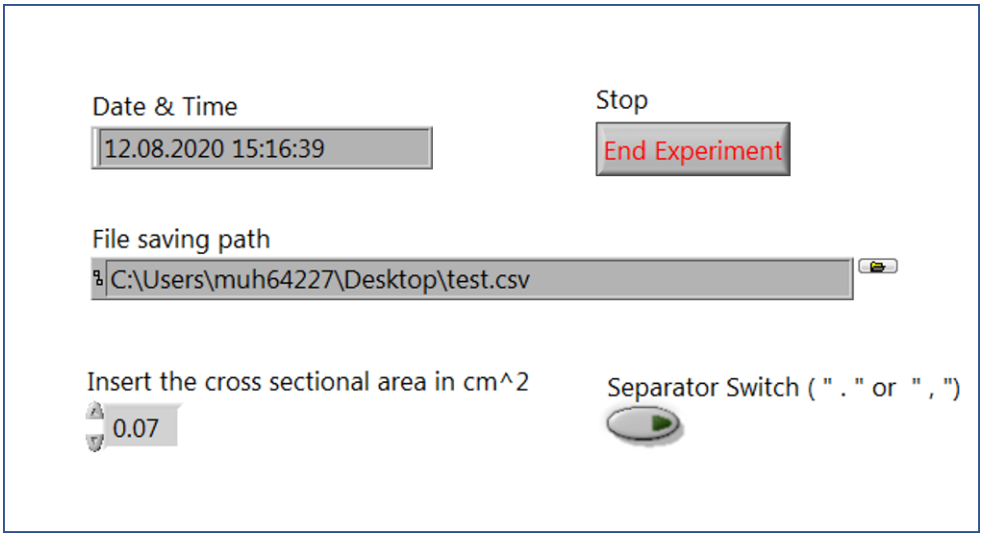

FIGURE 5.8: Front panel of Virtual Instrument: User controlled interface.

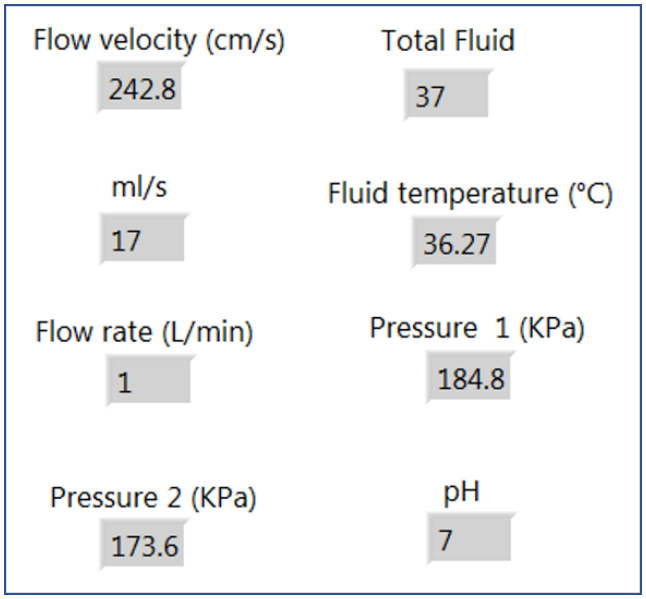

FIGURE 5.9: Front panel of Virtual Instrument: Digital display interface.

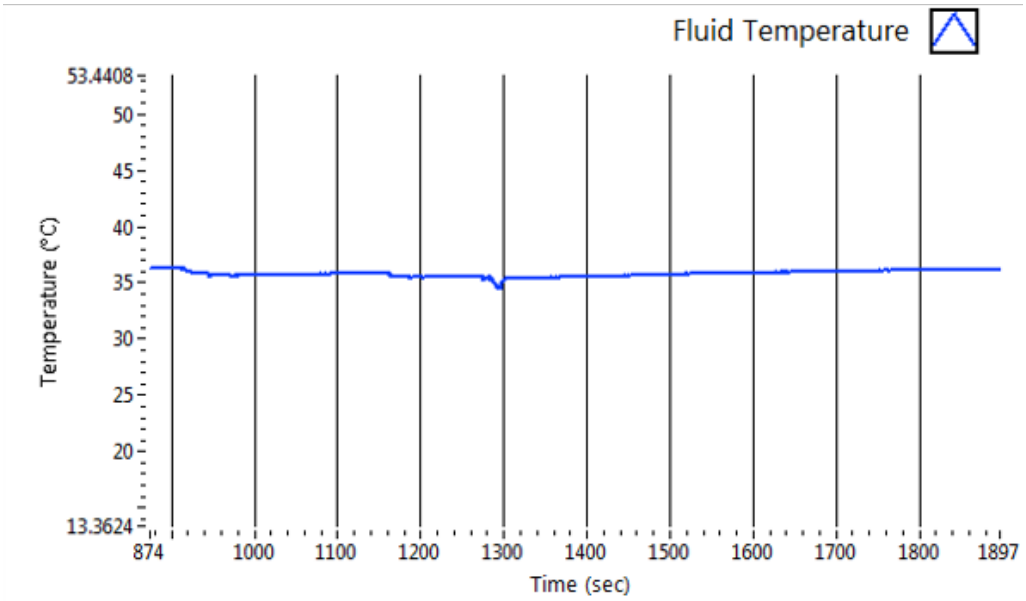

FIGURE 5.10: Front panel of Virtual Instrument: Graphical display interface.

5.5 Working of the experimental setup

Based on the 3Rs strategy for animal trials (Replacement, Reduction and Refinement), in vitro tests possess an important role in medical device testing. To overcome a still existing gap between *in vitro* and *in vivo* results, replication of the similar physiological conditions in the lab is essentially important.

The presented fludic dynamic experimental setup is capable to provide physiological conditions of the parameters with the controlling of the pH. Whenever pH value changes, the pH control unit (Saint Clair System, USA) of the setup works and adds dilute HCl (to lower the pH) or any other buffering solution to the fluid until it reaches the setpoint. The amount of buffering solution can be set according to the experimental needs. In this setup, samples of different geometries (square, rectangular and round discs, hollow tubes, polymer films and complex implant structures e.g. stents) can be tested. The setup can be used for both short- and long-term experiments and has already been applied for testing of different implant structures. Table 5.2 shows the typical ranges of different parameters can be used with the setup.

All the parameters continuously store in the excel file at the given file saving path throughout the experiment until user press the END button. During experiment, the display of graphs can be manipulated by various options available in graph palette with each graph (e.g. Zoom in , Zoom out, Scale change etc.). The graph values can also be copied to clipboard or export to the excel during experiment manually. User can also delete the graph data in running experiment in case of garbage values in the beginning of experiment.

TABLE 5.2: System parameters and their range.

Parameters	Range and Values
Ambient temperature	0 °C to +60 °C
Fluid temperature	0 °C to +120 °C
Fluid viscosity	up to approx. 35 cP
pH	0-14
Fluid pressure	$\leq$ 2.0 MPa
Experiment duration	upto 6 months

5.6 Conclusions

A standard fluid dynamic setup has been developed with the integration of various sensors including temperature, pressure, flow rate, pH for the inline monitoring and controlling of these parameters to ensure standardized degradation. pH is regulated with the addition of dilute HCl to the simulated body fluid. The system is capable to degrade different stent types and materials. All sensors are integrated using the Arduino Mega 2560 platform. The system is supported with user-friendly software built on the LabVIEW platform. The software allows the live recording of all the parameters with various manipulation options during a running experiment.

6 Influence of in vitro test conditions on coated metallic stents in fluid-dynamic biostability test

In vitro test conditions significantly influence the outcome of the degradation tests. This Chapter highlights the effect of the various testing conditions on TiO_XN_Y stents in fluid-dynamic environment. Section 6.1 introduces the whole topic, whereas the different experimental approaches that have been adopted were presented in Section 6.2. Section 6.3 presents the experimental results of one-week degradation of TiO_XN_Y stents with SBF with (Ca^{++} and Mg^{++} ions). Section 6.4 addresses the effect of different cleaning protocols on TiO_XN_Y coated stents using similar experimental conditions except for SBF (without Ca^{++} and Mg^{++} ions). Section 6.5 discusses the degradation of TiO_XN_Y stents for a longer period such as 30 days. Section 6.6 highlights the effect of puriflex tubing with SBF (without Ca^{++} and Mg^{++} ions) in 30 days of the fluid dynamic test of TiO_XN_Y stents. In last, Section 6.7 concludes the whole chapter.

6.1 Background

In vitro and *in vivo* experiments on stents end up with salt depositions or crystallization on the stent surface [30, 222]. The chemical composition and characteristics of these depositions are highly dependent on the stent material and the fluid composition [223].

To evaluate the in vitro biostability of coated stents, mass loss measurements, and corrosion measurements are crucial [224, 225, 226]. For this purpose, deposition-free degradation is desired to take a closer look at the coating itself and to ensure the possibility of mass loss and corrosion measurements.

In fluid dynamic experiments, the degree of degradation is controlled by varying different parameters like pressure, flow rate, shear stress, viscosity, flow velocity, temperature etc. whereas, the experimental setup and the type of fluid [227, 228] influence the degradation products on the implant surface. Furthermore, cleaning procedures [229] to remove the degradation products are also crucial in order to avoid any damage to the implant surface.

Augthun et al 1998 [229] performed *in vitro* studies and investigated the effect of cleaning methods on different implant surfaces. They found that cleaning procedures may cause damage to the implant surface and in case of incomplete cleaning it is not possible to evaluate the damaging effect of that method on the implant surface.

Until now, no such studies were reported to optimize the experimental setup and conditions for coated stents to show the their influence on stent degradation . This chapter aims to present the influence of *in vitro* test conditions on coated metallic

stents in fluid dynamic biostability test optimization strategy to obtain deposition less degradation in coated stents.

6.2 Experimental conditions

The fluid-dynamic experimental setup presented in [30] was used for all the experiments with different variants of simulated body fluid, artificial vessel, and duration of experiments and cleaning procedure. All experiments were conducted at 37°C. The flow velocity of the experiments was 180 cm/s and the pH was 7.4. Simulated body fluid presented in [230] and Hanks balanced salt solution (Lonza, without Ca^{++} and Mg^{++} ions) was used as artificial blood plasma. Silicon tubes and Puriflex tubes were used as an artificial vessel. The fluid dynamic loading of 7 days and 30 days was used to degrade TiO_XN_Y coated stents.

The chemical composition of smilated body fluids used here are given in Appendix A. For simplicity we named SBF^{++} (with Ca^{++} and Mg^{++} ions) to SBF with Ca^{++} and Mg^{++} ions, SBF^{--} to SBF without Ca^{++} and Mg^{++} ions, and $HBSS^{--}$ to Hanks balanced salt solution (HBSS) without Ca^{++} and Mg^{++} ions .

Following experiments were conducted to optimize the experimental conditions to get deposition free degradation.

1. Experiment 1: 1-week fluid-dynamic experiment with silicon tube and SBF^{++}.
2. Experiment 2: 1-week fluid-dynamic experiment with silicon tube and SBF^{--}.
   (a) Cleaning with water.
   (b) Cleaning with water, isopropanol, acetone.
3. Experiment 3: 30-days fluid-dynamic experiment with silicon tube and $HBSS^{--}$.
4. Experiment 4: 30-days fluid-dynamic experiment with puriflex tube and $HBSS^{--}$.

6.3 Experiment 1: 1-week fluid-dynamic experiment with silicon tube and SBF^{++}

Firstly, three different ratios of TiO_XN_Y coated stainless steel planar samples and stents (O_2/N_2 - 1:2, 1:5, 1:10) were degraded for 7 days. In this group of samples, the coating adhesion was not satisfactory in stents as reported in [30]. However, planar samples adhere to homogenous coating throughout the sample surface.

Similar kinds of degradation products were observed in all samples. However, the form of deposition was different in planar samples and stents. In planar samples, deposition sheets were observed, whereas, in the case of stents deposition was observed in the form of crystallization (Figure 6.1).

Despite the poor adhesion of the coating, it can be estimated that the TiO_XN_Y coating does not influence the nature of depositions. This can be evident by the fact that 316L samples have shown similar degradation products to the TiO_XN_Y coated samples (Figure 6.2 and 6.3). All the planar samples showed cracked surfaces after the degradation of seven days. Research groups working on similar kinds of surfaces for studying biomimetic coating [231, 232] have also been reported these cracked deposition layers on the TiO_2 surface.

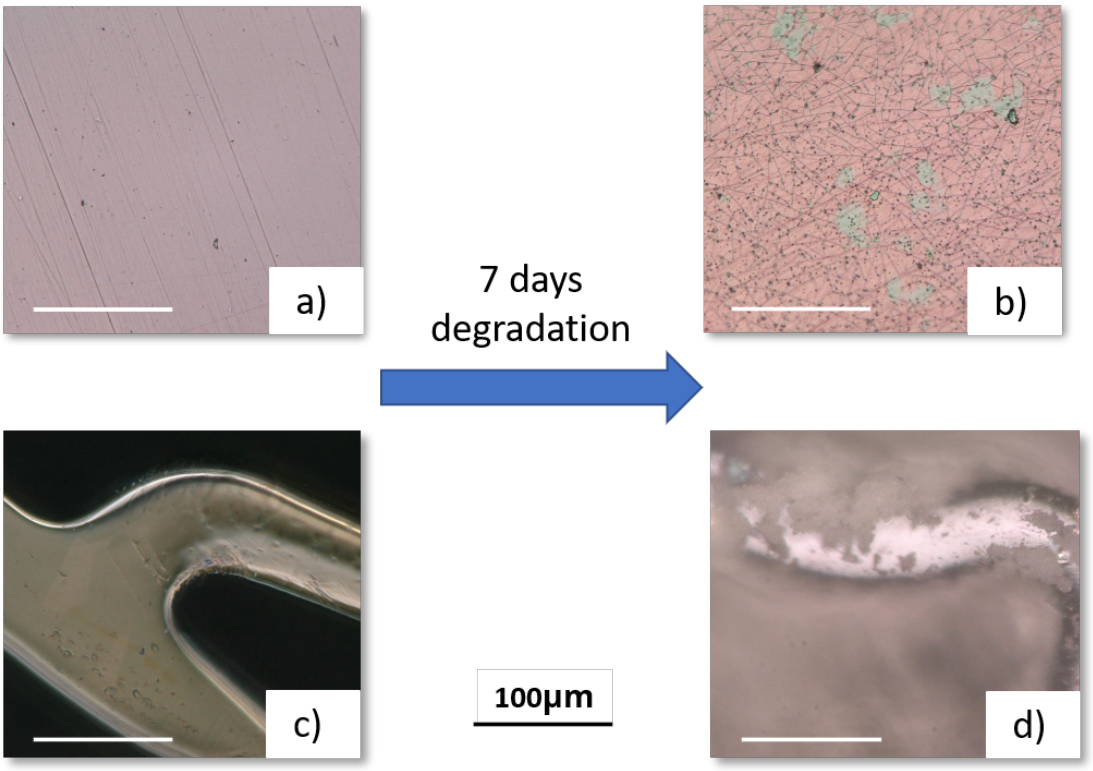

FIGURE 6.1: Microscopic images of TiO_XN_Y planar (top) and stent (bottom) samples: a)+c) Undegraded samples seven days, and b)+d) Degraded samples in fluid dynamic loading for seven days.

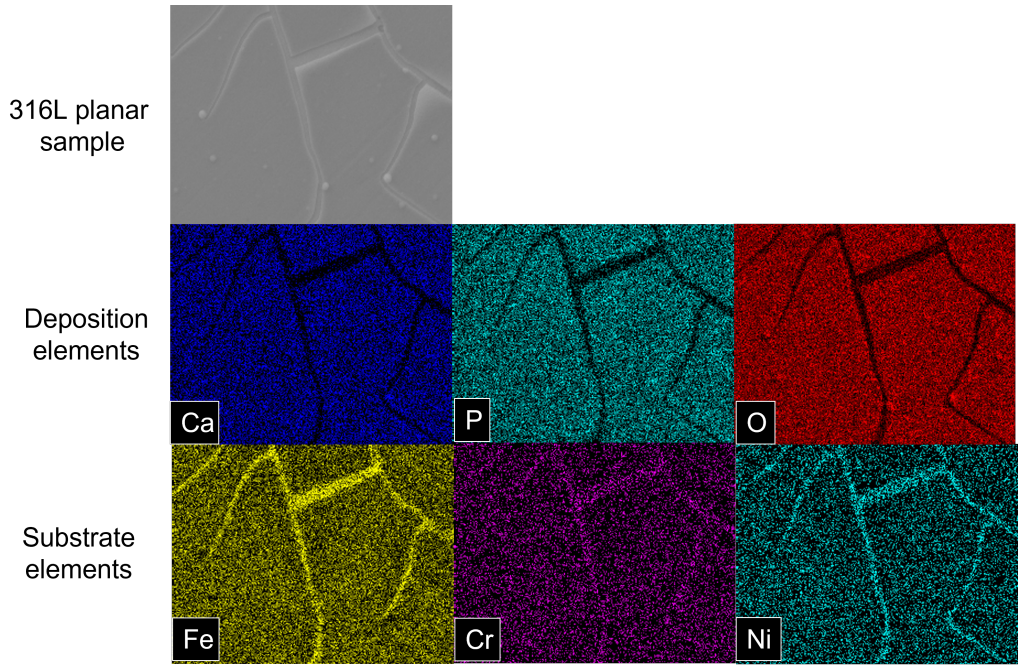

FIGURE 6.2: EDX analysis of planar 316L sample. Elemental mapping of the degradation product.

Element	Wt%	At%
Ca	10.56	7.62
P	5.38	5.02
O	26.22	47.36
Fe	30.14	15.6
Cr	8.97	4.99
Ni	9.02	4.44

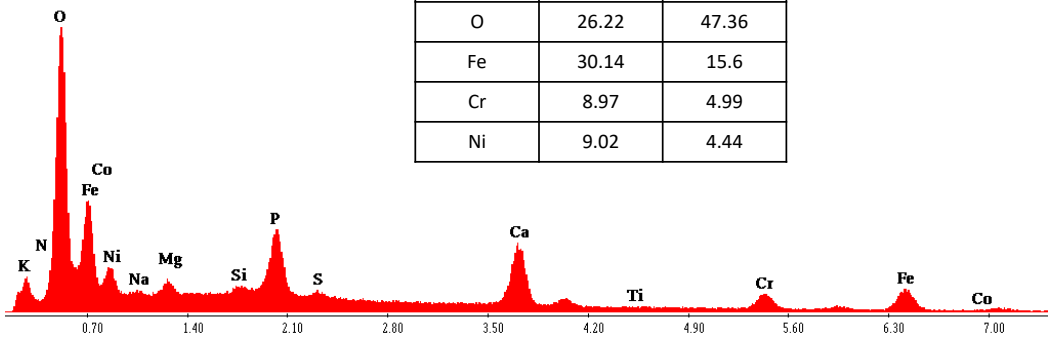

FIGURE 6.3: EDX analysis of planar 316L sample. The spectrum of surface (Figure 6.2) with elemental quantification.

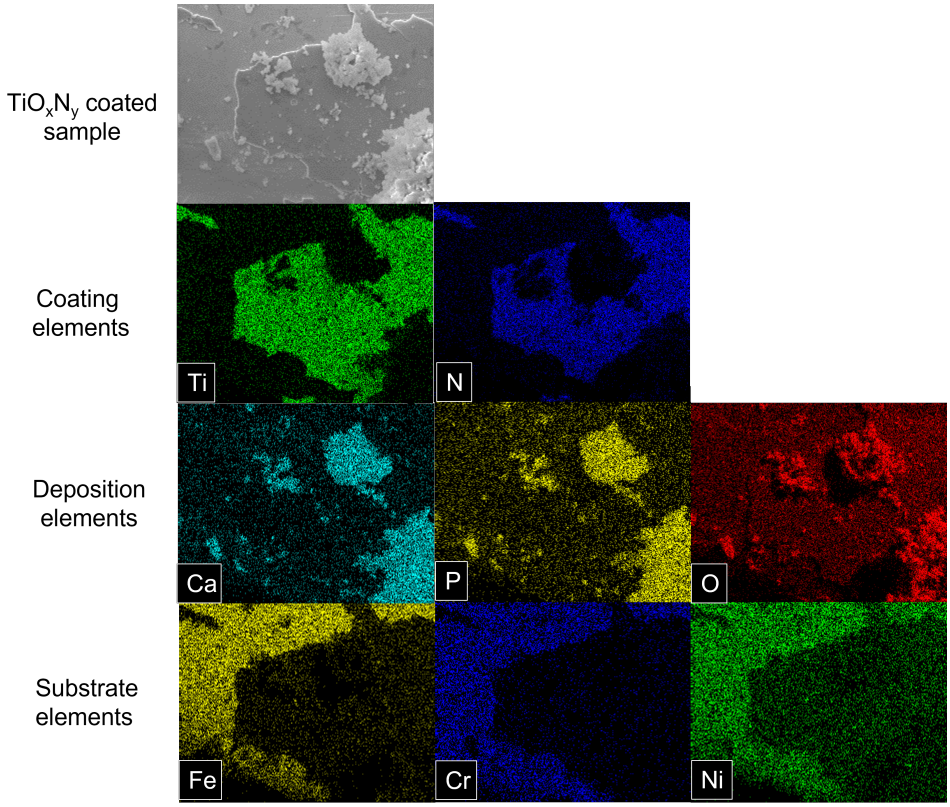

FIGURE 6.4: EDX analysis of TiO_XN_Y coated stainless steel stent. Elemental mapping of degradation products.

Figure 6.2 shows the presence of hydroxyapatite after the degradation period. The presence of Ca/P can be seen in the elemental mapping of degradation products. All other planar samples also showed similar degradation products. Furthermore, the higher peaks of Ca, P, and O in Figure 6.3 prove the formation of Ca/P hydroxyapatite crystals on the sample surface. The quantification of elements further stresses their considerable presence.

Element	Wt%	At%
Ti	13.9	9.35
N	14.08	32.39
Ca	3.74	3.01
P	2.06	2.14
O	10.0	20.15
Cr	8.11	5.03
Fe	16.52	9.53
Ni	7.51	4.12

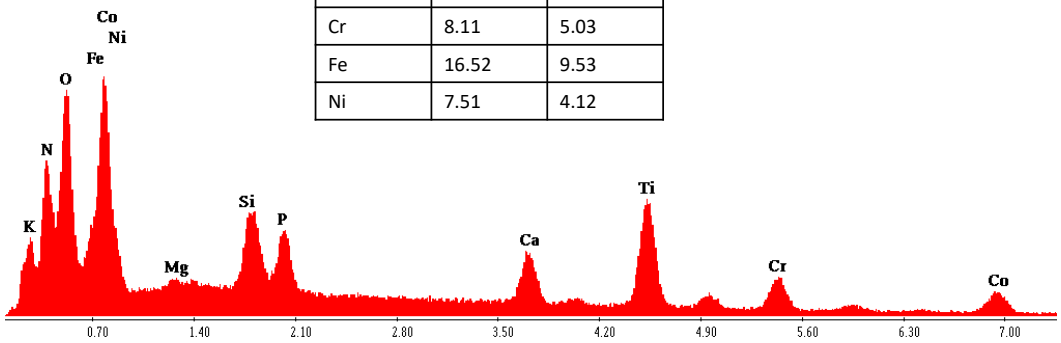

FIGURE 6.5: EDX analysis of TiO_XN_Y coated stainless steel stent. The spectrum of surface (Figure 6.4) with elemental quantification.

The upper surface of the stents was in contact with the silicon tube and has no direct influence on simulated body fluid. Therefore the degradation products were observed in the other three sides of the stent strut especially in the inner side which is in direct influence of flowing SBF.

Figure 6.4 shows the elemental mapping of the upper surface of the TiO_XN_Y coated stent surface after seven days of degradation. Like planar samples, the stent samples also show the presence of Ca, P, and O in degradation products. The peaks of hydroxyapatite elements are also clearly visible in the stent samples (Figure 6.5) with a reasonable amount present as wt% and at%.

The possible reason for these crystallizations is the hydrophilic nature of TiO_2 that tends to form titanium hydroxide groups [231], when in contact with c-SBF [233]. As a consequence of this phenomenon, these Ti-OH groups induce apatite nucleation and crystallization, as reported by Toshihiro et al. [230].

6.4 Experiment 2: 1-week fluid-dynamic experiment with silicon tube and SBF^{--}

To remove the depositions from the surface of the stents, two different cleaning protocols were adopted. In the first protocol only distilled water is used with ultrasonication. In the second protocol, acetone, isopropanol, and distilled water were used in ultrasonic bath with 5 min for each liquid.

6.4.1 Cleaning with water

Before getting treated with the simulated blood plasma in the physiological conditions, all the stent samples were characterized via SEM-EDX measurements. The surface morphology of all the stents [three different ratios O_2/N_2 (6:10, 13:10, 27:10) of TiO_XN_Y] showed better adhesion of the coating to the substrate in all the samples and no or few pits were seen. In Figure 6.6, it can be seen the coating quality is very good as compared to the samples used in the previous experiment.

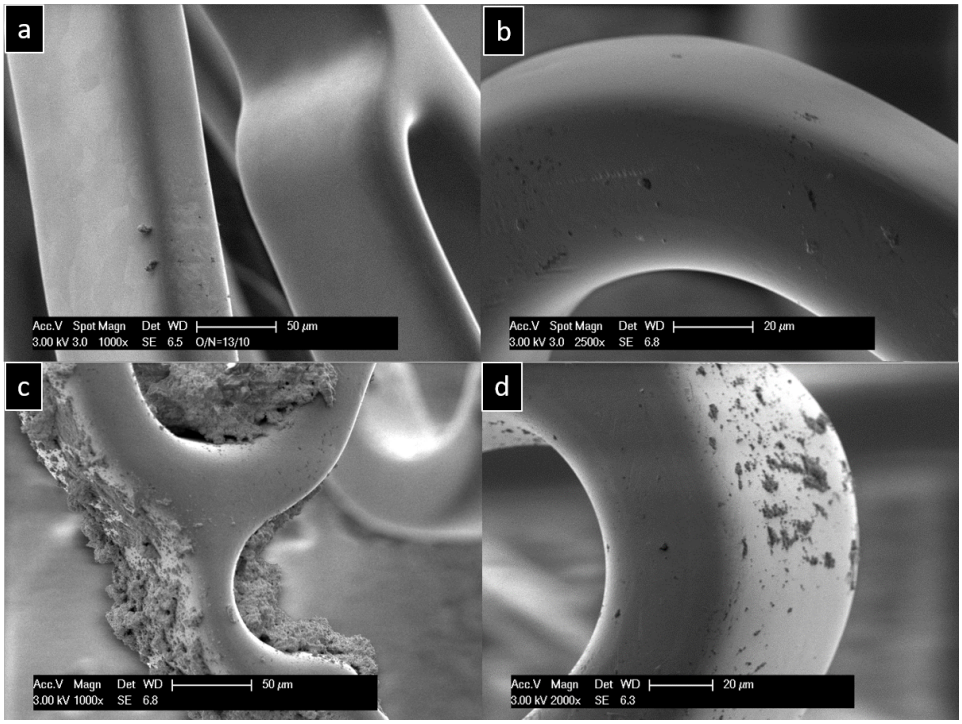

FIGURE 6.6: Stent surface before and after degradation test: (a)+(b) undegradded stent surface, and (c)+(d) 7-days degraded stent surface

No delamination is found anywhere in the samples however no or few pits are seen in stents. In the first experiment, the heavy deposition of Ca phosphates was found on the stents after exposure to simulated blood plasma. The groups around the world working on the stent characterization used the simulated blood plasma without Ca^{++} and Mg^{++} ions to avoid these kinds of depositions and to better characterize the coatings [217, 20]. Therefore, in this experiment, we also used simulated blood plasma without Ca^{++} and Mg^{++} ions to avoid unnecessary depositions.

It is expected that the stents will show better resistance against the aggressive biological medium to the delamination or degradation due to better coating quality as compared to the last stents and there should be no deposition after avoiding Ca^{++} and Mg^{++} ions in the SBP. After 7 days of exposure to SBP, the samples were cleaned in distilled water for 5min in an ultrasonic bath. The SEM analysis shows that the coatings resist the effect of aggressive biological medium however the depositions are still there in all three stents.

Interestingly, the deposition is at different levels i.e non-uniform in different stent sides (Figure 6.6). Elemental mapping of the stent area with depositions suggests the deposition include C, Si, and O. Elemental mapping shows the absence of Ca and P in the deposition crystal which is obvious after the modification in simulated blood plasma, whereas, surprisingly the presence of C, Si, O were observed in all the three samples (Figure 6.7). Moreover, the EDX spectra of the same region show the higher peaks of C, Si, and O, while the peaks of Ca, P, and Mg were not present (Figure 6.8).

Similar stents were used for SEM before the degradation test. Therefore, Si and Al peaks suggest the presence of residues of carbon adhesive tabs. Al and Si are the constituents of these tabs along with O and C [234]. These are the elements present in the Carbon tab used to stick stent on a sample holder for SEM-EDX measurements.

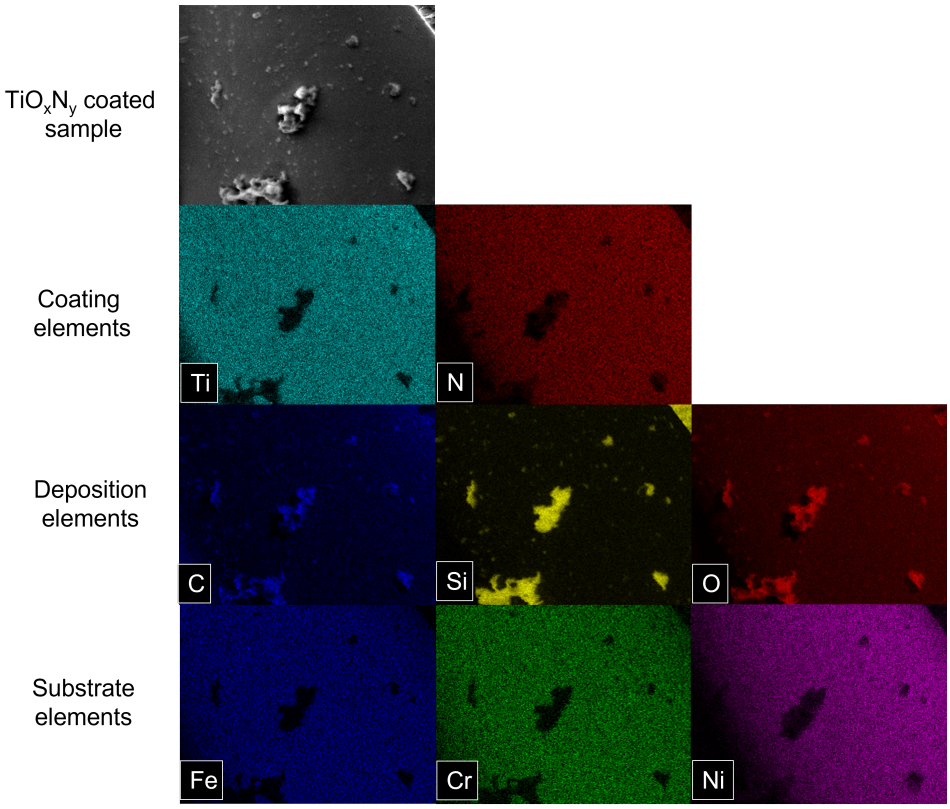

FIGURE 6.7: EDX analysis of TiO_XN_Y coated stainless steel stent. Elemental mapping of degradation products

Element	Wt%	At%
Ti	9.76	3.95
N	11.36	15.7
C	28.02	45.16
Si	8.19	5.64
O	16.4	19.85
Cr	5.83	2.17
Fe	14.45	5.01
Ni	4.37	1.44

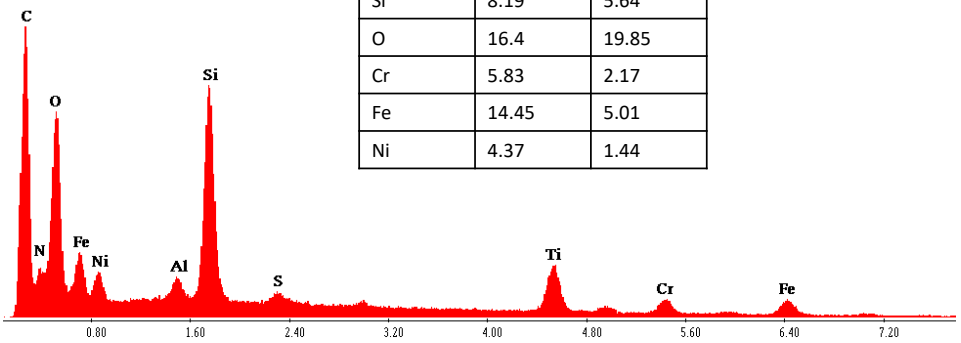

FIGURE 6.8: EDX analysis of TiO_XN_Y coated stainless steel stent. The spectrum of surface (Figure 6.7) with elemental quantification.

Avoiding Ca^{++} and Mg^{++} ions did not solve to deposition issue. Therefore, the samples were cleaned with acetone, isopropanol, and distilled water to remove the depositions.

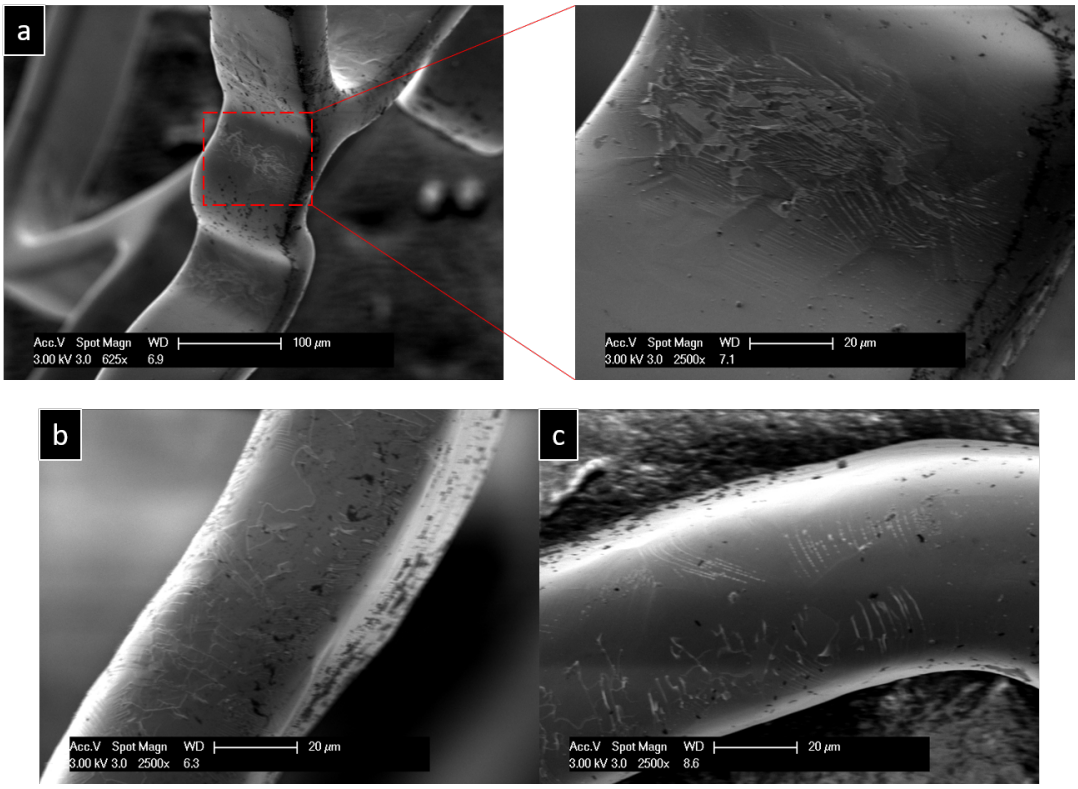

FIGURE 6.9: Stent surface after cleaning with water, isopropanol, and acetone in ultrasonication: (a)upper surface, (b)inner surface, (c) right surface, and (d) left surface of the stent wire.

6.4.2 Cleaning with water, isopropanol, acetone

Figure 6.9 shows the presence of depositions in all sides of the stent strut showing no effect of cleaning with isopropanol and acetone. This cleaning protocol caused two issues; i) it did not remove the depositions, and ii) it caused damage to coating (Figure 6.10). In Figure 6.10, it can be seen that by using this cleaning protocol coating damaged in all areas of stent wire. Furthermore, elemental mapping from one of the damaged part also shows the absence of coating elements from that part (Figure 6.11). The degradation products found after this protocol are similar to that of cleaning with water. The EDX spectrum of the surface showed in Figure 5c with the quantification of elements further proves the presence of degradation products including C, Si, and O (Figure 6.12).

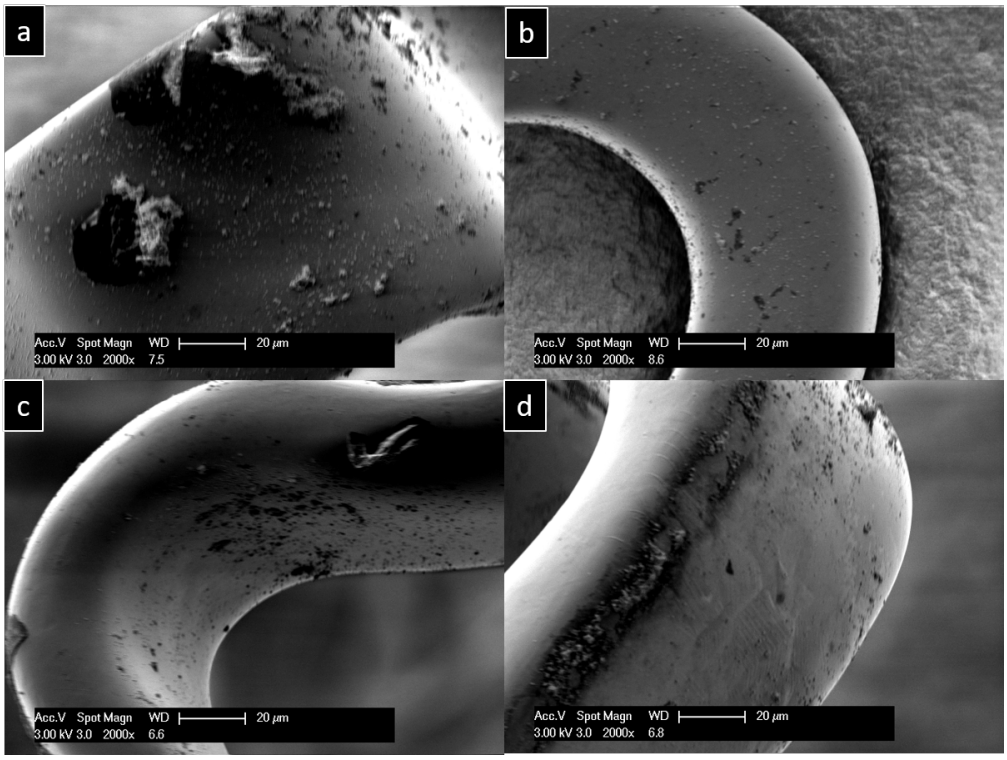

FIGURE 6.10: Damaged stent surfaces: (a) curved surfaces, (b) and (c) flat surfaces.

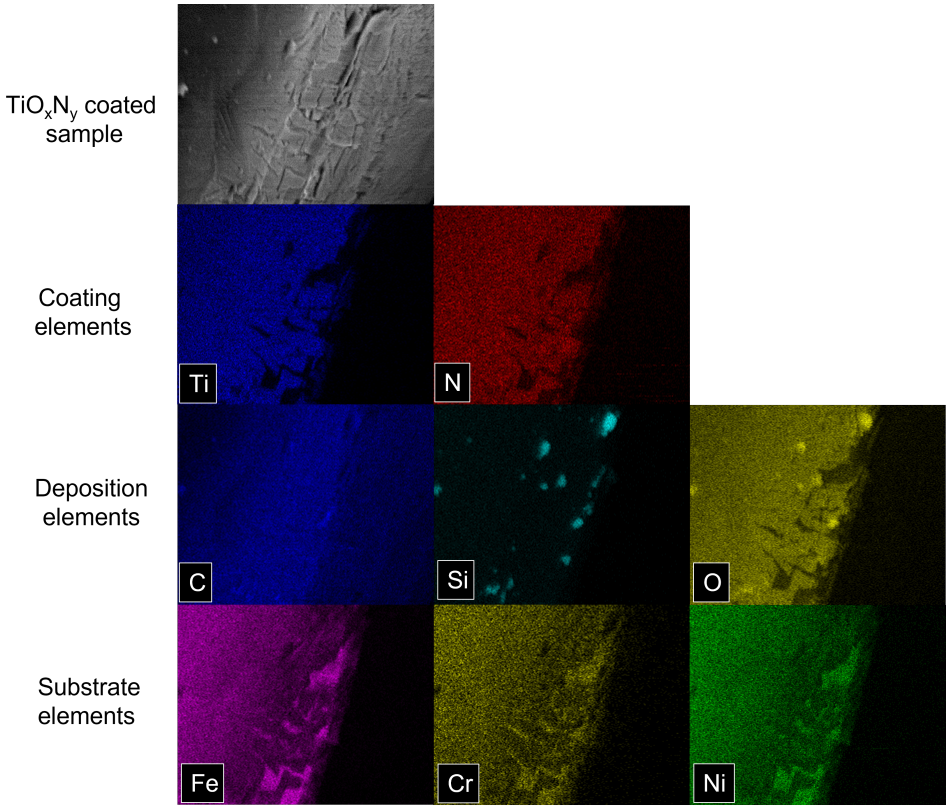

FIGURE 6.11: Elemental mapping of the damaged stent surface.

Element	Wt%	At%
Ti	8.14	5.5
N	10.07	23.25
C	3.55	9.55
Si	0.56	0.64
O	10.47	21.17
Cr	12.02	7.48
Fe	39.51	22.88
Ni	14.01	7.72

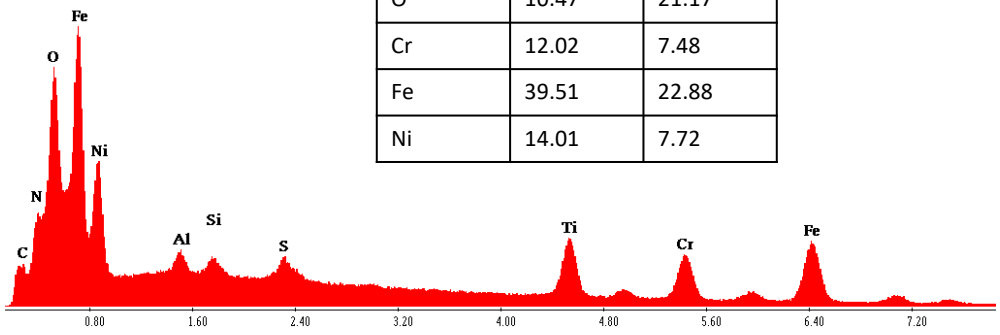

FIGURE 6.12: EDX spectrum of the damaged stent surface with the quantification of the elements.

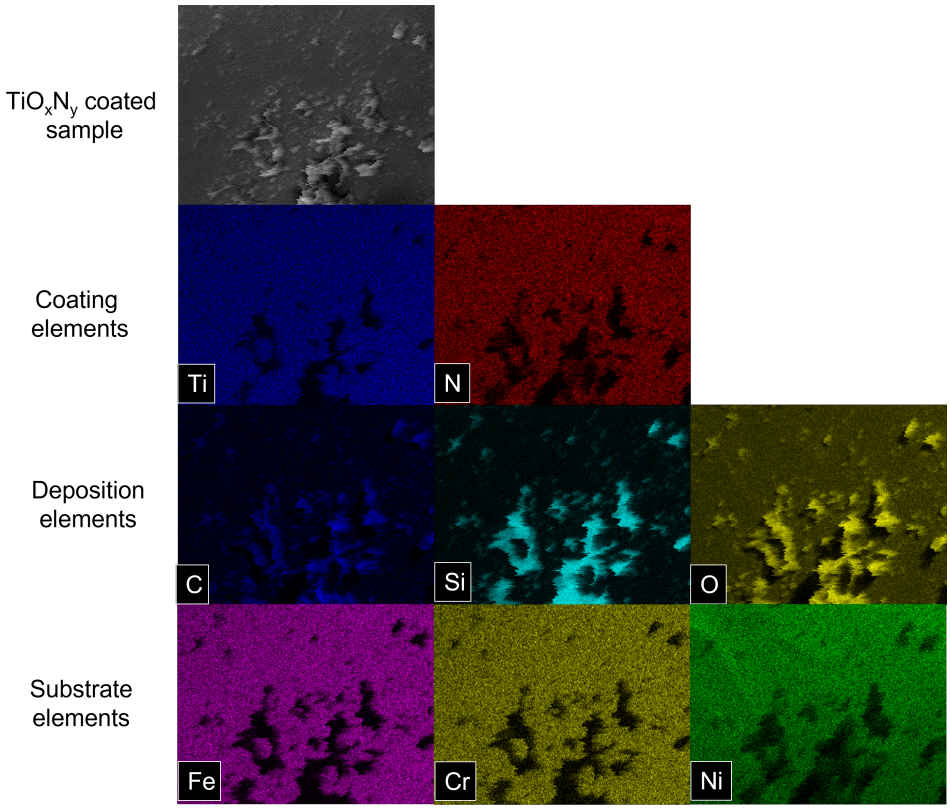

FIGURE 6.13: EDX analysis of TiO_XN_Y coated stainless steel stent. Elemental mapping of degradation products.

Element	Wt%	At%
Ti	5.25	3.29
N	6.64	14.23
C	6.29	15.71
Si	5.44	5.82
O	14.03	26.33
Cr	12.41	7.17
Fe	37.28	20.34
Ni	10.22	5.23

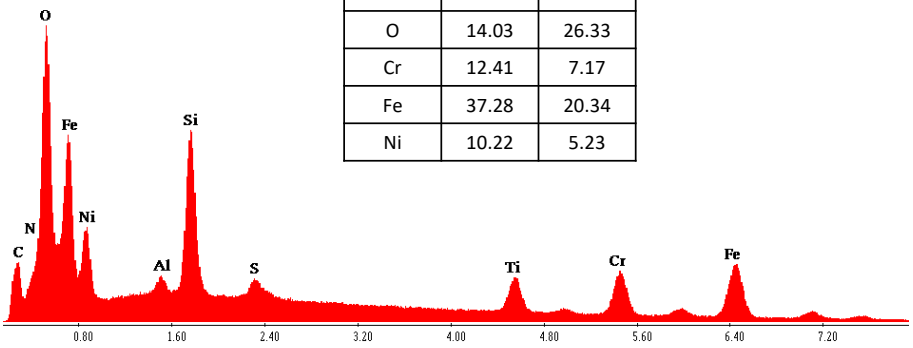

FIGURE 6.14: EDX analysis of TiO_XN_Y coated stainless steel stent. Spectrum of surface (Figure 6.13) with elemental quantification.

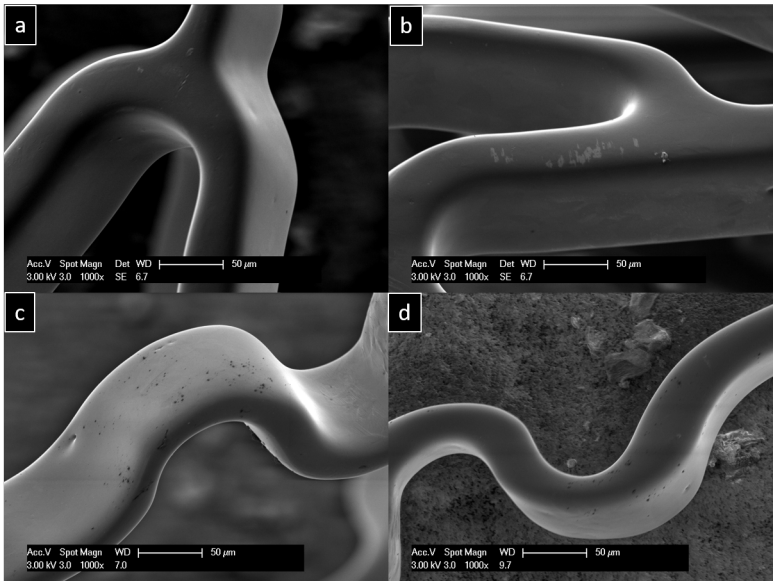

FIGURE 6.15: Stent surface before and after degradation test: (a) + (b) undegradded stent surface, and (c) + (d) 30-days degraded stent surface.

6.5 Experiment 3: 30-days fluid-dynamic experiment with silicon tube and HBSS −−

After getting undesired depositions (C, Si, and O) in the second experiment possibly from carbon adhesive tabs. The experiment was repeated with new stents for a longer period i.e. 30 days for two reasons: i) to evaluate the durability of coatings in a longer degradation period, and ii) to avoid the depositions induced by carbon adhesive tabs to enable stents for mass loss measurements.

Interestingly, similar kind of results was obtained as in the previous experiment. Figure 6.13 shows the elemental mapping of degradation products formed on the stent surface. Similar elements in the degradation products were found i.e. C, Si, and O. However, the carbon peak is lower as compared to the 2nd experiment (Figure 6.14). This is because of no contact with stents and carbon adhesive tabs. The peaks are almost similar as in the 2nd experiment. The aforementioned results suggest that there is another reason exists for these depositions in addition to carbon adhesive tabs. After analyzing these facts, Puriflex tubes were used in the next experiment (instead of silicon tubes).

6.6 Experiment 4: 30-days fluid-dynamic experiment with puriflex tube and HBSS −−

In this experiment, the different O_2/N_2 ratios (1/1, 2/1, 2/3) were used. The used coatings showed a biostable response after 30 days of degradation test. Figure 6.15 shows the stent surface before and after the degradation. By using puriflex tubes in this experiment negligible depositions were found on the stent surface.

The deposition this time contains only C, as observed in the elemental mapping of EDX analysis (Figure 6.16). EDX spectra also verify the presence of only C peak other than the coating and substrate materials (Figure 6.17). The presence of the

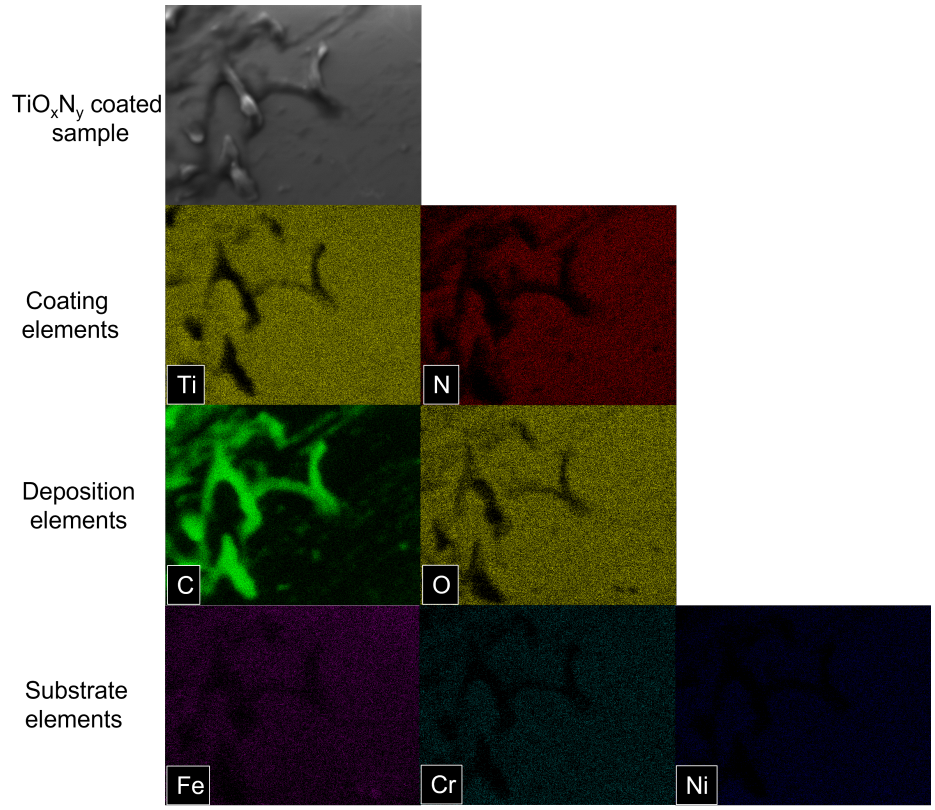

FIGURE 6.16: EDX analysis of TiO_XN_Y coated stainless steel stent. Elemental mapping of degradation products.

Element	Wt%	At%
Ti	30.80	13.67
N	13.30	20.19
C	23.95	42.39
O	12.14	16.14
Cr	4.21	1.72
Fe	11.62	4.42
Ni	3.07	1.11

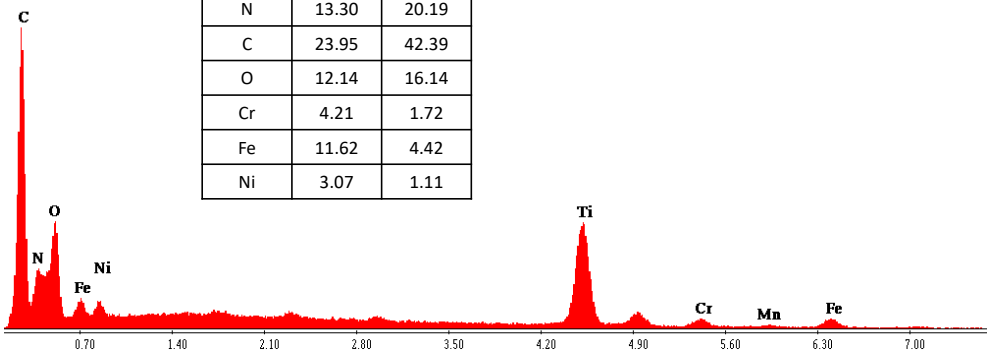

FIGURE 6.17: EDX analysis of TiO_XN_Y coated stainless steel stent. Spectrum of surface (Figure 6.16) with elemental quantification.

only C on the stent surface suggests, there is no chemical reaction occurs between the coating material and the fluid. The possible source of these minimal depositions could be the dust in the environment.

Figure 6.18 summarizes the optimization process to get deposition free experimental conditions for TiO_XN_Y coated stent.

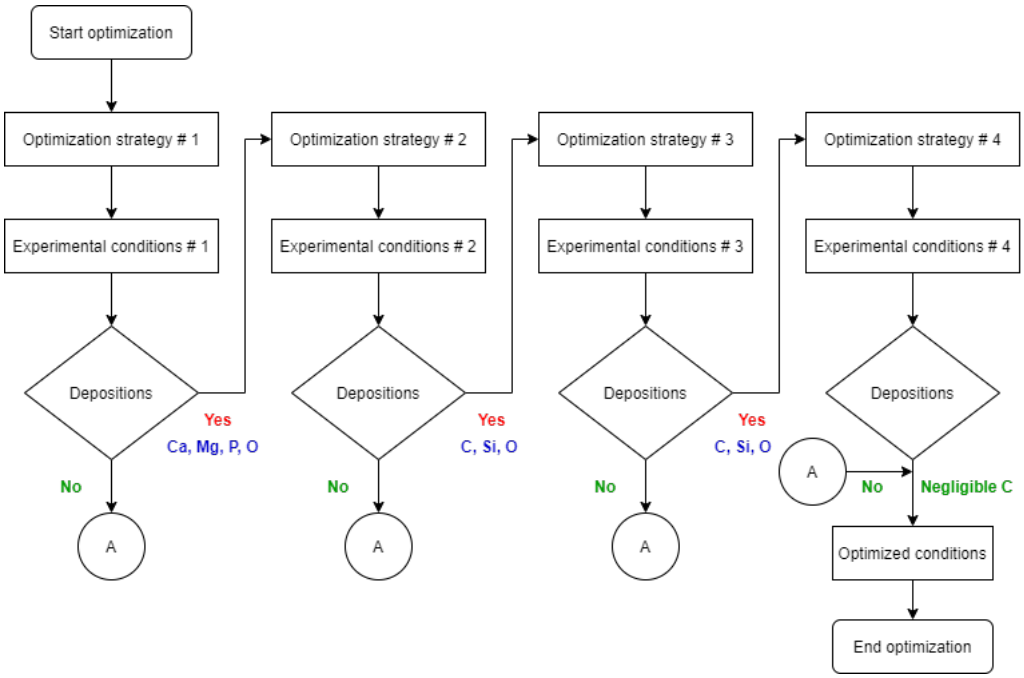

FIGURE 6.18: Schematic diagram of optimization process of experimental conditions to get deposition free degradation test of TiO_XN_Y stents.

6.7 Conclusions

Wihtin this Chapter, the TiO_XN_Y coated stainless steel planar and stent samples were degraded in fluid-dynamic environment. Effect of cleaning procedures and the experimental setup were also evaluated and discussed. The sample surface was characterized with the optical microscope and the SEM-EDX measurements. The main findings are:

- TiO_XN_Y coatings show resistance to aggressive biological medium and provide a significantly biostable response.
- The ratio of O_2/N_2 influence the level of depositions and degradation products but does not influence the chemical composition of depositions and degradation products.
- Substrate 316L stainless steel and TiO_XN_Y samples show similar degradation products.
- Cleaning of TiO_XN_Y coated stent with water in an ultrasonic environment does not harm coatings.
- Simulated blood plasma containing Ca^{++} and Mg^{++} ions induces the deposition of Ca and Mg phosphates on the stent surface.
- Cleaning of TiO_XN_Y coated samples with distilled water in an ultrasonic bath does not remove degradation products.
- Cleaning of TiO_XN_Y coated samples with acetone, isopropanol, and distilled water in an ultrasonic bath also does not remove degradation products. However, it degrades the coating.

- Silicon tubes induce Si depositions on the stent surface.

Based on the presented results, the best practice to do a fluid dynamic experiment on TiO_XN_Y stents to get deposition free degradation is to use Puriflex tubing or a similar kind of artificial vessel, SBF without Ca^{++} and Mg^{++} ions, sample cleaning with distilled water in the ultrasonic bath.

7 Evaluation of in vitro biostability of TiO_XN_Y coated BMS (316L)

O_2/N_2 ratio influences the biostability and corrosion of TiO_XN_Y coated BMS. In this connection various coated stents mentioned in Section 3.3 were degraded in three different testing setups. Section 7.1 discusses the effect of static immersion test on biostability of TiO_XN_Y stents. To determine the effect of fluid flow on degradation, Section 7.2 describes the degradation of TiO_XN_Y stents in fluid dynamic test. Section 7.3 illustrates the corrosion rates of TiO_XN_Y stents under electrochemical environment. In last, Section 7.4 concludes the whole chapter.

7.1 Static immersion test

All the samples were immersed in HBSS at 37°C for 28 days with the sampling time of 1, 2, 4, 7, 14, and 28 days as recommended in [235]. The mass variation was measured after each interval by the gravimetric method using a microbalance (explorer pro, Ohaus Corporation, USA) having a measurement sensitivity of (0.1 mg). The ICPMS studies were also conducted after 7 and 28 days of immersion period. The following formula was used to estimate mass variation in the form of mass loss or mass gain.

Where $\triangle m$ is the mass variation in mg/cm^2, m_1 is the initial mass in mg, m_2 is the final mass in mg at each immersion period, A is the original surface area exposed to the corrosive media (HBSS) in cm^2. The exposed surface area was in the range of 1.72 - 2.25 cm^2. The surface areas were calculated by the methods presented in 4.

For different immersion periods, no significant mass loss was observed in all the samples except the uncoated sample. However, that mass loss was very small. No change was observed in the morphology of coated stents. All coated stents showed good stability against aggressive medium in static conditions.

7.1.1 Mass variation

Figure 7.1 shows the mass variation of all the samples in the static immersion test of 28 days. All the coated samples gain mass due to the formation of the passivation layer on their surface after the first day of the immersion and their mass variation is in the negative axis, whereas, the stainless steel sample loses mass. After the second day of immersion, the reaction kinetic reverses, and all the coated samples lose some mass and their graph shifted to the positive y-axis. This shift indicates the dissolution of the newly formed passivation layer or the release of ions (Ti, Cr, Mo, Mn, Ni, etc.) whereas the stainless steel sample gains some mass indicating the formation of the passivation layer simultaneously with the release of ions. After 4 days of immersion, the mass variation was shifted to the negative direction again and this process continued until 7 days of immersion. After 7 days of immersion, the equilibrium was reached and the mass variation was constant for the whole immersion period of 28 days except for sample A which loses its mass

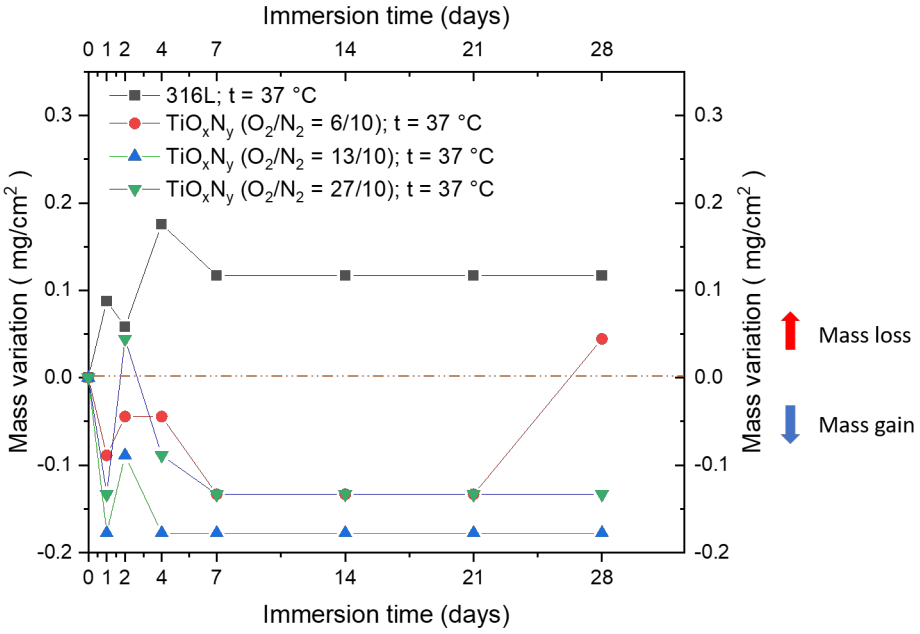

FIGURE 7.1: Mass variation of TiO_XN_Y coated and uncoated stent in 28 days static immersion test.

spontaneously after the 21 days of immersion which could be due to pits formation and the release of ions which is supported by the release of titanium in ICPMS studies. In general, all the coated samples did not show a significant mass loss due to the passivation on the surface whereas the 316L sample showed a small amount of mass loss.

7.1.2 ICPMS studies

Figure 7.2 shows the ICPMS studies of the fluid samples after the immersion of samples for 7 and 21 days (total of 28 days). In the static immersion test of coated samples, more titanium is released in TiO_XN_Y (O_2/N_2 = 6/10) as compared to TiO_XN_Y (O_2/N_2 = 13/10) and TiO_XN_Y (O_2/N_2 = 27/10). In the first seven days, more than half of the total amount of Ti is released for all the samples, less than half of the titanium is released in the next 21 days. In TiO_XN_Y (O_2/N_2 = 13/10), more Ni is released than TiO_XN_Y (O_2/N_2 = 6/10) and TiO_XN_Y (O_2/N_2 = 27/10). However, Cr release follows the same pattern as Ti in coated samples. In the 316L sample, the release of ions is lesser as compared to coated samples suggesting the formation of the passive layer.

Comparatively, the release of titanium is more in the first 7 days than in the last 21 days the release of titanium is similar for TiO_XN_Y (O_2/N_2 = 13/10) and TiO_XN_Y (O_2/N_2 = 27/10). The obtained results suggest that the release of titanium is influenced by the immersion period and the feeding ratio of oxygen and nitrogen in the coating. The more the nitrogen, the more the Ti release is. For instance, TiO_XN_Y (O_2/N_2 = 6/10) released more titanium in the static immersion test. Collectively, the degree of Ti release after 28 days of immersion is $C_{6/10} > C_{13/10} > C_{27/10}$.

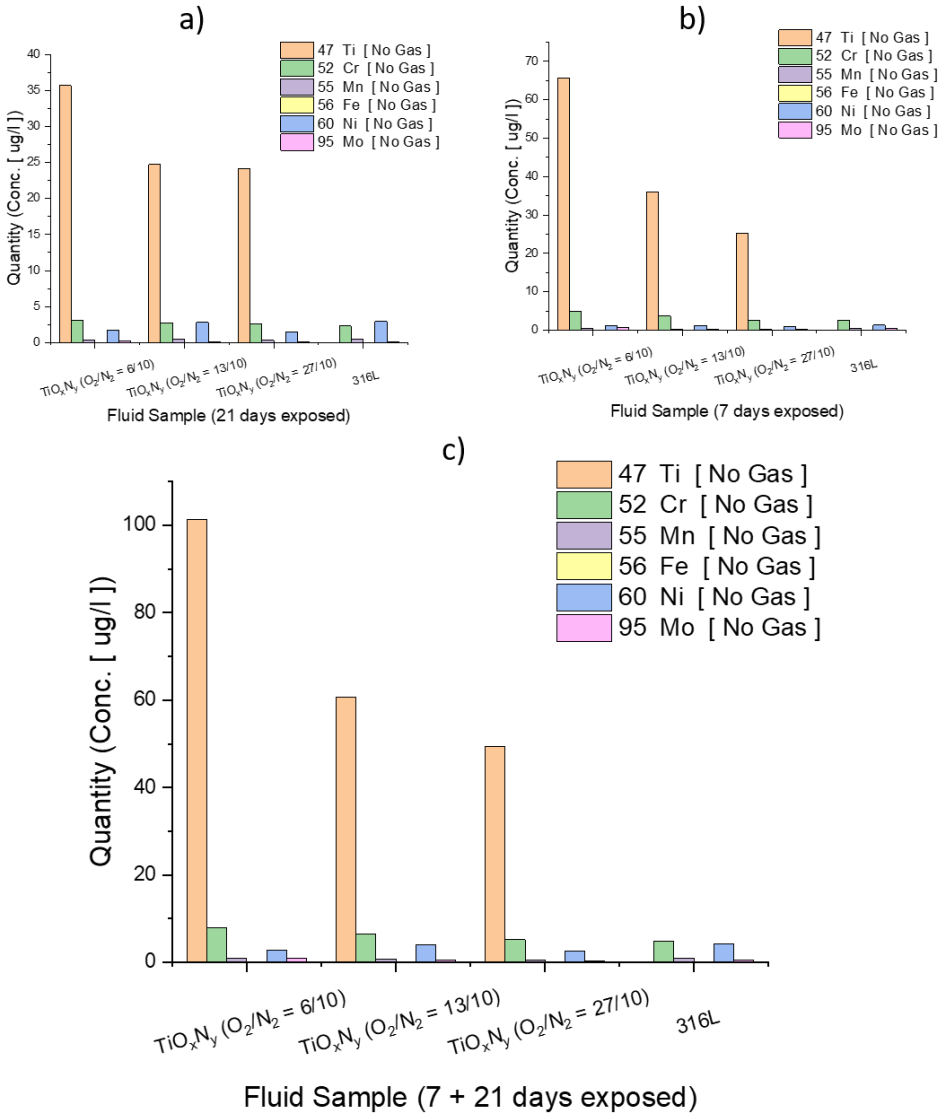

FIGURE 7.2: ICPMS studies of fluid samples of static immersion test (a) after 7 days (b) after next 21 days and (c) sum of the released ions in total 28 days.

7.2 Fluid-dynamic test

The fluid-dynamic experimental setup presented in [30] was used with a slight modification. Puriflex tubes (as an artificial blood vessel) were used instead of silicon tubes. 30 days experiment with a fluid velocity of 180 cm/s (5 times higher than the blood velocity in human arteries [236]) was undertaken at physiological pH 7.4.

After 30 days of immersion under a dynamic regime, the surface morphology was analyzed via SEM-EDX measurements. All the coated samples showed very good stability in dynamic fluidic loading against the fluid flow and shear stress (Figure 7.3). The peaks of Ti, O, and N can be seen before and after the fluid-dynamic degradation test (Figure 7.4 and 7.5). Table 7.1 shows the effect of fluid-dynamic load on TiO_XN_Y coatings from the quantitative data of elements from the EDX analyzer. There is a significant decrease in the at% values of all the

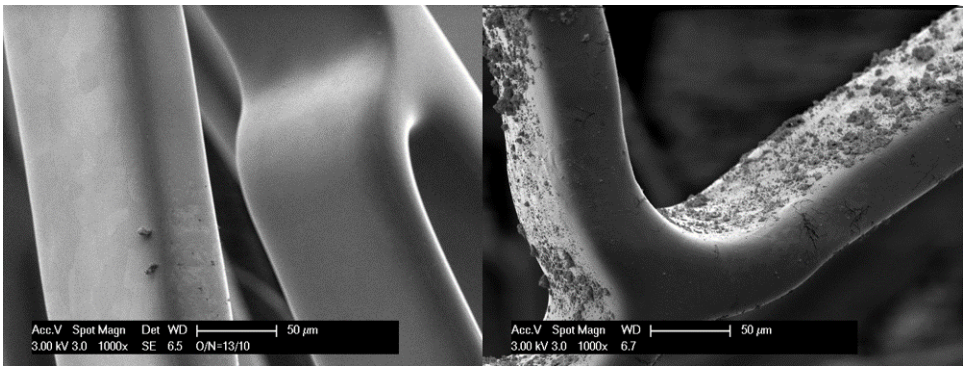

FIGURE 7.3: SEM images TiO_XN_Y (O_2/N_2 = 13/10) before (left) and after (right) 30 days fluid dynamic test.

TABLE 7.1: Chemical composition of TiO_XN_Y before and after 30 days fluid-dynamic exposure.

Sample	Element [At%]					
	Before fluid-dynamic test			After 30-days fluid-dynamic test		
	Ti	O	N	Ti	O	N
TiO_XN_Y (O_2/N_2 = 6/10)	3.43	21.6	17.78	2.43	23.85	13.53
TiO_XN_Y (O_2/N_2 = 13/10)	4.77	22.86	22.72	4.82	22.74	22.45
TiO_XN_Y (O_2/N_2 = 27/10)	9.39	27.86	24.12	4.67	22.68	21.61

three elements of coating (except the at% of Ti in TiO_XN_Y (O_2/N_2 = 13/10) and of O in TiO_XN_Y (O_2/N_2 = 6/10), which increased after fluidic load). In particular, no delamination of the coating was found after 30 days of exposure at a velocity of 180cm/s except TiO_XN_Y (O_2/N_2 = 6/10). Figure 7.6 is showing the absence of coating elements from the delaminated part. Based on this stable and corrosion-resistant response in the first two methods, electrochemical corrosion testing was conducted. These coatings showed very good adhesion to the substrate as compared to coatings presented in [30].

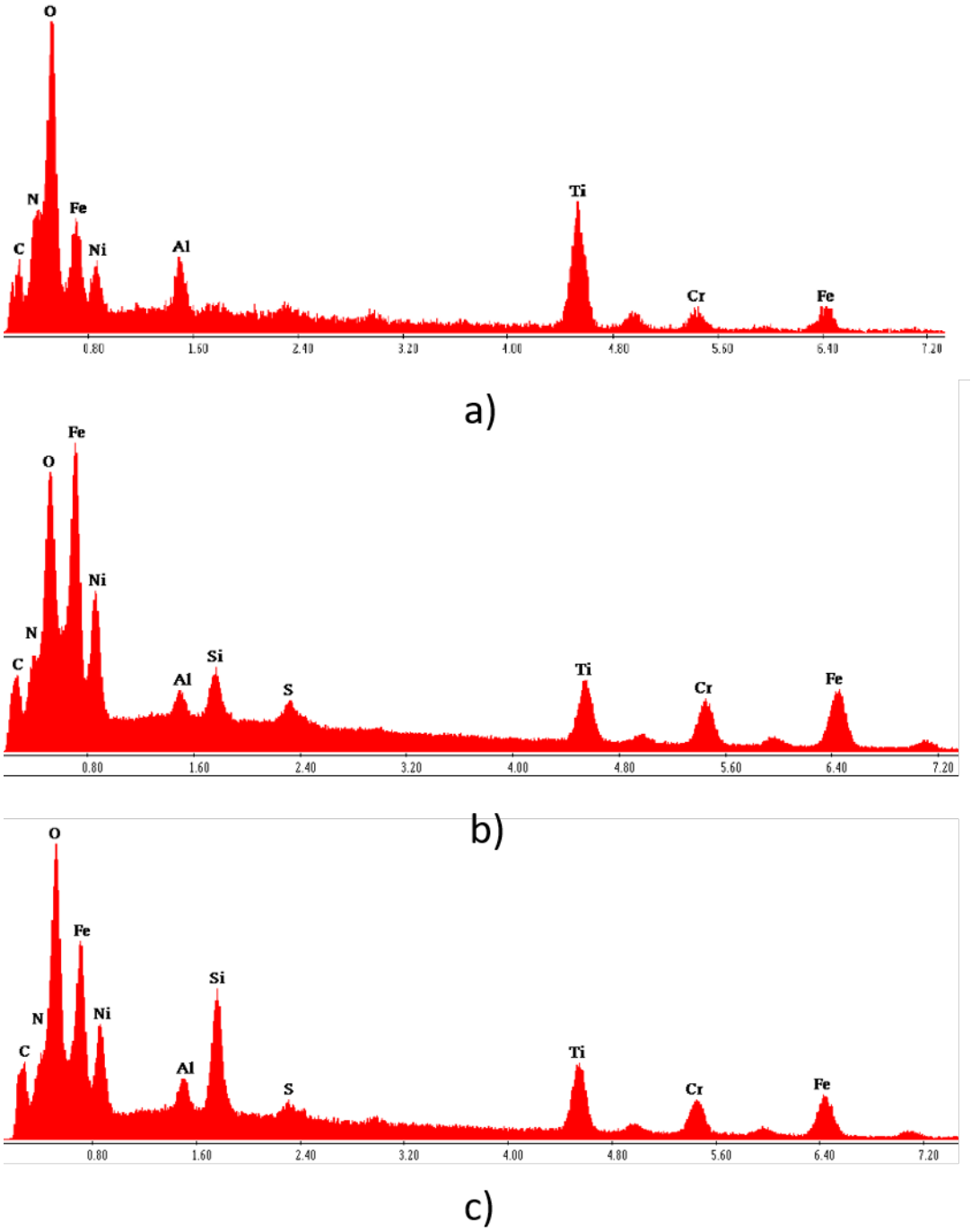

FIGURE 7.4: EDX spectrum before degradation in dynamic fluidic test a) TiO_XN_Y (O_2/N_2 = 6/10), b) TiO_XN_Y (O_2/N_2 = 13/10), c) TiO_XN_Y (O_2/N_2 = 27/10).

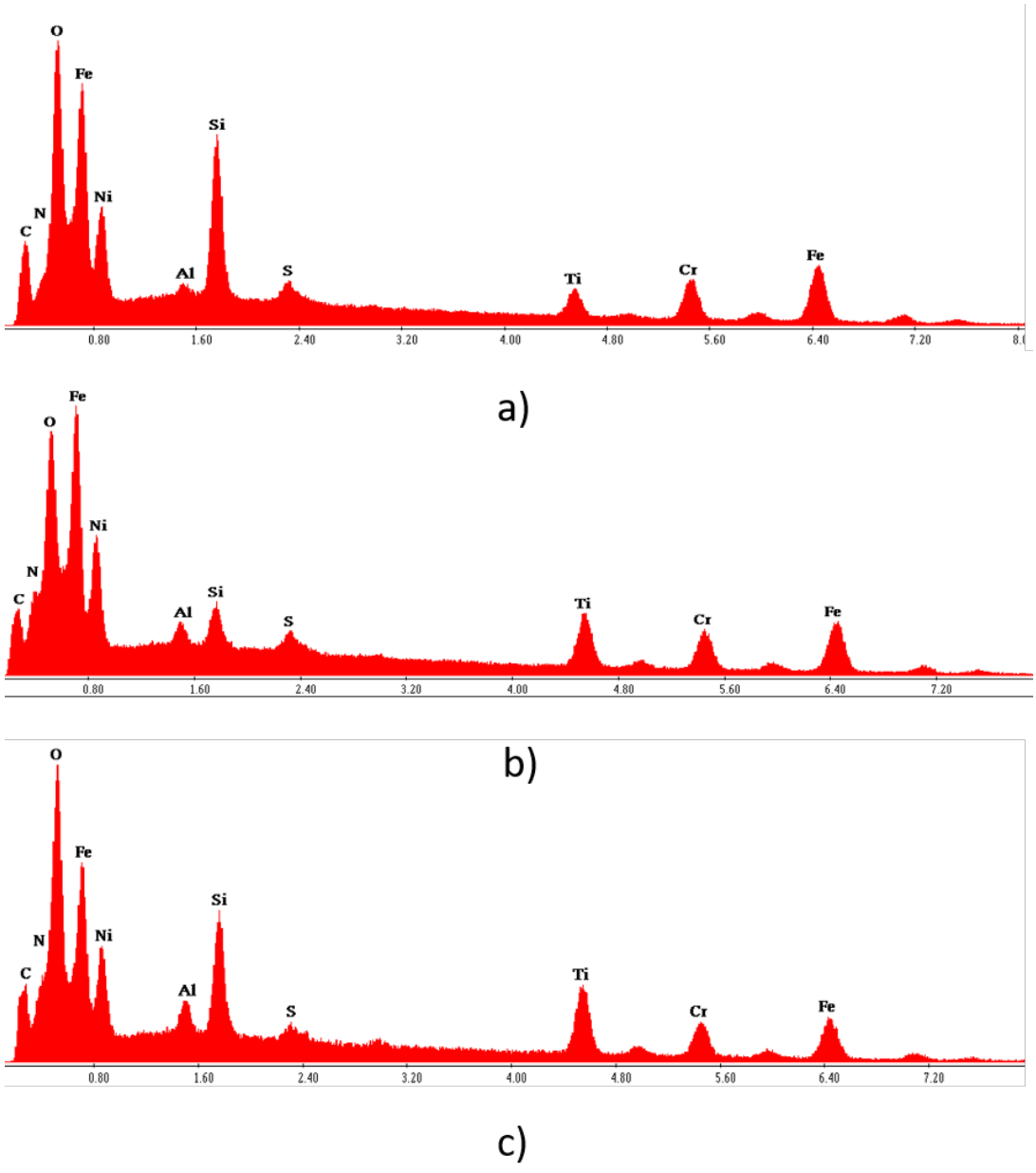

FIGURE 7.5: EDX spectrum after 30 days degradation in dynamic fluidic test a) TiO_XN_Y (O_2/N_2 = 6/10), b) TiO_XN_Y (O_2/N_2 = 13/10), c) TiO_XN_Y (O_2/N_2 = 27/10).

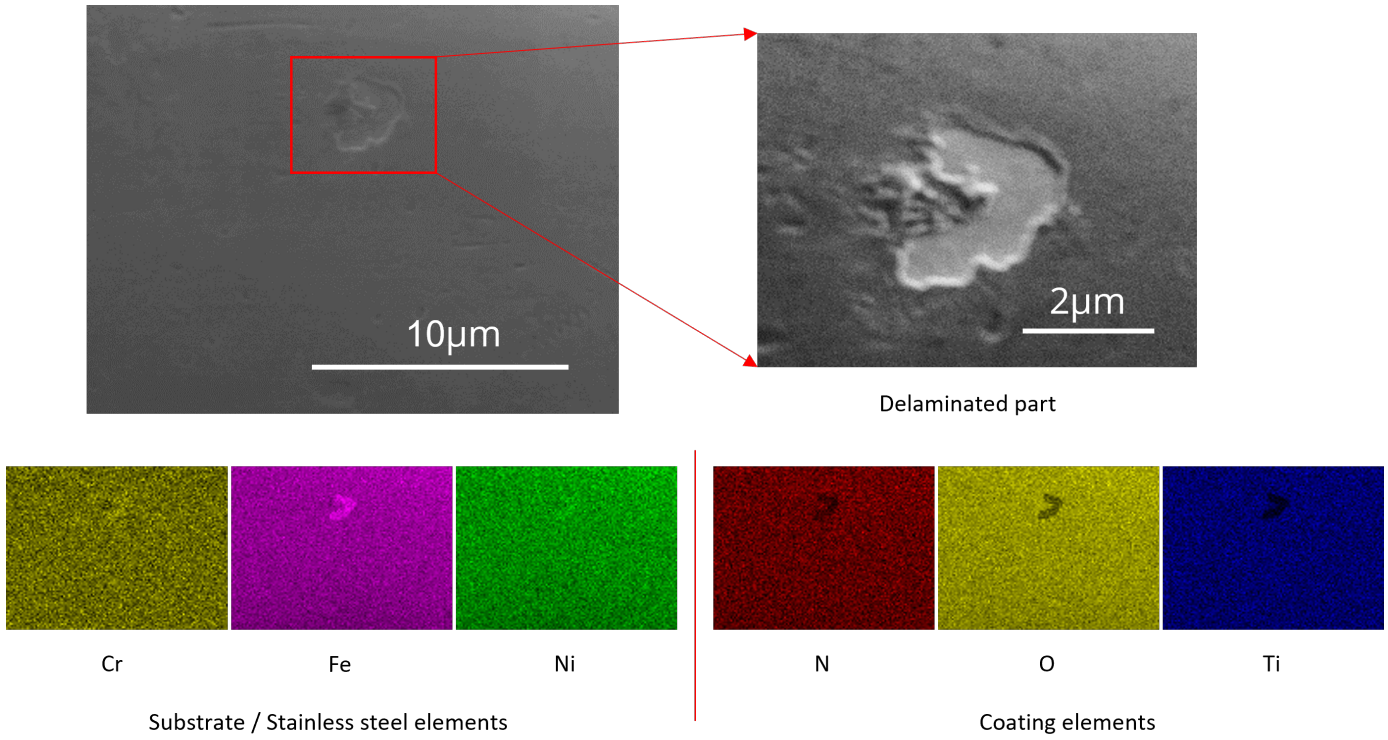

FIGURE 7.6: Elemental mapping of coating and substrate elements on the delaminated part of TiO_XN_Y (O_2/N_2 = 6/10) after 30 days dynamic fluidic exposure.

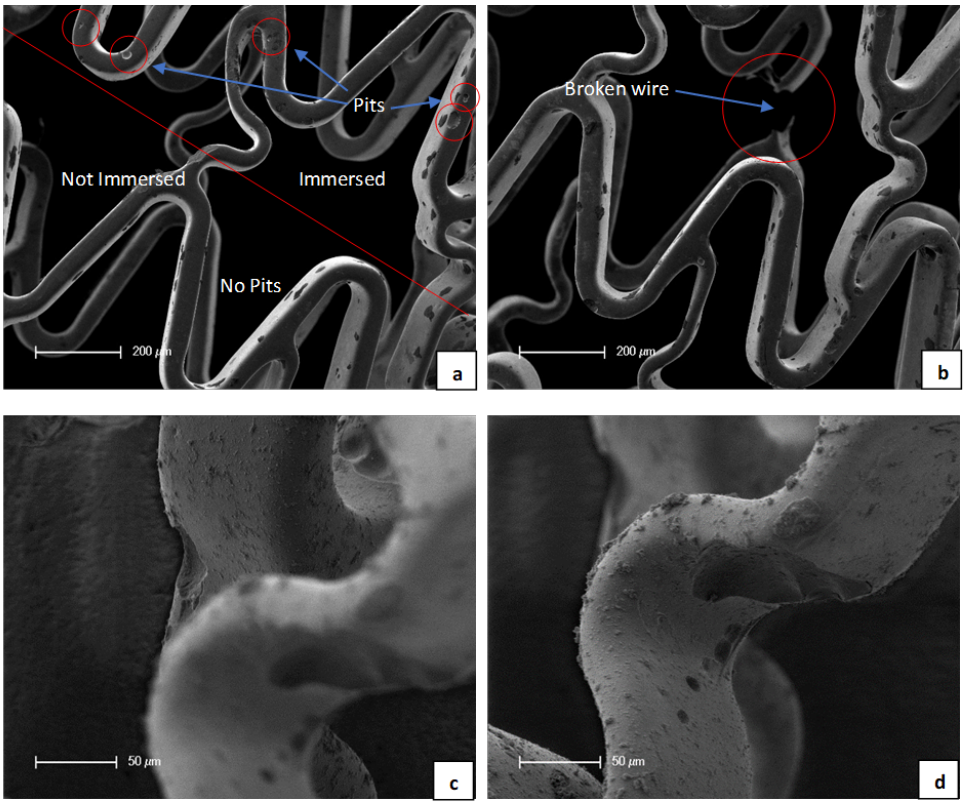

FIGURE 7.7: Surface morphology of TiO_XN_Y (O_2/N_2 = 6/10) after electrochemical corrosion experiment.

7.3 Electrochemical corrosion test

The electrochemical characterization was conducted at different temperatures i.e. 25°C, 30°C, 37°C, 50°C in the HBBS. The temperatures, higher than 50°C are not recommended with a saturated calomel electrode due to high oscillation and false measurements and the possibility of reference electrode breakage and mercury leakage. At temperatures, between 50-60°C the system will oscillate and may give false measurements in case of longer measurement and above 60°C, the saturated calomel electrode will be broken, and leakage of mercury occurs.

Open circuit potential (OCP): Before the potentiodynamic measurements, the open-circuit potential was measured after the 2-hour potential-stabilizing immersion period of the working electrode in the HBSS. The OCP measurement was restricted to 240 seconds for each sample at each temperature as reported by Hertel et al. [217] and the values obtained were averaged per second.

Potentiodynamic polarization curves (Tafel extrapolation): At each temperature and following the OCP measurement, the net current density (i [A/cm^2]) as a function of the shifting WE potential (E [V] vs. SCE) was recorded. Potentiodynamic polarization was used from 0.0 to +1.5 V for 316L stent, whereas, +0.6 to +1.8V used for all coated samples. The scan rate was set to 10mV for each measurement. The measurement data was then transferred to Origin 2017 (Origin Lab Corporation, Northampton, MA, USA). The logarithmic values of net current density were plotted as a function of WE potential (E [V] vs. SCE) for the Tafel

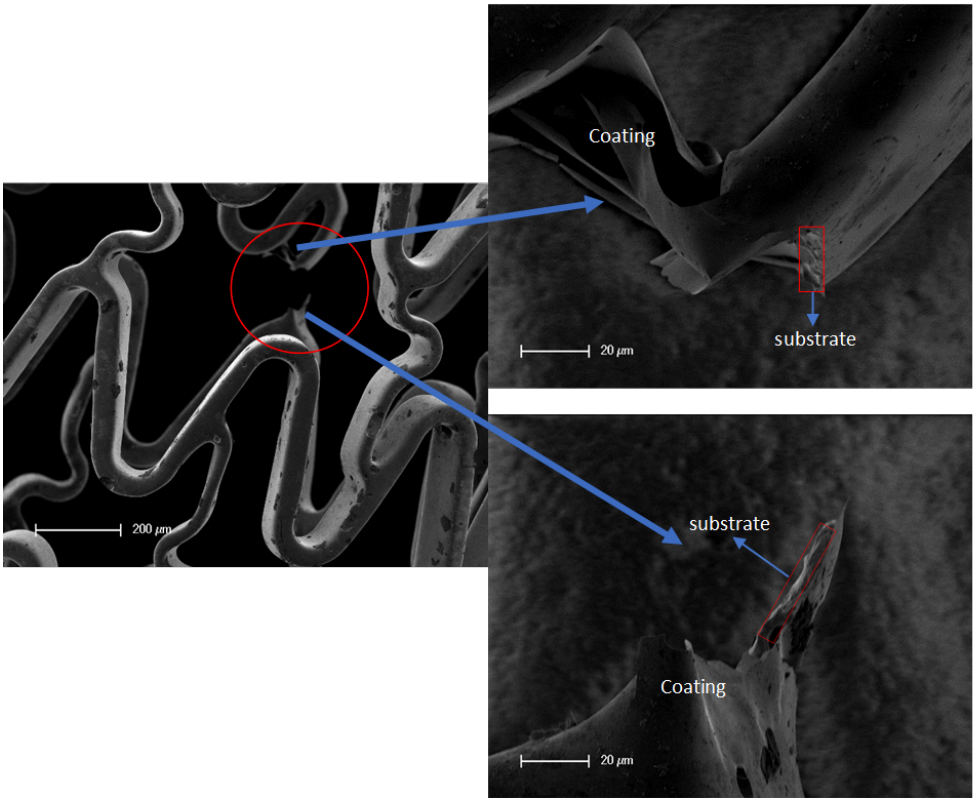

FIGURE 7.8: Surface morphology of TiO_XN_Y (O_2/N_2 = 6/10) after electrochemical corrosion experiment.

extrapolation. Three measurements were taken at each temperature for every sample for the result reproducibility evaluation. From these Tafel curves and via linear fitting, corrosion current density was calculated and then the corrosion rate was determined using the Equation (4).

7.3.1 Electrochemical measurements

All samples were attained a stable OCP before the potentiodynamic measurements were recorded. Potentiodynamic polarization curves (Figure 7.10) shows the similar cathodic and anodic polarization curves indicating identical conversion mechanism at all temperatures. It was observed that zero current potential is shifted towards the negative direction with the increase in temperature in all samples indicating the weakening of barrier for corrosion [237, 238] . The E_{corr} was in the range of 1.25V to 1.46V for all coated stents while from 0.91V to 1.05V for the uncoated samples showing the maximum shift of 0.21V from lowest to the highest temperature.

Table 7.2 shows the corrosion parameters i.e. i_{corr}, E_{corr}, and corrosion rate retrieved from the Tafel curves via linear fitting. All coated samples showed a good and stable response of these coatings in chemically aggressive environments, unlike the uncoated sample, which has a high effect of immersion period on its corrosion properties. This can be seen from the little or no variation on values of corrosion

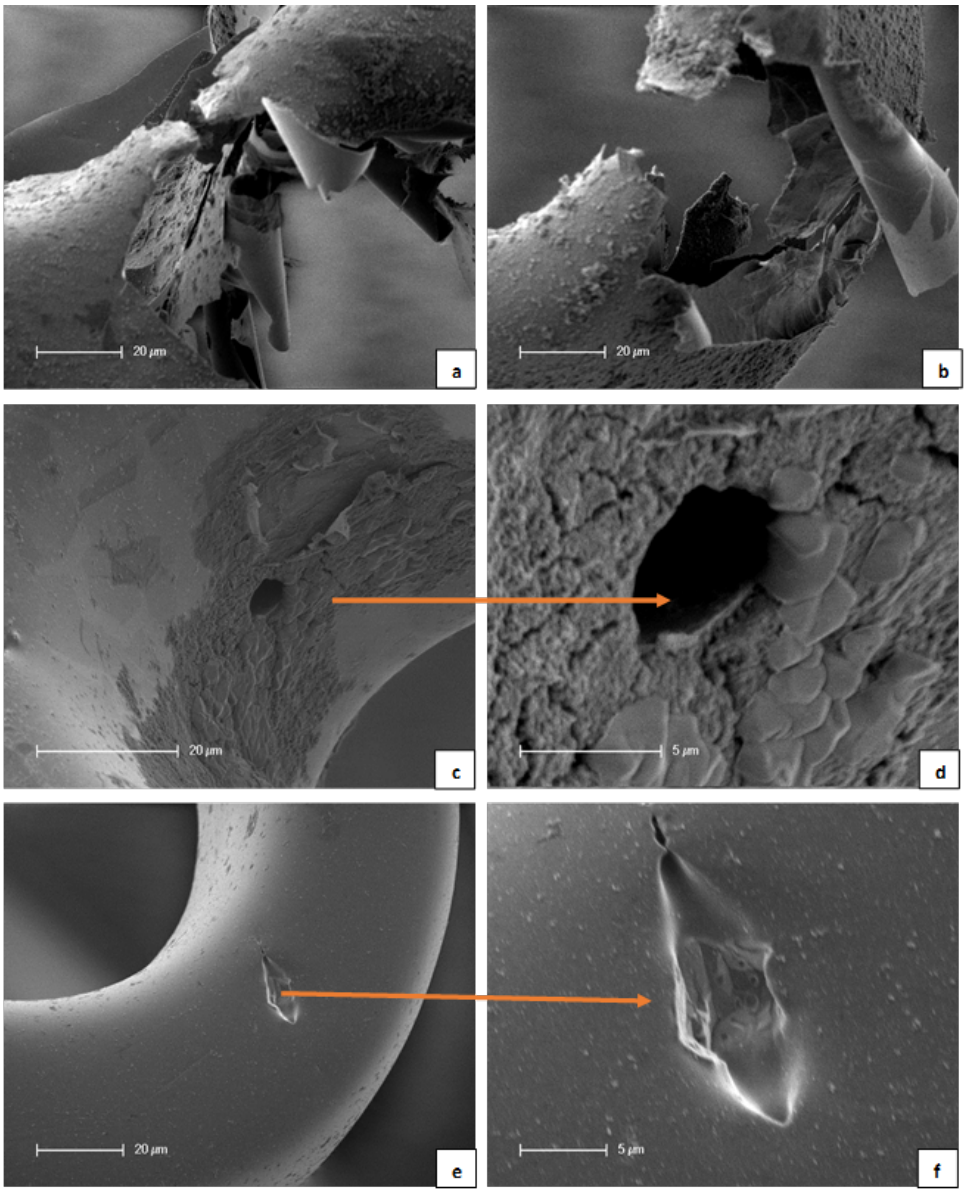

FIGURE 7.9: Degree of degradation attack on different coated stents: (a) and (b) TiO_XN_Y (O_2/N_2 = 6/10), (c) and (d) TiO_XN_Yy (O_2/N_2 = 13/10), (e) and (f) TiO_XN_Y (O_2/N_2 = 27/10).

potential (E_{corr}), corrosion current density (i_{corr}), corrosion rate (CR) for different coated stents compared to the high variation on uncoated stent's values which correlates to the higher effect of environmental conditions on corrosion properties. In general, a continuous decrease in i_{corr} and E_{corr} was observed (except at 37°C where a slight increase was found) in the case of 316L stent. This decrease indicates the formation of a strong passivation layer and the localization of corrosion due to the formation of pits which stabilizes after some time. Due to this fact, it is difficult to make a direct correlation of temperature with i_{corr} and E_{corr} at this point within the used range. In the case of coated stents, the increase in i_{corr} was observed at

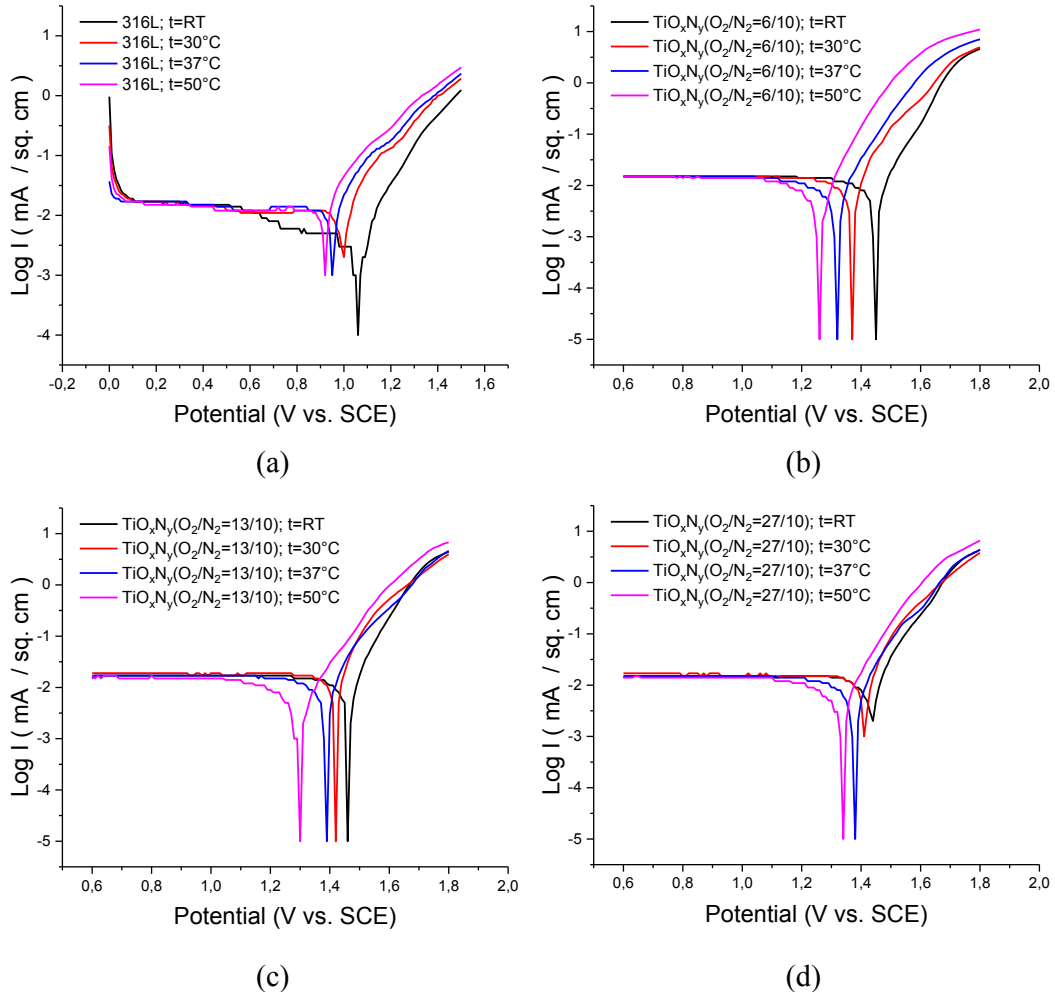

FIGURE 7.10: Tafel curves related to different coating types: (a) uncoated 316L stent, (b) TiO_XN_Y (O_2/N_2 = 6/10), (c) TiO_XN_Y (O_2/N_2 = 13/10), (d) TiO_XN_Y (O_2/N_2 = 27/10) at room temperature, 30°C, 37°C and 50°C.

30°C for TiO_XN_Y (O_2/N_2 = 6/10), and at 37°C for TiO_XN_Y (O_2/N_2 = 13/10). However, no increase was found for TiO_XN_Y (O_2/N_2 = 27/10). The less variation in the corrosion parameters suggests the stable response of the used coated stents in comparison to the uncoated stent.

Figure 7.11 is showing that E_{corr} of all coated samples has an almost similar region at 37°C whereas the uncoated have a very different value and more negative than coated ones. The more positive E_{corr} of coated stents indicated that these stents are more corrosion resistant. In all coated stents, TiO_XN_Y (O_2/N_2 = 13/10) and TiO_XN_Y (O_2/N_2 = 27/10) showed more resistance to the external harsh and corrosive environment as compared to TiO_XN_Y (O_2/N_2 = 6/10). The formation of pits and broken wires were observed in SEM measurements after the electrochemical corrosion test (Figure 7.7). Corrosion, especially the pitting corrosion is considered as the main contributor to stent fracture in the periphery [239, 240]. The difference in the immersed and un-immersed surface of stents can easily be seen in Figure 7.6. Only the immersed part of the stent has pits. The broken wires and large pits of 70-80 µm were found in TiO_XN_Y (O_2/N_2 = 6/10), whereas in TiO_XN_Y (O_2/N_2 = 13/10) and TiO_XN_Y (O_2/N_2 = 27/10) no broken

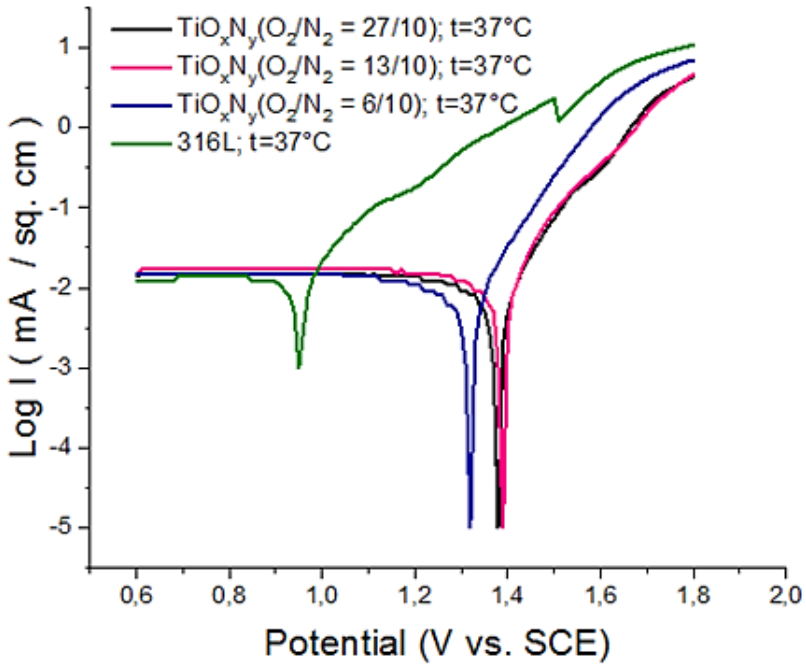

FIGURE 7.11: Tafel curves related to different coating types: uncoated 316L stent, TiO_XN_Y (O_2/N_2 = 6/10), TiO_XN_Y (O_2/N_2 = 13/10) and TiO_XN_Y (O_2/N_2 = 27/10) at 37°C.

wires were observed. However, the latter two samples have smaller pits in the exposed area and some delamination was also observed (Figure 7.9). The coating of the broken wire was still attached; however, the bulk material was dissolved in the solution (Figure 7.8). The presence of coating in the broken part proving the durability of the coating. The degree of degradation (D) based on SEM imaging was $D_{27/10} < D_{13/10} < D_{6/10}$ which means that the higher the oxygen ratio the lower the degradation rate (Figure 7.9). These results were also supported by ICPMS results of the static immersion test. It proves that TiO_XN_Y (O_2/N_2 = 27/10) has very stable behavior on aggressive conditions which also satisfies by the Tafel curves where it shows stable corrosion rates at different temperatures.

It is known that the corrosion behavior of metal alloys is influenced by electrolyte composition and temperature. The increase in the temperature creates a rupture of the formed oxide film and facilitates the charge transfer process [241]. Due to the formation of the passivation layer in the stainless-steel sample, the corrosion rate decreases even after increasing temperature, which starts to increase at 37°C again. In the case of coated stents, there is a negligible effect of the external environment causing the corrosion rate to increase with the increase in temperature.

In general, corrosion rates of all samples were in the range of 0.146-0.151 mm/yr at 25°C. The decrease in the corrosion rate of 316L stent at higher temperatures is not because of the increasing temperature, but due to the formation of the passive film on the exposed surface. For instance, at 30°C, coated samples showed a slight decrease in corrosion rates [excluding TiO_XN_Y (O_2/N_2 = 13/10), which showed an increase in CR proving the negligible effect of the external

TABLE 7.2: Summary of corrosion parameters: I_{corr}, E_{corr}, and Corrosion rate (CR).

Sample	Corrosion parameter	25°C	30°C	37°C	50°C
316L	E_{corr} (V)	1.047	0.953	0.854	0.682
	I_{corr} ($\mu A/cm^2$)	13.544	9.243	10.425	6.469
	CR (mm/yr)	0.151	0.103	0.117	0.072
TiO_XN_Y (O_2/N_2 = 6/10)	E_{corr} (V)	1.474	1.358	1.293	1.227
	I_{corr} ($\mu A/cm^2$)	13.083	12.658	11.28	12.125
	CR (mm/yr)	0.146	0.141	0.126	0.135
TiO_XN_Y (O_2/N_2 = 13/10)	E_{corr} (V)	1.401	1.361	1.375	1.343
	I_{corr} ($\mu A/cm^2$)	13.51	14.283	13.597	11.897
	CR (mm/yr)	0.151	0.16	0.152	0.133
TiO_XN_Y (O_2/N_2 = 27/10)	E_{corr} (V)	1.419	1.437	1.398	1.371
	I_{corr} ($\mu A/cm^2$)	13.127	13.04	12.553	12.14
	CR (mm /yr)	0.147	0.146	0.14	0.136

environment including temperature. The reason for increasing the corrosion rate of the TiO_XN_Y (O_2/N_2 = 13/10) may suggest that the conduction properties of this sample are better than others. As with the increase in temperature the corrosion current density also increased. At further elevated temperatures i.e. 37°C and 50°C, all coated samples showed stable response except TiO_XN_Y (O_2/N_2 = 6/10). In TiO_XN_Y (O_2/N_2 = 6/10) at 50°C corrosion rate starts to increase due to the wire fracture and exposing of bulk material to the HBSS.

The coatings delamination occurs mainly because of adhesive failure due to the occurrence of electrochemical corrosion processes [242]. The broken wires of TiO_XN_Y (O_2/N_2 = 6/10) at 50°C suggest plenty of collisions between the coating and bulk molecules. The good elasticity of the coating layer and the high hardness of stainless steel caused broken wires. Because of the aforementioned facts, the bulk particles dissolved in the fluid, whereas, the coating layer remained in its place.

7.3.2 Corrosion rates

Figure 7.12 shows the corrosion rates of all samples were in the range of 0.146-0.151 mm/yr at 25°C. TiO_XN_Y (O_2/N_2 = 6/10) and TiO_XN_Y (O_2/N_2 = 27/10) have fewer corrosion rates then sample TiO_XN_Y (O_2/N_2 = 13/10) and 316L samples. After increasing temperature to 30°C, only sample TiO_XN_Y (O_2/N_2 = 13/10) corrosion rate increases, whereas, the corrosion rates of the other two samples and 316L were decreased. The decrease is due to the formation of the passive layer on the surface which was not influenced by an increase of temperature as in the case of sample TiO_XN_Y (O_2/N_2 = 13/10). The passivation layer was strongest in the 316L sample, and in the coated samples, TiO_XN_Y (O_2/N_2 = 6/10) had the strongest passivation layer. After the further increase in temperature to 37°C, the corrosion rates of all samples were not affected and decrease due to the passivation layer. At 37°C, TiO_XN_Y (O_2/N_2 = 13/10) has the highest corrosion rate whereas the 316L sample has the lowest corrosion rate.

Elevation of temperature to 50°C caused an increase of corrosion rate in TiO_XN_Y (O_2/N_2 = 6/10), whereas the corrosion rates of all samples continue to decrease. The reason for the increased corrosion rate of TiO_XN_Y (O_2/N_2 = 6/10) is the fracture in the wires (Fig 9). Broken wires were found and the base material is exposed. In general, TiO_XN_Y (O_2/N_2 = 27/10) found more consistent and no increase in corrosion rate was found by increasing temperature.

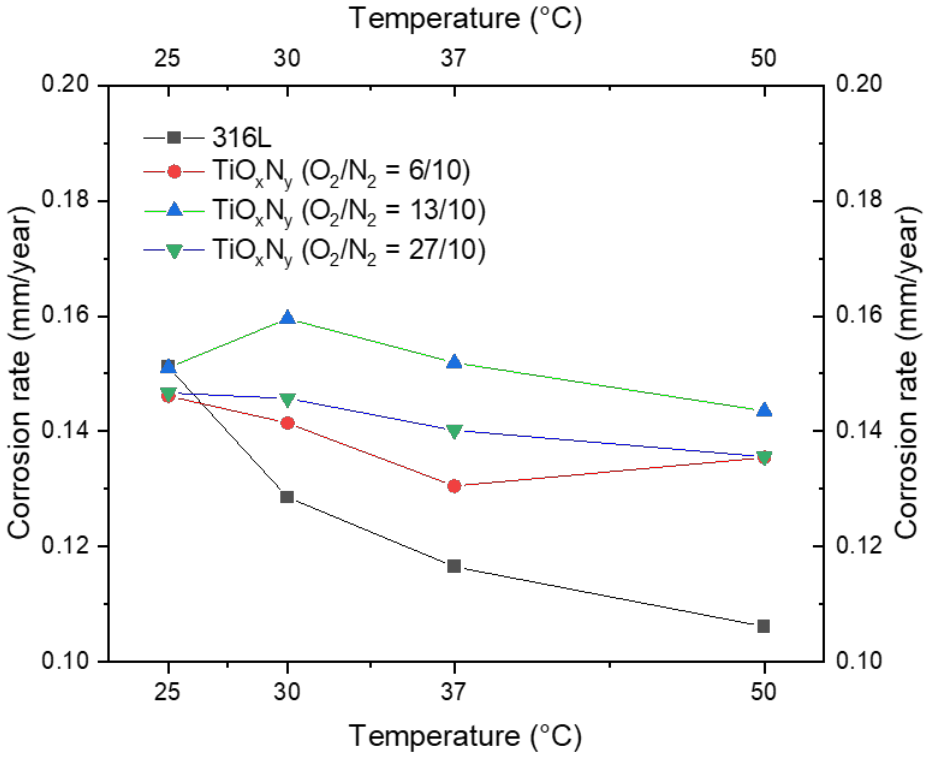

FIGURE 7.12: Corrosion rates of different coating types: uncoated 316L stent, TiO_XN_Y (O_2/N_2 = 6/10), TiO_XN_Y (O_2/N_2 = 13/10) and TiO_XN_Y (O_2/N_2 = 27/10) at 25°C, 30°C, 37°C and 50°C.

7.3.3 ICPMS studies

Figure 7.13 shows the ICPMS studies of all coated samples after the electrochemical corrosion tests at 25°C, 30°C, 37°C, and 50°C. In the electrochemical test, the release of Ti was found similar for all coated samples. It suggests that the electrochemical environment has no or negligible influence on the release of Ti. In TiO_XN_Y (O_2/N_2 = 6/10), the release of Cr, Mo is higher. Fe is released higher in TiO_XN_Y (O_2/N_2 = 13/10), whereas, Ni and Mn release is higher in TiO_XN_Y (O_2/N_2 = 27/10). The variation of elemental release during electrochemical tests is due to the random behavior of the formation of pits in all samples. For instance, TiO_XN_Y (O_2/N_2 = 6/10) has broken wire and pits and more Cr release is found. Whereas TiO_XN_Y (O_2/N_2 = 13/10) and TiO_XN_Y (O_2/N_2 = 27/10) do not have broken wires and have only pits, less Cr is found. In general, coatings were found stable in the electrochemical environment and showed a negligible influence of applied potential and temperature. The Ti release was very little in all samples as compared to the release of base material elements. The base material elements release after the formation of pits.

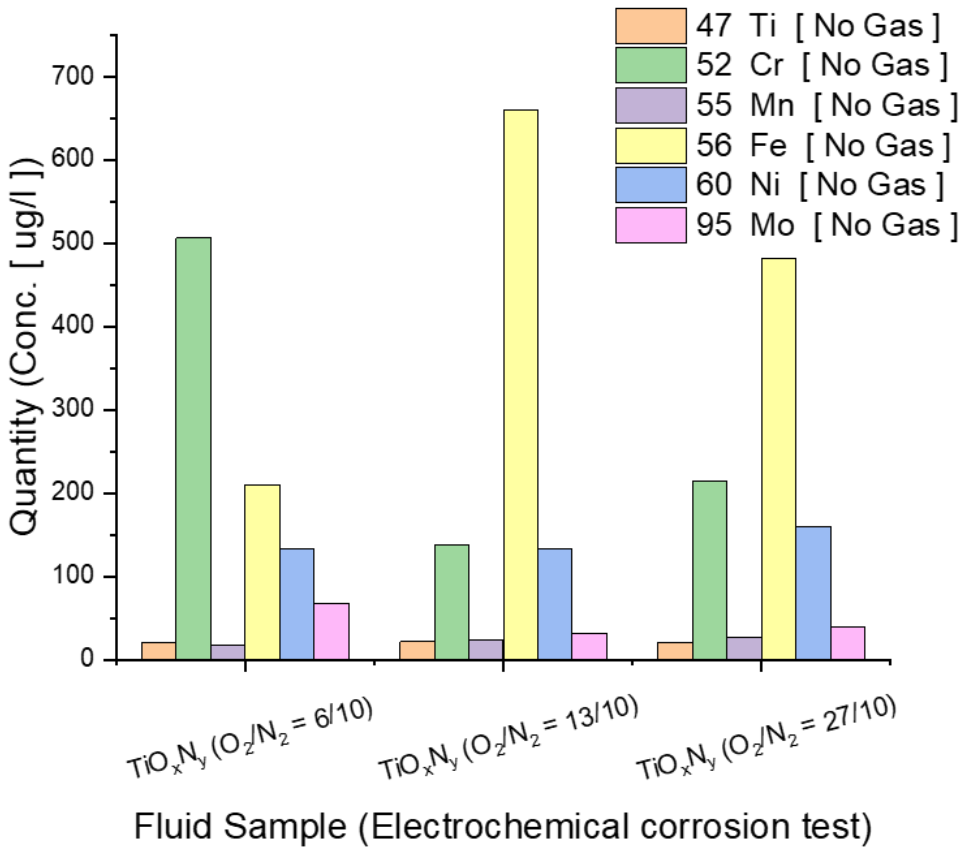

FIGURE 7.13: ICPMS studies of fluid samples of coated stents after electrochemical corrosion test.

7.4 Conclusions

In this chapter, the degradation tests of TiO_XN_Y coated stainless steel stents obtained by using three different deposition conditions, especially O_2/N_2 ratio. Quantitative corrosion and degradation tests were performed on the entire stent surface (for the first time) instead of the upper surface or using simpler samples. Based on the surface morphology using SEM-EDX measurements, ICPMS results, mass variation, and corrosion rates after corrosion tests, it can be concluded that the TiO_XN_Y coatings improve the stability and corrosion resistant behavior of the stainless steel (316L) stents. The coated stents showed better temperature resistance in comparison to the uncoated sample as the temperature has a very low or no effect on the corrosion rate of the coated ones.Moreover, it is proved that O_2/N_2 affects the corrosion properties as noticeable differences were observed for all coated samples. The higher oxygen ratio ensures higher stability in harsh environments. Among all tested samples, TiO_XN_Y (O_2/N_2 = 27/10) stents were found to be more resistant to harsh environments as witnessed by its steady corrosion behavior. Further studies are needed to find the exact relationship. Reversible hydrogen electrode (RHE) can be used for temperatures higher than the values presented in this work.

8 Evaluation of in vitro biodegradation of AZ31 (Mg-alloy) in fluid dynamic environment

This chapter presents the *in vitro* biodegradation properties of plasma electrolytic oxidized (PEO) AZ31 (Mg-alloy) in fluid dynamic conditions. Section 8.1 discusses the impact of Mg-alloys (especially AZ31) in implants. Section 8.2 introduces the experimental conditions of biodegradation test of AZ31 samples. The surface morphology of all AZ31 samples is described in Section 8.3 using SEM and EDX measurements. Section 8.4 demonstrates the mass loss and corrosion rates of AZ31 samples. The contact angle measurements are shown in Section 8.5 before and after the 30 days degradation using cleaned and uncleaned surfaces. Section 8.6 highlights the effect of cleaning AZ31 samples in chromic acid. While, Section 8.7 discusses the degaradation behaviour of polymer-coated samples. In last, Section 8.8 concludes the whole chapter.

8.1 Background

Magnesium and its alloys are being widely used as a biodegradable material in implantation due to better biocompatibility and non-toxicity [243, 184, 244, 245, 246, 247, 248, 249]. Among all Mg Alloys; AZ31, AZ91D, Mg–Li–Ca and WE43 got more attention of the researchers and attempts have been made to use them as bio-absorbable stents [227]. However, AZ31 is preferred because of reduced aluminum content, microstructure refinement, low fatigue, corrosion resistance similar to other Mg alloys [243, 249, 250, 251, 252, 253].

Despite the promising material properties, the poor corrosion resistance of Mg alloys is observed during in vivo tests [227]. As a consequence, Mg Alloys can not be used as biodegradable stent material due to the insufficient support to the blood vessel wall. Therefore, it is important to modify the surface properties of existing Mg-Alloys to improve their corrosion properties.

In this chapter, the in vitro degradaton behaviour of PEO treated AZ31 samples (with and without polymer coating) will be discussed.

8.2 In vitro biodegradation of AZ31 (Mg-alloy) in fluid dynamic environment

The AZ31 samples used in this chapter are described in Table 3.3 within Section 3.3. The samples are named as A, B, C, D, and E for simplicity. All samples are plasma electrolytic oxidized AZ31 samples using NaOH and Na_2SiO_3 as anodizing agents. Samples A, B, and C have anodized layer on AZ31 surface, whereas, sample D and E have additional polymer coating is present.

All the samples were degraded using fluid dynamic setup presented in Figure 5.6 for 30 days with the measurement time points of 1, 2, 4, 7, 14, 21, and 30 days. After each abovementioned interval, the samples were taken out from the running experiment and cleaned as mentioned in Section 3.3.2 before mass loss measurements.

8.3 Surface morphology

Figure 8.1 show the surface morphology of all the samples. It can be seen that the anodizing conditon influence the size and no. of pores in samples A, B and C. In sample D, and E porosity can not be seen due to the polymer coating on oxide layer. Sample C has the lowest pore size and the largest amount of pores in comparison to Sample A and B. Whereas, Sample B has the largest pore size in comparison to Sample A and C.

The anodized layer has already removed from the surface within first two days of degradation period in Sample A, B and C. For example, Figure 8.2 and 8.3 show the elemental mapping and the spectrum with the quantification of elements after two days of degradation period of Sample B. It is evident from 8.2 that the degradation products contain Mg in less quantity, whereas, O and P are dominating the corrosion product layer. These corrosion products also prove that the oxide layer has already been removed within first two days.

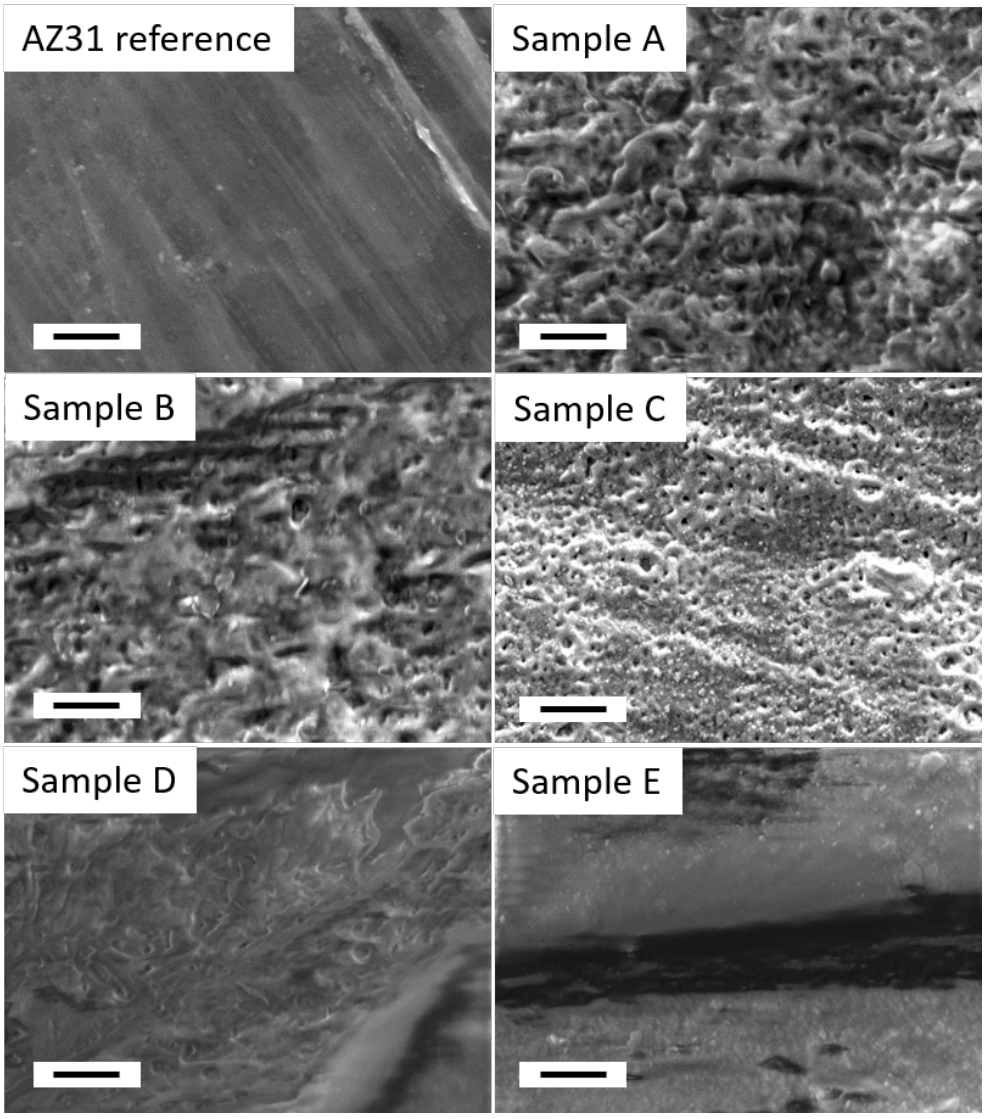

FIGURE 8.1: Surface morphology of AZ31 samples with scale bar 2μm..

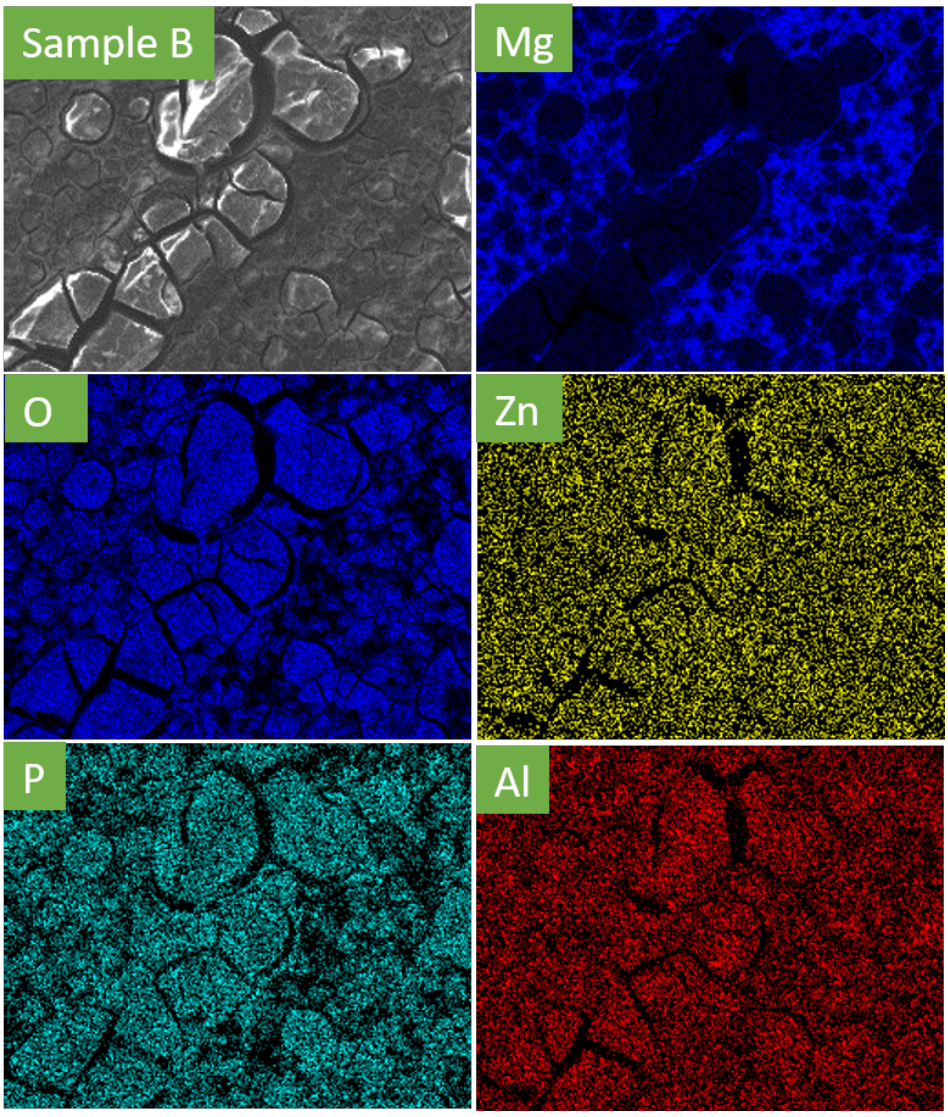

FIGURE 8.2: Elemental mapping of Sample B after 2 days of degradation.

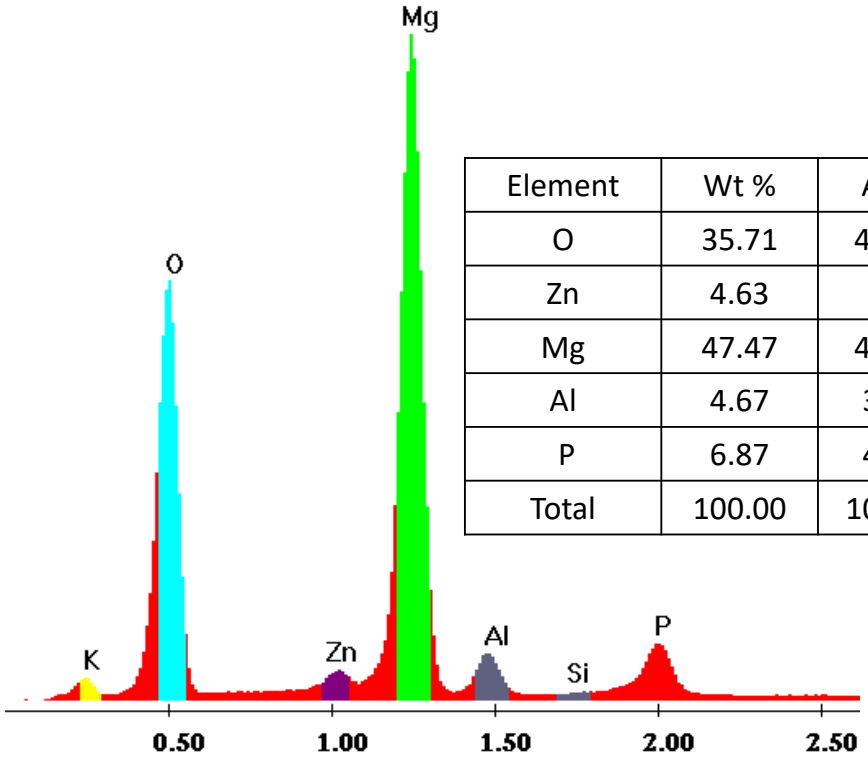

Element	Wt %	At %
O	35.71	47.76
Zn	4.63	1.51
Mg	47.47	41.78
Al	4.67	3.71
P	6.87	4.75
Total	100.00	100.00

FIGURE 8.3: EDX spectrum with quantification of Sample B after 2 days of degradation.

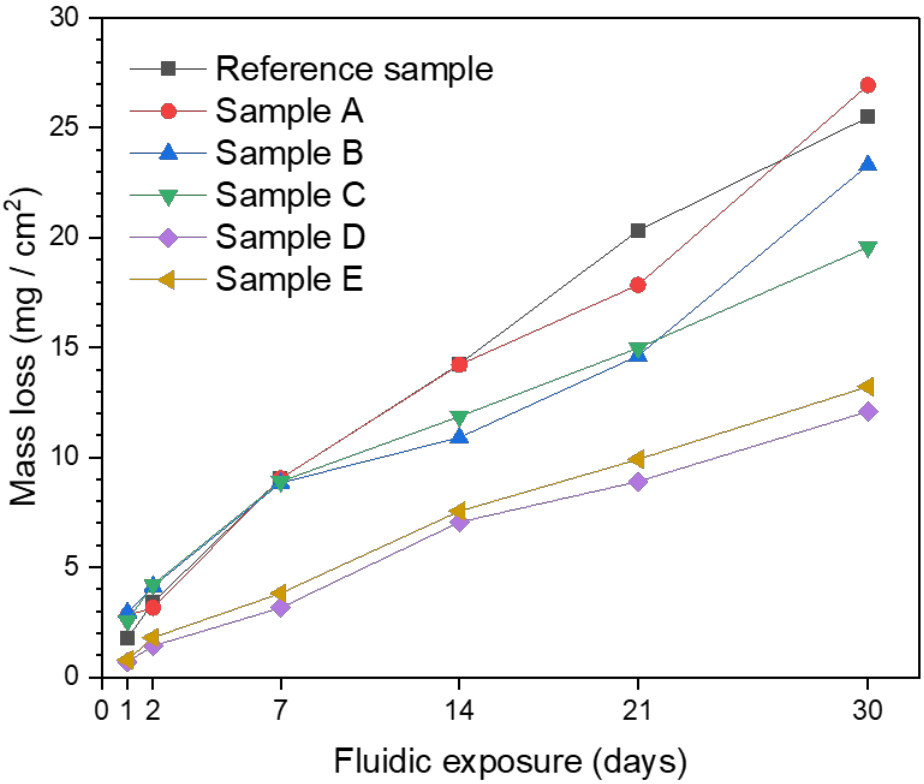

FIGURE 8.4: Mass loss rates of AZ31 samples in 30 days fluid dynamic experiment.

8.4 Mass loss (MLRs) and corrosion rates (CRs)

Figure 8.4 and 8.6 show the MLRs and CRs of AZ31 samples in the 30 days fluid dynamic experiment respectively. Whereas, Figure 8.5 and 8.7 show the similar results with error bars. The obtained results indicate the influence of anodizing time and drying protocol on degradation. For instance, Sample A has the highest MLR and CR after 30 days. Whereas, the Sample C had minimum MLR and CR after 30 days among non polymer-coated anodized samples.

Initially, The anodized samples have slightly higher MLRs to the reference AZ31 surface. This is because of the removal of anodized layer in the first two days. Whereas, polymer-coated anodized samples have lesser MLRs throughout the experiment than all other samples. The polymer coating prevented the anodized layer removal. The additional ML in anodized samples without polymer coating is due to the removal of the oxide layer from the AZ31 surface.

Both polymer-coated samples D and E have the lower MLRs and CRs, where, sample D has the lowest among all samples. Polymer-coated samples show steady behavior and did not show too much variation in the MLRs as anodized samples.

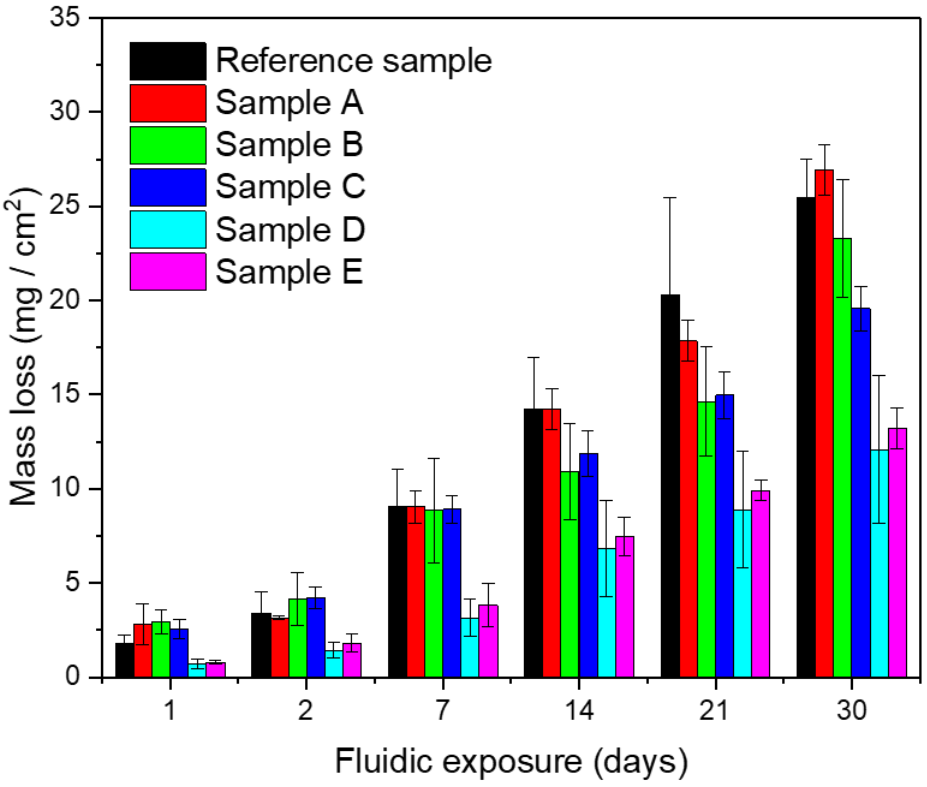

FIGURE 8.5: Bar chart with error bars of mass loss rates of AZ31 samples in 30 days fluid dynamic experiment.

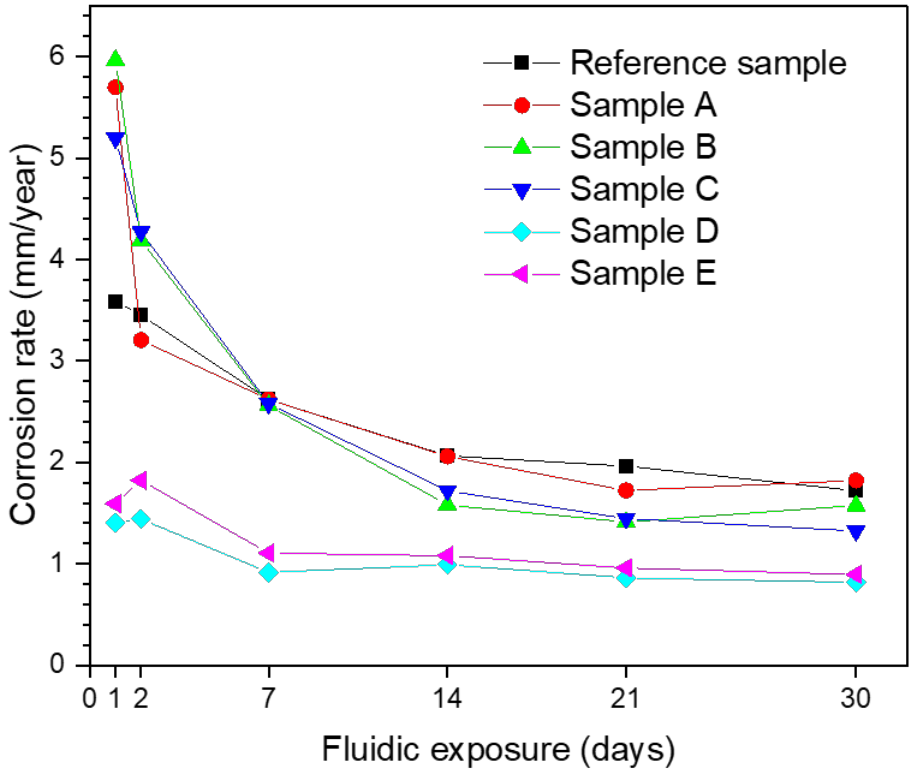

FIGURE 8.6: Corrosion rates of AZ31 samples in 30 days fluid dynamic experiment.

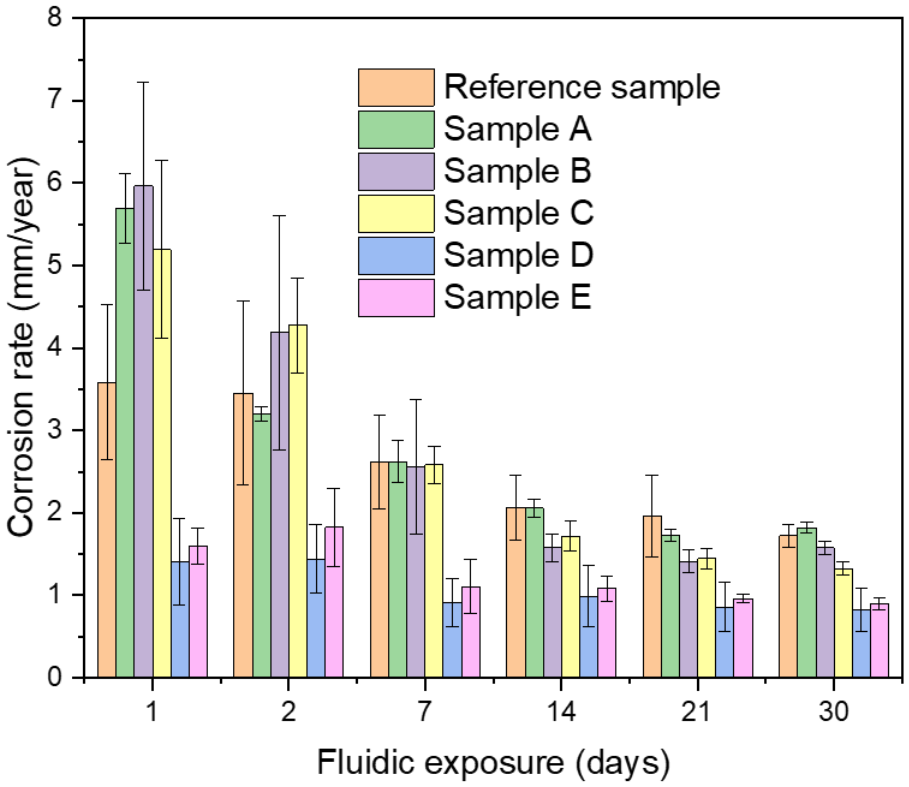

FIGURE 8.7: Bar chart with error bars of corrosion rates of AZ31 samples in 30 days fluid dynamic experiment.

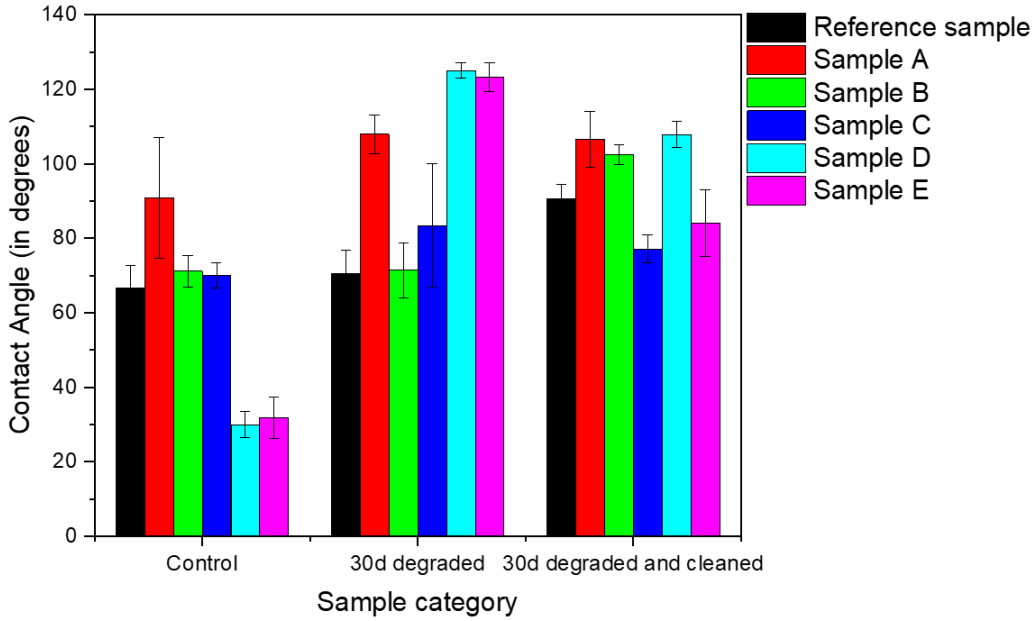

FIGURE 8.8: Bar chart with error bars of contact angles of AZ31 samples in 30 days fluid dynamic experiment.

8.5 Contact angle

Figure 8.8 shows contact angle (CA) of samples in three different states: i) undegraded, ii) 30 days degraded and uncleaned, and iii) 30 days degraded and cleaned. Among all samples, sample A is the only hydrophobic sample whose CA is slightly higher than 90°. Similarly, all other samples including reference sample are hydrophilic whose CA is less than 90°. Polymer coated samples (i.e. sample D and E) are more hydrophilic whose CA are in the range of 28° - 36°. Low CA indicates the enhanced wettability of polymer coated samples which ultimately result in improved biocompatibility [254].

After 30 days of degradation, all the samples become more hydrophobic. Where, sample A and polymer coated samples shifted heavily towards hydrophobic in comparison to other samples. After cleaning of the samples, the CA was decreased for sample C, sample D, and sample E. The CA of sample A nearly the same after cleaning, whereas the CA of reference sample and sample B was increased, and they become hydrophobic. Figure 8.9 show the CA of sample E in: a) undegraded state which less than 90°, b) 30 days degraded and cleaned which is nearly equal to 90°, c) 30 days degraded and uncleaned which is greater than 90°.

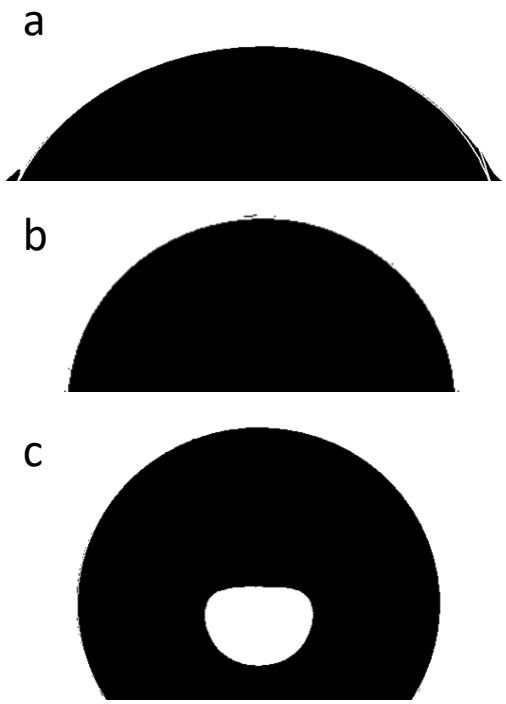

FIGURE 8.9: AZ31 samples contact angle illustration of Sample E in : a) undegraded state which less than 90°, b) 30 days degraded and cleaned which is nearly equal to 90°, c) 30 days degraded and uncleaned which is greater than 90°.

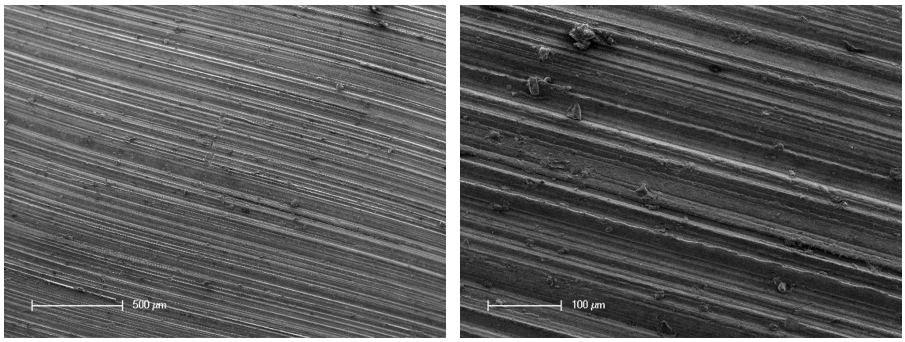

FIGURE 8.10: Undegraded sample C (Magnification 250: left, Magnification 500: right).

8.6 Effect of chromic acid cleaning

Figure 8.10 shows the surface of undegraded sample C at 2 different magnifications. Figure 8.11 shows degradation after 1 day of fluid-dynamic load where the anodized layer is fully corroded and some of the corrosion products are removed from the surface and formed pits. After cleaning the surface in chromic acid, all of the corrosion products are removed and the surface with and without an anodized layer can be seen. After 2 days of fluid dynamic loading, the anodization oxide layer was completely removed by a dynamic fluidic load (Figure 8.12).

In Figure 8.12 two different kinds of surfaces were found in the whole sample

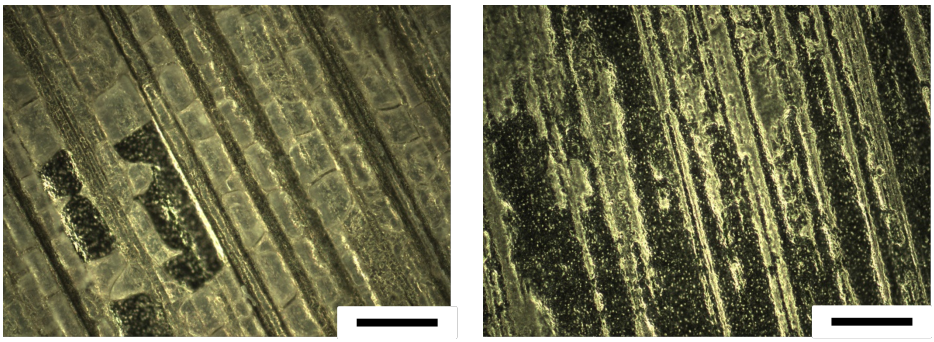

FIGURE 8.11: Sample C after 1 day of degradation (Uncleaned : left, cleaned in chromic acid: right), Scale bar: 100 μm.

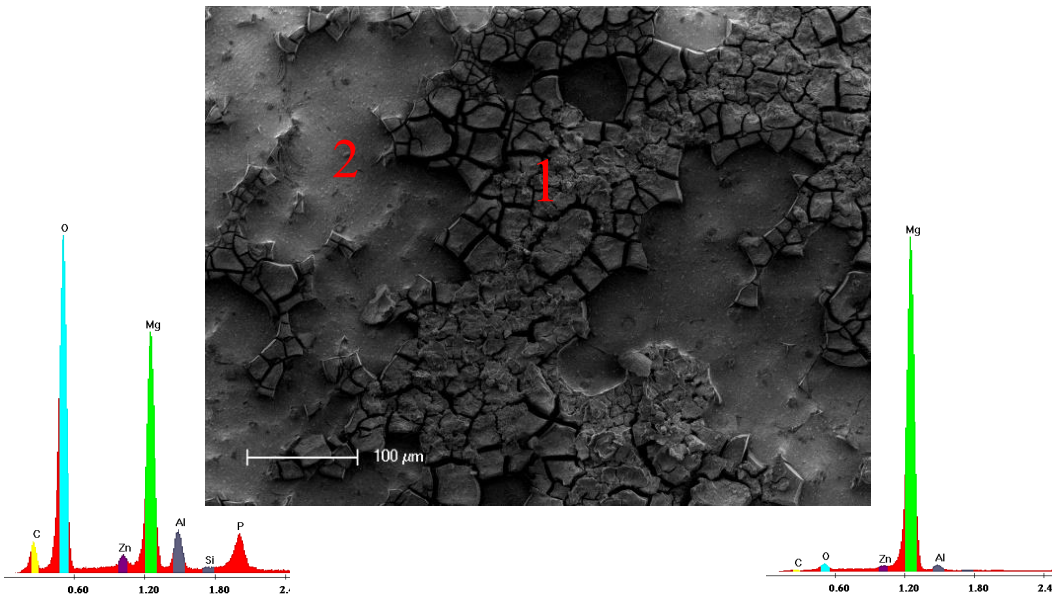

FIGURE 8.12: Uncleaned sample C after 2 days of degradation (Magnification: 500).

surface. At point 1, the spectrum suggests that the sample surface only has degradation products as phosphates of Mg along with AZ31 surface in cracks. Whereas, Point 2 shows only the AZ31 surface. The aforementioned results prove the absence of an anodized layer after 2 days of degradation testing before cleaning with chromic acid. However, after 1 day of degradation some of the anodized part was retained on the sample surface even after chromic acid cleaning.

8.7 Degradation behavior of polymer-coated samples

Unlike the only anodized samples (Sample A, B, and C), polymer-coated samples (Sample D and E) retained the oxide layer because of additional polymer coating in the first two days. However, the samples contain areas where polymer layer starts delaminating (Figure 8.13). The sample surface shows the two different morphologies marked as point 1 and point 2 as shown in Figure 8.13. At higher magnification, it is visible that Point 1 contains polymer coating, whereas, Point 2

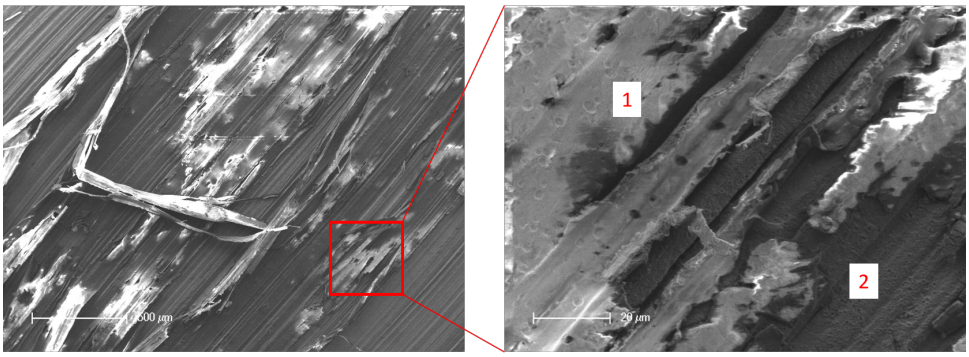

FIGURE 8.13: Surface morphologyof sample D after 2 days of degradation.

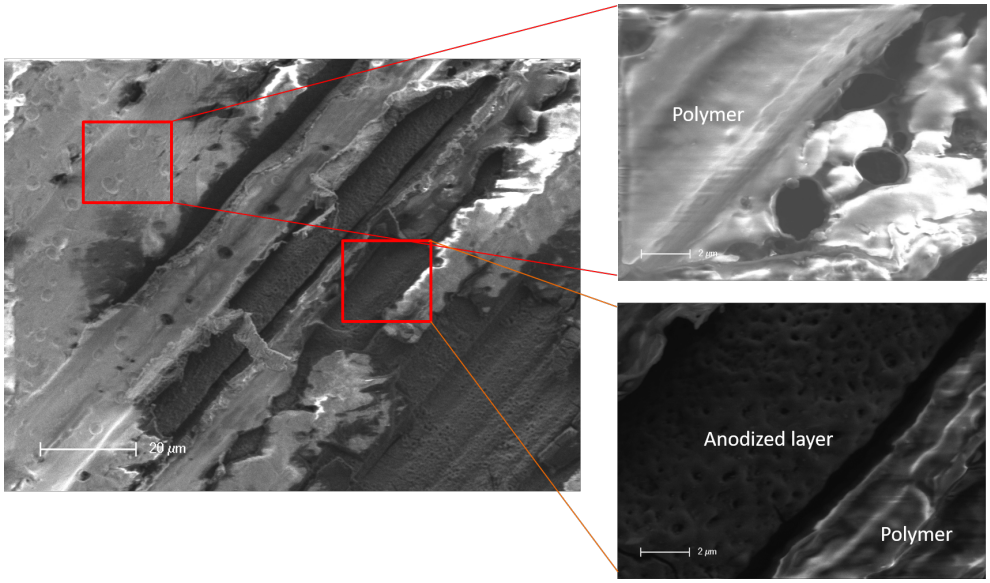

FIGURE 8.14: Presence of anodized and polymer layer on sample surface after 2 days of degradation.

contains an anodized oxide layer after removal of polymer coating from this part (Figure 8.14). Here, the delamination of the polymer coating is initiated by the flow-induced shear stress in fluid-dynamic conditions.

After 7 days of degradation, most of the polymer coating was delaminated and an anodized oxide layer was exposed throughout the sample surface. As a consequence, cracks were also developed in the oxide layer (Figure 8.15). This suggests the phenomenon that the oxide layer was first cracked and then those fragments or chips were removed from the surface of anodized samples.

Figure 8.16 shows the surface morphology after 14 days of degradation. Two different surfaces were visible which were marked as points 1 and 2. Both points 1 and 2 show the presence of only AZ31 material, no signs of oxide layer were found. Similar results were obtained after the 30 days of degradation (Figure 8.17).

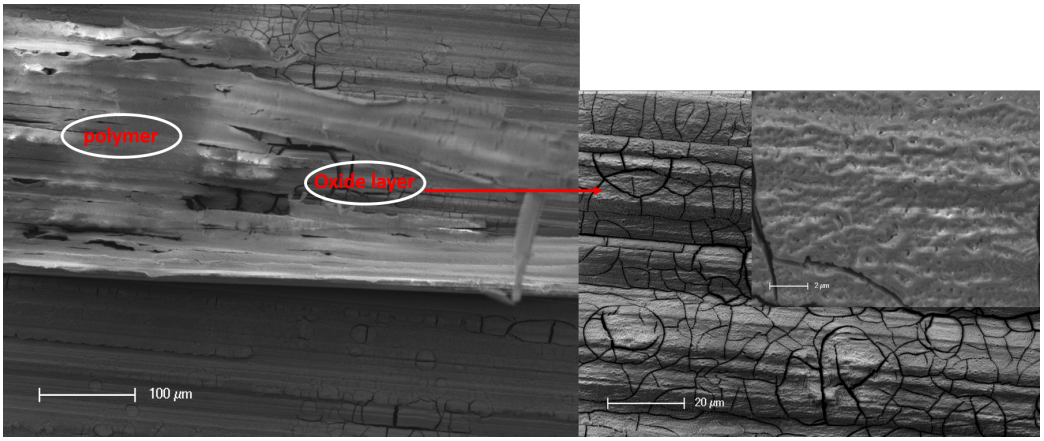

FIGURE 8.15: Surface morphologyof sample D after 7 days of degradation.

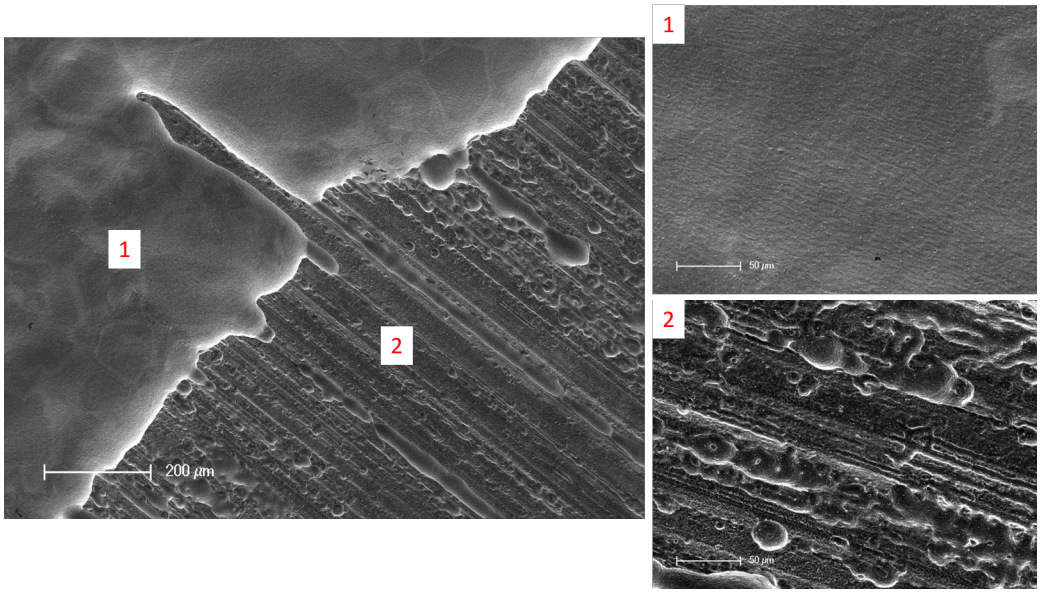

FIGURE 8.16: Surface morphologyof sample D after 14 days of degradation.

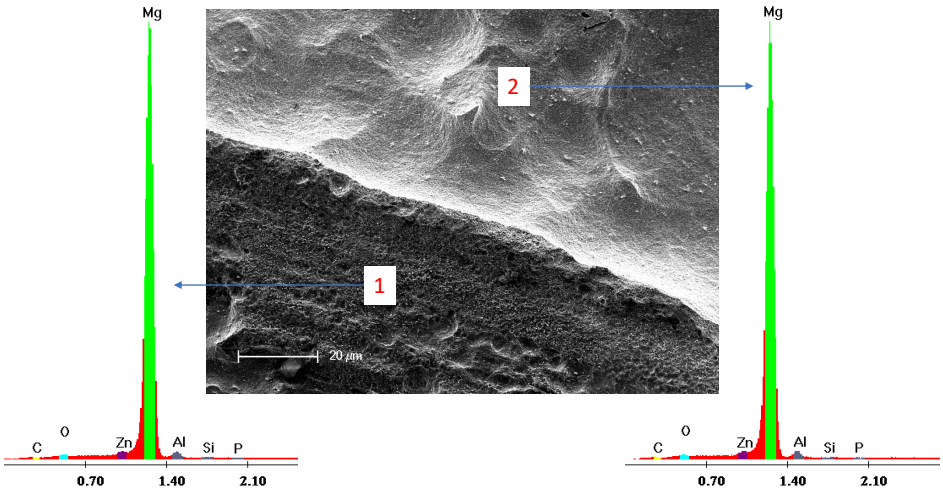

FIGURE 8.17: Surface morphologyof sample with the EDX spectrum of sample D after 30 days of degradation.

8.8 Conclusions

AZ31 is a preferred choice as a biodegradable magnesium alloy because of reduced aluminum content, refined microstructure, low fatigue, corrosion resistance similar to other Mg alloys. In this Chapter, the fluid dynamic degradation of PEO treated AZ31 samples were presented. The PEO treated samples with and without polymer coating were used. The main findings within this Chapter are:

- Using the plasma electrolytic oxidation process the degradation properties of AZ31 can be influenced.
- Anodizing time and the drying protocol have a significant impact on the degradation properties of Mg alloy.
- Sample A is the only hydrophobic sample, whereas, Sample D and E were the more hydrophilic.
- After 30 days of degradation, the CAs of all samples were increased and Sample D and E become most hydrophobic.
- Sample D and E have the lowest MLRs and CRs among all samples, whereas, Sample C had the lowest MLR and CR among non-polymer-coated anodized samples.
- After 1 day half of the anodized layer was removed from the sample surface.
- After 2 days of degradation anodized layer was completely removed during the experiment due to shear stress in non-polymer-coated anodized samples.
- In the case of polymer-coated anodized samples, the polymer coating starts removing after two days of degradation, and the anodized layer is exposed to the fluid flow.
- Polymer-coated anodized samples retained the polymer coating and oxide layer for one week, they lost the oxide layer between days 8 and 14 during the degradation test.
- No significant effect of chromic acid cleaning was found for the used time points.
- Polymer coating reduces the MLRs and CRs.

9 Analytical degradation model: Flow induced shear stress corrosion model

This Chapter presents the effect of shear stress on the corrosion rate of the biodegradable alloy materials. AZ31 semi rods were used as a biodegradable material. Section 9.1 introduces the flow induced shear stress (FISS) phenomenon. Section 9.2 presents the FISS corrosion model with the help of fluid dyanamic experiment on AZ31 semi rods. The mass loss and corrosion rates with the surface morphology of semi rods after degradation at each shear stress is also presented in this Section. Section 9.3 describes the FISS corrosion mechanism. In last, Section 9.4 concludes the whole chapter.

9.1 Flow induced shear stress (FISS)

Shear stress induced on the surface of the sample due to the fluid flow called as flow induced shear stress (FISS). FISS has a great influence on the degradation of materials. Wang et al. 2014 [177] reported the significance of fluid flow shear stress for the determination of the corrosion behavior of AZ31 Mg stents in simulating in vivo vascular conditions. They concluded that the higher FISS values : (i) lead to an increase in corrosion; (ii) increase the uniform corrosion layer thickness, localized corrosion coverage ratios and depth, as well as acceleration of corrosion product removal; and (iii) areas facing the flow direction have higher shear stress, which caused corrosion product detachment and led to strut fracture [177].

In the human physiological environment, shear stress is affected by the flow rate, radius of the vessel, and the viscosity of the fluid. In a blood vessel, when the viscosity increases, shear stress increases as well [255]. The main reason for the increased shear stress in human arteries is the increase in the viscosity due to the thickening of blood or decrease in the radius due to the plaque formation.

9.2 Flow induced shear stress (FISS) corrosion model

Considering the significant effects of FISS on corrosion behaviour of implant materials, with the help of experimental data FISS corrosion model is developed. For this purpose, different shear stresses were generated by changing flow rates whereas the radius of the tube and viscosity of the fluid was kept constant. The experimental setup showed in Figure 5.6 was used to conduct the fluid dynamic experiments to degrade AZ31 semi rods under different FISSs. Table 9.1 shows the shear stresses used in this study and their corresponding flow rates and flow velocities. The range of 0 to 100 dyn/cm^2 was chosen to cover all the FISS values in the normal and diseased veins and arteries (Figure 9.1) [8]. The FISS values were

TABLE 9.1: Relationship between the values of shear stress, flow velociy, and flow rates in the experiment.

Flow rate ml/min	**Flow velocity** cm/s	**Shear stress** dyn/cm^2
0	0	0
24.1	10	2.5
48.255	20	5
96.51	40	10
193.02	80	20
482.55	200	50
675.57	280	70
965.1	400	100

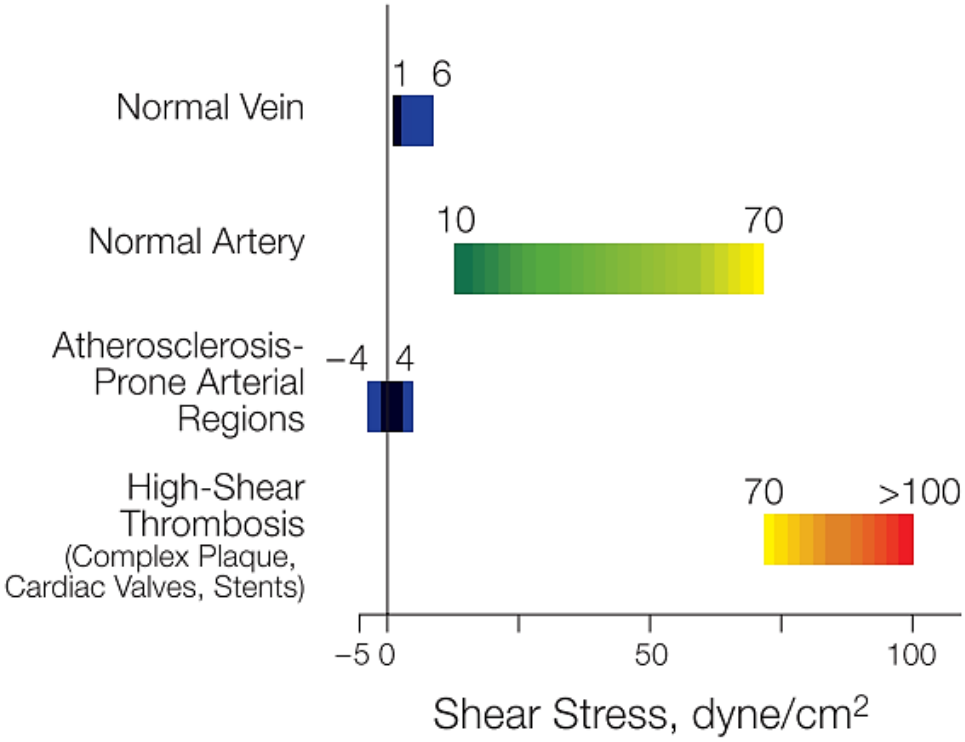

FIGURE 9.1: Range of shear stress magnitudes in veins, arteries, and in low-shear and high-shear pathologic states [8].

calculated by using the Poiseuille's law for shear stress inside the human vasculature (Equation (9.1)).

According to Poiseuille's Law, the shear stress inside the human vasculature can be calculated by the following equation.

$$\tau_s = \frac{4\mu Q}{\pi R^3} \tag{9.1}$$

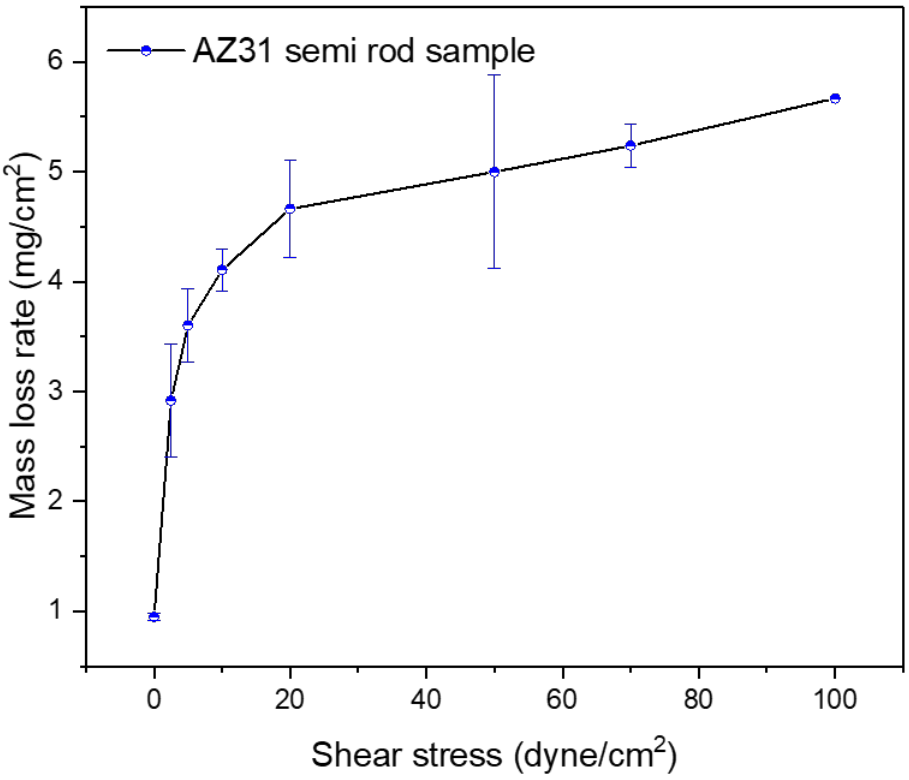

FIGURE 9.2: Mass loss rates of semi rods under various FISSs.

where τ_s: shear stress; μ: fluid viscosity; Q: flow rate; R: radius of the vessel.

9.2.1 Mass loss (MLRs) and corrosion rates (CRs)

Figure 9.2 shows the mass loss rates (MLRs) of AZ31 semi rod samples at the FISS values of 0, 2.5, 5, 10, 20, 50, 70, and 100 dyn/cm^2. The MLRs were calculated by using the Equation (2). At zero FISS, the MLR of 0.95 mg/cm^2 was obtained. The MLR was increased to 2.92 mg/cm^2 at 2.5 dyn/cm^2. In the beginning, the increment in MLR was rapid that shown to be slower at shear stresses after 5 dyn/cm^2 and further slow down at FISSs more than 20 dyn/cm^2. The obtained results suggest that the MLR will no longer be affected significantly at higher shear stresses.

Figure 9.3 shows the corrosion rates (CRs) of AZ31 semi rod samples at the FISS values of 0, 2.5, 5, 10, 20, 50, 70, and 100 dyn/cm^2. These corrosion rates were calculated by using the Equation (3) based on ML measurements. Predictably, the shape of the corrosion rate graph is similar to that of mass loss (Figure 9.2) due to its known influence. Similarly, at zero FISS, the CR of 2.03 mm/year was obtained. The CR was increased to 5.92 mm/year at 2.5 dyn/cm^2. Like MLR, the increment in CRs was higher in the beginning that was shown to be slower at shear stresses after 5 dyn/cm^2 which further slow down at FISSs more than 20 dyn/cm^2. The obtained results indicate that the CR will no longer be affected significantly at higher shear stresses, like MLR.

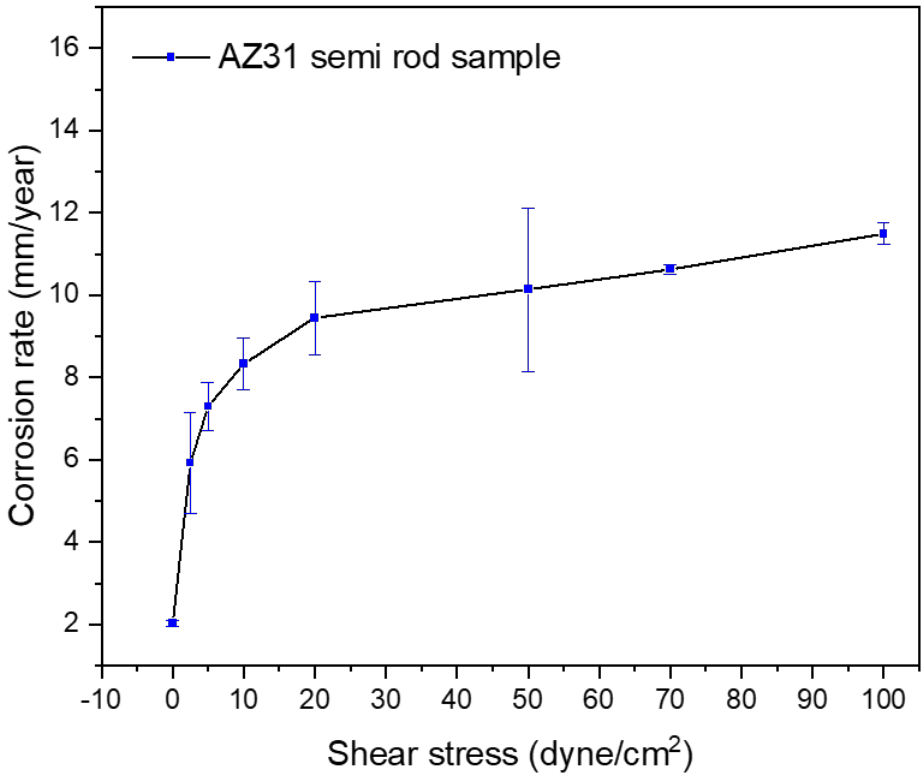

FIGURE 9.3: Corrosion rates of semi rods under various FISSs.

Importantly, the MLR and CR due to the FISS (subtracting the MLR and CR at static condition i.e. zero FISS) at 2.5 dyn/cm^2 are 1.97 mg/cm^2 and 3.89 mm/year respectively. Simply, it can be illustrated by the Equations (27) and (28).

$$MLR_{(due\ to\ FISS=X)} = MLR_{(at\ FISS=X)} - MLR_{(at\ FISS=0)} \tag{27}$$

$$CR_{(due\ to\ FISS=X)} = CR_{(at\ FISS=X)} - CR_{(at\ FISS=0)} \tag{28}$$

9.2.2 Analytical model for FISS corrosion

Figure 9.4 shows the fitted curve for the FISS corrosion rates. The rational model (Equation (29)) was obtained via fitting of the obtained curve in the Origin Pro 2021.

$$CR = \frac{a + b\tau_s}{1 + c\tau_s + d\tau_s^2} \tag{29}$$

Where: $a = 1.98979 \pm 0.44413$; $b = 3.9742 \pm 0.54205$; $c = 0.40305 \pm 0.06112$; and $d = -6.29285 \times 10^{-4} \pm 1.6591 \times 10^{-4}$

The abovementioned presented model is developed using shear stresses in the range of 0 and 100 dyn/cm^2. The chosen range covers the shear stresses present in healthy and diseased vessels in humans. Therefore the FISS values higher than 100 dyn/cm^2 is not in the scope of this work. However, based on the obtained results, it

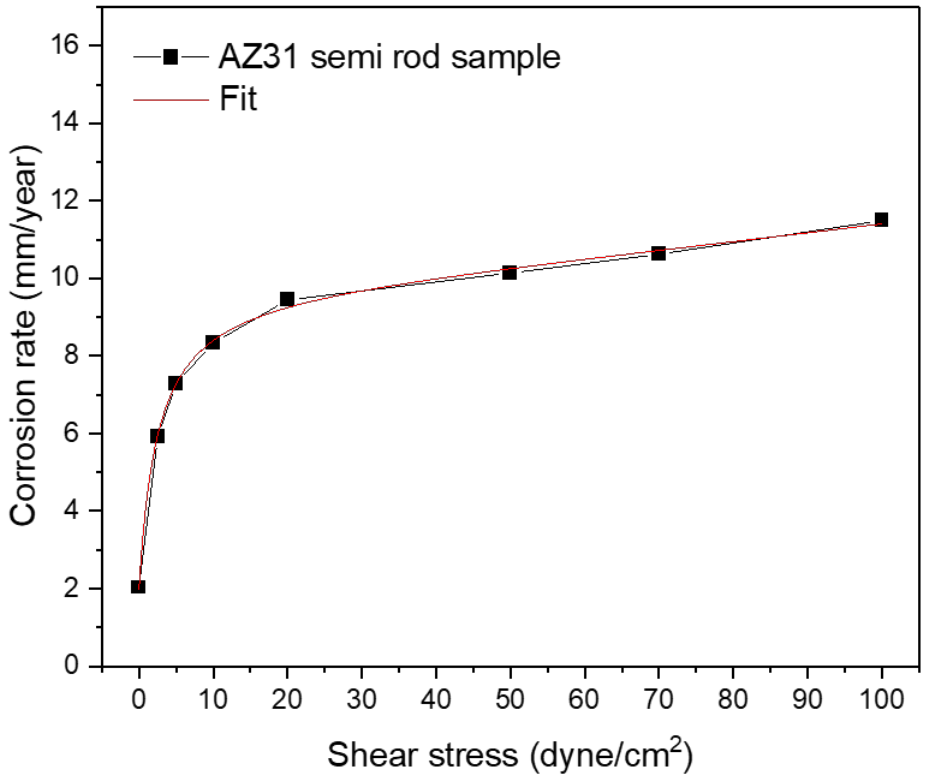

FIGURE 9.4: Fitted curve: Corrosion rate v/s shear stress. Flow induced shear stress corrosion model under the fluid dynamic loading of 0, 2.5, 5, 10, 20, 50, 70, and 100 dyn/cm^2) .

is assumed that for the shear stresses higher than 100 dyn/cm^2 the effect of FISS on CR will not be significant.

9.2.3 Surface morphology

Figure 9.5 and 9.6 show the surface morphology for each corroded surface with and without FISS exposure (i.e. static and dynamic conditions). In the static condition, without the influence of FISS, the pitting and localized corrosion were dominated in comparison to uniform corrosion.

In the dynamic condition, the uniform corrosion throughout the surface was dominant for FISS of 0, 2.5, 5, 10, 20 dyn/cm^2. Further increase in FISS leads to the dominance of pitting corrosion with uniform corrosion. At FISS of 50 dyn/cm^2 the increment in localized corrosion was observed. Whereas, at the FISS of 70 dyn/cm^2, unfirm and pitting corrosion was dominant. At the 100 dyn/cm^2 the greater localized corrosion was observed. In general, the static condition and the shear stress over 70 dyn/cm^2 propagated the localized corrosion. The FISS between 0 and 70 dyn/cm^2 which also replicates the FISS in the normal arteries, generates the uniform and pitting corrosion. However, the FISS over 70 dyn/cm^2 replicating the narrowed arteries due to plaque formation or stent implantation, generates localized corrosion and leads to the fast degradation of the stent material.

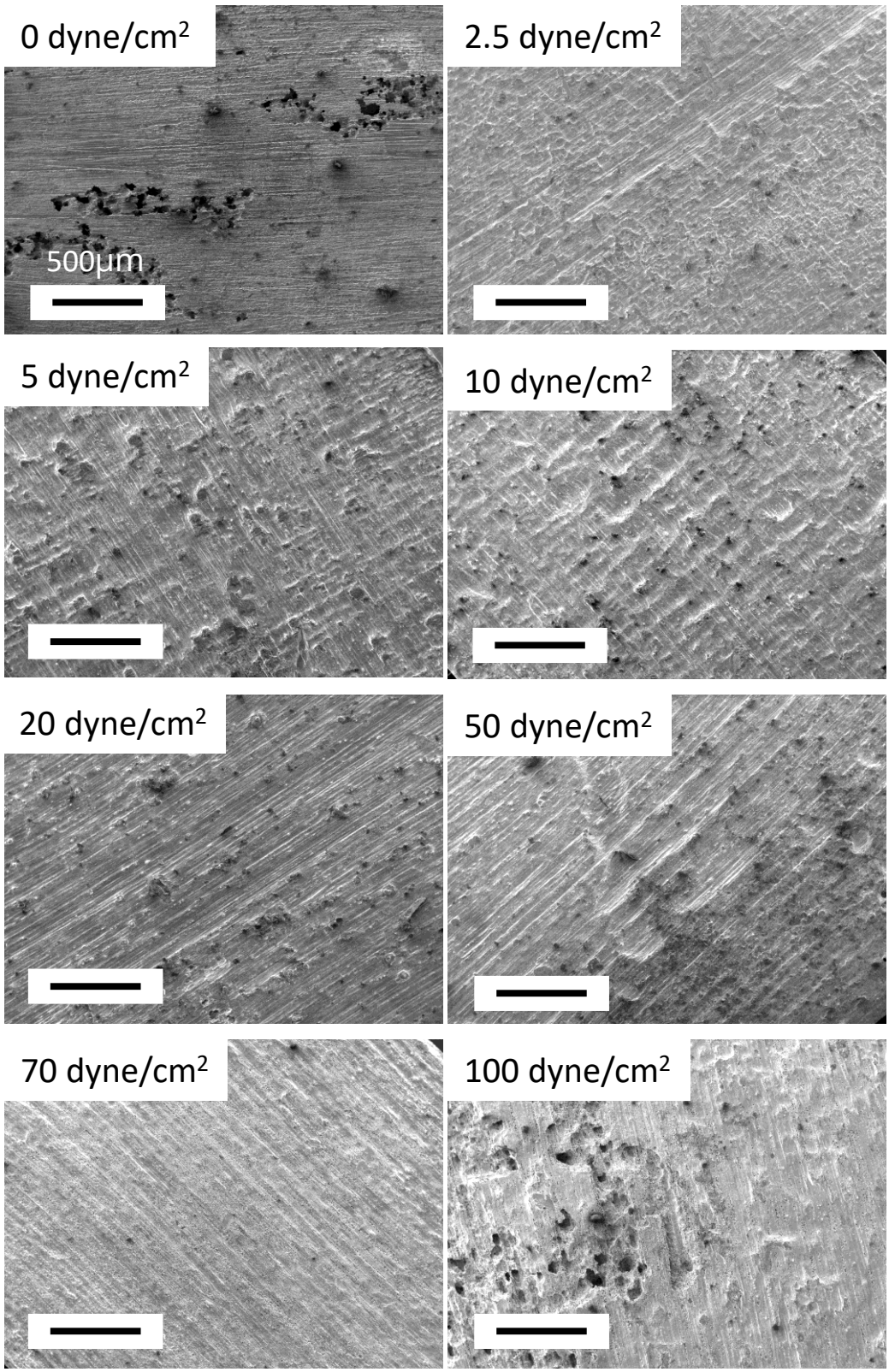

FIGURE 9.5: Surface morphology of AZ31 surface after exposure to FISS of (0, 2.5, 5, 10, 20, 50, 70, 100 dyn/cm^2) with scale bar 500μm.

The FISS values influence the corrosion type. It also influences the dominating corrosion type under various FISS ranges. Table 9.2 summarizes the types of

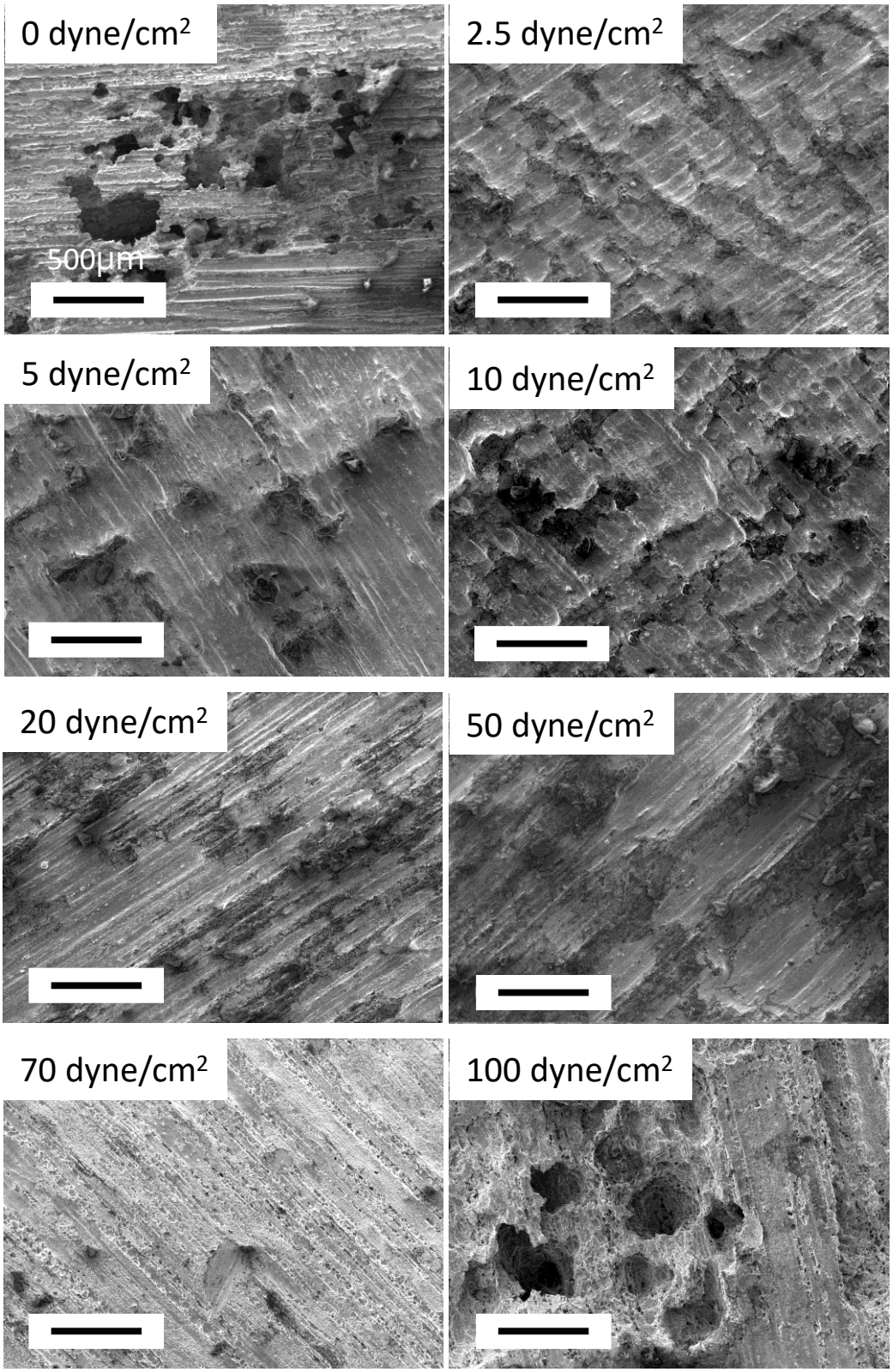

FIGURE 9.6: Surface morphology of AZ31 surface after exposure to FISS of (0, 2.5, 5, 10, 20, 50, 70, 100 dyn/cm^2)with scale bar 100μm.

corrosion at various FISSs presented in Figure 9.5 and 9.6. The dominating corrosion type is represented by **bold** text for the three different FISS ranges: FISS =

TABLE 9.2: Types of corrosion under various FISSs.

FISS value	Type of corrosion
FISS = 0 dye/cm^2	**Pitting** , uniform, localized
0 $<$ FISS $<$ 70 dye/cm^2	**Uniform**, pitting
FISS $<$ 70 dye/cm^2	Uniform, pitting, **localized**

0 dye/cm^2, 0 $<$ FISS $<$ 70 dye/cm^2, and FISS $<$ 70 dye/cm^2.

9.3 FISS corrosion mechanism

Considering the presence and absence of FISS, the corrosion rate can be classified into two types: i) Static corrosion rate (CR_S), and ii) Dynamic corrosion rate (CR_D). The corrosion rates calculated in the static environment without the influence of any fluid flow may be termed as static corrosion rates, whereas, the corrosion rates calculated in the fluid-dynamic experiments may be termed as dynamic corrosion rates. The value of static corrosion rate is highly influenced by the material properties and by the degradation medium and external factors such that temperature and pH. Similarly, the value of dynamic corrosion rates is mainly influenced by the flow velocity and shear stress including all factors influencing the static corrosion rate. Figure 9.7 illustrates the basic mechanism of FISS corrosion for biomedical materials. For any given environment keeping all parameters constant, the corrosion rate starts from CR_S where point A represents the max. CR_S for a given material. With the application of flowing fluid, the corrosion rate becomes CR_D from CR_S. In the beginning, the CR_S increases largely with the slight increase in FISS. However, this increases continues but slows down when the FISS is further increased. This region of the curve is called the unstable region due to varied increments and instability in corrosion rates at increasing FISS. After reaching point B, the CR_S moves to the stable region where the increase in FISS does not influence CR_D significantly.

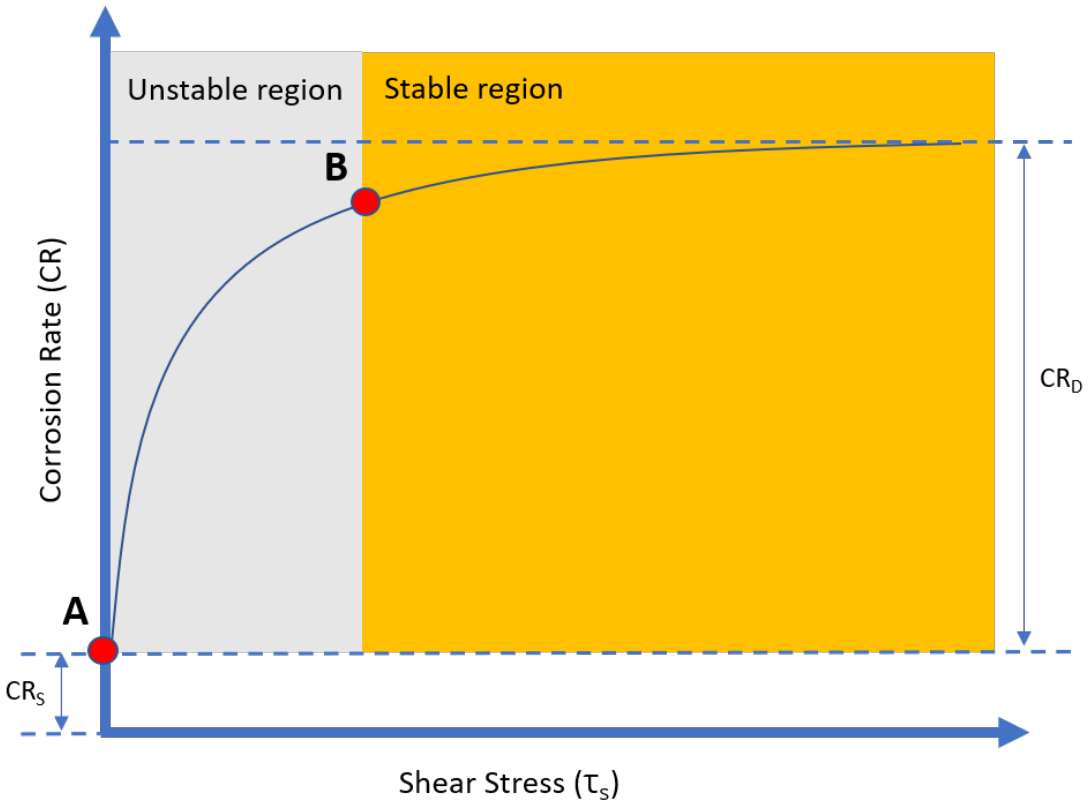

FIGURE 9.7: Flow induced shear stress corrosion mechanism illustration.

9.4 Conclusions

Within this Chapter, the flow induced shear stress corrosion model has been developed using AZ31 semi rod samples. The AZ31 samples were degraded at different FISS values using static and dynamic environment. The main findings are:

- Static and dynamic conditions influence the type of corrosion on biodegradable materials.
- Lower shear stresses cause the uniform and pitting corrosion with dominance to uniform corrosion.
- Shear stresses above the level of normal arteries replicating the arteries with plaque and stent implantation causes uniform, pitting, and localized corrosion. However, localized corrosion dominated the other two types.
- Localized corrosion enhances in static condition (i.e. FISS = 0 dyn/cm^2) and at the FISS above 70 dyn/cm^2 (max. FISS in normal arteries).

10 Summary and Outlook

Stents are the tiny tubular structures commonly used for the treatment of coronary artery disease. Upon implantation, the stent is supposed to provide the desired mechanical strength with an adequate corrosion resistance and the good biocompatibility. Generally, the stents can be permanent, temporary, and drug eluting. The materials used for the permanent stents are stainless steel (316L), cobalt–chromium (Co–Cr), platinum–iridium (Pt–Ir) alloys, tantalum (Ta), and nitinol (Ni–Ti). The permanent stents or bare metal stents (BMS) are the most corrosion resistant stents as compared to the temporary stents or biodegradable stents (BDS), but with various issues associated to them e.g., neointimal restenosis, late thrombosis formation, and limited biocompatibility.

To evaluate the degradation behavior of metallic stents, corrosion experiments are used. For the corrosion rate calculation with different methods—for example, static immersion test, fluid dynamic test, and electrochemical corrosion test—we need the exposed surface area of the sample. For the standard geometrical shape, it is simple but for the samples that have complex geometry, like stents, it is very complex. For this purpose, innovative approaches are required to determine the entire stent surface area.

The application of micro-CT for the determination of the entire stent surface area is presented. The reference volume used in the determination of surface area with the micro-CT was calculated by density formula.

However, micro-CT is a time-consuming and expensive method and is not a standard characterization method in most research labs. As an alternative non-destructive approach to estimate the surface area of stents, a novel mathematical model has been developed and validated with micro-CT data. This is the first ever model to calculate the ESSA. This could offer the possibility for a faster, reliable stent characterization. The equipment which is needed for the introduced mathematical model will be an SEM, and most labs have access to it.

By using the proposed model, corrosion tests on stents can be conducted easily. The exposed surface area of stents is inversely proportional to the corrosion rate. Based on the difference we got in ESSA calculation by the newly developed model and micro-CT, the corrosion rate calculated by using ESSA obtained from the model will be 12.34% ($\pm$ 0.46%), less than that ESSA obtained by micro-CT.

The proposed model was applied on Mg alloy samples and provided good results. However, surface area calculations of other stent samples including different materials and designs are necessary. The surface area calculations of the drug eluting stents (DES) and coated stents are of interest here.

A possible reason for the smaller surface area values from micro-CT could be that the visualization of the stent wires is influenced by X-ray beam hardening at the metal surface, which could result in an underexposed stent wire volume. Another possible reason is that the SOSA used in the calculation of ESSA is based on the mass of the sample. The study by Karoly et al. 2013 [219] discussed that the manual and automatic stent scanning methods to calculate SOSA are more accurate. The application of these methods may further reduce this difference.

A limitation of the developed model is the use of the average width of the upper surface. This is also very important and it highly depends on the number of lengths taken for getting an average. In the presented study, 200 measurements were undertaken. However, we observed that the result was similar for 100 measurements. In future studies, and with other stent designs, the number of measurements for the weighted average may be standardized.

In this work, the fluid-dynamic experimental setup is also introduced that mimics the physiological environment for the degradation of implant materials.The system is capable to monitor the important parameters during degradation tests such that pressure, temperature, pH, flow rate, and flow velocity. Another important addition is the ability to control the pH level during degradation test which is critical in the case of some implant materials e.g Mg and its alloys.

The setup can be used for both short- and long-term experiments to predict the degradation behavior of biodegradable and permanent implant structures. Especially successful studies have been performed on different stent structures consisting of biodegradable and non-biodegradable alloys. The setup is also capable to conduct accelerated degradation tests e.g. by increased temperature.

The degradation studies are supported by the application of various characterization techniques like SEM-EDX, FTIR, contact angle, TEM, AFM, Laser profilometry to name a few for analyzing the degradation-induced changes in implant volume and on its surface before and after the degradation test.

In each degradation test, degradation products are formed on the surface of the implant material and those particulates include in the fluid during the test. This phenomenon might affect the degradation of the material and would be important to filter out these particulates. Therefore, the particulate filtration mechanism would further enhance the applicability of the testing setup.

Mass loss measurements at different time intervals are also crucial to assess the degradation behavior of implant material. For the AZ31 samples (square-shaped), each sample was measured for all time points. However, for stents, it is still a complicated task to take stents out from the setup at each time point in a fluid dynamic experiment.

To take mass measurements on stents at different time points, the development of a custom-made vessel or a sample holder for stents needs to be designed.

In this research, the degradation studies of biostable and bioabsorbable stents were focused on. The degradation behavior of titanium oxynitride (TiO_XN_Y) coated stainless steel stents, and AZ31 (Mg-alloy) samples were studied. Resoloy (Mg-alloy) stents were also used for the development of the entire stent surface model.

TiO_XN_Y coatings are an ideal candidate to reduce the clinical issues associated with bare-metal stents. They showed significant resistance to aggressive biological medium providing a better biostable response based on surface morphology using SEM-EDX measurements, ICPMS results, mass variation, and corrosion rates after corrosion tests.

The ratio of O_2/N_2 influences the level of depositions and degradation products without influencing their chemical compositions. Moreover, O_2/N_2 also affects the corrosion properties as noticeable differences were observed for all coated samples.

Cleaning of TiO_XN_Y coated stent with water in an ultrasonic environment does not harm coatings. However, Cleaning with acetone, and isopropanol degrades the coating and that too without removing degradation products.

Degradation products on the sample surface highly depend on the ions present in the fluid. Artificial vessels may also induce some depositions If they are not capable to provide resistance against a chemically aggressive environment.

The optimum and best practice presented in this thesis to do a fluid dynamic experiment on TiO_XN_Y stents to get deposition free degradation is to use Puriflex tubing or a similar kind of artificial vessel, SBF without Ca^{++} and Mg^{++} ions, sample cleaning with distilled water in the ultrasonic bath.

Quantitative corrosion and degradation tests were performed on the entire stent surface (for the first time) instead of the upper surface or using simpler samples using the ESSA model. Based on corrosion results presented, stents with a higher oxygen ratio ensure higher stability in harsh environments as witnessed by their steady corrosion behavior.

In this work, the highest temperature used was 50°C with SCE. Higher temperatures can be applied using an alternate reference electrode e.g. reversible hydrogen electrode (RHE).

Further studies are needed to evaluate other feeding ratios and coating parameters and their effect on stent degradation behavior.

AZ31 is a widely used biodegradable magnesium alloy for research purposes. AZ31 samples anodized using the plasma electrolytic oxidation process were used for this study. It was found that the degradation properties of AZ31 can be influenced by varying anodization parameters.

It is reported that anodizing time and the drying protocol significantly affect the degradation properties of Mg alloy. Moreover, polymer coating on PEO treated AZ31 samples increased the hydrophilicity and reduces the corrosion rate. Polymer-coated samples had reduced MLRs and CRs among all samples.

Chromic acid cleaning is a standard cleaning method for Mg-alloys. Like cleaning effects of various chemicals on TiO_XN_Y, there was no significant effect of chromic acid cleaning was found on the sample surface.

However, all the anodized samples (except polymer coated) lost the oxide layer in the initial days of the corrosion experiment due to pressure exerted by the flowing fluid. Further research is needed to make the oxide layer more durable.

In the presented thesis, the flow induced shear stress corrosion model has been developed. The AZ31 semi rods were used in the fluid dynamic and static environment. It was observed, that FISS values and experimental conditions influence the type of corrosion on biodegradable materials. The dominance of corrosion type also shifts because of changes in FISS values.

In this thesis, the FISS values 0 - 100 dyn/cm^2 were used to develop the model. Higher FISS values can also be implemented to further validate the model. Moreover, the degradation tests with some other Mg- alloys and materials will further validate the model.

Publications

Peer reviewed publications

1. **Muhammad Saqib**, M. S. Draz, H. Kraśkiewicz, Ł. Wasyluk, O. Kuzmin, O. Duta, D. Ficai, R. Trusca, A. Ficai, V. F. Pichugin, E. Andronescu, J. Opitz, G. Cuniberti, N. Beshchasna, "Evaluation of in vitro biostability and corrosion behavior of titanium oxynitride coated stainless steel stents", IEEE Access, 2021.

2. S. Goreninskii, E. Bolbasov, N. Danilenko, A. Evtina, M. Buldakov, N. Cherdyntseva, **Muhammad Saqib**, N. Beshchasna, J. Opitz, V. Filimonov, S. Tverdokhlebov, "Hexafluoroisopropanol as a new solvent for fabrication of electrospun poly(ξ-caprolactone)/polyvinylpyrrolidone scaffolds for controllable drug release",J. Appl. Polym. Sci, 2021.

3. **Muhammad Saqib**, R. Bernhardt, M. Kästner, N. Beshchasna, G. Cuniberti, J. Opitz, "Determination of the entire stent surface area by a new analytical method", materials, 2020.

4. N. Beshchasna, **Muhammad Saqib**, H. Kraśkiewicz, Ł. Wasyluk, O Kuzmin, O. C. Duta, D. Ficai, Z. Ghizdăveţ, A. Ficai, Z. Sun, V. F. Pichugin, J. Opitz, E. Andronescu "Recent advances in manufacturing innovative stents", Pharmaceutics, 2020.

5. N. Beshchasna, A. Y. K. Ho, **Muhammad Saqib**, J. Opitz; H. Kraśkiewicz, Ł. Wasyluk, O. Kuzmin, O. Duta, D. Ficai, R. Trusca, A. Ficai, E. Andronescu, "Surface evaluation of titanium oxynitride coatings used for developing layered cardiovascular stents", Mat Sci Eng C, 2019.

6. **Muhammad Saqib**, R. Bernhardt, M. Kästner, N. Beshchasna, G. Cuniberti, J. Opitz, "Application of μCT for the determination of total surface area of stents", in Proc. IEEE International Conference on e-Health and Bioengineering (EHB) 2019, 21-23 November 2019, Iasi, Romania (IEEE Xplore).

Patents

1. Syeda Suha Tirmizi, Shariq Ramzan Ali Khoja, Muhammad Abdul Muqeet, Hafiz Imtiaz Ahmed, Saad Abdullah, **Muhammad Saqib** Eijaz Hussain, "Device and mechanism for facilitating non-invasive, non-piercing monitoring of blood glucose," U.S Patent: WO/2015/130332, Int. Appl. No.: PCT/US2014 /041788, IPC: A61B 5/1455, publication date: Sep 3, 2015.

2. Syeda Suha Tirmizi, Shariq Ramzan Ali Khoja, Muhammad Abdul Muqeet, Hafiz ImtiazAhmed, Saad Abdullah, **Muhammad Saqib** Eijaz Hussain, "Device and mechanism for facilitating non-invasive, non-piercing monitoring of blood hemoglobin," U.S Patent: WO/2015/130333, Int. Appl. No.: PCT/ US2014/041789, IPC: A61B 5/1455, publication date: Sep 3, 2015.

Selected conferences

1. **Muhammad Saqib**, R. Bernhardt, M. Kästner, N. Beshchasna, G. Cuniberti, J. Opitz, "Application of μCT for the determination of total surface area of stents", IEEE International Conference on e-Health and Bioengineering (EHB) 2019, 21-23 November 2019, Iasi, Romania. (Oral presentation)

2. **Muhammad Saqib**, M. S. Draz, H. Kraśkiewicz, Ł. Wasyluk, O. Kuzmin, O. Duta, D. Ficai, R. Trusca, A. Ficai, V. F. Pichugin, E. Andronescu, J. Opitz, G. Cuniberti, N. Beshchasna, "Effect of Titanium Oxynitride (TiO_XN_Y) coatings on corrosion behavior of stainless steel stents", 11th International Workshop on Engineering of Functional Interfaces (EnFi 2018), July 01-03, 2018 at Leucorea in Wittenberg/Germany. (Poster presentation)

3. O. Duta, D. Ficai, A. Ficai, E. Andronescu, N. Beshchasna, **Muhammad Saqib**, J. Opitz, H. Kraśkiewicz, Ł. Wasyluk, O. Kuzmin, V. F. Pichugin, "Titanium Oxynitride Coatings Deposited By Magnetron Sputtering For Improvement Of Cardiovascular Stent Design", In Proceedings of the World Congress on New Technologies 2018 (pp. ICNFA-112).

Curriculum Vitae

Education

Oct 2016 - 2022 (Planned)	Doctor of Engineering (Dr.-Ing) in Biomedical Engineering *Technical University of Dresden, Dresden, Germany*
Oct 2011 - Sep 2013	Master of Engineering (M.E.) in Electronics Engineering *Hamdard University, Karachi, Pakistan*
Jan 2005 - Dec 2008	Bachelor of Science (B.S.) in Biomedical Engineering *Sir Syed University of Engineering & Technology, Karachi, Pakistan*
2002 - 2004	Higher Secondary School Certificate (H.S.S.C.) *D.J. Sindh Govt. Science College, Karachi, Pakistan*
2000 - 2002	Secondary School Certificate (S.S.C.) *M.H. Grammar Secondary School , Karachi, Pakistan*

Work Experience

Oct 2016 - Present	Researcher *Department of Bio and nanotechnology, Fraunhofer IKTS, Dresden, Germany*
Jan 2011 - May 2016	Lecturer *College of Biomedical Engineering, Ziauddin University, Karachi, Pakistan*
Feb 2009 - Oct 2009	Visiting Lecturer *Indus University, Karachi, Pakistan*
Dec 2008 - Dec 2010	Biomedical Engineer *Hitech Instruments, Karachi, Pakistan*
Jun 2007 - Jul 2007	Internship Student *Liaquat National Hospital, Karachi, Pakistan*

A Simulated body fluids

Composition	Concentration (g/L)		
	SBF^{++}	SBF^{--}	$HBSS^{--}$
NaCl	6.800	6.800	8.000
KCl	0.400	0.400	0.400
$MgSO_4$	0.100	-	-
$CaCl_2$	0.200	-	-
$NaHCO_3$	2.200	2.200	0.350
Na_2HPO_4	0.130	0.130	0.009
NaH_2PO_4	0.030	0.030	-
KH_2PO_4	-	-	0.006
$C_6H_{12}O_6$ (Dextrose)	-	-	1.000
$C_{19}H_{14}O_5S$ (Phenol red)	-	-	0.002

FIGURE A.1: Composition of simulated body fluids.

B Protocol to use the fluid-dynamic system

B.1 Setting up experimental setup

- Fill the water in the circulating water bath up to the mentioned mark.
- Connect the tubing to the sensor in the sequence presented in the block diagram.
- 6mm outer diameter (OD) tubes for temperature, pressure, and flow sensor, 11 mm OD tubes for pH sensor hose, and main circulation loop through the pump and the fluid reservoir.
- Connect all sensors to the sensor integration box carefully in their respective positions.
- Connect the sensor integration box to the PC via USB cable.
- Assemble pH sensor into the pH sensor housing.
- Turn on the PC .
- Login to the PC with your login details provided by the IT department of Fraunhofer IKTS.
- Double click on the shortcut of the LabView program on the desktop with the filename Fluid-dynamic system.
- Switch on the circulating water bath 30 min before starting the experiment to attain 37°C. more time is needed if a higher temperature is required.
- The pump is programmed 11mm OD tubing, please adjust these settings if another tubing diameter is used. Check the pump settings in the manual.
- Turn the pump ON, the system is calibrated that the flow sensor will experience the fluid flow first. If this direction is opposite, then please change it by pressing the escape button in the pump.
- Turn ON the pH controller unit and login as Supervisor or Operator. In Supervisor mode settings can be manipulated. In Operator Mode, the only pH can be seen and controlled but settings can not be altered.
- If the pH sensor gives the value " -1.8" that means the pH sensor is not immersed in the fluid or there may be air bubbles. Remove the pH sensor and assemble it again.

- Fill the pH control solution i.e HCl in a conc. 0.001% V/V and connect it with the solenoid valve. Flush the solenoid valve manually by pressing the INCR button many times until all air bubbles are removed and the continuous buffering solution is flowing when the valve is open.

B.2 Using Software

- Select the serial port.
- Provide the file saving path with filename.
- Insert the cross sectional area (in cm^2) of the container where samples are placed. This should be correct, wrong values of cross section lead to the wrong values of flow velocity.
- Press the "RUN" button in the LabVIEW platform to start the experiment.
- Use Graph pallete located on top left of every graph to manipulate the view. Various options such as zoom in, zoom out, pan, to choose specific x and y axes region etc.
- By default, all the graph values are recorded in the given file address. User can manually be export any graph data at any instant by right clicking on the graph and selecting option "Export to Excel" or "copy to clipboard" and then pasting the values on desired place.
- Press the "Stop" button to end the experiment when the desired exposure time is reached.

Bibliography

1. Wilkins, E *et al.* European Cardiovascular Disease Statistics 2017 edition. *European Heart Network, Brussels.* ISSN: 1522-9645. arXiv: 978-2-9537898-1-2 (2017).
2. Andre, D. *Coronary artery disease in elderly: Prevention and natural remedies* https://www.belmarrahealth.com/coronary-artery-disease-elderly-prevention-natural-remedies/. (Accessed on 07/07/2021). 2016.
3. Neale, T. *New-Generation DES Better Than Older Stents Over 10 Years, Regardless of Polymer Type | tctmd.com* https://www.tctmd.com/news/new-generation-des-better-older-stents-over-10-years-regardless-polymer-type. (Accessed on 07/07/2021). 2018.
4. DeSaix, P. *et al.* Anatomy & Physiology: OpenStax (2018).
5. Medicine, J. H. *Anatomy and Function of the Coronary Arteries | Johns Hopkins Medicine* https://www.hopkinsmedicine.org/health/conditions-and-diseases/anatomy-and-function-of-the-coronary-arteries (2020).
6. Wolverine. *The Effect Of Sugar On Arteries | Roar of Wolverine* http://roarofwolverine.com/archives/1377 (2020).
7. *Over 2 Million Stents Implanted per Year in the U.S. - iData Research* https://idataresearch.com/stents-implanted-per-year-in-the-u-s/. (Accessed on 07/07/2021). 2021.
8. Malek, A. M., Alper, S. L. & Izumo, S. *Hemodynamic Shear Stress and Its Role in Atherosclerosis* tech. rep. (). www.jama.com.
9. Galvin, E., Macdonald, B. & Lally, C. *Characterisation of the performance of an absorbable magnesium stent by experimental and numerical analysis* tech. rep. (2014).
10. Holzapfel, G. A. & Ogden, R. W. *Biomechanical relevance of the microstructure in artery walls with a focus on passive and active components* 2018. www.ajpheart.org.
11. Serruys, P. W. *et al.* Percutaneous Coronary Intervention versus Coronary-Artery Bypass Grafting for Severe Coronary Artery Disease. en. *N. Engl. J. Med* **360,** 2605–2615 (2009).
12. Schmidt, T. & Abbott, J. Coronary Stents: History, Design, and Construction. en. *J. Clin. Med* **7,** 126. https://doi.org/10.3390/jcm7060126. (2018).
13. Silvain, J., Cayla, G., Collet, J.-P., Montalescot, G. & Fargeot, C. Coronary Stents: 30 Years of Medical Progress. en. *Medecine/Sciences.* https://doi.org/10.1051/medsci/20143003019. (2014).
14. MacNeill, B., Jang, I. & Wong, P. en. in *Clinical, Interventional and Investigational Thrombocardiology* 453–472 (CRC Press, 2005). https://doi.org/10.5005/jp/books/12559_39..

15. Mani, G., Feldman, M., Patel, D. & Agrawal, C. Coronary stents: A materials perspective. en. *Biomaterials* **28,** 1689–1710 (2007).
16. Zhu, Y. *et al.* The current status of biodegradable stent to treat benign luminal disease. en. *Mater. Today* **20,** 516–529 (2017).
17. Yoon, N. *et al.* Stent technology in ischemic stroke. nl. *Neurosurg Focus* **42,** 11 (2017).
18. Khan, W., Farah, S. & Domb, A. Drug eluting stents: Developments and current status. en. *J. Control. Release* **161,** 703–712 (2012).
19. Camici, G. What is an optimal stent? Biological requirements of drug eluting stents. en. *Cardiovasc Med* **11,** 2–25 (2008).
20. Wu, T. & McCarthy, S. en. in *InTech* (ed Chaikovsky, I.) 197–224 (Rijeka, Croatia, 2012).
21. Koo, Y., Tiasha, T., Shanov, V. & Yun, Y. Expandable Mg-based Helical Stent Assessment using Static, Dynamic, and Porcine Ex Vivo Models. en. *Sci Rep.-Uk* **7,** 1–10 (2017).
22. Roguin, A. Stent: The man and word behind the coronary metal prosthesis. en. *Circulation: Cardiovascular Interventions* (2011).
23. Kesselheim, A., Xu, S. & Avorn, J. Clinicians' contributions to the development of coronary artery stents: A qualitative study of transformative device innovation. it. *PLoS One* (2014).
24. Beshchasna, N. *et al.* Recent advances in manufacturing innovative stents. *Pharmaceutics* **12.** ISSN: 19994923 (2020).
25. Kommineni, N., Saka, R., Khan, W. & Domb, A. Non-polymer drug-eluting coronary stents. en. *Drug Deliv. Transl. Res* **8,** 903–917 (2018).
26. Vo, T. *et al.* Modelling drug release from polymer-free coronary stents with microporous surfaces. en. *Int. J. Pharm* **544,** 392–401 (2018).
27. Hossainy, S. *et al.* Primer coatings for stents with oxide, anionic, or hydroxyl surface moieties. en. *U.S. Patent* **9,101,689 B2** (Aug. 11, 2015).
28. Wise, S., Waterhouse, A., Kondyurin, A., Bilek, M. & Weiss, A. Plasma-based biofunctionalization of vascular implants. en. *Nanomed. -Uk* **7,** 1907–1916 (2012).
29. Popov, B. N. *Corrosion engineering: principles and solved problems* (Elsevier, 2015).
30. Beshchasna, N. *et al.* Surface evaluation of titanium oxynitride coatings used for developing layered cardiovascular stents. en. *Mat. Sci. Eng. C-Mater* **99.** CrossRef, 405–416 (2019).
31. Yang, P. *et al.* Bloodcompatibility improvement of titanium oxide film modified by phosphorus ion implantation. en. *Nucl Instrum Meth. B* **242.** CrossRef, 15–17 (2006).
32. Pichugin, V. *et al.* In-vitro Dissolution and Structural and Electrokinetic Characteristics of Titanium-Oxynitride Coatings Formed via Reactive Magnetron Sputtering. en. *J. Surf. Invest. X-RaySynchroton Neutron Tech* **10.** CrossRef, 282–291 (2016).
33. Pustovalova, A., Pichugin, V., Ivanova, N. & Bruns, M. Structural features of N-containing titanium dioxide thin films deposited by magnetron sputtering. en. *Thin. Solid. Film* **627.** CrossRef, 9–16 (2017).

34. Lehtinen, T., Airaksinen, K., Ylitalo, A. & Karjalainen, P. Stent strut coverage of titanium-nitride-oxide coated stent compared to paclitaxel-eluting stent in acute myocardial infarction: TITAX-OCT study. en. *Int. J. Cardiovas. Imag* **28.** CrossRef, 1859–1866 (2012).
35. Karjalainen, P. *et al.* Titanium-nitride-oxide coated stents versus paclitaxel-eluting stents in acute myocardial infarction: A 12-months follow-up report from the TITAX AMI trial. en. *Eurointervention* **4.** CrossRef, 234–241 (2008).
36. Karjalainen, P., Annala, A., Ylitalo, A. & Airaksinen, K. Long-term clinical outcome with titanium-nitride-oxide-coated stents, paclitaxel eluting stents and bare-metal stents for coronary revascularization in an unselected population. en. *Eur. Heart J* **29,** 456 (2008).
37. Karjalainen, P. *et al.* Two-year follow-up after percutaneous coronary intervention with titanium-nitride-oxide-coated stents versus paclitaxel-eluting stents in acute myocardial infarction. en. *Ann. Med* **41.** CrossRef, 599–607 (2009).
38. Karjalainen, P., Annala, A., Ylitalo, A., Vahlberg, T. & Airaksinen, K. Long-term clinical outcome with titanium-nitride-oxide-coated stents and paclitaxel-eluting stents for coronary revascularization in an unselected population. en. *Int. J. Cardiol* **144.** CrossRef, 42–46 (2010).
39. Huang, N. *et al.* Hemocompatibility of titanium oxide films. en. *Biomaterials* **24.** CrossRef, 2177–2187 (2003).
40. Zhai, Z., Zou, K., Feng, W. & Wang, Q. Experimental Study on Nitrogen-Doped Nano-Scale TiO2 Prepared by Microwave-Assisted Process at Low Temperature. it. *Mod. Appl. Sci* **4,** 95–100 (2010).
41. Erne, P., Schier, M. & Resink, T. The road to bioabsorbable stents: Reaching clinical reality? Cardiovasc. en. *Inter. Rad* **29.** CrossRef, 11–16 (2006).
42. Garg, S. & Serruys, P. W. Coronary stents: Looking forward. *Journal of the American College of Cardiology* **56,** S43–S78. ISSN: 07351097. http://dx.doi.org/10.1016/j.jacc.2010.06.008 (2010).
43. Ho, M. *et al.* The Development of Coronary Artery Stents: From Bare-Metal to Bio-Resorbable Types. en. *Met.-Basel* **6.** CrossRef, 168 (2016).
44. Boland, E., Shine, R., Kelly, N., Sweeney, C. & McHugh, P. A Review of Material Degradation Modelling for the Analysis and Design of Bioabsorbable Stents. en. *Ann. Biomed. Eng* **44.** CrossRef, 341–356 (2016).
45. Mishra, S. Structural and Design Evolution of Bio-resorbable Scaffolds: The Journey so Far. en. *Curr. Pharm. Des* **24.** CrossRef, 402–413 (2018).
46. Hytonen, J., Taavitsainen, J., Tarvainen, S. & Yla-Herttuala, S. Biodegradable coronary scaffolds: Their future and clinical and technological challenges. en. *Cardiovasc. Res* **114.** CrossRef, 1063–1072 (2018).
47. Charpentier, E., Barna, A., Guillevin, L. & Juliard, J. Fully bioresorbable drug-eluting coronary scaffolds: A review. en. *Arch. Cardiovasc Dis* **108,** 385–397 (2015).
48. Peuster, M. *et al.* A novel approach to temporary stenting: Degradable cardiovascular stents produced from corrodible metal-results 6–18 months after implantation into New Zealand white rabbits. en. *Heart* **86,** 563–569 (2001).

49. Heublein, B. *et al.* Biocorrosion of magnesium alloys: A new principle in cardiovascular implant technology? es. *Heart* **89,** 651–656 (2003).
50. Zhu, S. *et al.* Biocompatibility of pure iron: In vitro assessment of degradation kinetics and cytotoxicity on endothelial cells. en. *Mat. Sci. Eng. C* **29,** 1589–1592 (2009).
51. Gu, X., Zheng, Y., Cheng, Y., Zhong, S. & Xi, T. In vitro corrosion and biocompatibility of binary magnesium alloys. en. *Biomaterials* **30,** 484–498 (2009).
52. Bowen, P. *et al.* Biodegradable Metals for Cardiovascular Stents: From Clinical Concerns to Recent Zn-Alloys. en. *Adv. Healthc Mater* **5.** CrossRef, 1121–1140 (2016).
53. Lyon, P. *The Benefits of Magnesium Alloy for Medical Implants - Medical Design Briefs* https://www.medicaldesignbriefs.com/component/content/article/mdb/features/articles/27329 (2020).
54. Riaz, U., Shabib, I. & Haider, W. The current trends of Mg alloys in biomedical applications—A review. *Journal of Biomedical Materials Research Part B: Applied Biomaterials* **107,** 1970–1996 (2019).
55. Ghali, E. *Performance, and Testing; Wiley* en. New Jersey, NJ, USA, 2010.
56. Cao, N. *et al.* In Vitro Corrosion Properties of Mg Matrix In Situ Composites Fabricated by Spark Plasma Sintering. en. *Met. –Basel* **7.** CrossRef, 358 (2017).
57. Lewis, G. Reduction in the Corrosion Rate of Magnesium and Magnesium Alloy Specimens and Implications for Plain Fully Bioresorbable Coronary Artery Stents: A Review. en. *J. Eng. Technol* **4.** CrossRef, 572–597 (2016).
58. Patil, A. *et al.* Anticorrosive Self-Assembled Hybrid Alkylsilane Coatings for Resorbable Magnesium Metal Devices. en. *Acs Biomater Sci. Eng* **3.** CrossRef, 518–529 (2017).
59. Campos, C. *et al.* Bioresorbable Drug-Eluting Magnesium-Alloy Scaffold for Treatment of Coronary Artery Disease. en. *Int. J. Mol. Sci* **14.** CrossRef, 24492–24500 (2013).
60. Fang, Z. *et al.* A DFT study of the adsorption of short peptides on Mg and Mg-based alloy surfaces. en. *Phys. Chem. Chem. Phys* **20.** CrossRef, 3602–3607 (2018).
61. Liu, L. *et al.* Biodegradability and platelets adhesion assessment of magnesium-based alloys using a microfluidic system. *PLoS ONE.* ISSN: 19326203 (2017).
62. Torne, K., Ornberg, A. & Weissenrieder, J. Influence of strain on the corrosion of magnesium alloys and zinc in physiological environments. en. *Acta Biomater* **48.** CrossRef, 541–550 (2017).
63. Liu, J., Wang, P., Chu, C. & Xi, T. Anovel biodegradable andbiologically functional arginine-based poly(ester urea urethane) coating for Mg-Zn-Y-Nd alloy: Enhancement in corrosion resistance and biocompatibility. en. *J. Mater. Chem. B* **5.** CrossRef, 1787–1802 (2017).
64. Chen, H. & Kassab, G. S. Microstructure-based biomechanics of coronary arteries in health and disease. *Journal of Biomechanics* **49,** 2548–2559. ISSN: 18732380. http://dx.doi.org/10.1016/j.jbiomech.2016.03.023 (2016).

65. Mueller, P., May, T., Perz, A., Hauser, H. & Peuster, M. Control of smooth muscle cell proliferation by ferrous iron. en. *Biomaterials* **27,** 2193–2200 (2006).

66. Peuster, M. *et al.* Long-term biocompatibility of a corrodible peripheral iron stent in the porcine descending aorta. en. *Biomaterials* **27,** 4955–4962 (2006).

67. Jurgeleit, T., Quandt, E. & Zamponi, C. Magnetron Sputtering as a Fabrication Method for a Biodegradable Fe32Mn Alloy. en. *Materials* **10,** 1196 (2017).

68. Bowen, P., Drelich, J. & Goldman, J. Zinc Exhibits Ideal Physiological Corrosion Behavior for Bioabsorbable Stents. en. *Adv. Mater* **25.** CrossRef, 2577–2582 (2013).

69. Werkhoven, R., Sillekens, W. & Lieshout, J. Processing Aspects of Magnesium Alloy Stent Tube. fr. *Magnes. Technol,* 419–424 (2011).

70. Jin, H. *et al.* Novel high-strength, low-alloys Zn-Mg (< 0.1 wttheir arterial biodegradation. en. *Mater. Sci. Eng. C-Mater. Biol. Appl* **84,** 67–79 (2018).

71. Jarzebska, A. *et al.* A new approach to plastic deformation of biodegradable zinc alloy with magnesium and its effect on microstructure and mechanical properties. en. *Mater. Lett* **211.** CrossRef, 58–61 (2018).

72. Bowen, P. *et al.* Evaluation of wrought Zn-Al alloys (1, 3, and 5 wt through mechanical and in vivo testing for stent applications. en. *J. Biomed. Mater. Res. Part. B-Appl. Biomater* **106.** CrossRef, 245–258 (2018).

73. Asgari, M. *et al. Biodegradable Metallic Wires in Dental and Orthopedic Applications: A Review. Met* en. CrossRef. Basel, 2018.

74. Zhao, S. *et al.* Structural Characteristics and In Vitro Biodegradation of a Novel Zn-Li Alloy Prepared by Induction Melting and Hot Rolling. en. *Met. Mater. Trans. A* **48A.** CrossRef, 1204–1215 (2017).

75. Shomali, A., Guillory, R., Seguin, D., Goldman, J. & Drelich, J. Effect of PLLA coating on corrosion and biocompatibility of zinc in vascular environment. en. *Surf. Innov* **5.** CrossRef, 211–220 (2017).

76. Drelich, A., Zhao, S., Guillory, R., Drelich, J. & Goldman, J. Long-term surveillance of zinc implant in murine artery: Surprisingly steady biocorrosion rate. en. *Acta Biomater* **58.** CrossRef, 539–549 (2017).

77. Yang, H. *et al.* Evolution of the degradation mechanism of pure zinc stent in the one-year study of rabbit abdominal aorta model. en. *Biomaterials* **145.** CrossRef, 92–105 (2017).

78. Levy, G., Goldman, J. & Aghion, E. *The Prospects of Zinc as a Structural Material for Biodegradable Implants-A Review Paper. Met* en. CrossRef. Basel, 2017.

79. Yue, R. *et al.* Microstructure, mechanical properties and in vitro degradation behavior of novel Zn-Cu-Fe alloys. en. *Mater. Charact* **134.** CrossRef, 114–122 (2017).

80. Shukla, S., Shukla, S., Govender, P. & Giri, N. Biodegradable polymeric nanostructures in therapeutic applications: Opportunities and challenges. en. *Rsc Adv* **6.** CrossRef, 94325–94351 (2016).

81. Tamai, H. *et al.* A biodegradable poly-l-lactic acid coronary stent in the porcine coronary artery. en. *J. Interv Cardiol* **12.** CrossRef, 443–449 (1999).

82. Tamai, H. *et al.* Initial and 6-month results of biodegradable poly-l-lactic acid coronary stents in humans. en. *Circulation* **102,** 399–404 (2000).

83. Ong, A. & Serruys, P. Technology insight: An overview of research in drug-eluting stents. nl. *Nat. Clin. Pr. Card* **2.** CrossRef, 647–658 (2005).
84. Commandeur, S., Van Beusekom, H. & Van Der Giessen, W. Polymers, drug release, and drug-eluting stents. nl. *J. Interv. Cardiol* **19.** CrossRef, 500–506 (2006).
85. Neamtu, I. *et al.* Current Concepts on Cardiovascular Stent Devices. en. *Mini-Rev. Med. Chem* **14,** 505–536 (2014).
86. Strohbach, A. & Busch, R. Polymers for Cardiovascular Stent Coatings. en. *Int. J. Polym. Sci,* 11 (2015).
87. Hermawan, H., Dube, D. & Mantovani, D. Degradable metallic biomaterials: Design and development of Fe-Mn alloys for stents. en. *J. Biomed. Mater. Res. A* **93A.** CrossRef, 1–11 (2010).
88. Waksman, R. *et al.* Short-term effects of biocorrodible iron stents in porcine coronary arteries. en. *J. Interv. Cardiol* **21.** CrossRef, 15–20 (2008).
89. Fischman, D. *et al.* A Randomized Comparison of Coronary-Stent Placement and Balloon Angioplasty in the Treatment of Coronary-Artery Disease. N. en. *Engl J. Med* **331,** 496–501 (1994).
90. Lyakishev, A. A polymer-based, paclitaxel-eluting stent in patients with coronary artery disease. Results of TAXUS IV. en. *Kardiologiya* **44,** 77 (2004).
91. Stone, G. *et al.* A polymer-based, paclitaxel-eluting stent in patients with coronary artery disease. en. *N. Engl. J. Med* **350.** CrossRef, 221–231 (2004).
92. Puranik, A., Dawson, E. & Peppas, N. Recent advances in drug eluting stents. en. *Int. J. Pharm* **441.** CrossRef, 665–679 (2013).
93. Zhao, J. *et al.* Drug loaded nanoparticle coating on totally bioresorbable PLLA stents to prevent in-stent restenosis. en. *J. Biomed. Mater. Res. B* **106.** CrossRef, 88–95 (2018).
94. Wykrzykowska, J. *et al.* Bioresorbable Scaffolds versus Metallic Stents in Routine PCI. en. *New Engl. J. Med* **376.** CrossRef, 2319–2328 (2017).
95. Sorrentino, S. *et al.* Everolimus-Eluting Bioresorbable Scaffolds Versus Everolimus-Eluting Metallic Stents. de. *J. Am. Coll Cardiol* **69.** CrossRef, 3055–3066 (2017).
96. Feng, G. *et al.* Long Term Comparison between Novel Fully Bioresorbable Scaffolds and Drug-Eluting Stents: A Twenty-Four-Month Study in Porcine Coronary Arteries. en. *J. Am. Coll Cardiol* **68.** CrossRef, 57– 58 (2016).
97. Gastaldi, D. *et al.* Continuum damage model for bioresorbable magnesium alloy devices-Application to coronary stents. en. *J. Mech Behav. Biomed* **4.** CrossRef, 352–365 (2011).
98. Ernst, A. & Bulum, J. New generations of drug-eluting stents-A brief review. en. *Emj Int. Cardiol* **1,** 100–106 (2014).
99. Ormiston, J. & Serruys, P. Bioabsorbable coronary stents. en. *Circ. Cardiovasc. Interv* **2.** CrossRef, 255–260 (2009).
100. Waksman, R. Biodegradable stents: They do their job and disappear. en. *J. Invasive. Cardiol* **18,** 70–74 (2006).
101. Finn, A. *et al.* Pathological correlates of late drug-eluting stent thrombosis-Strut coverage as a marker of endothelialization. en. *Circulation* **115.** CrossRef, 2435–2441 (2007).

102. Hoffmann, R. *et al.* Patterns and mechanisms of in-stent restenosis-A serial intravascular ultrasound study. en. *Circulation* **94.** CrossRef, 1247–1254 (1996).

103. Togni, M. *et al.* Sirolimus-eluting stents associated with paradoxic coronary vasoconstriction. en. *J. Am. Coll. Cardiol* **46.** CrossRef, 231–236 (2005).

104. Barlis, P., Tanigawa, J. & Di Mario, C. Coronary bioabsorbable magnesium stent: 15-month intravascular ultrasound and optical coherence tomography findings. en. *Eur. Heart J* **28.** CrossRef, 2319 (2007).

105. Garg, S. & Serruys, P. Biodegradable stents and non-biodegradable stents. no. *Minerva. Cardioangiol* **57,** 537–565 (2009).

106. Serruys, P., Garcia-Garcia, H. & Onuma, Y. From metallic cages to transient bioresorbable scaffolds: Change in paradigm of coronary revascularization in the upcoming decade? Eur. en. *Heart J* **33.** CrossRef, 16–25 (2012).

107. Waksman, R. *et al.* Safety and efficacy of bioabsorbable magnesium alloy stents in porcine coronary arteries. en. *Catheter. Cardio. Inte* **68.** CrossRef, 607–617 (2006).

108. Waksman, R. Current state of the absorbable metallic (magnesium) stent. en. *EuroIntervention* **5.** CrossRef, 94– 97 (2009).

109. Waksman, R. *et al.* Early- and Long-Term Intravascular Ultrasound and Angiographic Findings After Bioabsorbable Magnesium Stent Implantation in Human Coronary Arteries. en. *Jacc-Cardiovasc Inte* **2.** CrossRef, 312–320 (2009).

110. Lan, Z. *et al.* Novel Biodegradable Drug-Eluting Stent Composed of Poly-L-Lactic Acid and Amorphous Calcium Phosphate Nanoparticles Demonstrates Improved Structural and Functional Performance for Coronary Artery Disease. en. *J. Biomed. Nanotechnol* **10.** CrossRef, 1194–1204 (2014).

111. Carlquist, J. *et al.* Cardiovascular risk among patients on clopidogrel anti-platelet therapy after placement of drug-eluting stents is modified by genetic variants in both the CYP2C19 and ABCB1 genes. en. *Thromb. Haemost* **109,** 744–754 (2013).

112. Egashira, K. *et al.* Local delivery of anti-monocyte chemoattractant protein-1 by gene-eluting Stents attenuates in-stent stenosis in rabbits and monkeys. en. *Arter. Throm. Vas* **27.** CrossRef, 2563–2568 (2007).

113. Goh, D. *et al.* Nanotechnology-Based Gene-Eluting Stents. nl. *Mol. Pharm* **10.** CrossRef, 1279–1298 (2013).

114. Ohtani, K. *et al.* Anti-monocyte chemoattractant protein-1 strategy via local gene transfer with gene-eluting stents inhibits in-stent restenosis in hypercholesterolemic rabbits and monkeys. en. *Circulation* **112,** 715 (2005).

115. Sharif, F. *et al.* Gene-eluting stents: Adenovirus-mediated delivery of eNOS to the blood vessel wall accelerates re-endothelialization and inhibits restenosis. en. *Mol. Ther* **16.** CrossRef, 1674–1680 (2008).

116. Sharif, F. *et al.* Gene-eluting stents: Non-viral, liposome-based gene delivery of eNOS to the blood vessel wall in vivo results in enhanced endothelialization but does not reduce restenosis in a hypercholesterolemic model. en. *Gene Ther* **19.** CrossRef, 321–328 (2012).

117. Sharif, F. *et al.* Gene-eluting stents: Comparison of adenoviral and adeno-associated viral gene delivery to the blood vessel wall in vivo. en. *Hum. Gene Ther* **17.** CrossRef, 741–750 (2006).

118. Walter, D. *et al.* Local gene transfer of phVEGF-2 plasmid by gene-eluting stents-An alternative strategy for inhibition of restenosis. en. *Circulation* **110.** CrossRef, 36–45 (2004).

119. Yin, R., Yang, D. & Wu, J. Nanoparticle Drug-and Gene-eluting Stents for the Prevention and Treatment of Coronary Restenosis. en. *Theranostics* **4.** CrossRef, 175–200 (2014).

120. Lekshmi, K., Che, H.-L., Choan, C.-S. & Park, I.-K. Drug- and gene-eluting stents for preventing coronary restenosis. nl. *Chonnam. Med. J* **53.** CrossRef, 14–27 (2017).

121. Luderer, F. *et al.* Nanoparticles as Drug Delivery System for the Prevention of In-Stent Restenosis in Coronary Stent Application. en. *J. Biomater. Appl* **25.** CrossRef, 851–875 (2011).

122. Stolnik, S. *et al.* The Preparation of Sub-200nmBiodegradable Colloidal Particles from Poly(Beta-Malic Acid-Co-Benzyl Malate) Copolymers and Their Surface Modification with Poloxamer and Poloxamine Surfactants. en. *J. Control. Release* **30.** CrossRef, 57–67 (1994).

123. Baquet, M., Jochheim, D. & Mehilli, J. Polymer-free drug-eluting stents for coronary artery disease. en. *J. Interv. Cardiol* **31.** CrossRef, 330–337 (2018).

124. Hausleiter, J. *et al.* FASTTRACK-Prevention of restenosis by a novel drug-eluting stent system with a dose-adjustable, polymerfree, on-site stent coating. en. *Eur. Heart J* **26.** CrossRef, 1475–1481 (2005).

125. Gershlick, A. *et al.* Inhibition of restenosis with a paclitaxel-eluting, polymer-free coronary stent-The European evaLUation of pacliTaxel Eluting Stent (ELUTES) trial. en. *Circulation* **109.** CrossRef, 487–493 (2004).

126. Chen, W., Habraken, T., Hennink, W. & Kok, R. Polymer-Free Drug-Eluting Stents: An Overview of Coating Strategies and Comparison with Polymer-Coated Drug-Eluting Stents. en. *Bioconjugate Chem* **26.** CrossRef, 1277–1288 (2015).

127. Song, D., Hsu, L. & Au, J. Binding of taxol to plastic and glass containers and protein under in vitro conditions. en. *J. Pharm. Sci* **85,** 29–31 (1996).

128. Farah, S., Khan, W. & Domb, A. Crystalline coating of rapamycin onto a stent: Process development and characterization. en. *Int. J. Pharm* **445.** CrossRef, 20–28 (2013).

129. Wu, S. *et al.* ro. *U.S. Patent 10/911,968,* (2005).

130. Mikhalovska, L. *et al.* Inorganic coatings for cardiovascular stents: In vitro and in vivo studies. en. *J. Biomed. Mater. Res. B* **96B.** CrossRef, 333–341 (2011).

131. Stevenson, C., Santini, J. & Langer, R. Reservoir-based drug delivery systems utilizing microtechnology. nl. *Adv. Drug Deliv. Rev* **64.** CrossRef, 1590–1602 (2012).

132. Bartorelli, A. *et al.* Synergy of passive coating and targeted drug delivery. en. *J. Interv. Cardiol* **16.** CrossRef, 499–505 (2003).

133. Kollum, M. *et al.* Particle debris from a nanoporous stent coating obscures potential antiproliferative effects of tacrolimus-eluting stents in a porcine model of restenosis. en. *Catheter. Cardio. Inte* **64.** CrossRef, 85–90 (2005).

134. Martin, F. *et al.* Tailoring width of microfabricated nanochannels to solute size can be used to control diffusion kinetics. en. *J. Control. Release* **102.** CrossRef, 123, (2005).

135. Ruan, C., Bayer, T., Meth, S. & Sukenik, C. Creation and characterization of n-alkylthiol and n-alkylamine self-assembled monolayers on 316L stainless steel. en. *Thin Solid Film* **419.** CrossRef, 95–104 (2002).

136. Acharya, G. & Park, K. Mechanisms of controlled drug release from drug-eluting stents. nl. *Adv. Drug Deliv. Rev* **58.** CrossRef, 387–401 (2006).

137. Perrin, J. Sustained and controlled release drug delivery systems. en. *J. Pharm. Sci* **69.** CrossRef, 485 (1980).

138. Allen, L. & Ansel, H. *Ansel's Pharmaceutical Dosage forms and Drug Delivery Systems* en (Lippincott Williams & Wilkins, Baltimore, MD, USA, 2013).

139. Chien, Y. *Novel Drug Delivery Systems* 2nd. en (CRC Press, Boca Raton, FL, USA, 1991).

140. Saltzman, W. *Drug Delivery: Engineering Principles for Drug Therapy* en (Oxford University Press, Oxford, UK, 2001).

141. Rathbone, M., Hadgraft, J. & Roberts, M. *Modified-release Drug Delivery Technology* nl (Marcel Dekker, NewYork, NY, USA, 2003).

142. Park, K. *Controlled drug delivery: challenges and strategies* (Amer Chemical Society, 1997).

143. Leon, M., Abizaid, A. & Moses, J. *The CYPHERTM stent: A New Gold Standard in the Treatment of Coronary Artery Disease* en (The Cardiovascular Research Foundation, New York, NY, USA, 2003).

144. Russell, M. *Comprehensive Review ofthe Polymer-Based Taxol Release Kinetics and Animal Data: INSIGHTS into Efficacy and Toxicity* en. Miami, FL, USA, 2002.

145. Heldman, A. *et al.* Paclitaxel stent coating inhibits neointimal hyperplasia at 4 weeks in a porcine model of coronary restenosis. en. *Circulation* **103.** CrossRef, 2289–2295 (2001).

146. Lansky, A. *et al.* Non-polymer-based paclitaxel-coated coronary stents for the treatment of patients with de novo coronary lesions-Angiographic follow-up of the DELIVER clinical trial. en. *Circulation* **109.** CrossRef, 1948–1954 (2004).

147. Farb, A. *et al.* Pathological analysis of local delivery of paclitaxel via a polymer-coated stent. en. *Circulation* **104.** CrossRef, 473–479 (2001).

148. Finkelstein, A. *et al.* Local drug delivery via a coronary stent with programmable release pharmacokinetics. en. *Circulation* **107.** CrossRef, 777–784 (2003).

149. Whelan, D. *et al.* Biocompatibility of phosphorylcholine coated stents in normal porcine coronary arteries. en. *Heart* **83.** CrossRef, 338–345 (2000).

150. Hara, H., Nakamura, M., Palmaz, J. & Schwartz, R. Role of stent design and coatings on restenosis and thrombosis. nl. *Adv. Drug Deliv. Rev* **58.** CrossRef, 377–386 (2006).

151. Shi, F. Introductory Chapter: Basic Theory of Magnetron Sputtering. *Magnetron Sputtering [Working Title].* https://www.intechopen.com/online-first/63559 (Nov. 2018).

152. Swann, S. Magnetron sputtering. *Physics in technology* **19,** 67 (1988).

153. Engineering, A. *Magnetron Sputtering Overview* https://angstromengineering.com/tech/magnetron-sputtering/. (Accessed on 12/25/2021).

154. Silva, H. F. M. D. *et al.* Obtaining an Optical Trap Type Surface by Plasma Electrolytic Oxidation. *Materials Research* **20,** 905–909. ISSN: 1516-1439. http://www.scielo.br/j/mr/a/ng7knwm4gr5dMP4V4KKVx3C/?lang=en (Mar. 2018).

155. Simchen, F., Sieber, M., Kopp, A. & Lampke, T. Introduction to plasma electrolytic oxidation-an overview of the process and applications. *Coatings* **10.** ISSN: 20796412 (2020).

156. Kailas, S. V. *Material Science* in (2007).

157. *corrosion types summary photo* https://mechasource.blogspot.com/2018/06/corrosion-types-summary-photo{_}30.html (2020).

158. Ghali, E., Dietzel, W. & Kainer, K.-U. General and localized corrosion of magnesium alloys: a critical review. en. *JMater Eng Perform* **13,** 7–23 (2004).

159. Ghali, E., Dietzel, W. & Kainer, K.-U. Testing of general and localized corrosion of magnesium alloys: a critical review. en. *JMater Eng Perform* **13,** 517–29 (2004).

160. Levesque, J., Hermawan, H. & D, D. Design of a pseudo-physiological test bench specific to the development of biodegradable metallic biomate- rials. en. *Acta Biomater* **4,** 284–95 (2008).

161. Li, N., Guo, C. & Y, W. Comparative study on corrosion behaviour of pure Mg and WE43 alloy in static, stirring and flowing Hank's solution. en. *Corrosion Eng Sci Technol* **47,** 346–51 (2012).

162. Ballerini, G., Bardi, U. & R, B. About some corrosion mechanisms of AZ91D magnesium alloy. cs. *Corrosion Sci* **47,** 2173–84 (2005).

163. Avedesian, M. & Baker, H. ASM Specialty Handbook: Magnesium And Magnesium Alloys. en. *ASM International, Acta Biomaterialia, Elsevier,* 274 (1999).

164. Song, G. Recent progress in corrosion and protection of magnesium alloys. fr. *Adv Eng Mater* **7,** 563–86 (2005).

165. Lafront, A., Zhang, W. & S, J. Pitting corrosion of AZ91D and AJ62x magnesium alloys in alkaline chloride medium using electrochemical techniques. fr. *Electrochim Acta* **51,** 489–501 (2005).

166. Arrabal, R., Mingo, B. & A, P. Pitting corrosion of rheocast A356 aluminium alloy in 3.5wt.NaCl solution. it. *Corrosion Sci* **73,** 342–55 (2013).

167. Winzer, N., Atrens, A. & G, S. A critical review of the stress corrosion cracking (SCC) of magnesium alloys. en. *Adv Eng Mater* **7,** 659–93 (2005).

168. M, B. K., W, D. & C, B. *Stress corrosion cracking of rare-earth containing magnesium alloys ZE41, QE22 and Elektron 21 (EV31A) compared with AZ80* en. Mater SciEngi A. 2008.

169. Cui, Z., Li, X. & K, X. Atmospheric corrosion of field-exposed AZ31 magnesium in a tropical marine environment. it. *Corrosion Sci* **76,** 243–56 (2013).

170. Chen, J., Wang, J. & E, H. ESEM observation of the process of hydrogen generation around the micro-droplets forming on AZ91 magnesium alloy. fr. *Electrochem Commun* **10,** 577–81 (2008).

171. Jones, R. The influence of hydrogen on the stress-corrosion cracking of low-strength Al-Mg alloys. en. *JOM* **55,** 42–6 (2003).

172. Song, R., Blawert, C. & al, D. W. A study on stress corrosion cracking and hydrogen embrittlement of AZ31 magnesium alloy. fr. *Mater Sci Eng A* **399,** 308–17 (2005).

173. Scamans, G., Holroyd, N. & Tuck, C. The role of magnesium segregation in the intergranular stress corrosion cracking of aluminium alloys. en. *Corrosion Sci* **27,** 329–47 (1987).

174. Aperador, W., Delgado, A. & Franco, F. Improved resistance to intergranular corrosion in the AZ31B magnesium alloy by friction stir welding. fr. *Int J Electrochem Sci* **8,** 9568–77 (2013).

175. Corrosionpedia. *What is a Flow Velocity? - Definition from Corrosionpedia* https://www.corrosionpedia.com/definition/528/flow-velocity (2020).

176. Marieb, E. N. E. & Hoehn, K. *Human Anatomy & Physiology, Ninth Edition* 1159. ISBN: 9780805395693 (2006).

177. Wang, J. *et al.* Flow-induced corrosion behavior of absorbable magnesium-based stents. *Acta biomaterialia* **10,** 5213–5223 (2014).

178. Wang, J., Smith, C. E., Sankar, J., Yun, Y. & Huang, N. Absorbable magnesium-based stent: physiological factors to consider for in vitro degradation assessments. *Regenerative Biomaterials.* ISSN: 2056-3418 (2015).

179. Lévesque, J., Hermawan, H., Dubé, D. & Mantovani, D. Design of a pseudo-physiological test bench specific to the development of biodegradable metallic biomaterials. *Acta biomaterialia* **4,** 284–295 (2008).

180. Doriot, P.-A. *et al.* In-vivo measurements of wall shear stress in human coronary arteries. *Coronary artery disease* **11,** 495–502 (2000).

181. Wentzel, J. J. *et al.* Coronary stent implantation changes 3-D vessel geometry and 3-D shear stress distribution. *Journal of biomechanics* **33,** 1287–1295 (2000).

182. Jun Kang, Y., Yeom, E. & Lee, S. J. A microfluidic device for simultaneous measurement of viscosity and flow rate of blood in a complex fluidic network. *Biomicrofluidics* **7.** ISSN: 19321058. /pmc / articles / PMC3799722 / ?report = abstracthttps : //www.ncbi.nlm.nih.gov/pmc/articles/PMC3799722/ (2013).

183. Gordon, D. & Lowe, O. Blood viscosity and cardiovascular diseases (1992).

184. Witte, F. *et al.* Degradable biomaterials based on magnesium corrosion. *Current Opinion in Solid State and Materials Science.* ISSN: 13590286. arXiv: 0006034v4 [arXiv:quant-ph] (2008).

185. Kirkland, N., Lespagnol, J., Birbilis, N. & Staiger, M. A survey of bio-corrosion rates of magnesium alloys. fr. *Corros. Sci* **52.** CrossRef, 287–291 (2010).

186. Liu, L. *et al.* Degradation Rates of Pure Zinc, Magnesium, and Magnesium Alloys Measured by Volume Loss, Mass Loss, and Hydrogen Evolution. *Applied Sciences.* ISSN: 2076-3417 (2018).

187. Kirkland, N. T., Birbilis, N & Staiger, M. P. Assessing the corrosion of biodegradable magnesium implants: A critical review of current methodologies and their limitations. *Acta Biomaterialia* **8,** 925–936 (2012).

188. King, A. D., Birbilis, N. & Scully, J. R. Accurate electrochemical measurement of magnesium corrosion rates; A combined impedance, mass-loss and hydrogen collection study. *Electrochimica Acta* **121,** 394–406. ISSN: 00134686 (2014).

189. Jang, Y., Collins, B., Sankar, J. & Yun, Y. Effect of biologically relevant ions on the corrosion products formed on alloy AZ31B: An improved understanding of magnesium corrosion. *Acta Biomaterialia.* ISSN: 17427061 (2013).

190. Benson, T., Nerem, R. & Pedley, T. Assessment of wall shear stress in arteries, applied to the coronary circulation. *Cardiovascular research* **14,** 568–576 (1980).

191. Gonzalez, J., Hou, R. Q., Nidadavolu, E. P., Willumeit-Römer, R. & Feyerabend, F. *Magnesium degradation under physiological conditions – Best practice* 2018.

192. Luo, Q. *et al.* Degradation model of bioabsorbable cardiovascular stents. *PLoS ONE.* ISSN: 19326203 (2014).

193. Otsuka, F. *et al. Acute Thrombogenicity of a Durable Polymer Everolimus-Eluting Stent Relative to Contemporary Drug-Eluting Stents with Biodegradable Polymer Coatings Assessed Ex Vivo in a Swine Shunt Model* 2015.

194. Boskey, E. *What In Vitro Means in Research Studies* https://www.verywellhealth.com/what-is-in-vitro-biological-3132872#citation-1 (2020).

195. Moleiro, A., Conceicao, G, Leite-Moreira, A. & Rocha-Sousa, A. A critical analysis of the available in vitro and ex vivo methods to study retinal angiogenesis. *Journal of ophthalmology* **2017** (2017).

196. Yun, Y. H., Dong, Z., Shanov, V. N. & Schulz, M. J. Electrochemical impedance measurement of prostate cancer cells using carbon nanotube array electrodes in a microfluidic channel. *Nanotechnology* **18,** 465505. ISSN: 0957-4484. https://iopscience.iop.org/article/10.1088/0957-4484/18/46/465505https://iopscience.iop.org/article/10.1088/0957-4484/18/46/465505/meta (46 Oct. 2007).

197. Labs, P. *Stent Fatigue Tester* https://protomedlabs.equipment/medical-device-testing/customized-equipment/stent-fatigue-tester/ (2020).

198. Services, M. D. T. *Instruments* https://devicetesting.com/tools_stent.cfm (2020).

199. Instron. *Fatigue Testing Stent Materials and Structures* https://www.instron.us/testing-solutions/by-test-type/high-cycle-fatigue/stent-materials (2020).

200. Labs, D. *UST Stent Tester* https://dynateklabs.com/ust-stent-tester/ (2020).

201. instruments, T. *Drug Coated Stent Devices* http://www.tainstruments.com/wp-content/uploads/TA_Drug-Coated-Stent-Devices.pdf (2020).

202. *SEM-EDX* https://www.nanophysics.nl/services-view/edx-analysis/ (2020).

203. *EDX Analysis with a Scanning Electron Microscope (SEM): How Does it Work? | Thermo Fisher Scientific - DE* https://www.thermofisher.com/de/de/home/global/forms/industrial/edx-analysis-sem.html (2020).

204. Lyman, C., Newbury, D., Goldstein, J & Williams, D. *Scanning electron microscopy, X-ray microanalysis, and analytical electron microscopy: a laboratory workbook* https://books.google.com/books?hl=en{\&}lr={\&}id=rG4KBwAAQBAJ{\&}oi=fnd{\&}pg=PA1{\&}dq=+Joseph+Goldstein+(2003).+Scanning+Electron+Microscopy+and+X-Ray+Microanalysis.+Springer.+ISBN+978-0-306-47292-3.+Retrieved+26+May+2012.{\&}ots=mnNdTVbVvi{\&}sig=5MIDS3K-jB1I5TGWqAStyLLvZ (2012).

205. *Micro-CT Imaging (Micro-computed Tomography) | PerkinElmer* https://www.perkinelmer.com/category/microct-imaging-micro-computed-tomography (2020).

206. *What is Micro-CT? An Introduction | Micro Photonics* https://www.microphotonics.com/what-is-micro-ct-an-introduction/ (2020).

207. *Micro CT | X-Ray Tomography | Thermo Fisher Scientific - DE* https://www.thermofisher.com/de/de/home/electron-microscopy/products/microct.html (2020).

208. *Inductively Coupled Plasma Mass Spectrometry (ICP-MS) | SHIMADZU EUROPA* https://www.shimadzu.eu/icp-ms (2020).

209. *ICP-MS - General Instrumentation* https://www.ru.nl/science/gi/facilities-activities/elemental-analysis/icp-ms/ (2020).

210. ASTM. ASTM G102 - 89 Standard Practice for Calculation of Corrosion Rates and Related Information from Electrochemical Measurements. *ASTM INTERNATIONAL* (2010).

211. Wong, L. L., Martin, S. I., Rebak, R. B., Columbia, B. & Wong Sue I Martin Raúl B Rebak, L. L. *Methods to Calculate Corrosion Rates for Alloy 22 from Polarization Resistance Experiments* in *ASME Pressure Vessels and Piping Conference* (2006), 571–580.

212. Grogan, J. A., Leen, S. B. & McHugh, P. E. A physical corrosion model for bioabsorbable metal stents. *Acta Biomaterialia.* ISSN: 18787568 (2014).

213. Grogan, J. A., Leen, S. B. & McHugh, P. E. Computational micromechanics of bioabsorbable magnesium stents. *Journal of the Mechanical Behavior of Biomedical Materials.* ISSN: 17516161 (2014).

214. Ma, Z. M., Dong, H. Y. & Qi, M. A Study on Fatigue Test for Cardiovascular Stent. *Applied Mechanics and Materials* **157-158,** 197–201. ISSN: 1662-7482. https://www.scientific.net/AMM.157-158.197 (2012).

215. Pelton, A. *et al.* Fatigue and durability of Nitinol stents. *Journal of the Mechanical Behavior of Biomedical Materials* **1,** 153–164. ISSN: 1751-6161. https://www.sciencedirect.com/science/article/pii/S1751616107000161?via{\%}3Dihub (2008).

216. Hertel, M. *Elektrochemische Charakterisierung von Stents mit Hilfe des adaptierten Mini- Cell- Systems (MCS) - Teil II* PhD dissertation (Charité-Universitätsmedizin Berlin, 2012), 1–50.

217. Hertel, M., Laule, M., Zinelis, S., Imiolczyk, S. M. & Mueller, W.-D. Electrochemical characterization of vascular bare-metal stents. A novel approach modifying the mini-cell system. *SDRP journal of biomedical engineering* **1,** 1–11 (2016).

218. Károly, D., Asztalos, L. & Fazakas, É. *CORROSION BEHAVIOUR OF OVERLAPPING CORONARY ARTERY STENTS* in *34th Danubia-Adria Symposium on Advances in Experimental Mechanics* (Trieste, Italy, 2017), 1–3.

219. Károly, D., Kovács, M., Terdik, A. A. & Bognár, E. Investigation of metallic surface area of coronary stents. *Biomechanica Hungarica* **6,** 205–212 (2013).

220. Kovács, M., Károly, D. & Dévényi, L. Comparing two examination methods for measuring metal to artery ratio of coronary stents. *Materials Science Forum* **812,** 113–118. ISSN: 02555476 (2015).

221. ISO. *ISO 25539-2: Cardiovascular implants-Endovascular devices-Part 2: Vascular stents* tech. rep. (2012).

222. Wang, Z. *et al.* Biological behavior exploration of a paclitaxel-eluting poly-l-lactide-coated Mg-Zn-Y-Nd alloy intestinal stent: In vivo. *RSC Advances* **10,** 15079–15090. ISSN: 20462069 (2020).

223. Barrere, F, Van Blitterswijk, C. A., De Groot, K & Layrolle, P. *Nucleation of biomimetic Ca-P coatings on Ti6Al4V from a SBF Â 5 solution: influence of magnesium* tech. rep. (2002), 2211–2220.

224. Saqib, M. *et al. Application of μCT for the determination of total surface area of stents* in *2019 7th E-Health and Bioengineering Conference, EHB 2019* (Institute of Electrical and Electronics Engineers Inc., Iasi, 2019). ISBN: 9781728126036.

225. Saqib, M. *et al.* Determination of the Entire Stent Surface Area by a New Analytical Method. *Materials* **13,** 5633. ISSN: 1996-1944. https://www.mdpi.com/1996-1944/13/24/5633 (2020).

226. Saqib, M. *et al.* Evaluation of in vitro corrosion behavior of titanium oxynitride coated stainless steel stents. *IEEE Access,* 1–1. ISSN: 21693536 (2021).

227. Li, L. Y. *et al.* In vitro corrosion of magnesium alloy AZ31 — a synergetic influence of glucose and Tris. *Frontiers of Materials Science* **12,** 184–197. ISSN: 20950268 (2018).

228. Tkacz, J. *et al.* Influence of the composition of the hank's balanced salt solution on the corrosion behavior of AZ31 and AZ61 magnesium alloys. *Metals* **7,** 1–17. ISSN: 20754701 (2017).

229. Augthun, M., Tinschert, J. & Huber, A. In Vitro Studies on the Effect of Cleaning Methods on Different Implant Surfaces. *Journal of Periodontology* **69,** 857–864. ISSN: 0022-3492 (1998).

230. Kokubo, T. & Takadama, H. How useful is SBF in predicting in vivo bone bioactivity? *Biomaterials* **27,** 2907–2915. (2020) (May 2006).

231. Kasuga, T., Kondo, H. & Nogami, M. Apatite formation on TiO2 in simulated body fluid. *Journal of Crystal Growth* **235,** 235–240. ISSN: 00220248 (2002).

232. Jalota, S., Bhaduri, S. B. & Tas, A. C. Effect of carbonate content and buffer type on calcium phosphate formation in SBF solutions. *Journal of Materials Science: Materials in Medicine* **17,** 697–707. ISSN: 09574530. https://link.springer.com/article/10.1007/s10856-006-9680-1 (2006).

233. Kokubo, T., Kushitani, H., Sakka, S., Kitsugi, T. & Yamamuro, T. Solutions able to reproducein vivo surface-structure changes in bioactive glass-ceramic A-W3. *Journal of Biomedical Materials Research* **24,** 721–734. (2021) (June 1990).

234. Instruments, L. *EDX Spectra for PELCO Tabs™ and Spectro Tabs* http://loeneninstruments.com/sites/html/tabs_tapes_sheets.html. (Accessed on 04/08/2022).

235. ISO. *ISO 10993-15 : 2019 - Biological evaluation of medical devices - Part 15 : Identification and quantification of degradation products from metals and alloys* 2019. https://www.iso.org/standard/68937.html.

236. Scanlon, V. C. & Sanders, T. *Essentials of Anatomy and Physiology* Fifth. ISBN: 9780803615465 (F. A. Davis, 2007).

237. Hajar, H. M., Zulkifli, F., Suriani, M. J., Mohd Sabri, M. G. & Wan Nik, W. B. Lawsonialnermis Extract Enhances Performance of Corrosion Protection of Coated Mild Steel in Seawater. *MATEC Web of Conferences* **78.** ISSN: 2261236X (2016).

238. Wang, Z. *et al.* Effect of temperature on electrochemical corrosion of Zn-30Sn lead-free solder. *Proceedings - 2018 19th International Conference on Electronic Packaging Technology, ICEPT 2018,* 10–14 (2018).

239. Bates, M. C., Campbell, J. R. & Campbell, J. E. Late complication of stent fragmentation related to the "lever-arm effect". *Journal of Endovascular Therapy* **15,** 224–230. ISSN: 15266028 (2008).

240. Halwani, D. O., Anderson, P. G., Brott, B. C., Anayiotos, A. S. & Lemons, J. E. Clinical device-related article surface characterization of explanted endovascular stents: Evidence of in vivo corrosion. *Journal of Biomedical Materials Research - Part B Applied Biomaterials* **95,** 225–238. ISSN: 15524973 (2010).

241. Moretoa, J. A. *et al.* Effect of temperature, electrolyte composition and immersion time on the electrochemical corrosion behavior of CoCrMo implant alloy exposed to physiological serum and Hank■*ssolution*. *Materials Research* **21.** ISSN: 15161439 (2018).

242. Calderon, S., Alves, C. F. A., Manninen, N. K., Cavaleiro, A. & Carvalho, S. Electrochemical Corrosion of Nano-Structured Magnetron-Sputtered Coatings. *Coatings* **9,** 682. ISSN: 2079-6412 (10 Oct. 2019).

243. Witte, F. *et al.* In vivo corrosion of four magnesium alloys and the associated bone response. *Biomaterials* **26,** 3557–3563. ISSN: 0142-9612 (2005).

244. Ascencio, M., Pekguleryuz, M. & Omanovic, S. An investigation of the corrosion mechanisms of WE43 Mg alloy in a modified simulated body fluid solution: The influence of immersion time. *Corrosion Science* **87,** 489–503. ISSN: 0010-938X (2014).

245. Ascencio, M., Pekguleryuz, M. & Omanovic, S. An investigation of the corrosion mechanisms of WE43 Mg alloy in a modified simulated body fluid solution: The effect of electrolyte renewal. *Corrosion Science* **91,** 297–310. ISSN: 0010-938X (2015).

246. Mao, L. *et al.* A promising biodegradable magnesium alloy suitable for clinical vascular stent application. *Scientific Reports 2017 7:1* **7,** 1–12. ISSN: 2045-2322. https://www.nature.com/articles/srep46343 (2017).

247. Song, G. & Song, S. A Possible Biodegradable Magnesium Implant Material. *Advanced Engineering Materials* **9,** 298–302. ISSN: 1527-2648. https://onlinelibrary.wiley.com/doi/full/10.1002/adem.200600252https://onlinelibrary.wiley.com/doi/abs/10.1002/adem.200600252https://onlinelibrary.wiley.com/doi/10.1002/adem.200600252 (2007).

248. Xiong, H. *et al.* Mechanical Properties and Degradation Behavior of Mg(100-7x)Zn6xYx(x = 0.2, 0.4, 0.6, 0.8) Alloys. *Metals 2018, Vol. 8, Page 261* **8,** 261. https://www.mdpi.com/2075-4701/8/4/261/htmhttps://www.mdpi.com/2075-4701/8/4/261 (2018).

249. Veleva, L., Fernández-Olaya, M. G. & Feliu, S. Initial Stages of AZ31B Magnesium Alloy Degradation in Ringer´s Solution: Interpretation of EIS, Mass Loss, Hydrogen Evolution Data and Scanning Electron Microscopy Observations. *Metals.* ISSN: 2075-4701 (2018).

250. Duygulu, O., Kaya, R. A., Oktay, G. & Kaya, A. A. Investigation on the Potential of Magnesium Alloy AZ31 as a Bone Implant. *Materials Science Forum* **546-549,** 421–424. ISSN: 1662-9752. https://www.scientific.net/MSF.546-549.421 (2007).

251. Srinivasan, A., Shin, K. S. & Rajendran, N. Influence of bicarbonate concentration on the conversion layer formation onto AZ31 magnesium alloy and its electrochemical corrosion behaviour in simulated body fluid. *RSC Advances* **6,** 49910–49922. ISSN: 2046-2069. https://pubs.rsc.org/en/content/articlehtml/2016/ra/c6ra08478hhttps://pubs.rsc.org/en/content/articlelanding/2016/ra/c6ra08478h (2016).

252. Gray-Munro, J. E., Seguin, C. & Strong, M. Influence of surface modification on the in vitro corrosion rate of magnesium alloy AZ31. *Journal of Biomedical Materials Research Part A* **91A,** 221–230. ISSN: 1552-4965. https://onlinelibrary.wiley.com/doi/full/10.1002/jbm.a.32205https://onlinelibrary.wiley.com/doi/abs/10.1002/jbm.a.32205https://onlinelibrary.wiley.com/doi/10.1002/jbm.a.32205 (2009).

253. Zhang, L., Zhang, J., fu Chen, C. & Gu, Y. Advances in microarc oxidation coated AZ31 Mg alloys for biomedical applications. *Corrosion Science* **91,** 7–28. ISSN: 0010-938X (2015).

254. Menzies, K. L. & Jones, L. The impact of contact angle on the biocompatibility of biomaterials. *Optometry and Vision Science* **87,** 387–399. https://journals.lww.com/optvissci/Fulltext/2010/06000/The{_}Impact{_}of{_}Contact{_}Angle{_}on{_}the.4.aspx (2010).

255. Gogineni, A. Flow characteristics and wall shear stresses in bifurcated peripheral arteries. PhD Dissertation (2015).